GPS tropospheric modelling: new developments and insights

Salim Masoumi

A thesis submitted for the degree of
Doctor of Philosophy
of the Australian National University

August 2018

Except where otherwise indicated, this thesis is my own original work.

Salim Masoumi
3 August 2018

To my beloved mother and father.

Acknowledgements

First and foremost, I would like to thank my supervisor, Simon McClusky, for his continued support during the ups and downs of my PhD research. Simon was a great support for me in learning new skills and gaining new knowledge. Like any research project, I experienced both enjoyable and unpleasant days, but I am extremely grateful to have a supervisor who was always there to help me, and always encouraged me to proceed even at the times when my research did not go as expected. I would also like to thank my advisers Paul Tregoning, Achraf Koulali, and Peter Steinle for their help and encouragement throughout my PhD studies. Paul helped me a lot with his thoughtful comments and with publishing a paper on modelling tropospheric horizontal gradients in GPS analysis. Achraf was an amazing advisor and friend with whom I spent a lot of time discussing research problems. I would also like to acknowledge Thomas Herring for his helpful comments throughout my PhD research.

I would like to thank the postdocs and PhD candidates in the Research School of Earth Sciences at ANU who were all great colleagues and friends, making my PhD experience more enjoyable. In particular, I would like to acknowledge Michael Moore and Sebastien Allgeyer. Mike kindly provided his ESM code to me which I could then use for my tropospheric modelling studies. Sebastien helped me a lot in improving my Python knowledge.

My friends in the Graduate and University House helped a lot to make the past few years an enjoyable experience for me. I am extremely delighted that I could find such an amazing group of friends, and I am sure our friendship will last forever. I was lucky to find Iranian friends here in Canberra who were so supportive and kind-hearted that I felt at home from the very beginning of my PhD life. Among the very long list of people I am deeply thankful to, I would like to mention Mehdi, Alireza, Ehsan and Hajar for their support, advice and help at different stages of my PhD.

Last but not least, I would like to thank my beloved family. My parents were the first people who encouraged me to pursue learning the unknown, and they did whatever they could to support me doing that. My brother Salman was a great role model for me during my school days. Finally, my dearest sister Sahar always brought excitement and enthusiasm to my life by her endless energy and support even from afar over the past few years.

Abstract

GPS is widely used to monitor temporal and spatial variations of Earth's crust, oceans and atmosphere. Of particular interest to this research is the use of GPS for studying variations in the Earth's lower atmosphere. While there have been significant advances in the techniques and models used in GPS analyses over the past two decades, there is still room for improvement. In particular, observations at very low elevation angles still suffer greatly from modelling errors. These low-elevation observations provide useful information about the moisture content of the atmosphere and its variability around a GPS station, and are thus valuable data for meteorological studies if properly modelled.

The main focus of this thesis is on optimization of the techniques and models used in GPS analysis for more accurate estimates of the tropospheric delays. Particular attention is paid to modelling low-elevation observations and challenging weather conditions. Throughout the thesis, we investigate several different aspects of modelling techniques and how each of them affect the tropospheric estimates.

By applying a previously developed empirical model [Moore, 2015], the site-specific errors are shown to have large impacts on the tropospheric delay estimates: empirical mitigation of site-specific errors leads to improved repeatabilities of heights and tropospheric zenith delays for the majority of the stations in our analysis. The empirical site-specific model also significantly reduces the sensitivity of tropospheric zenith delay estimates to the choice of elevation cut-off.

Another important potential source of error, the GPS estimates of tropospheric horizontal gradients are shown to be more accurate than the model values currently available. However, the conventional two-axis planar model of gradients does not accurately represent the actual gradients of the refractivity under weather conditions with asymmetric horizontal changes of refractivity. Such abnormal conditions may occur due to topography-driven gravity waves in the troposphere, and the mismodelled tropospheric horizontal gradients induce errors in the parameter estimates, sometimes leading to skewed position time series and inaccurate tropospheric zenith delays. A new parametrization of tropospheric gradients whereby an arbitrary number of gradients are estimated as discrete directional wedges is shown via both simulations and real case studies to largely improve the accuracy of recovered tropospheric zenith delays in asymmetric gradient scenarios. The new directional model significantly improves the repeatabilities of the station height time series in asymmetric gradient situations while causing slightly degraded repeatabilities for the stations in normal symmetric gradient conditions.

The constraints on the temporal variations of the tropospheric delays are also investigated. It is shown via simulations and real experiments that it is generally preferable to avoid constraints on both tropospheric zenith delays and horizontal

gradients. However, since the conventional model of horizontal gradients oversimplifies the horizontal variations of the refractivity in asymmetric gradient conditions, it is important to use a more complete model of gradients like the directional gradient model introduced in this thesis in conjunction with the relaxed constraints to avoid errors caused by the simplifying assumption of symmetric gradients by the conventional model.

Contents

List of Figures

List of Tables

Chapter 1

Introduction

Severe weather events can lead to both human loss and economic damage to societies. Much of the damage is caused by flash flooding following unforecasted extreme precipitation events. Examples of such heavy rainfall events in Australia are the Queensland floods in December 2010 and January 2011, which resulted in at least 33 deaths and a minimum estimated cost of $5 billion [Holmes, 2012; Queensland Reconstruction Authority, 2011]. Numerical weather prediction (NWP) models are able to help governments foresee the possible occurrence of extreme rainfalls by solving initial value problems that simulate the future state of the atmosphere given an estimate of its current state. In addition to the need for a realistic model of the atmosphere, an initial value problem requires accurate initial conditions in order to make accurate forecasts [Kalnay, 2003]. In addition to traditional ground-based and satellite observations, tropospheric zenith total delays (ZTD) or precipitable water (PW) derived from Global Positioning System (GPS) are important measurements that can be assimilated into a NWP [e.g. Bennitt and Jupp, 2012]. The GPS-derived zenith delays need to satisfy both accuracy and latency requirements for data assimilation purposes. In addition to the use of GPS-derived zenith delays as input data for operational assimilation systems, some research has been dedicated to investigating the relationship between water vapour accumulation and precipitation systems [e.g. Champollion et al., 2004; Van Baelen et al., 2011; Labbouz et al., 2015].

For over two decades, techniques and models used in GPS processing have been continuously improved. Much improvement has been achieved in troposphere delay models used in GPS analyses, including the implementation of stochastic process models as constraints on temporal changes of tropospheric delays [Herring et al., 1990], time-varying mapping functions used as partials for zenith total delays [Böhm et al., 2006b], estimation of tropospheric horizontal gradients to compensate for the symmetry of mapping functions [Chen and Herring, 1997; Bar-Sever et al., 1998], and a priori modelling of hydrostatic part of the ZTD [Tregoning and Herring, 2006].

Despite the above (and several other) improvements in modelling tropospheric delays, there is still room for further improvement. Spatial asymmetry of the tropospheric refractivity field remains a challenge particularly in extreme weather scenarios. Although the model of tropospheric horizontal gradients introduced by Chen and Herring [1997], which assumes a two-axis tilted plane for the refractivity field of the troposphere, is able to well represent the tropospheric gradients at most at-

mospheric conditions, it fails to provide an accurate representation of the gradients where there are isolated and rapid spatial changes of tropospheric refractivity at discrete azimuths around a GPS station. Site-specific errors, including multipath and incomplete receiver antenna models, are other sources of error that impact the estimates of tropospheric delay [Moore et al., 2014], and therefore should be mitigated during or before the GPS processing for the generation of tropospheric products.

While several sets of observations, including but not limited to measurements from land surface stations, ships and drifting buoys, radiosondes, atmospheric infrared sounding and GPS radio occultation measurements, are now being operationally assimilated into the Australian Community Climate and Earth System Simulator (ACCESS) suite of NWP systems operated by the Australian Bureau of Meteorology [Bureau of Meteorology, 2010], ZTD data from the ground-based GPS measurements of more than 450 stations across Australia are yet to be assimilated into the ACCESS systems. Hence, it is now an appropriate time to perform research on strategies and processing techniques for the purpose of generating tropospheric products with focus on challenging weather conditions where the conventional techniques are not able to accurately recover the tropospheric delays.

Under normal stable atmospheric conditions, tropospheric zenith delays can be retrieved with accuracies of around 6-16 mm [e.g. Tregoning et al., 1998; Liou et al., 2001; Braun et al., 2003; Pérez-Ramírez et al., 2014] from GPS measurements, but we are generally limited to the use of GPS observations at elevation angles higher than about 7-10°, because the low-elevation observations are typically contaminated by unmodelled errors, including multipath, incomplete antenna models, and errors in modelling of horizontal gradients. By improving the modelling of low-elevation observations, one can improve the accuracy of tropospheric slant (line-of-sight) delays, which can in turn be used in GPS tomography applications, and provided that they reach sufficient accuracy, can eventually replace zenith delays in the assimilations into numerical weather prediction models. The use of low-elevation signals in GPS analyses also provides more information on the spatial variabilities of the tropospheric refractivity in terms of tropospheric horizontal gradients, which gives the researchers a tool to study particular weather phenomena.

This thesis aims to investigate recent advances in GPS modelling and their impacts on the estimates of tropospheric delays, as well as to develop new techniques and methodologies for better modelling the tropospheric delay, with particular attention on challenging weather conditions and modelling of low-elevation observations. Focus will be made on the aspects that have been understudied previously. For instance, Tregoning and Watson [2009] performed an extended study on several atmospheric modelling techniques such as mapping functions and a priori modelling of hydrostatic delays, and we refrain from repeating tests on these models. The major issues addressed in this thesis are as follows. The impact of including low-elevation measurements in GPS analysis is discussed in Chapter 3; the errors present in low-elevation observations, including site-specific errors and horizontal gradients, are discussed in the same chapter. The empirical site-specific model (ESM) developed by Moore et al. [2014] will be investigated and will be shown to consistently

reduce the repeatability of the position time series, including the height time series, leading to more accurate tropospheric delay estimates, particularly when including low-elevation observations. The North-South and East-West horizontal gradients of the troposphere estimated from a GPS analysis will be shown to be more accurate than the the gradients derived from the European Centre for Medium Range Weather Forecasts (ECMWF) reanalysis, leading to a conclusion that these planar tropospheric gradients are well captured by the current GPS modelling techniques, but the planar assumption for the horizontal gradients may not be an accurate model in particular weather conditions. A new directional model of tropospheric horizontal gradients will be introduced in Chapter 4. We will provide evidence through the simulations that this directional model of gradients is able to provide a more accurate representation of the tropospheric refractivity than the conventional model in particular weather situations with asymmetric gradient conditions, leading to significant improvements in the accuracy of height and zenith delay estimates. We will also show through several case studies that the directional gradient model removes the majority of outliers in the height time series of stations in particular weather scenarios, leading to improved zenith delay estimates, and provides a more accurate image of the tropospheric horizontal gradients. In Chapter 5, the choice of temporal constraints on tropospheric parameters is discussed. The investigation into the effect of temporal constraints on tropospheric parameters shows that it is generally preferable to apply loose constraints on these parameters no matter how much of a priori information there is about the temporal changes of the tropospheric refractivity.

This thesis provides a comprehensive framework for analysts who are interested in producing tropospheric estimates from GPS observations for a range of applications including but not limited to the use of ZTD estimates in the assimilation systems, studying the spatial movements of atmospheric moisture during particular weather phenomena such as rapid transitions of water vapour in severe storm events, GPS tomography applications, and use of the tropospheric slant delays for GPS tomography or assimilation purposes. Moreover, the results from Chapter 4 of this study are able to solve issues regarding highly scattered time series of positions in GPS analyses that are imposed by improper modelling of horizontal gradients of the troposphere.

1.1 Thesis Outline

Several distinctly different aspects of tropospheric delay modelling in GPS processing are discussed in this thesis; while the chapters are ordered in a way that allows each to be read independently, they also follow each other in a logical way. It is recommended that a reader who is less familiar with the tropospheric modelling in GPS data analysis first reads Chapter 2, which summarizes the theory underlying the modelling of tropospheric delay in GPS signals and provides a brief history of developments made by different authors to improve the technique. While the chapters can be read independently, they are primarily sorted by the order the verified techniques

are used; e.g. after the positive impact of the ESM is presented in Chapter 3, the ESM is used in all other analyses in the next chapters. However, we have tried to make minimum reference to the previous chapters as much as possible. A detailed outline of the following chapters of this thesis is given below:

- **Chapter 2: Background** - Provides an overview of tropospheric delay modelling in GPS analysis and how it has developed over time. This chapter also presents the processing strategies and briefly describes the simulation technique and case studies that are studied in the thesis.

- **Chapter 3: Low-elevation observations, site-specific errors and tropospheric horizontal gradients** - This chapters starts from a discussion of the effect of including low-elevation observations in GPS analysis and the scheme used for weighting the observations. Some possible sources of errors present in low-elevation phase observations, including site-specific errors and improper modelling of the tropospheric horizontal gradients, are then discussed. The impact of an empirical site-specific model on the estimates of ZTD in the GPS analysis is studied. Finally, the North-South and East-West tropospheric gradients are compared with the ray-traced gradients, and an introduction is given about the possible inaccuracies in modelling the tropospheric horizontal gradients.

- **Chapter 4: Directional model of tropospheric horizontal gradients** - Introduces a new parametrisation of tropospheric horizontal gradients that estimates the gradients in distinct azimuths around a GPS station rather than estimating them as a two-axis tilted plane. Simulations are performed to verify the capability of the new directional model to recover the gradients and its impact on tropospheric and position components, and a few real case studies are analysed with the new and with the conventional model of gradients to study the impacts in real situations.

- **Chapter 5: Temporal constraints on tropospheric parameters** - Investigates the impact of process noise levels on the tropospheric parameters, and whether having a priori information on the temporal variations of these parameters enables to reduce the correlations between tropospheric parameters and position components (particularly heights), thus leading to more accurate estimates.

- **Chapter 6: Conclusion** - Gives a summary of our findings in this thesis, provides recommendations for the analysts who carry out GPS processing with the purpose of tropospheric and meteorological applications, and underscores possible future directions for this area of research.

Chapter 2

Background

The delay in GPS L-band frequency signals caused by the presence of atmospheric water vapour molecules is widely used for monitoring temporal and spatial changes of the troposphere using permanent ground-based GPS stations. The information retrieved from GPS observations is generally in the form of tropospheric zenith total delay that could also be converted into precipitable water above the GPS site [Bevis et al., 1992]. This chapter provides background information on GPS estimation in general and modelling of the tropospheric delay in particular. We start with a brief review of the GPS observables used in our study. We then introduce the models that are chosen to be used throughout this thesis based on the previous studies, and the parameters we estimate. Then we focus on the tropospheric parameters and the models used for estimating them. Some of the most important improvements over the past two decades in modelling techniques for tropospheric estimation are discussed. In the last section, we describe the simulation technique and the case studies that will be used for this research.

2.1 GPS observables, modelling and parameters

The GPS system works on the basis of measurements of microwave frequency signals transmitted by a set of GPS satellites revolving around the earth and tracked by the receivers on the ground (or sometimes on-board other satellites). The most common frequencies currently tracked by GPS receivers are L_1 with a frequency of $f_1 = \sim$1.58 GHz (wavelength of 19.0 cm) and L_2 with a frequency of $f_2 = \sim$1.23 GHz (wavelength of 24.4 cm). The basic observables generally used in GPS estimation are the code pseudorange and carrier phase observations. The code pseudorange observable P_r^s for a GPS signal transmitted from satellite s and received by a receiver s is the measured difference between the transmission time of the signal in the satellite time scale and the arrival time of the signal in the receiver time scale, and can be written in meters in a reference time scale called the GPS time (t) as

$$P_r^s(t) = \rho_r^s(t) + c(\delta t_r(t) - \delta t^s(t)) + d_{ion}(t) + d_{trop}(t) + \varepsilon(P(t)) \tag{2.1}$$

where $\rho_r^s(t)$ is the geometric distance (in meters) between the satellite s and the receiver s at GPS time t, c is the speed of light (m/sec), $\delta t_r(t)$ and $\delta t^s(t)$ are the receiver and satellite clock offsets from the GPS time in seconds, $d_{ion}(t)$ and $d_{trop}(t)$ are the delays caused by the passage of the signal through the ionosphere and troposphere (in meters), and $\varepsilon(P(t))$ contains measurement errors and other unmodelled delays in the code pseudorange observable.

A much less noisy observable of the GPS signals is the measured difference in the carrier phases of the transmitted signal in the satellite and the received signal in the receiver, which can be referred to as carrier phase or simply phase observable ($\phi_r^s(t)$) and can be written in units of meters as

$$\phi_r^s(t).\lambda = \rho_r^s(t) + c(\delta t_r(t) - \delta t^s(t)) + \lambda.N - d_{ion}(t) + d_{trop}(t) + \varepsilon(P(t)) \tag{2.2}$$

where λ is the frequency of the carrier phase, N is the integer number of cycles of phase between the satellite and receiver before the receiver is locked on tracking the signal, and is called the initial phase ambiguity. Note that unlike the code pseudorange observation, the ionosphere advances the phase measurement.

The geometric distance between the satellite and the receiver (ρ_r^s in Equation 2.1 and 2.2) implicitly contains the Cartesian coordinates of both satellite and receiver. One may choose to either estimate the satellite coordinates along with the receiver coordinates, or model the satellite coordinates using predetermined satellite orbit information.

Linear combinations of the observables may be used to eliminate or reduce some of the terms represented in Equation 2.1 and 2.2. For example, one can use the dispersive property of the ionosphere for microwave frequencies (which means that the ionospheric effect is frequency-dependent) and form the so-called ionosphere-free combination

$$L_3 = \frac{1}{f_1^2 - f_2^2}(f_1^2 L_1 - f2^2 L_2) \tag{2.3}$$

which is free of the first-order ionospheric delay. In the above equation, L_1 and L_2 could be replaced by either of phase or code observables of L_1 and L_2 frequencies to form ionosphere-free phase observable or ionosphere-free code observable.

By differencing the observables between receivers, satellites and/or time epochs one can further eliminate or reduce some of the delays in Equation 2.1 and 2.2. By differencing observations between two receivers (forming a single-difference observable), the common clock offsets of the satellite is removed, and by further differencing measurements between two satellites (forming a double-difference observable) the receiver clock offsets are also removed from the observation equations. However, some of the terms still remain after using such combinations and/or differences and need to be modelled. For instance, the tropospheric delay can not be removed by using a linear combination of the observations because unlike the ionosphere, the troposphere is a non-dispersive medium for the microwave frequencies; i.e. the delay caused by the troposphere does not depend on the frequency of the signal. For more comprehensive description of the GPS system, signal structure, and the observables

the reader is referred to e.g. Seeber [2003], Hofmann et al. [2001], Xu and Xu [2016], and Wells et al. [1987].

In this thesis, double-differenced ionosphere-free carrier phase observations are used to eliminate satellite and receiver clock offsets and the first-order ionospheric delay. The International Global Navigation Satellite Systems (GNSS) Service (IGS) final orbit products [Dow et al., 2009] are used to model the satellite coordinates, and we do not attempt to estimate adjustments to the satellite positions. A summary of the models that are generally used in the experiments in this thesis is given in Table 2.1. We use IERS values [McCarthy and Petit, 2004] for the diurnal and semi-diurnal terms of the earth orientation parameters (EOP), and do not attempt to estimate the EOP. The yaw attitudes of satellites during eclipse period are modelled using the equations introduced by Kouba [2009], the BERNE model for direct solar radiation pressure [Springer et al., 1999] is applied, and the EGM2008 Earth gravitational field [Pavlis et al., 2012] is used. IGS ANTEX files are used for modelling the Phase Centre Variations (PCV) and Phase Centre Offsets (PCO) of both satellite and receiver antennas [Schmid et al., 2007]. Atmospheric pressure loading is corrected for tidal (S1+S2) and non-tidal loading at the observation level. Ocean tidal loading is also corrected by the FES2004 model [Lyard et al., 2006], and solid earth tides are applied using IERS 2003 convention [McCarthy and Petit, 2004].

The modelling of satellite positions, elimination of the ionospheric delay using the ionosphere-free linear combination, and removal of clock offsets in the double-difference, and modelling the remaining effects using the models detailed in Table 2.1 leaves the estimation of Cartesian positions of the stations, the tropospheric delay, and phase ambiguities (see Equation 2.2).

The phase ambiguity resolution is attempted using the algorithms described in Herring et al. [2016] and Blewitt [1989]. The station positions and tropospheric delays are estimated in a least-squares approach. The station positions are estimated once a day; i.e. we assume that the position of the stations remain constant throughout a day. The models used for the estimation of tropospheric delays are described in detail in Section 2.2.

We process the observations using GAMIT software [Herring et al., 2015b], which uses a least squares approach for estimating the solution parameters in daily batch processing. The solution is performed in at least two iterations; a pre-fit solution with 10-minute sampling interval of the observations is run to update model parameters, and a second post-fit solution is then run with 2-minute sampling interval. If the fit is significantly improved from the pre-fit to post-fit solution, a third iteration will be run to ensure linear adjustments. An elevation-dependent weighting is applied to the observations that uses the following equation as the variance of the observations:

$$\sigma^2 = a^2 + \frac{b^2}{\sin^2(\varepsilon)} \tag{2.4}$$

where ε is the elevation angle of the observation. The values of a and b are predefined for the pre-fit solution but are determined for the post-fit solution by fitting Equation 2.4 to the one-way phase residuals from the pre-fit solution. Clock correc-

Model/Parameter	Setting
Software	GAMIT 10.5 [Herring et al., 2015b]
Orbits	IGS final orbits (fixed) [Dow et al., 2009]
Data weighting	Elevation-dependent
Reweight data	Yes, based on the phase residuals of the first iteration
Ambiguity resolution	Resolved using wide-lane combination [e.g. Bock and Melgar, 2016]
Zenith delay estimation interval	2 h
Zenith delay a priori source	VMF1 [Böhm et al., 2006b] for ZHD; GPT + Saastamoinen [1972] for ZWD (ZWD residuals still estimated)
Zenith delay constraints on the daily mean value	0.5 m
Zenith delay point-to-point variance	0.02 m/$\sqrt{\text{h}}$
Zenith delay correlation time	100 h
Zenith delay mapping functions	VMF1 [Böhm et al., 2006b] for both hydrostatic and wet parts
Gradient estimation interval	6 h
Gradient constraints for overall level	0.03 m
Gradient point-to-point variance	0.01 m/$\sqrt{\text{h}}$
Gradient correlation time	100 h
Gradient mapping function	Chen and Herring [1997]
Position constraints	5 cm
Solid earth tide model	IERS 2003 [McCarthy and Petit, 2004]
Ocean loading	FES2004 [Lyard et al., 2006]
Atmospheric loading	Tidal and nontidal applied at observation level [Tregoning and Watson, 2009]
Antenna phase variations	IGS 08 [Schmid et al., 2007]
Satellite Yaw	Kouba [Kouba, 2009]
Earth gravitational field	EGM2008 [Pavlis et al., 2012]
Solar radiation pressure	BERNE [Springer et al., 1999]
A priori coordinates	ITRF2008 [Altamimi et al., 2011]

Table 2.1: Processing strategies applied to most of the GPS analyses performed in this thesis. Unless otherwise stated, all the analyses are performed using these settings.

tions are estimated from code observations and removed from the one-way phase residuals.

Unless otherwise stated, we apply loose constraints to station positions and tropospheric parameters to ensure unbiased adjustments to these parameters when testing new models. After performing the least-squares solution using GAMIT, we use GLOBK [Herring et al., 2015a] to run a Kalman filter on the GAMIT solutions, and

generate position time series. The Kalman filter takes in the primary daily position estimates (with loose constraints on the uncertainties) with the relevant covariance matrices as "quasi-observations", and generates time series of the positions. The measurement precision can be assessed using the repeatability of the time series. A description of the Kalman filtering algorithms in geodetic analyses is provided by Herring et al. [1990].

2.2 Tropospheric delay modelling in GPS analyses

In GPS analysis, the troposphere is usually considered to be azimuthally symmetric around the zenith direction above the GPS station. This symmetric delay (L_{sym}) is separated into hydrostatic (dry) and wet parts. The hydrostatic component of the tropospheric delay is due to the induced dipole moment of the dry atmosphere, and the wet part is related to the permanent dipole moment of water vapour [Saastamoinen, 1972; Davis et al., 1985; Duan et al., 1996]. Each of the hydrostatic and wet parts of the tropospheric delay is mapped from the zenith direction to the elevation angle of the observation by the use of an elevation-dependent-only mapping function, as described e.g. by Davis et al. [1985]:

$$L_{sym}(\varepsilon) = L_h^z m_h(\varepsilon) + L_w^z m_w(\varepsilon) \tag{2.5}$$

where L_h^z and L_w^z are tropospheric delays for the hydrostatic and wet components at zenith direction, ε is the elevation angle of the observation, and $m_h(\varepsilon)$ and $m_w(\varepsilon)$ are mapping functions for the hydrostatic and wet components.

In carrier phase geodetic analyses, the zenith wet delay (L_w^z or ZWD) is estimated together with other estimation parameters in a least-squares solution, since the wet part is difficult to model due to the highly variable nature of water vapour in the atmosphere. Also, direct measurement of the water vapour above each GPS station (using radiometers e.g.) is too expensive to be practically applied. The hydrostatic part, which is larger in magnitude but less variable and easier to model, is usually fixed to an a priori value. Tregoning and Herring [2006] performed an investigation into the effect of a priori model of zenith hydrostatic delay (L_h^z or ZHD) in the GPS estimates of heights and ZTD, and indicated that use of inaccurate ZHD leads to large biases into the height (up to 10 mm) and consequently errors in the estimation of zenith total delays. They suggested that the use of time-varying a priori ZHD extracted from a numerical weather prediction model would improve the GPS solutions compared to the use of static standard sea level pressure.

Much effort has been made to develop more accurate models for a priori hydrostatic delays, and also for both hydrostatic and wet mapping functions used in Equation 2.5. The most common models that are currently implemented in geodetic analyses are the Vienna Mapping Functions 1 (VMF1) that contain both hydrostatic and wet time-varying mapping functions and zenith hydrostatic delays ray-traced from the ERA-40 reanalysis of the ECMWF data [Böhm et al., 2006b], empirical Global Mapping Functions (GMF) which are the expansion of VMF1 mapping functions

into spherical harmonic coefficients up to degree and order of 9 [Böhm et al., 2006a], and a similar harmonic expansion of 3 years of ERA-40 data called Global Pressure and Temperature (GPT) and GPT2 that can be used as sources for deriving a priori zenith hydrostatic delay [Böhm et al., 2007; Lagler et al., 2013]. For a detailed description of these models, the reader is referred to Böhm [2007], which contains a complete review on the most important models developed for tropospheric modelling in geodetic analyses.

Several studies have been carried out to examine how using different atmosphere-related models can affect geodetic solutions. A thorough investigation was performed by Tregoning and Watson [2009] to study the impact of using different mapping functions, a priori sources and atmospheric loading deformation (ATML) models on time correlated noise structure of GPS coordinate time series. They concluded that using VMF1 mapping functions and the time-dependent a priori ZHD results in lower noise levels compared to using GMF and GPT empirical functions, particularly when ATML is accounted for.

Horizontal heterogeneities in the tropospheric refractivity field are known to exist [e.g. Gardner, 1976; Davis et al., 1993; Gegout et al., 2011], and the symmetric assumption imposed on the tropospheric delay in Equation 2.5 could create errors of a few decimetres in modelling the delay at low elevation angles [Böhm, 2007]. The most commonly used approach for bringing into effect the azimuthal asymmetry of the troposphere is to estimate additional linear horizontal gradient parameters in both the North-South (L_{NS}) and East-West (L_{EW}) directions [Davis et al., 1993]; thus, the formulation for the azimuth-dependent part of the delay (L_{az}) becomes:

$$L_{az}(\varepsilon, \alpha) = L_{NS} m_{az}(\varepsilon) \cos\alpha + L_{EW} m_{az}(\varepsilon) \sin\alpha \tag{2.6}$$

where α is the azimuth angle of the observation, and m_{az} is the mapping function for gradients. The mapping function that is most widely used by analysts is the model introduced by Chen and Herring [1997]:

$$m_{az}(\varepsilon) = \frac{1}{\sin(\varepsilon)\tan(\varepsilon) + C} \tag{2.7}$$

in which the constant C was derived to be 0.0031 by fitting the function to a tilted atmosphere model for different elevation angles from 90 to 5 degrees [Herring, 1992]. This mapping function is preferable over the $\cot(\varepsilon)$ form used e.g. by MacMillan [1995], which approaches infinity at zero elevation angle, and is not therefore applicable at very low elevations.

Although the above tropospheric horizontal gradient model sufficiently models the tropospheric refractivity field under normal stable tropospheric conditions, there are cases where this model is too simple to be able to accurately represent apparent non-symmetrical and non-linear horizontal tropospheric conditions. The use of a more complicated model will be discussed in Chapter 4.

In static GPS analyses, the data for one day are usually processed in a batch least-squares solution. Unlike the position components which can normally be assumed

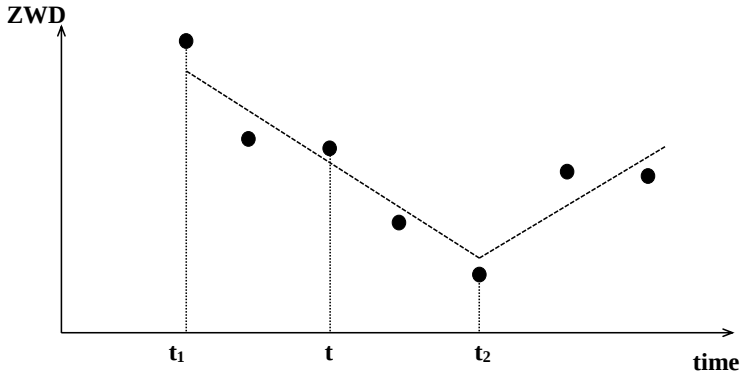

Figure 2.1: An example of a piecewise linear function fitted to a set of data points (ZWD in this case). t_1 and t_2 are two of the estimation nodes of the PWL function.

constant over the whole day, the tropospheric delays are variable during a day; therefore, we need to estimate these parameters at multiple epochs over the processing period. One way to model the tropospheric zenith delays and horizontal gradients is the use of a piecewise linear function (PWL) with stochastic constraints at multiple epochs. There are a range of other approaches regarding the temporal model of the delays (for example using a random walk withe updates every 5 minutes) [Bar-Sever et al., 1998]. A mean value of the ZWD is estimated for the whole processing period, and adjustments to this mean value at each estimation epoch are solved for by the use of the PWL function. One may consider estimating zenith delays every T hours, such that there is $24/T + 1$ estimation nodes for each day. Considering that there are several observations between the estimation nodes, the partials of the phase observations with respect to the zenith wet delays will follow the chain rule. As an example, assuming that the estimation nodes occur at epochs t_1 and t_2 (see Figure 2.1), and there is an observation at epoch t, the partial derivative of the phase observation at epoch t (ϕ) with respect to the zenith wet delay at the two estimation nodes (zwd_1 and zwd_2) will be:

$$\frac{\partial \phi}{\partial zwd_1} = \frac{\partial \phi}{\partial zwd} \times \frac{\partial zwd}{\partial zwd_1} = m_w \times (1 - \frac{t - t_1}{t_2 - t_1}) = m_w \times (1 - \frac{t - t_1}{T}) \tag{2.8}$$

$$\frac{\partial \phi}{\partial zwd_3} = \frac{\partial \phi}{\partial zwd} \times \frac{\partial zwd}{\partial zwd_2} = m_w \times (\frac{t - t_1}{t_2 - t_1}) = m_w \times (\frac{t - t_1}{T}) \tag{2.9}$$

where m_w is the wet mapping function at time t.

A first-order Gauss-Markov process is used for the stochastic constraints of the PWL function. Considering l as the variance of ZWD over the whole day, the variance-covariance matrix used for the ZWD parameters at several epochs through-

out the day is set as:

$$C = \begin{bmatrix} l & lu & lu^2 & lu^3 & \cdots \\ lu & l & lu & lu^2 & \cdots \\ lu^2 & lu & l & lu & \cdots \\ lu^3 & lu^2 & lu & l & \cdots \\ \vdots & \vdots & \vdots & \vdots & \ddots \end{bmatrix} \tag{2.10}$$

where u is an exponential function of the time interval between the estimates (Δt) and correlation time of the process (τ):

$$u = \exp(\frac{-\Delta t}{\tau}) \tag{2.11}$$

Since the daily mean value of ZWD is estimated as a separate parameter to the deviation of ZWD from the mean, the condition that the mean of the process should be almost zero is also applied to the covariance matrix via a Kalman filter observation equation stating that sum of the estimates needs to be zero (with a small variance).

A similar approach as above is also taken for the estimation of gradient parameters at several epochs over a day with a slight difference: no daily mean gradient is estimated, and instead of applying a zero-mean constraint on the estimates, an overall level of gradient is added to all elements of the covariance matrix of Equation 2.10. A theoretical description of the first-order Gauss-Markov processes is given in Appendix B.

Choice of appropriate correlation time and process noise levels in Equation 2.10 is important to ensure that constraints on the tropospheric parameters mitigate as far as possible the effects of correlations with other estimated parameters. Most analysts use constant values for the correlation time of the Gauss-Markov process for all the stations (usually ∼100 hours such that a random-walk process is assumed), and apply relatively loose constraints for the process noise level whereby allowing relatively large hourly variation in both zenith delay and horizontal gradient estimates. A detailed investigation of the impact of the level of constraints applied to tropospheric parameters on geodetic solutions is discussed in Chapter 5.

Using the temperature at the GPS station (which could be extracted from meteorological reanalysis models), the zenith wet delay (ZWD) can be converted into the amount of precipitable water (PW) in a vertical column above the site using the relation given by Askne and Nordius [1987] and Bevis et al. [1994]:

$$PW = ZWD \times \frac{1 \times 10^{-6}}{\rho \times R_v \times (\frac{k_3}{T_m} + k_2')} \tag{2.12}$$

where $\rho = 1$ (g/cm^3) is the density of liquid water, $T_m = 70.2 + 0.72T$ is the weighted mean temperature of the atmosphere in units of Kelvin, and the specific gas constant for water vapour (R_v) and the two other constants are as below:

$$R_v = \frac{8.314}{18.0152} \times 10^7$$

$$k_3 = \frac{3.739 \times 10^5}{1.013 \times 10^3}$$

$$k_2' = \frac{22.1}{1.013 \times 10^{-3}}$$

For the assimilation purposes, it is preferable to use the raw ZTD estimates rather than ZWD or PW; this has the advantage that the observation errors are less complicated by the approximations in the a priori ZHD and assumptions made during the conversion of ZWD into PW [e.g. Bennitt and Jupp, 2012]. For the purpose of comparison with other measurements (e.g. microwave radiometry observations) or for more tangible understanding of the level of humidity, however, PW estimates are useful.

We usually estimate zenith delays every two hours, and horizontal gradients of the troposphere every 6 hours. The equations introduced by Saastamoinen [1972] can be used to determine approximate ZHD and ZWD from pressure and temperature values at a site:

$$ZHD = 0.002277 \times P \times (\frac{g_0}{g}) \tag{2.13}$$

$$ZWD = 0.002277 \times (\frac{1255}{T} + 0.05) \times e \times (\frac{g_0}{g}) \tag{2.14}$$

In the above equations, P is the pressure at site in mbar, and T is the temperature in Kelvin. $g_0 = 9.784 \times 10^{-3}$ m/s^2 is the acceleration of gravity at the centroid of the atmosphere, and g is the acceleration of gravity at the site in m/s^2, which is given by

$$g = g_0 \times (1 - 0.00266\cos(2\phi) - 0.00028h) \tag{2.15}$$

where ϕ is the latitude of the site, and h is the station height in km. Also, e is the water vapour pressure in mbar, which can be derived from the station Celsius temperature (t):

$$e = rh \times 6.11 \times 10^{7.5t/(t+237.3)} \tag{2.16}$$

where rh is the relative humidity at the site location as a fraction of 1. We use GPT2 global grids of temperature and pressure [Lagler et al., 2013] and Equation 2.14 above to set approximate initial values for zenith wet delays, and we will then estimate the adjustments to the ZWD in our least-squares solution. For the hydrostatic delays, however, we use the more accurate VMF1 grids Böhm et al. [2006b], because we use the ZHD values a priori and do not attempt to estimate adjustments to them. We also use VMF1 mapping functions for both wet and hydrostatic components of the tropospheric delays.

2.3 Simulations and Experiments

The choice of simulations or experiments in each chapter of this thesis depends on the model or technique we are testing. For the most part however, we use regional experiments since we are mostly interested in the improvements in tropospheric esti-

mates, particularly in special weather scenarios. The standard reference experiment we use in many of the chapters is a network of 31 GPS stations in the Australian and south-east Asian region (Figure 2.2). We selected this network, because we wanted to include some equatorial sites with humid weather conditions, as well as a few mid-latitude stations in the Australian continent. Also, previous research has shown that for geodetic analyses with the purpose of estimating absolute tropospheric zenith delays, sufficient de-correlation of tropospheric zenith delays and heights is acquired by inclusion of long baselines of at least about 2000 km [Tregoning et al., 1998; Rocken et al., 1993; Duan et al., 1996]; the selected network for the analyses in this thesis includes such long baselines, and therefore is appropriate for our meteorological purposes. A comprehensive set of metadata for all the GPS stations used throughout this thesis is provided in Appendix A.

Comparing the GPS-derived water vapour measurements with external data is an appropriate tool for validating our measurements. There are three microwave radiometry stations located in Darwin, Nauru Island and Manus Island, called the Tropical Western Pacific (TWP) network, established in 1996 by the Atmospheric Radiation Measurement (ARM) Climate Research Facility. These two-channel microwave radiometers (MWRs) measure the radiation downwelling from the atmosphere at 23.8 and 31.4 GHz frequencies, which are sensitive to water vapour and cloud liquid water. Detailed descriptions of the retrieval and calibration processes of MWR can be found e.g. in Askne and Westwater [1986] and Cadeddu et al. [2013]. The data collection at the Manus Island facility ended on 30 August 2014, the one at the Nauru Island ended on 30 August 2013, and the Darwin facility was closed on 31 December 2014 (ARM [2014] and Riihimaki [2014]).

Three GPS sites (SA39, SA40 and SA42) were selected to be part of the network, since they are co-located with the three MWR stations. Three other stations in the vicinity of these three sites (DARW, NAUR and GUAM) were also included in the network for comparison purposes. The location of the MWR sites and the co-located GPS stations are given in Table 2.2. The MWR coordinates are according to the ARM facility (https://www.arm.gov/capabilities/observatories/twp), and the GPS coordinates are estimated. The heights in Table 2.2 are above the mean sea level. The maximum discrepancy between the heights of the co-located sites is for the Manus Island instruments with about 17 meters difference in height. The other two pairs of instruments are only different in height by a few meters. One can determine the approximate difference in zenith wet delay made by the height difference between the GPS and MWR stations. We first need to transfer the differences in pressure and temperature between the two heights using the equations given by Saastamoinen [1972]:

$$P_2 = P_1 \times (\frac{T_2}{T_1})^{(\frac{g}{R_d \times lr})} \tag{2.17}$$

$$T_2 = T_1 - lr \times h \tag{2.18}$$

In the above equations, P_1 and P_2 are the pressure at the two sites in mbar, T_1 and

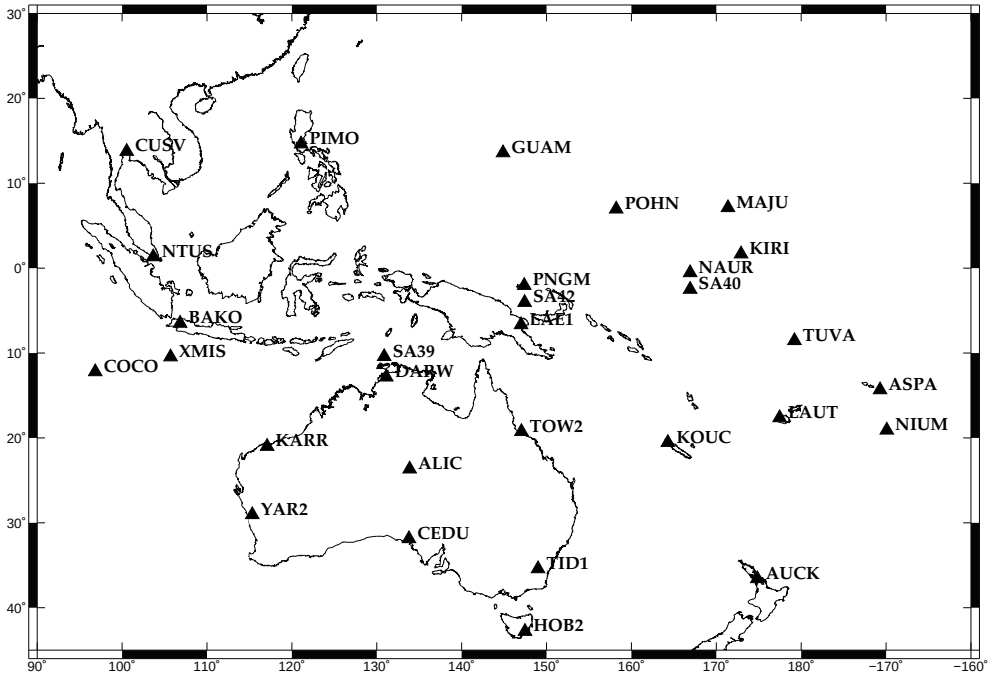

Figure 2.2: The typical GPS network for many of the experiments used in this thesis; the stations SA39, SA40 and SA42 are intentionally shifted in latitude to avoid masking the nearby sites mask each other.

T_2 are the temperature at the two sites in Kelvin, $R_d = 2.89644 \times 10^{-4}$ is the specific gas constant for dry air, and lr is the lapse rate which is usually assumed about 6.5 °K/km. We can then use Equation 2.14 to calculate the ZWD difference between the stations. Using Equation 2.14 and 2.12, one can easily calculate that a deviation of 10 metres in the height of two stations will result in only about 1-2 mm difference in ZWD, and less than 0.5 mm difference in precipitable water. Considering that the one-sigma uncertainties of the GPS estimates are generally of the order of 5-30 mm for ZWD and 1-2 mm for PW, the height differences of the co-located GPS and MWR sites in the experiment of Figure 2.2 are insignificant.

Besides the above typical network (Figure 2.2), we will also carry out experiments in other regional networks based on our needs. In Chapter 4, for example, we perform analyses on two different case studies, in southern France and in California, because of the specific weather phenomena (isolated horizontal changes in the atmospheric water vapour field) that these two regions are known to possess. These specific networks will be introduced in the relevant sections.

In addition to the real experiments, we use simulations to test the models and techniques. We use modified versions of the GAMIT software to simulate observations that satisfy our purposes. For the simulations, we defined the station geometry by a set of 8 existing permanent GPS stations spanning the Australian continent (shown in Figure 2.3). We use the actual GPS constellation observation geometry for

Site	Instrument	Site code	Latitude	Longitude	Height
Manus Island	MWR	C1	2° 3′ 39.64″ S	147° 25′ 31.43″ E	4.00 m
	GPS	SA42	2° 3′ 39.17″ S	147° 25′ 31.06″ E	21.07 m
Nauru Island	MWR	C2	0° 31′ 15.60″ S	166° 54′ 57.60″ E	7.10 m
	GPS	SA40	0° 31′ 14.22″ S	166° 54′ 57.73″ E	12.42 m
Darwin	MWR	C3	12° 25′ 28.56″ S	130° 53′ 29.75″ E	29.90 m
	GPS	SA39	12° 25′ 28.53″ S	130° 53′ 29.67″ E	31.52 m

Table 2.2: The locations of the microwave radiometer (MWR) stations and the co-located GPS sites in the experiment of Figure 2.2. The heights in the last column are above mean sea level.

these sites on the 16 July 2010, simulating the GPS phase and pseudo-range observations using the standard models and parameters of Table 2.1. We then add the desired term to our simulated signals for the specific testing goal.

Several different criteria are used for evaluating the quality of models and solutions. Improper modelling of zenith total delays, most often causes errors in the station height estimates, because of the high correlations between the ZTD and height parameters [e.g. Tregoning and Herring, 2006]. These errors often appear as highly scattered time series of position vertical components. Thus, we use short-term repeatabilities of the height time series as indicators for the quality of the zenith delay estimates. We also look at the weighted root-mean-square (WRMS) error of the zenith delay estimates at the overlap epochs between consecutive days as another measure for the accuracy of zenith delay estimates. The absolute water vapour estimates are also compared to the MWR measurements of PW; it should be noted, however, that the MWR measurements are not necessarily more accurate values than the GPS-derived measurements. There is evidence that indicates overestimation of several millimetres in MWR-driven PW values compared to GPS estimates of PW in humid conditions [Tregoning et al., 1998], which could be related to GPS modelling errors, but could also be due to microwave radiometry hardware issues. We also use simulations, where possible, to show how using different strategies and models could lead to reduction in or increase of errors in the estimates. Investigating the known weather events and comparing the water vapour accumulation with precipitation data is another approach by which we validate the models (mostly in Chapter 4).

2.4 Summary

In this chapter, we have summarized the techniques and models we generally use throughout this thesis in our experiments. Many of the processing strategies that were discussed in this chapter are similar to tropospheric modelling of GPS observations previously investigated and documented in terms of their impact on GPS solutions in [e.g. Tregoning and Watson, 2009]. However, less focus has been set on

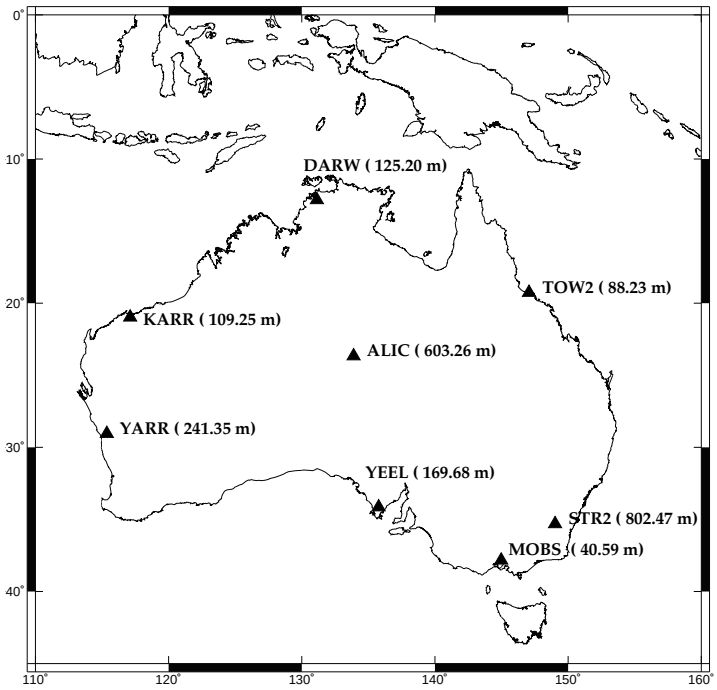

Figure 2.3: The selected network for performing the simulations. The station ellipsoidal heights are given in the brackets next to the site names

the use of low-elevation observations in GPS modelling and data analysis. In the next chapter, we will discuss the impact of using low-elevation signals and issues related to including these measurements, such as site-specific errors and insufficient modelling of tropospheric horizontal gradients. We will then discuss the impact of using an empirical model of site-specific errors in GPS analyses on the tropospheric estimates, and compare the accuracy of the GPS-estimated horizontal gradients of the tropospheric delay with the gradients derived from ray-tracing of a weather model.

Chapter 3

Low-elevation observations, site-specific errors and tropospheric horizontal gradients

While there have been several advances in different aspects of modelling the GPS signals, observations that are measured at very low elevation angles still suffer considerably from several unmodelled effects, including errors in the modelling of atmospheric delays, antenna phase centre models and other unmodelled errors such as multipath [e.g. Hatanaka et al., 2001]. Many analysts simply ignore low-elevation observations, usually setting an elevation cut-off angle of 7-10° in their solutions. Analysts who are interested in GPS meteorological products, however, would like to include lower-elevation observations to help decorrelate tropospheric zenith delays and height parameters. For GPS tomography applications, the use of near-horizontal low-elevation measurements are vital for improving the vertical resolution of the tomography. In this chapter, we focus on how low-elevation observations affect the GPS estimates of position and tropospheric zenith delays, and we will investigate different sources of errors in modelling low-elevation measurements. In Section 3.1, we discuss the impact of using different elevation cut-off angles on the solutions and the function used for weighting the observations. In Section 3.2, the site-specific errors and their impact on the tropospheric zenith delays are studied. An empirical site-specific model developed by Moore et al. [2014] is applied to a set of stations in an experiment, and the impact on GPS tropospheric delays is investigated. In Section 3.3, the tropospheric horizontal gradients - if not properly modelled - are discussed as a possible source of error. The planar (north-south and east-west) horizontal gradients estimated from GPS observations are compared to their ray-traced counterparts generated by Böhm and Schuh [2007]. The impact of using these ray-traced horizontal gradients or an empirical model derived by spherical harmonic expansion of the ray-traced gradients (Böhm et al. 2013) as a priori in the GPS solutions is studied. Section 3.4 will provide a summary of the conclusions about the GPS low-elevation observations and different error sources they are contaminated with.

3.1 Elevation cut-off angle and weighting scheme

The elevation cut-off angle, the elevation angle below which we decide to remove the GPS observations from the solution as being heavily contaminated by unmodelled errors, has a large impact on the accuracy of the estimated parameters [e.g. Rothacher and Beutler, 1998]. In meteorological applications, care should be taken in removing low-elevation observations as the GPS signals at low elevation angles contain important information about the far-field lower layers of the troposphere. As a rough estimate, a GPS signal at 10° elevation angle enters the troposphere at about 60 km distance from the GPS station, while a signal with 3° elevation angle enters the troposphere at around 200 km away from the site.

Some researchers have previously studied the effect of elevation cut-off angle choice on GPS estimates. Rothacher and Beutler [1998] discovered high correlations between tropospheric zenith delays and station heights, and also discovered that by including more low-elevation data, the correlation between the zenith delays and the vertical component of the position is reduced. However, when including low-elevation observations, uncertainties of the mapping functions (particularly because of the increased effect of azimuthal asymmetry), as well as other unmodelled site-specific errors such as multipath and phase centre variations, are significantly increased [e.g. Tregoning et al., 1998; Fang et al., 1998]. Tregoning et al. [1998] suggested that using low-elevation observations increases the sensitivity of the solutions to the tropospheric zenith delay/precipitable water. They compared the GPS water vapour estimates with microwave radiometry estimates of precipitable water for a site at Cape Grim, Australia at different cut-off angles from 10° to 19°, and found out that the cut-off angle of 12° results in the minimum bias with MWR estimates at that specific experiment. While the observations at low elevation angles increase the sensitivity to the amount of water vapour, the use of low-elevation measurements may increase the risk of the observations being contaminated by mapping function errors and unmodelled site-specific errors (multipath and incomplete antenna models). Selecting an optimal elevation cut-off angle is a trade-off between the errors in the low-elevation observations and the increased sensitivity to the water vapour content. Since this trade-off elevation cut-off angle varies between stations, largely depending on the station local environment and antenna characteristics, it is difficult to determine beforehand the optimum cut-off. Therefore, it is important to reduce the sensitivity of the GPS ZWD estimates to the choice of the cut-off angle as much as possible. Rothacher and Beutler [1998] suggested that by applying an elevation-dependent weighting that reduces the weights given to the observations at lower elevation angles, and by estimating tropospheric gradients, one can get improved height estimate repeatabilities by going into lower elevation angles. The elevation-dependent weighting currently used in the GAMIT software uses Equation 2.4 for the variance of the observations (σ^2), which we repeat here:

$$\sigma^2 = a^2 + \frac{b^2}{\sin^2(\varepsilon)} \tag{3.1}$$

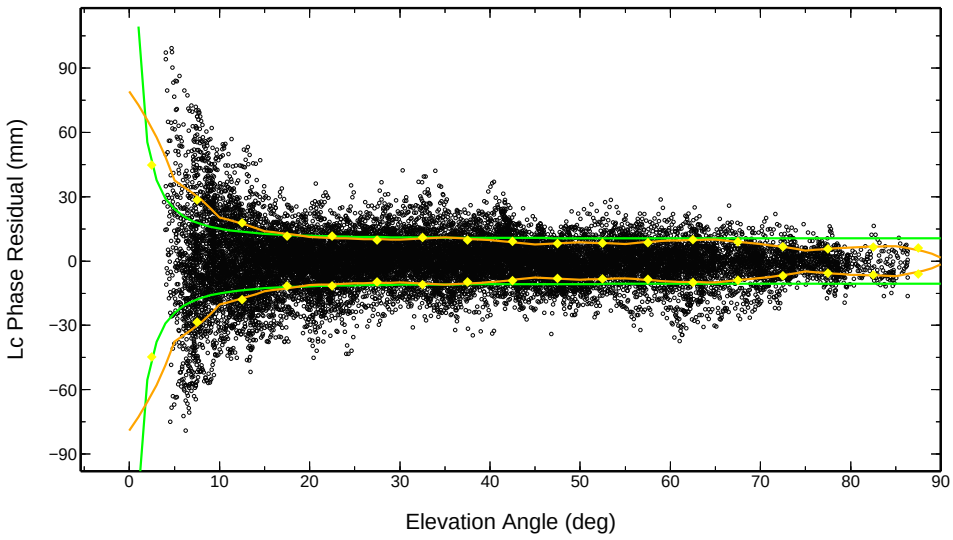

Figure 3.1: Ionosphere-free (LC) phase residuals (black dots) as a function of elevation angle for site NIUM on 1 January 2012. The green line is the elevation-dependent function of Equation 3.1 fitted to the mean residuals at elevation bins (yellow dots), and the orange line is the piecewise linear fit to the residuals.

where ε is the elevation angle of the observation, and a and b are determined by fitting the above function to the one-way phase residuals of a first least-squares iteration averaged at e.g. 5° elevation bins. GNSS analysts who use other software packages may implement different weighting schemes as above, but most analysts use some form of elevation-dependency in their analyses.

Using the above function for weighting the observations causes a gradual decrease in the weights of the observations as we go down to lower elevation angles, and thus helps a trade-off between including information from lower elevation data, while reducing the weight given to them according to the amount of noise. However, since Equation 3.1 tends to infinity at zero elevation angle, the fit becomes corrupted when including very low elevation observations, leading to overweighting of these low-elevation data. Figure 3.1 is an example of the one-way phase residuals and the fitted elevation-dependent function given in Equation 3.1. The figure clearly shows that the elevation-dependent function (green line) underestimates residual RMS values at low elevation angles compared to the actual residuals. Also shown on Figure 3.1 is a piecewise linear fit to the residuals with 5° grid spacing (orange line), which matches more accurately to the actual residuals. Using such PWL function to weight the observations leads to more realistic weights for the low-elevation data based on the phase residuals compared to the weights given by Equation 3.1.

In this section, we will examine the sensitivity of the GPS estimates to the choice of elevation cut-off angle by performing a set of GPS analyses on the network of Figure 2.2 for one month of data (January 2012). We use the settings of table 2.1 for our analyses, but we also perform the same experiments using a piecewise linear

weighting scheme instead of the elevation-dependent weighting of Equation 3.1 to study how the choice of weighting function could impact the results. For the piecewise linear weighting function, we modified the GAMIT software to include the PWL weighting option. We performed both analyses (with elevation-dependent weighting scheme of Equation 3.1 and with PWL weighting) at different elevation cut-off angles from 20° to 3°. We then performed a Kalman filter with the daily position estimates and the covariance matrices as the input using the GLOBK software, and calculated the WRMS error of position time series for each individual GPS station. For details about the deterministic and stochastic models used in the Kalman filter, see e.g. Herring et al. [1990] and Dong et al. [1998]. For each position component, we then took the average of the WRMS values for all the sites, and plotted the mean WRMS as a function of elevation cut-off angle in Figure 3.2. We also calculated the overlap WRMS of the zenith total delay estimates at midnight epochs in the boundary of consecutive days. We then averaged these overlap WRMS values over the whole month for each station. The mean overlap WRMS of ZTD estimates averaged for all the stations in the network is shown in Figure 3.2d. The overlap epochs occur because we estimate ZTD at midnight epochs twice, once per each daily batch least-squares inversion of the consecutive days.

It is inferred from Figure 3.2 that the mean repeatabilities of the position components (particularly height estimates) generally tend to improve when the elevation cut-off angle is reduced from 20° to around 10°, but is degraded when further reducing the cut-off angle. The minimum mean WRMS (using the weighting function of Equation 3.1; red lines) occurs when setting the elevation cut-off angle at 10° (1.44 mm WRMS) for North component, 13° (1.63 mm WRMS) for East component, and 10° (5.90 mm WRMS) for vertical component. Of importance to note about the solution using Equation 3.1 as the observation weighting function is the sudden increases in the position repeatabilities when including observations immediately below 5°; this is when an elevation bin is added to the data to which the weighting function is fitted. A similar but smaller jump is also observed when moving from 10° cut-off to 9° cut-off. Looking back at Figure 3.1, the reason lies in the shape of the weighting function which tends to infinity at low elevation angles, and thus underestimates the noise given to low-elevation observations. The piecewise linear weighting scheme (black lines in Figure 3.2) is able to remove this artefact of sensitivity to observation weighting as a function of cut-off angle seen when using the standard elevation dependent weighting function given in Equation 3.1. While the optimum cut-off remains around the same as when the weighting of Equation 3.1 is used (10° for Northing and height, and 13° for Easting), the WRMS values of the position components do not grow significantly when including observations lower than 10°.

The optimum elevation cut-off angle for the overlap WRMS of the ZTD estimates is lower than the optimum cut-off angles for positions (Figure 3.2d). The minimum WRMS of 6.55 mm occurs at 6° cut-off when using Equation 3.1 as the weighting scheme. The minimum WRMS is reduced to 6.41 mm at 4° cut-off when using the PWL weighting. Using either of the two observation weighting functions, the WRMS

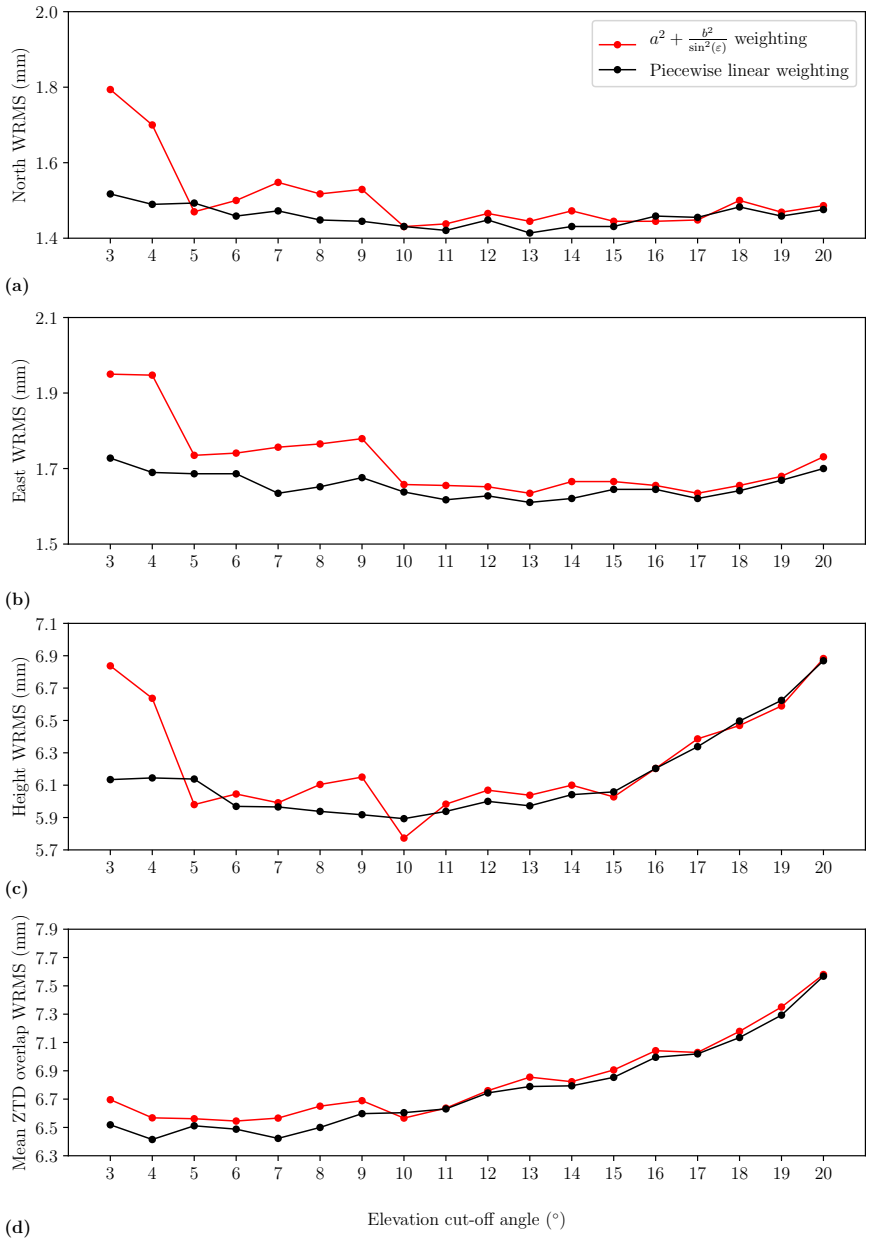

Figure 3.2: WRMS of estimated parameters averaged over all the GPS stations in the experiment of Figure 2.2 for January 2012 as a function of the selected elevation cut-off angle for the solutions with the elevation-dependent weighting scheme of Equation 3.1 (red) and with a piecewise linear weighting formulation (black): (a) North position component; (b) East position component; (c) vertical position component; and (d) overlap zenith total delay averaged for the whole month for each station.

of ZTD is significantly reduced when lowering the elevation cut-off angle from 20° to about 10° but, unlike the position components, does not significantly increase when

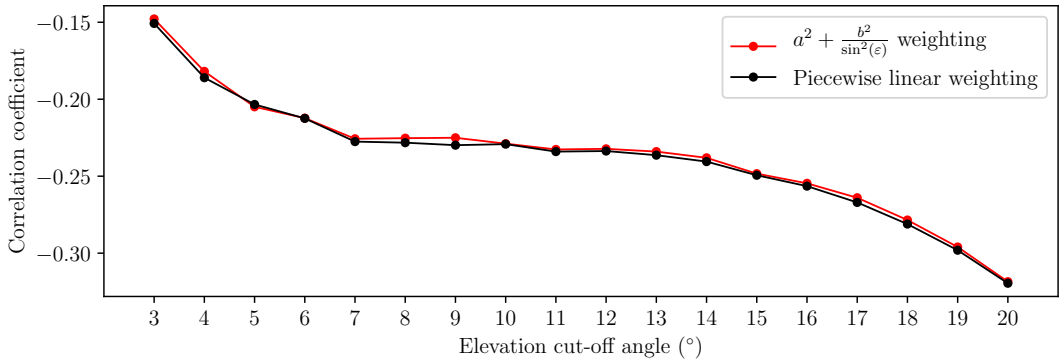

Figure 3.3: Correlations between height and zenith total delay parameters averaged for all the stations in the experiment of Figure 2.2 for January 2012 as a function of the selected elevation cut-off angle for the solutions with the elevation-dependent weighting function of Equation 3.1 (red) and with a piecewise linear weighting formulation (black).

still including lower elevation observations (with some further reduction until 6° for the Equation 3.1 weighting and 4° for PWL weighting). This verifies the idea that on average, it would be better to include lower elevation observations than 10° for generating tropospheric zenith delays. By including the low-elevation observations, we are able to reduce the correlations between the ZTD and height parameters through increasing the sensitivity of the solutions to zenith total delays. Figure 3.3 shows the correlation coefficients between the zenith total delay and height parameters averaged over all the stations for the same experiment as a function of elevation cut-off angle. It can be seen that the negative correlations are consistently reduced when including lower elevation observations.

It should be noted, however, that the cut-off dependencies depicted in Figures 3.2 and 3.3 are the average over all the stations, and that the individual stations may show different behaviours. As examples of the different characteristics of the stations, the elevation cut-off angle sensitivity of the ZTD mean WRMS for three of the stations are displayed in Figure 3.4. The ZTD WRMS of the station GUAM (which has tracked observations only down to a minimum elevation angle of 7°) increases when including observations lower than 16° elevation angle and using the elevation-dependent weighting of Equation 3.1, but a piecewise linear weighting of the observations help reduce this elevation cut-off angle dependency (Figure 3.4a). Comparing Figures 3.4b and 3.4c, stations NAUR and SA40 show opposite behaviours in the changes of the ZTD WRMS as a function of elevation cut-off angle: for station NAUR, the ZTD WRMS is reduced when including observations lower than 11° elevation angle, while the WRMS values for SA40 increase when using observations lower than 14°. These two stations are only about 3.6 km away from each other, which means that the different elevation cut-off angle sensitivity is not resulted from the mapping

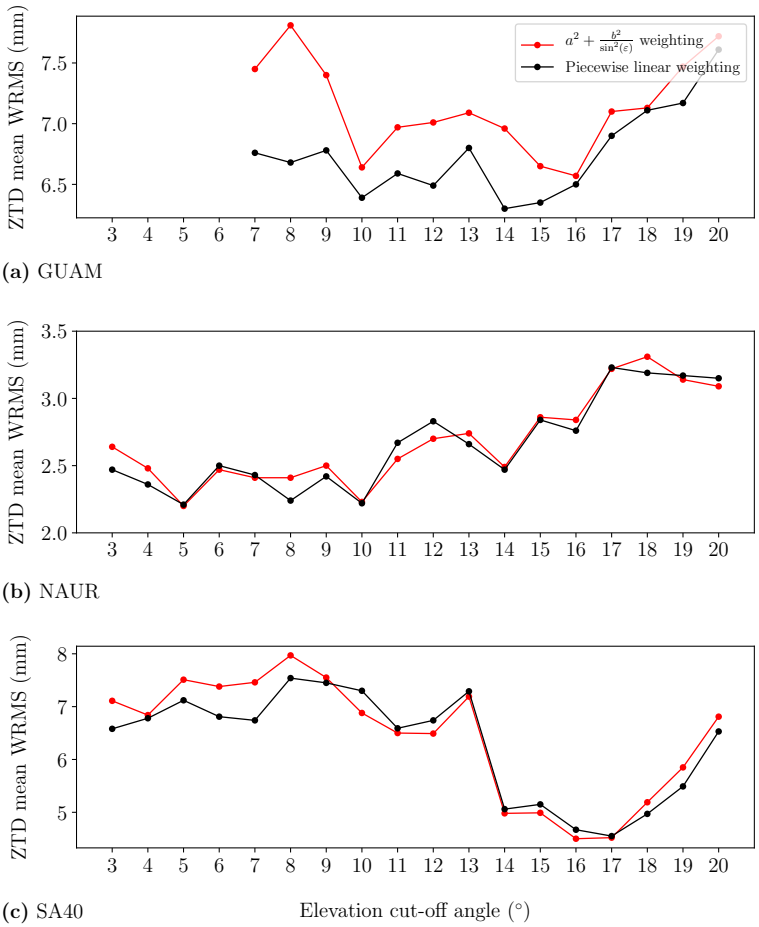

Figure 3.4: Mean WRMS of estimated tropospheric zenith total delays for three of the GPS stations in the experiment of Figure 2.2 for January 2012 as a function of the selected elevation cut-off angle for the solutions with the elevation-dependent weighting scheme of Equation 3.1 (red) and with a piecewise linear weighting formulation (black): (a) station GUAM; (b) station NAUR; and (c) station SA40.

function errors, but is most likely due to site-specific errors.

3.1.1 Sensitivity of the estimates to the elevation cut-off angle

More important than how the WRMS and correlation coefficients change when varying the elevation cut-off angle, is how much the estimates of ZTD or equivalent PW differ when changing the cut-off angle, and whether the change in the estimates is significant. We analysed the same experiment of Figure 2.2 for a two-year period (2011-2012) using two different elevation cut-off angles of 3° and 10°. The mean differences in the estimates of ZTD between the solutions with elevation cut-off angles of 3° and 10° (the estimates from the 10° solution minus the estimates from 3° solution) are shown in Figure 3.5a along with their 1-sigma uncertainties. We use

the elevation-dependent weighting of Equation 3.1 for these two-year analyses. The mean differences in the estimates of zenith total delay (Figure 3.5a) are small and insignificant when considering the 1-sigma uncertainties. However, when studying the extreme weather events, we should focus on individual days instead of average statistics. The maximum differences occurred in 2011-2012 between the estimates of ZTD from the solutions with the two different elevation cut-off angles are displayed for each station in Figure 3.5b. There are significant differences occurred by varying the elevation cut-off angle between 10° and 3° for all the stations in our network, which are all well above their 1-sigma uncertainty levels. Figure 3.5c shows the number of ZTD differences larger than their 1-sigma uncertainties occurred throughout the whole two-year period of study for each station. TOW2, located in Townsville, Queensland, shows the highest number of "significant" ZTD differences among all the stations in the network; From about 8200 estimation epochs for the whole processing period, there are nearly 2200 epochs at which the difference between the ZTD estimates from the solutions with 3° and 10° elevation cut-off angle is larger than the 1-sigma uncertainty level of the ZTD difference, and the maximum difference in the ZTD estimates is $\sim$36.3$\pm$7.5 mm, which occurred on 9 December 2011 (18:00 UTC). Other stations with high number of occurrences of ZTD differences larger than 1-sigma uncertainty include CEDU in Ceduna, South Australia, YAR2 in Yarragadee in Western Australia, CUSV in Bangkok, Thailand, KARR in Karratha, Western Australia, and XMIS in Christmas Island. As examples, the ZTD differences (the estimates from the 10° cut-off solution minus the estimates from the 3° cut-off solution) are displayed for the whole period of 2011-2012 for stations TOW2 and CEDU in Figures 3.6 and 3.7. For both stations, larger differences are observed between the ZTD estimates from the two solutions in the wetter summer periods. Over 2011 and 2012, the mean precipitable water content for TOW2 over December, January and February is $\sim$48 mm, while the mean PW content for the same station is $\sim$22 mm for June, July and August. For CEDU, the 2011-2012 summer-time PW mean is $\sim$24 mm, while the winter-time PW mean is $\sim$13 mm.

Another observation from Figures 3.5, 3.6 and 3.7 is that a 3° cut-off solution typically leads to smaller estimates of the ZTD than a 10° cut-off solution. One can not automatically conclude which solution is more accurate; low-elevation observations help to decorrelate ZTD and height parameters (Figure 3.3) and increase the sensitivity of the solution to the amount of precipitable water, but there may be unmodelled errors in the low-elevation signals which could lead to biases in the estimates of ZTD when including these observations in the solution. Comparing the solutions with an external source of measurement could be helpful to more deeply understand the difference in the estimates when including low-elevation observations.

3.1.2 Comparison with MWR

As mentioned in Chapter 2, there are three microwave radiometry stations installed by the ARM Climate Research Facility that are co-located with three of the GPS stations in our network (Table 2.2). These instruments in the Tropical Western Pacific

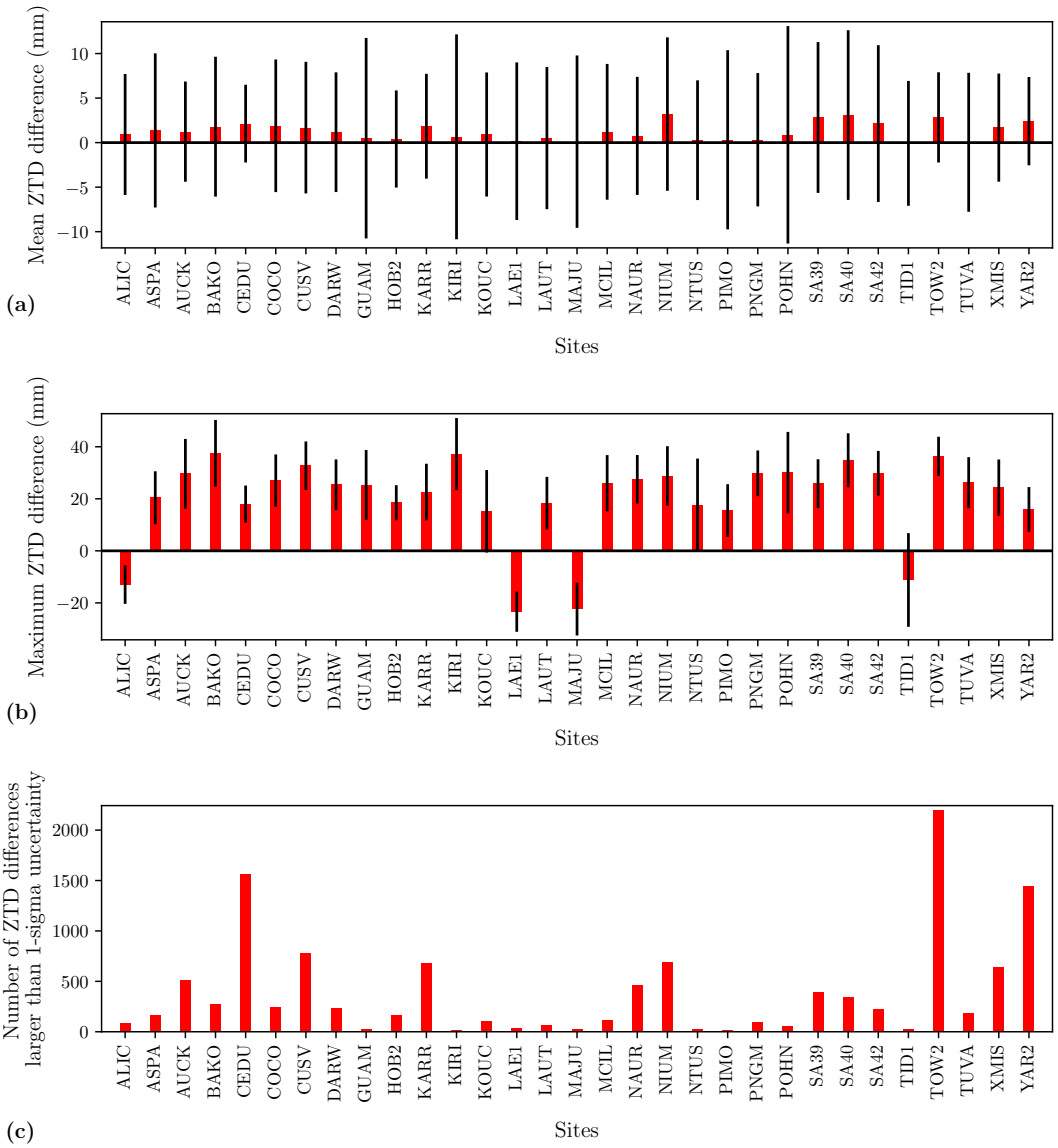

Figure 3.5: The differences between the tropospheric zenith delay estimates from the solutions with elevation cut-off angles 3° and 10°, for the experiment of Figure 2.2 using the elevation-dependent weighting of Equation 3.1: (a) the mean differences between the ZTD estimates over 2011-2012; (b) the maximum differences occurred over the same period; (c) the number of occurrences for ZTD differences larger than 1-sigma uncertainty of the difference. Error bars on the two top plots are 1-sigma uncertainties of the mean/maximum differences. The differences shown on the two top plots are the ZTD estimates from the 10° cut-off solution minus the estimates from the 3° cut-off solution.

network are upward-looking (with ∼5°-6° field-of-view) two-channel microwave ra-

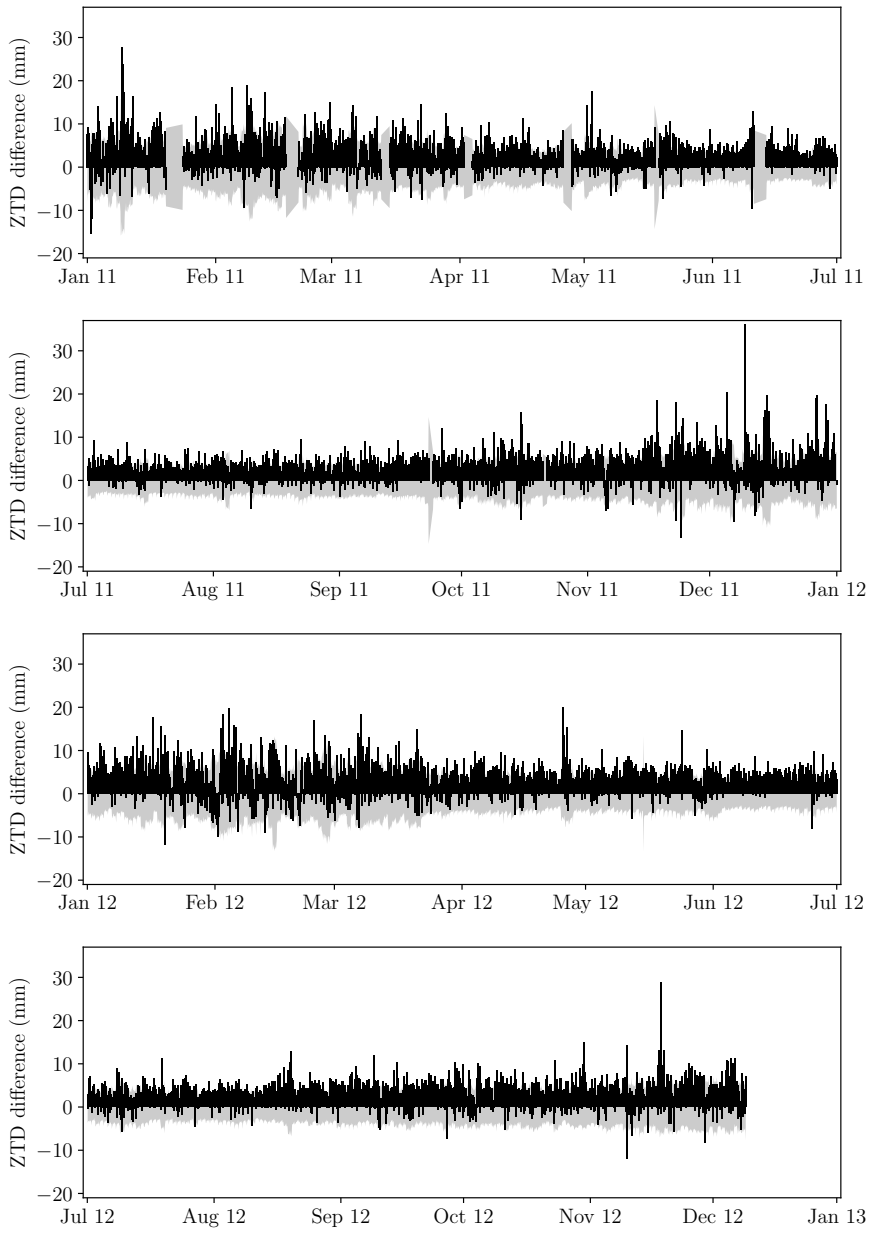

Figure 3.6: The differences between the tropospheric zenith delay estimates from the solutions with elevation cut-off angles 3° and 10° for TOW2. The elevation-dependent weighting of Equation 3.1 is used for both solutions. The grey shades are the 1-sigma uncertainty levels of the ZTD differences. The differences shown are the ZTD estimates from the 10° cut-off solution minus the estimates from the 3° cut-off solution.

diometers that measure the radiative intensity from the Earth's atmosphere at microwave frequencies in which water vapour and cloud liquid water dominate the emission and absorption in the atmosphere (23.8 and 31.4 GHz). They measure the

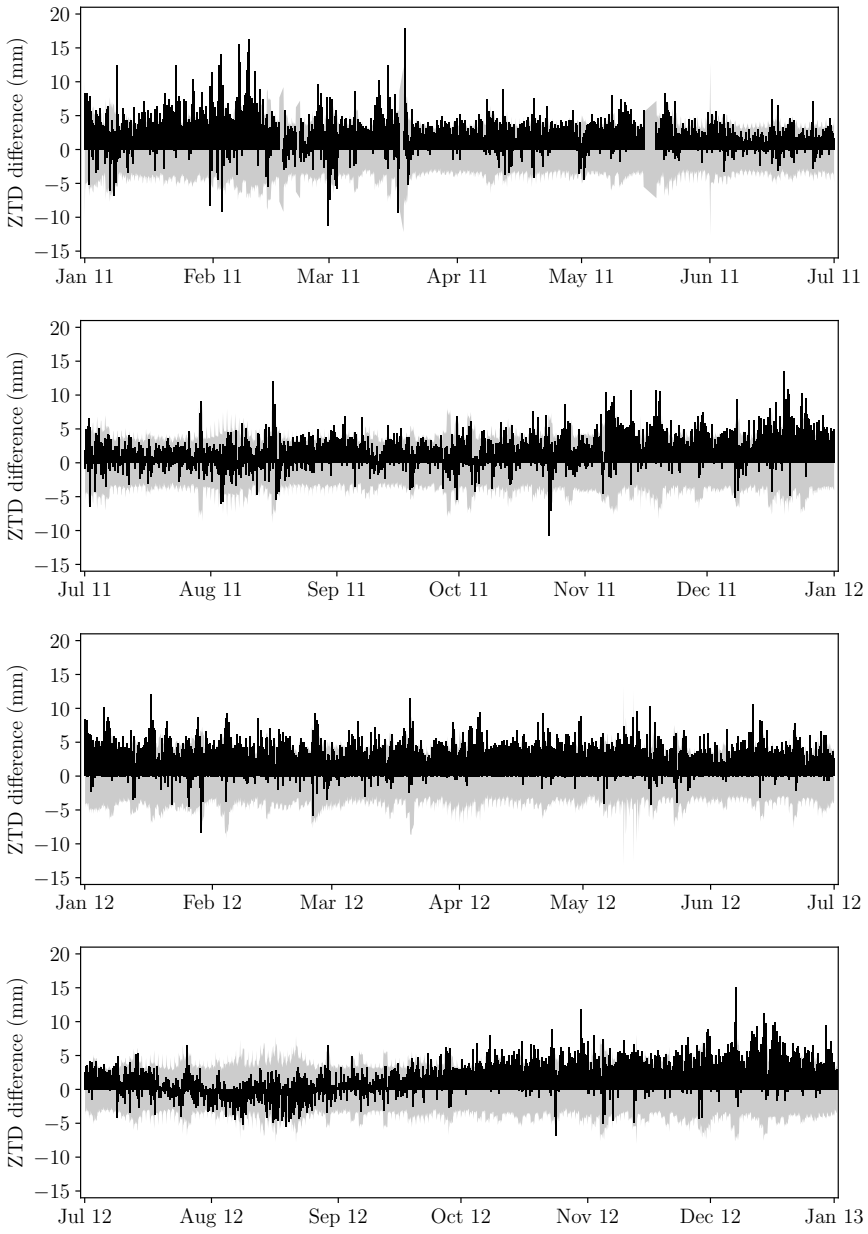

Figure 3.7: The differences between the tropospheric zenith delay estimates from the solutions with elevation cut-off angles 3° and 10° for CEDU. The elevation-dependent weighting of Equation 3.1 is used for both solutions. The grey shades are the 1-sigma uncertainty levels of the ZTD differences. The differences shown are the ZTD estimates from the 10° cut-off solution minus the estimates from the 3° cut-off solution.

radiative intensity in terms of an equivalent brightness temperature, the temperature at which a black body with equilibrium with its surroundings duplicates the radiative intensity of a grey body at a specified frequency. The atmosphere emits black body radiation following the Planck's law, which can be approximated by Rayleigh-

Jeans law at low-enough microwave frequencies and high-enough tropospheric temperatures. The observed brightness temperature is related to atmospheric quantities, including temperature, pressure, water vapour and liquid water, by an attenuation coefficient [e.g. Askne and Westwater, 1986; Liou et al., 2001]. The brightness temperature measured by the microwave radiometers is converted to precipitable water vapour and cloud liquid water by the means of statistical and physical retrievals. The real-time statistical retrievals are based on monthly linear regression coefficients which are computed by relating simulated datasets of precipitable water vapour and liquid water to brightness temperatures from statistical ensembles of radiosonde soundings with a radiative transfer model. These coefficients and the seasonal mean radiating temperatures are then used to derive PW and liquid water from the observed brightness temperatures. In the physical retrieval, the radiative transfer model is iterated to modify the PW and liquid water until the difference between the computed and observed brightness temperatures is within the uncertainty level of the observations [Cadeddu et al., 2013].

In order to compare the PW retrievals from the microwave radiometers and the GPS-derived measurements, we converted the ZTD estimates from our GPS analyses to precipitable water measurements using Equation 2.12 and VMF1 gridded values for ZHD as described in Chapter 2. We downloaded the physical retrievals of the precipitable water in the three stations at TWP network from the free data archive of the ARM (https://www.arm.gov/data) for the same two-year time span of 2011-2012 that we carried out our GPS analyses. Using the quality control flags provided with the radiometry data, we removed the observations that occurred when there was liquid water present on the radiometer window, since these observations are not reliable [Liou et al., 2001]. To compare the two-hourly PW measurements from our GPS analyses with the PW retrievals by MWR instruments, we took an average of all the MWR PW retrievals over a 30-minute window centred at each two-hourly time epoch corresponding to a GPS estimate. We then divided the whole time-span into four three-month periods or "*seasons*" (December to February, March to May, June to August, September to November), concatenating the data for 2011 and 2012 in the same season categories.

The comparison statistics are shown in Table 3.1 as biases and root-mean-square (RMS) differences. The biases shown in Table 3.1 are PW estimates from the MWR minus the PW estimates from the GPS. The MWR generally overestimates the PW when compared to the GPS estimates. Since the GPS estimates of ZTD/PW when including low-elevation observations down to 3° in the solution are generally lower than the GPS estimates from a 10° cut-off solution, the bias with MWR measurements of PW becomes larger when setting a lower cut-off angle. The RMS difference (RMSD) also increases when including low-elevation observations. For SA39 and in summer time (December to February), for instance, the bias is 1.34 mm for the 10° cut-off solution, while it is 1.78 mm for the 3° cut-off solution. The RMS differences are larger at 2.09 mm for the 10° cut-off analysis, which increases to 2.44 mm when including the low-elevation observations in the experiment. A similar pattern is observed for the two other stations and for other seasons.

			GPS03		GPS10	
Site	**Season**	**Mean PW (mm)**	**Bias (mm)**	**RMSD (mm)**	**Bias (mm)**	**RMSD (mm)**
SA39	Dec-Feb	55.53	1.78	2.44	1.34	2.09
	Mar-May	44.88	1.08	1.67	0.64	1.37
	Jun-Aug	23.26	0.47	0.89	-0.01	0.75
	Sep-Nov	41.42	0.74	1.71	0.21	1.42
SA40	Dec-Feb	46.46	1.41	1.93	1.00	1.62
	Mar-May	52.44	1.55	2.08	1.04	1.70
	Jun-Aug	53.64	2.03	2.42	1.50	1.96
	Sep-Nov	49.43	1.94	2.49	1.42	2.03
SA42	Dec-Feb	55.88	1.43	1.95	1.02	1.62
	Mar-May	59.59	1.47	1.99	1.07	1.66
	Jun-Aug	59.22	1.52	2.00	1.24	1.77
	Sep-Nov	57.67	1.46	1.91	1.16	1.69

Table 3.1: Comparison statistics of PW measurements from MWR and GPS for 2011-2012. Mean PW is the average PW for the corresponding time period as derived from MWR. GPS03 and GPS10 columns are related to the GPS experiments using 3° and 10° elevation cut-off angles. Bias is the MWR PW estimate minus GPS PW estimate averaged over the time period. RMSD is the root-mean-square deviation between the GPS and MWR estimates of PW.

A dependency is also observed on the amount of humidity at the station. For SA39, which has the largest variations of humidity over the whole year, the bias and RMSD are the largest in summer when the mean PW is ∼56 mm, while both bias and RMSD are reduced at drier seasons. The smallest bias and RMSD are observed in winter (June to August) and when not including observations at elevations lower than 10°: the bias is almost zero, and the RMS difference is only ∼0.75 mm. This is consistent with the results from previous research ([e.g. Tregoning et al., 1998; Liou et al., 2001]), which showed that the microwave radiometers generally overestimate the amount of precipitable water vapour compared to the GPS retrievals, particularly in humid weather conditions. Tregoning et al. [1998] reported an overestimation of several millimetres by MWR when PW was higher than 25 mm in Hobart, and Liou et al. [2001] observed similar overestimations for their experiment in a tropical region. Here, we also show that including lower-elevation observations further increases this bias between the GPS and MWR measurements of PW.

On the source of the discrepancy between the MWR and GPS estimates of precipitable water, Liou et al. [2001] discussed that while there are uncertainties in the MWR measurements, the amount of RMS difference between the two solutions is much larger than the uncertainties of the MWR retrievals of PW: the ∼0.3 K uncertainty in sensing brightness temperature yields a maximum uncertainty of 0.5 mm in PW estimates. Also, we have removed the MWR PW retrievals when liquid water was present on the radiometer window, and thus need not be concerned about the

unreliable PW measurements at these situations. There is also additional error in the bilinear regression technique used for the PW retrieval discussed by Liou et al. [2001], but is again considered negligible by the authors compared to the the RMS differences they observed with GPS estimates. Liou et al. [2001], therefore, suggested that the atmospheric heterogeneity may play a role in the RMS difference between the PW measurements from MWR and GPS. The microwave radiometers have an upward-looking observing geometry, which only penetrates the atmosphere at a field-of-view of $\sim$5°-6°. GPS, on the other hand, tracks the microwave signals down to a much lower elevation angle, and therefore measures the atmosphere at different volumes of the atmosphere. If there are horizontal inhomogeneities present in the atmosphere around the station, which are not properly considered for by the model we use, they may cause errors in the GPS estimates of ZTD/PW [Liou et al., 2001]. Following the same assumption, the GPS signals when including lower-elevation observations track larger volumes of the atmosphere, at larger horizontal distances, compared to when excluding these low-elevation observations. The horizontal asymmetries of the atmosphere around the station therefore enlarge the errors due to improper mapping functions used for the horizontal gradients of the atmosphere. Parts of the errors, however, could also relate to unmodelled site-specific errors, such as inaccurate antenna models and the presence of unmodelled multipath at the station.

3.1.3 Summary of elevation cut-off angle sensitivity tests

Despite the huge improvements over the past two decades in GPS modelling, low-elevation observations still greatly suffer from mis-modelling issues. We showed in this section that including observations lower than 10° elevation angle generally degrades short-term position repeatabilities at both horizontal and vertical components. Part of this error is an artefact of the commonly used weighting function fitted to one-way residuals, which fails to accurately predict phase observation noise at very low elevation observations. The impact on tropospheric zenith delays were less clear. The use of low-elevation observations reduced the negative correlations between height and tropospheric zenith delays, and a lower elevation cut-off angle than 10° (6° when using the conventional elevation-dependent weighting function and 4° when using a piecewise linear fit to the residuals as the weighting function) yields slightly improved overlap zenith total delay WRMS values than when setting the elevation cut-off angle at 10°. The sensitivity is variable between the stations to the point that stations which are located very close to each other show completely opposite behaviours when varying the elevation cut-off angle. This suggests that un-modelled site-specific errors can significantly affect the sensitivity of solutions to changes in elevation cut-off angle. When comparing the 10° cut-off solution with a 3° cut-off solution, we observed that the tropospheric zenith delay (or their equivalent precipitable water) are generally underestimated when including lower-elevation observations, which increases the bias and RMS difference between PW retrievals from GPS and the microwave radiometry measurements. Two possible error sources are identified: site-specific errors and errors in modelling the horizontal heterogeneities

in the atmospheric refractivity field. We will discuss these two error sources in the next two sections.

3.2 Impact of site-specific errors and their empirical modelling on GPS tropospheric estimates

Site-specific errors that we refer to in this section are the errors caused by unmodelled effects of GPS receiver, antenna and radome, and errors caused by multipath. Errors related to the receiver, antenna and radome remain constant in time unless there is a change in the station equipment, there is degradation of equipment or antenna performance, or tracking loop failures occur [Moore, 2015]. Detailed descriptions for different types of site-specific errors are given by e.g. Moore [2015], Johansson [1998], Elósegui et al. [1995], and King and Watson [2010]. In the following, we give a brief overview of the above site-specific error sources.

3.2.1 Overview of site-specific errors

3.2.1.1 Antenna and radome model errors

The GPS antenna receives signals at different locations, depending on the direction and intensity of the incoming signals. The location of a phase measurement at the antenna is determined by both the physical design and complex-valued gain pattern of the antenna. The measurement location of signals from different azimuths and elevation angles is not generally an ideal sphere, but rather forms an inhomogeneous shape (Figure 3.8). The mean electromagnetic phase centre of the antenna is a virtual point that is generally referred to as the antenna phase centre (APC). By definition, the antenna reference point (ARP) of a GPS receiver is where the vertical physical axis of the antenna intersects the lowest point of the antenna. The offset between APC and ARP is defined as the phase centre offset (PCO). In practice, the actual phase centre differs from the APC, depending on the elevation angle, azimuth and frequency of the arriving signal. The differences between the actual phase centres and APC are called phase centre variations (PCV).

In GPS analysis, both PCO and PCV should be taken into account for the observations. The PCO and PCV are usually determined using absolute calibration techniques [e.g. Wübbena et al., 1997; Bilich and Mader, 2010]., and the mean values of PCO and PCV are provided in the IGS antenna files [Schmid et al., 2016]. The corrections provided by the IGS are the mean values for antenna/radome types; however, different individual antennas of the same type may show different behaviours depending on the manufacturing conditions. It has been shown previously that individual calibration of the antennas can have significant impacts of up to 1 cm on the height estimates and smaller but still significant impacts on horizontal positions [e.g. Baire et al., 2014]. In addition to the differences in the antennas of the same types, the difference in the environment of where a calibration is performed and where the antenna is mounted to observe signals leads to errors in the modelling of PCO and

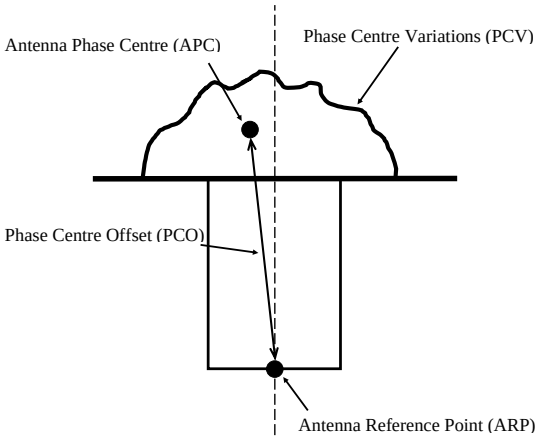

Figure 3.8: Schematic diagram for antenna characteristics (adapted from Seeber [2003]).

PCV. The pillar on which the antenna is mounted also plays a role in introducing errors into the antenna PCV and PCO by scattering the electromagnetic field transmitted by the antenna. Depending on the properties of the pillar, the signal scattering changes the amplitude and phase of the GPS signal received by the antenna [Moore, 2015].

A radome is an enclosing structure that covers a GPS antenna to protect it from the surrounding environment (e.g. snow or animals). A radome is designed to cause minimum attenuation in the radio frequency waves. In practice, however, they introduce alterations to the antenna phase patterns as a result of several effects. The GPS signal is distorted when propagating through the dielectric wall of the radome, which leads to a bending in the angle of the signal arrived (boresight error). The curvature in the radome wall may cause folding of the antenna energy from its original polarisation. Once the GPS signal arrives at the radome wall, part of it is reflected, thus causing a loss in signal strength. The signal strength is also lost when it propagates through the dielectric wall of the radome. Moore [2015] showed that an unmodelled radome results in a bias to the estimate of height of up to 2.5 cm for a signal arriving at an elevation angle of 10°. Kaniuth and Huber [2003] showed that the GPS heights are underestimated by up to several centimetres when a radome is mounted around the GPS antenna, and that the effect is dependent on the elevation cut-off angle. By comparing the tropospheric zenith delay estimates between the solutions with different elevation cut-off angles, they also argued that the dependency of the radome effect on height parameter is also reflected in the tropospheric zenith delays. However, since they did not include large baselines in their solutions, they did not discuss the impact of the radome on the absolute tropospheric delay estimates.

3.2.1.2 Multipath error

Multipath is the effect in which the signal transmitted by the satellite is reflected by the environment around the receiver and thus arrives at the receiver via more than one path. Phase multipath errors can reach 1/4 cycle of the phase, and increase for linear combinations of the phase. The multipath error can be as high as about 22 cm for the phase ionosphere-free combination [e.g. Hofmann et al., 2001; Seeber, 2003; Moore, 2015]. A GPS satellite is visible by a receiver on the ground with a period slightly less than one sidereal day (on average for all the GPS satellites, 23 hours, 55 minutes and 53 seconds) [Agnew and Larson, 2007]. Therefore, multipath errors, which are mainly dependent on the observation geometry, have an almost sidereal periodicity [Bock, 1991; Choi et al., 2004]. As a result, unmodelled multipath effects can be aliased into other estimation parameters at the "GPS year", the required time for the satellite to repeat its inertial orientation with respect to the sun (about 351.2 days), and its harmonics [Ray et al., 2008].

Several pieces of research have been performed to investigate and/or reduce the effects of multipath, which are nicely summarized in Moore et al. [2014]. These works include ray-tracing approaches to model the environment around an antenna (the satellite-reflector-antenna geometry) [Byun et al., 2002; Lau and Cross, 2007], using the spectral content of signal to noise ratio (SNR) to map the contributions of the different satellites to the multipath errors [Bilich and Larson, 2007], calibration of the near-field multipath during the estimation of PCV [Wübbena et al., 2006; Dilssner et al., 2001], calibration of far-field multipath by using a local network of temporary stations [Wübbena et al., 2011], prediction of the multipath using the sidereal periodicity of GPS satellites [Choi et al., 2004], and derivation of a day-to-day correlated multipath correction model by statistical analysis of carrier-phase residuals [Wu and Hsieh, 2010]. Another technique for mitigating the multipath errors, which we use in this thesis, is to use stacks of one-way (undifferenced) phase residuals from the historical datasets for each station to generate a site-specific correction map. This empirical technique helps to map not only the multipath effect, but also antenna phase centre and radome modelling deficiencies and any other site-specific effects.

3.2.2 Empirical mitigation of site-specific errors

The empirical modelling of site-specific errors was first introduced by Hurst and Bar-Sever [1998]. They generated a PCV map by stacking one-way phase residuals of each GPS station in their experiment over several days in bins of 2° elevation angle by 5° azimuth. They then used the newly constructed phase centre correction map to improve the phase centre map. The improved phase centre map is used in their repeated experiments, using a bi-linear interpolation between the bins to correct for the observations at different elevation and azimuth angles. They observed a reduction in the sensitivity of the estimates to the choice of elevation cut-off angle: as a result of correcting for site-specific errors at low elevation angles, the difference between the height estimates from the solutions with 15° and 7° elevation cut-off angles was reduced from 31 mm to 3.6 mm in one of the stations. They also observed

improvements in the solution quality when using the empirical phase centre map in terms of reduction in phase RMS, reduction in the number of observations rejected as outliers, and slight improvements in the repeatabilities of the station position estimates. Choi [2007] derived an ESM from 3 days of data using different bin sizes of 1°, 3° and 5°, but discovered that a much finer resolution is required to recover multipath errors below elevation angles of 45°.

In a more recent work, Moore et al. [2014] used bin sizes of only 0.5° for azimuth and elevation angle to derive an ESM. Their approach is to start with the IGS absolute antenna model for each station, and compute the block median of one-way post-fit phase residuals for each individual station. The block medians of one-way phase residuals are then added to a bi-linear interpolation of the antenna model. The resultant ESM for each station can be provided in the IGS antenna PCV format (ANTEX file) to be used for GPS processing in that particular site. A simulation study was performed by Moore et al. [2014] in which they found that the impact of the ESM on the height estimate is dependent on the station monument height. The largest improvements were obtained for a small range of monument heights between 0.18 and 0.25 m with an improvement in height error of up to 6 mm, while an average improvement of about 1 mm was observed for monuments with heights of 0.25-1.2 m. For monuments taller than 1.2 m, they observed little improvements, while they found that using an ESM could induce biases of up to 2 mm for a small range of low monuments (about 0.17 m). Moore [2015] investigated the effect of the ESM on global solutions, and found improvements in the phase RMS values and a reduction in the mean weekly RMS of the height estimates from 3.47 mm to 3.36 mm when applying the ESM. While the impact of the ESM seems small on position estimates, it could prove significant for estimation of epoch-to-epoch tropospheric estimates, in particular slant delays at low elevation angles. The elevation cut-off angle for the studies performed by Moore [2015] was 10° as the typical cut-off for geodetic purposes, and mostly focused on the position and orbit estimates. In the next section, we will study the effect of the ESM on the tropospheric estimates in a regional network. We particularly study how the ESM impacts the solutions when low-elevation observations are included.

It has been shown in the previous work, and will be shown in the forthcoming sections, that the stacking of the phase residual maps by an ESM generally improves the repeatabilities of the GPS station positions and ZTDs. It should be noted, however, that the systematic modelling errors affect the initial solutions from which the phase residual maps, hence the ESMs, are derived. While part of these errors is reflected in the phase residuals from the initial solutions, and will therefore be accounted for by the ESM, another part of the errors is absorbed into the parameters estimated in the initial solutions. This (unknown) part will not be accounted for by the ESMs, and will therefore continue to affect the ESM-corrected solutions. As a result, while using an ESM improves the precision of GPS solutions, its impact on the accuracy of the estimates is unknown.

3.2.3 Use of ESM for tropospheric delay estimation

For each of the stations in the experiment of Figure 2.2, we generated an ESM using the methodology introduced by Moore et al. [2014]. We derived the ESM by stacking two years of undifferenced post-fit phase residuals from the analysis results of the solution in section 3.1.1 with the elevation cut-off angle of 3°. We derived a new ESM for a station when there was a change in equipment (antenna or radome). We then performed a second set of analyses by implementing the ESMs as corrections to the PCVs of station antennas. The new ESM-applied solutions were also carried out using two different elevation cut-off angles of 3° and 10°.

Five of the stations in our experiment, namely LAUT, MAJU, PNGM, POHN and TUVA, have antenna model ASH701945C_M with SCIS radome for a long period in our study (see Appendix A). Unfortunately, the IGS standard PCV corrections for this antenna/radome type do not have an azimuth dependency (are only elevation-dependent). This caused issues in modelling low-elevation observations that resulted in many of the low-elevation observations being removed as outliers. For this reason, we exclude these stations from the results of this section such that the displayed results and the conclusions made are based on correct azimuth-dependent IGS PCV models. However, the separate results for these five stations and some more detailed discussion are given in Appendix C.

For each of the four solutions (3° and 10° cut-off, with and without the ESM applied), we estimated the monthly time series of the positions using the GLOBK Kalman filter software. We then took the average of the monthly WRMS of the positions over all the stations in the network. These mean monthly WRMS values are displayed in Figure 3.9.

At 10° elevation cut-off angle (blue and green colours in Figure 3.9), while there is generally a slight improvement to the mean WRMS of horizontal position estimates, the largest improvements are observed for the height component: the average reduction of the monthly mean WRMS is 0.20 mm for the vertical component, while it is 0.04 mm for each of the North and East components. When choosing a lower elevation cut-off angle at 3°, the differences between the WRMS of the solutions with and without ESM are less clear for the horizontal components, and slightly smaller for the vertical component. In some months, the ESM has degraded the solutions, while there are other months with an improvement of WRMS due to the ESM. The average reductions in the monthly mean WRMS for this cut-off angle is 0.04 mm for North, 0.03 mm for East, and 0.17 mm for the vertical component of the position.

To study the effect of the ESM on each of the individual stations, we also calculated the average of the monthly WRMS values of the position components for all the stations. Figure 3.10 displays the reductions in the average monthly WRMS values of the height time series when the ESM is applied. The reductions shown in Figure 3.10 are in terms of the square root of the reductions in squared values of WRMS. The scatter of height time series is generally reduced for almost all of the stations when using the ESM, with the largest reductions of about 3 mm for SA40 and SA42, either at 10° or 3° elevation cut-off angle. The only stations with higher scatter when using

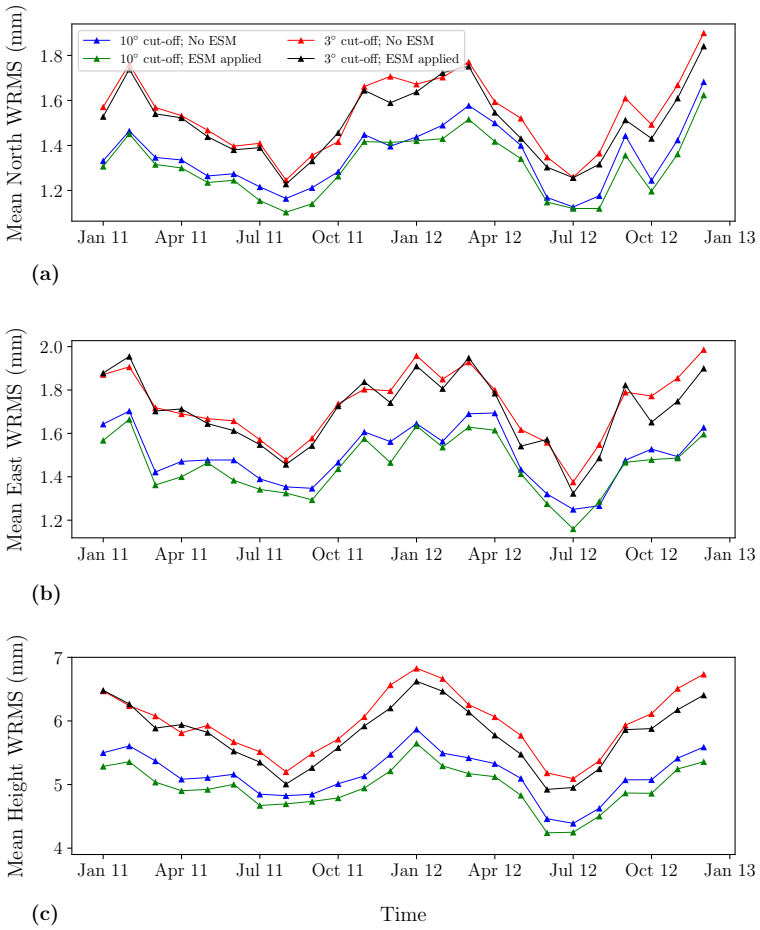

Figure 3.9: Monthly WRMS averaged over the whole stations in 2011-2012 for (a) North, (b) East and (c) Up components of the positions, using a 10° elevation cut-off angle and not applying an ESM (blue), a 3° elevation cut-off angle and not applying an ESM (red), a 10° elevation cut-off angle and applying an ESM (green), and a 3° elevation cut-off angle and applying an ESM (black). Stations with no azimuth dependency in the standard IGS antenna PCV model are excluded from the analysis.

the ESM are KIRI at 10° elevation angle cut-off and MCIL at 3° cut-off. The amounts of degradation, however, are very small and negligible. Other than these, all other stations are improved in terms of monthly height repeatabilities, whether using a 10° or a 3° elevation angle cut-off.

We also calculated the mean overlap WRMS of the zenith total delay estimates at midnight epochs between the consecutive days over the whole two-year period. We excluded ZTD estimates which had 1-sigma uncertainties of larger than 20 mm from our analysis as being too noisy and unreliable. The reductions in the mean overlap WRMS of the ZTD estimates are shown in Figure 3.11. At both elevation cut-off angles, the mean overlap WRMS of the ZTD estimates is reduced for the majority of stations with maximum reductions for SA40 and SA42 (similar to the

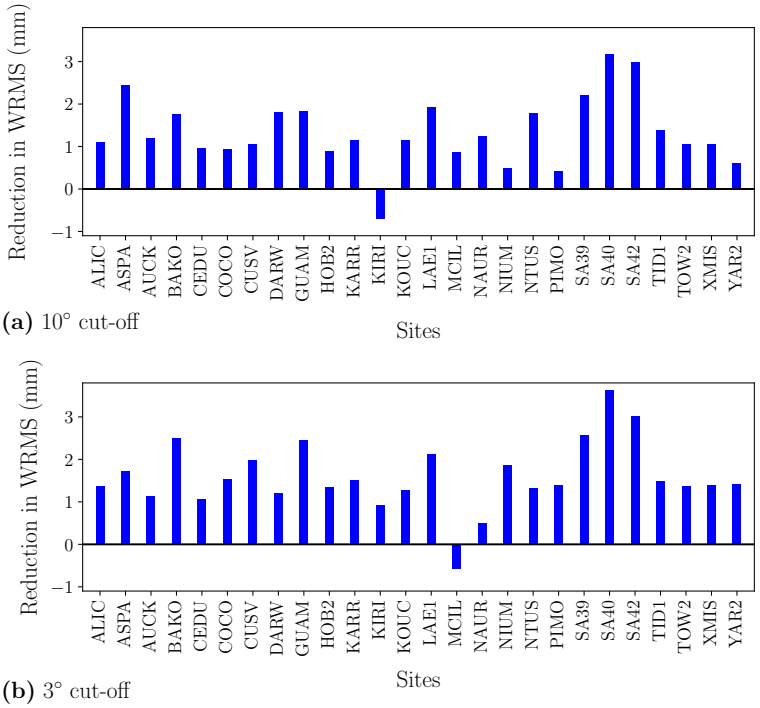

(a) 10° cut-off

(b) 3° cut-off

Figure 3.10: The reduction in the average monthly WRMS of the height estimates due to ESM for different stations when the elevation cut-off angle is set at (a) 10° and (b) 3°.

maximum reductions for height scatters). At 10° elevation angle cut-off, 20 of the stations see reductions in the mean ZTD overlap WRMS, as compared to 6 stations having degraded mean ZTD overlap WRMS. The amount of reductions, however, are much larger than the amounts of increased ZTD overlap scatters. The mean reduction of the ZTD overlap WRMS is 1.32 mm for the 20 stations with improved scatters (with a maximum of 3.19 mm for SA40), while the mean increase of the ZTD overlap WRMS is 0.64 mm for the remaining 6 stations (with a maximum increase of 1.01 mm for MCIL). The improvements are more consistent over the majority of the stations when including low-elevation observations in the solutions. Reductions in ZTD overlap WRMS occur for 23 of the stations with a mean reduction of 1.10 mm and a maximum reduction of 2.97 mm for SA40, while the increase in the ZTD overlap WRMS of the remaining 3 stations is only 0.46 mm on average (with a maximum increase of 0.59 mm for MCIL).

It was mentioned earlier that five of the stations are excluded from the analyses of this section because they use an antenna/radome type that does not include azimuth dependency in its standard IGS antenna PCV model, and there is a huge amount of low-elevation observations that are removed as outliers as a result of poor modelling by the standard IGS antenna PCV. Detailed results about the increase in the number of low-elevation data count for these five stations are separately presented

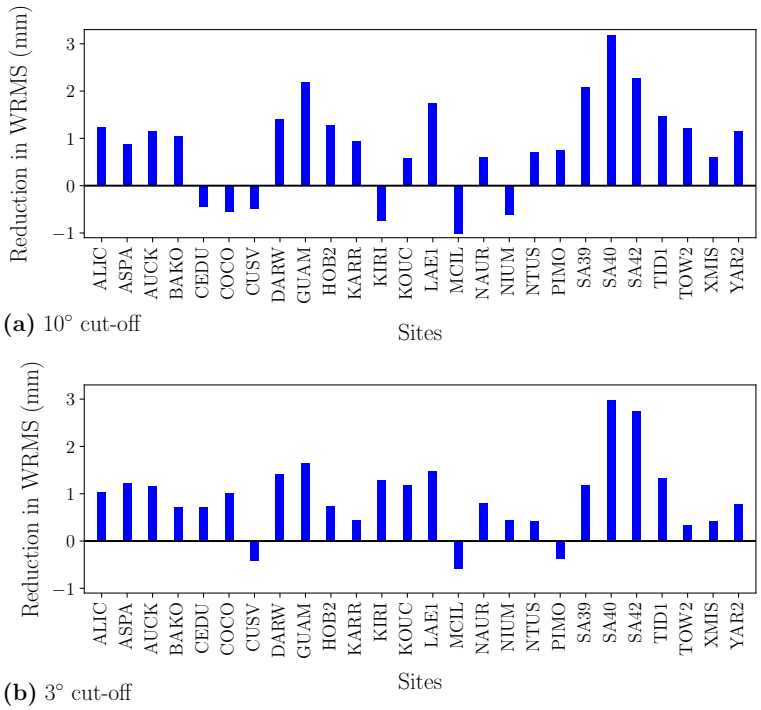

Figure 3.11: The reduction in the mean overlap WRMS of the zenith total delay estimates at midnight epochs due to ESM for different stations when the elevation cut-off angle is set at (a) 10° and (b) 3°.

in Appendix C. However, a similar behaviour was also observed, in a smaller scale, for the rest of the stations (which include azimuth dependency in their IGS standard antenna PCV models); i.e. the number of low-elevation observations was observed to generally increase when using a more accurate antenna PCV model. This is a result of the outlier detection procedure removing more number of observations as outliers when they are contaminated by PCV modelling errors, as explained in Appendix C.

Figure 3.12 shows the total monthly number of low-elevation observations included in the processing, still excluding the data for the five stations with no azimuth dependency in the standard IGS PCV model. The number of low-elevation observations kept in the processing after the outlier detection procedure is consistently higher for the solution in which the ESM is applied. The more low-elevation observations that are kept in the ESM-applied solution may still be contaminated by the errors such as the mapping function errors and the remaining unmodelled PCV and multipath effects. Therefore, care should be taken in the comparison of the quality of the results between the solutions with and without using the ESM, as the higher number of low-elevation measurements included by the ESM may lead to higher dispersions in the resultant time series, while the ESM in fact helps better modelling of these observations.

In order to make an unbiased comparison between the solutions with and with-

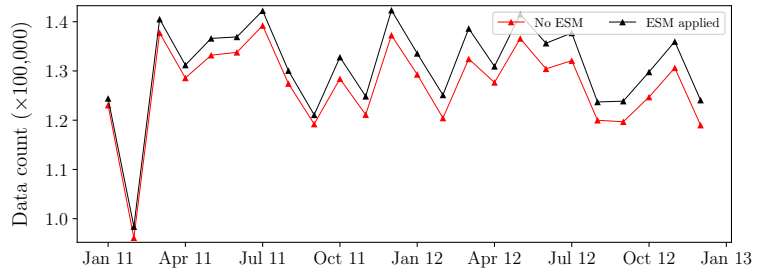

(a) number of data below 5°

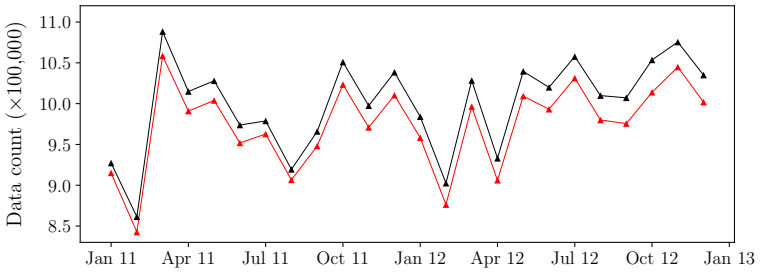

(b) number of data in 5°-10° range

Figure 3.12: Total monthly number of low-elevation observations passed through the outlier detection procedure and kept in the processing when not applying an ESM (red) versus when applying the ESM (black) over 2011-2012. (a) number of data below 5°; (b) number of data between 5° and 10°. Stations with no azimuth dependency in the standard IGS antenna PCV model are excluded from the analysis.

out the ESM, we carried out another set of analyses without applying the ESM but on the same observation geometry of the ESM-applied solution. In other words, after we derived the ESM and processed the network of Figure 2.2, we skipped the outlier-removal process and used the same set of observations that were used during the processing of the ESM-applied solution to perform another set of analyses without implementing the ESM. We performed these analyses at both 3° and 10° elevation cut-off angles. The reductions in the height WRMS and the mean ZTD overlap WRMS when using the ESM compared to when using the standard IGS08 antenna PCV and including exactly the same set of observations in the least-squares inversion are shown in Figures 3.13 and 3.14 for both cut-off angles of 3° and 10°. While the reductions in height scatter at 10° when keeping the observation geometry fixed between the two solutions (Figure 3.13a) are smaller compared to the reductions when allowing the outlier-detection procedure to change the observation geometry based on the pre-fit residuals (Figure 3.10a), the improvements are much more significant when including low-elevation observations down to 3° and keeping the same set of observations between the solutions with and without the application of the ESM (Figure 3.13b and comparison with 3.10b); On average, when using the same observation geometry for both solutions and including the low-elevation observations, the height WRMS values are reduced from a mean value of 6.54 mm for the solution with stan-

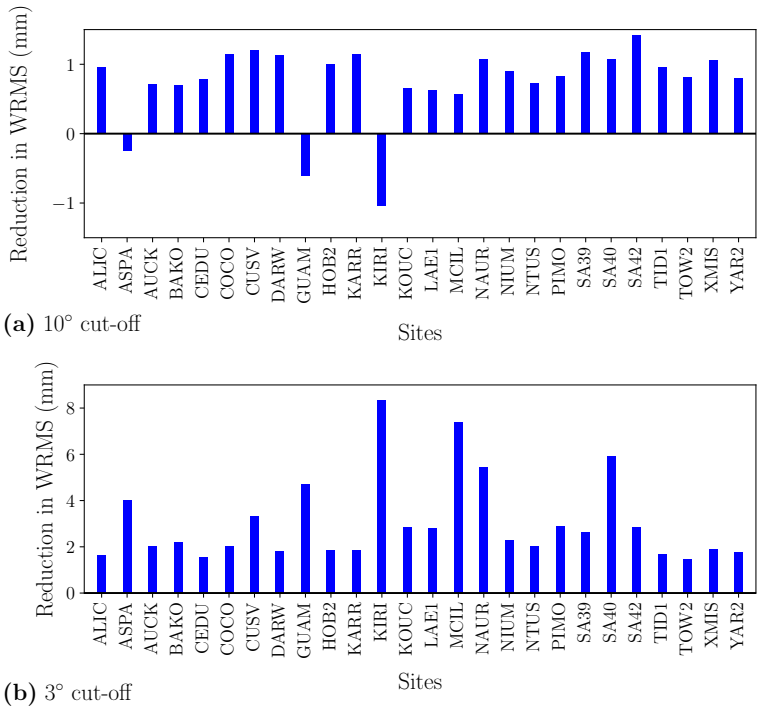

(a) 10° cut-off

(b) 3° cut-off

Figure 3.13: The reduction in the average monthly WRMS of the height estimates due to the ESM for different stations when the elevation cut-off angle is set at (a) 10° and (b) 3°. The observation geometry is held the same for both solutions with and without the ESM.

dard IGS PCVs to 5.64 mm for the solution with the ESM (∼19%). While station KIRI saw an increase in the height scatter when excluding observations below 10° elevation angle, the maximum reduction occurred for this station when using an elevation cut-off of 3°; the average monthly height WRMS for this station at 3° is reduced from 10.74 mm to 8.28 mm when using the ESM (∼23%). Unlike when we allowed the outlier detection routine to remove highly erroneous observations as outliers, there is no station with larger height scatters due to the ESM at 3° cut-off when using a fixed set of observations in the analysis.

Similar improvements are observed for the mean ZTD overlap WRMS values when using the ESM compared to when using the IGS08 antenna PCVs, and holding the observation geometry fixed between the two solutions (Figure 3.14). Unlike the height WRMS, however, the ZTD improvements are larger compared to when allowing the change of observation geometry between the solutions even at 10° cut-off. At 10° elevation cut-off angle, the mean ZTD overlap WRMS is reduced from 6.11 mm on average when using the IGS standard PCVs to 5.92 mm when using the ESM (∼3%). At 3°, the improvements are more significant; on average, the mean ZTD overlap WRMS is reduced from 6.39 mm when not using the ESM to 6.00 mm when using the ESM (∼6%); the maximum reduction occurred for SA40 at 10° elevation

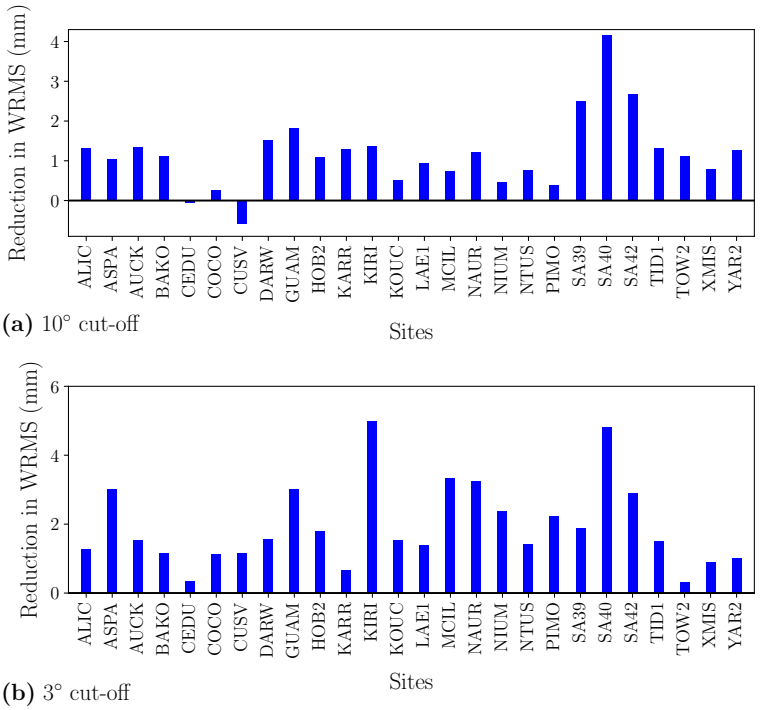

(a) 10° cut-off

(b) 3° cut-off

Figure 3.14: The reduction in the mean overlap WRMS of the zenith total delay estimates at midnight epochs due to the ESM for different stations when the elevation cut-off angle is set at (a) 10° and (b) 3°. The observation geometry is held the same for both solutions with and without the ESM.

cut-off (a ∼20% reduction from 6.93 mm to 5.54 mm), and for KIRI at 3° elevation cut-off (a ∼19% reduction from 8.54 mm to 6.92 mm).

By using the same observation geometry as used by the ESM-applied solutions for the analyses with the standard IGS antenna PCV models, we do not allow the poorly modelled low-elevation observations to be simply excluded from the least-square inversions, and therefore we can make an unbiased study on the effect of the ESM on the low-elevation observations. It is true that, in practice, we could improve the position and ZTD estimates by throwing out the observations which are poorly modelled. However, if the purpose of an analysis is to derive the slant tropospheric delays (for tomographic applications, e.g.), empirical modelling of site-specific errors is essential to have accurate slant delays. Using low-elevation observations in the analysis also provides us with more information about lateral variations of the refractivity in the local atmosphere around a GPS station, which is important in studying meteorological events such as extreme precipitation occurrences. Nevertheless, even when allowing the poorly modelled observations to be excluded from the analyses, the ESM still consistently improves height and ZTD estimates for the majority of the stations, as observed in Figures 3.10 and 3.11 and the relevant discussions.

3.2.4 Impact of the ESM on the elevation cut-off angle sensitivity

To assess the impact of the ESM on the estimates of ZTD when including low-elevation observations, one can study how the ESM is able to reduce the sensitivity of the ZTD estimates to the elevation cut-off angle. To do this, we compare the estimates of ZTD between the solutions with 3° and 10° elevation cut-off angles. We do this comparison for the solutions without and with the implementation of the ESM. The mean ZTD differences between the solutions with 3° and 10° cut-off are shown in Figure 3.15a for the solutions with the standard IGS08 antenna PCV model and the ESM for each station. The ESM clearly resulted in smaller differences between the two solutions with different cut-off angles. When using the standard IGS antenna model, the mean ZTD differences reach values larger than 3 mm, while the mean ZTD differences reaches just over 1 mm for the ESM-applied solutions. The mean ZTD difference for the solution with the standard IGS antenna model is 1.43 mm, which is reduced to 0.61 mm when the ESM is applied to the solutions (a reduction of ∼57%). The number of significant ZTD differences (which we define as the number of ZTD differences larger than 1-sigma uncertainty) between the two solutions with 3° and 10° cut-off also decreases when the ESM is applied. For TOW2, as an example of the station with the highest occurrence of significant ZTD differences, the number decreases from over 2000 epochs to about 1000 epochs. In total over all the stations, 11435 ZTD differences are larger than 1-sigma uncertainty level, but the number is reduced to 7743 when the ESM is used (a reduction of ∼32%).

The reduction in the differences of ZTD estimates between the solutions with 3° and 10° elevation cut-off angles due to applying the ESM shows that the site-specific effects are major contributors to the errors in modelling low-elevation observations. The empirical modelling of site-specific errors reduces the sensitivity of the estimates to the elevation cut-off angle by correcting the observations for the antenna/radome and multipath effects. Therefore, while the ESM improves the repeatability of the estimates at both conventional 10° and very low 3° cut-off angles (as observed by the reduction in parameter WRMS values), the use of a site-specific model is essential in the analyses where the low-elevation observations are included.

3.2.5 Comparison with MWR

Figure 3.16 shows the mean biases and RMS differences between the GPS-derived precipitable water estimates and the MWR-driven PWs over the whole 2011-2012 period for the three stations SA39, SA40 and SA42. For each station, the biases and RMSDs are displayed for when the ESM is applied and when the standard IGS08 antenna PCVs are used, and at two different elevation cut-off angles of 3° and 10°. Since the number of data is not very different between the solutions with and without the ESM, we used the solutions without constraining the observation geometries to be the same for the two solutions. The geometry-fixed solutions resulted in similar statistics. The mean biases shown in Figure 3.16a are the MWR-derived PWs minus the mean GPS-derived PWs. At 3° elevation cut-off angle, the application of the ESM during the GPS processing increases the PW estimates, leading to reduced biases

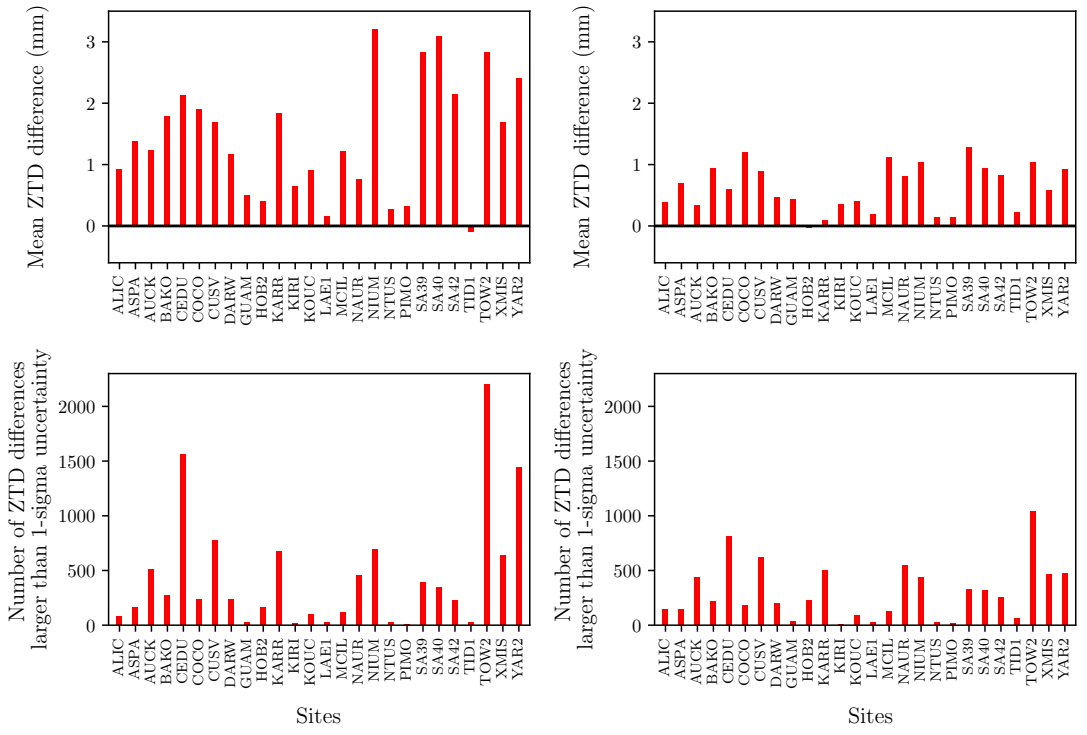

(a) No ESM **(b)** ESM applied

Figure 3.15: (Top) Mean differences between the ZTD estimates from the solutions with 3° and 10° elevation cut-off angles, and (bottom) number of ZTD differences which are larger than 1-sigma uncertainty levels, for the solutions with the use of (a) standard IGS08 antenna model and (b) empirical site-specific model.

with MWR. The reduction in the mean bias at 3° is very small for SA40, but is more significant for SA39 and SA42. At 10° cut-off, on the other hand, the ESM decreases the GPS-derived PW estimates and increases the bias with MWR for all the three stations. Similarly, the RMSD values of the PW measurements from MWR and GPS increase at 10° and decrease at 3° when using the ESM. While one can not easily interpret the source of differences between the PW estimates from the MWR and GPS measurements and which of the two instruments is more accurate, it is clear that the ESM reduces the sensitivity of the GPS estimates to the choice of elevation cut-off angle. The ESM results in lower PW estimates when a 10° cut-off is used and higher PW estimates when a 3° cut-off is chosen, which leads to smaller biases between the GPS-derived PW estimates with and without the observations below 10°. Part of the bias between the GPS and MWR estimates of PW could speculatively stem from the existence of unmodelled site-specific errors, such as antenna/radome PCV errors and multipath. It also shows that the use of an empirical site-specific model reduces the sensitivity of the GPS estimates to the choice of elevation cut-off angle by improved modelling of low-elevation observations.

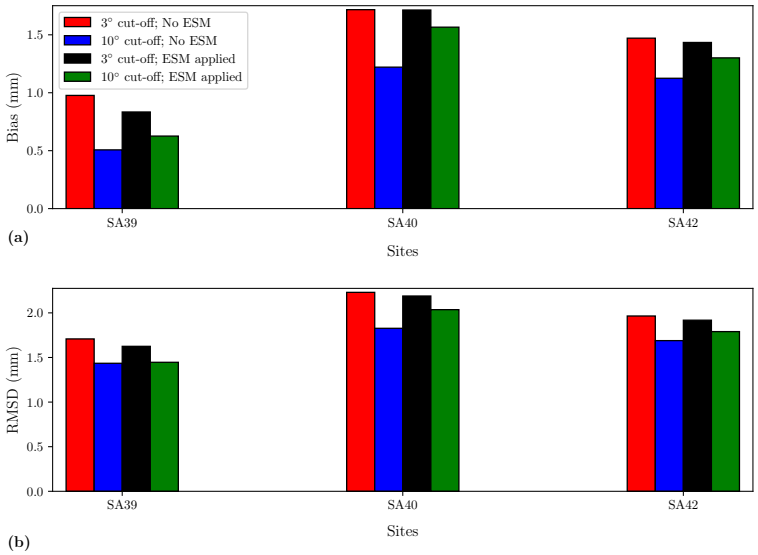

Figure 3.16: (a) Mean bias and (b) RMS difference between the precipitable water estimates from GPS and MWR during 2011-2012 for four different solutions: with and without the ESM, and using 3° and 10° elevation cut-off angles. The mean biases are the mean PW measurements from MWR minus the mean GPS-derived PWs.

3.3 Tropospheric horizontal gradients in GPS analysis

While the site-specific antenna/radome and multipath effects induce errors in the low-elevation observations (as observed in the previous section), there could be also errors in modelling the tropospheric delays at low elevation angles. Such errors could occur as a result of the assumption of symmetric refractivity field around a station used in the GPS inversion. The troposphere is usually considered azimuthally symmetric in modelling a GPS signal (Equation 2.5). To compensate for this assumption, horizontal inhomogeneities of the tropospheric delay are estimated generally in the form of two linear north-south and east-west gradient parameters (Equation 2.6). Together, these two parts assume a tilted two-axis plane for the horizontal changes of the tropospheric refractivity around a GPS site. A widely-accepted equation for the elevation-dependent part of the horizontal gradient mapping function was developed by Chen and Herring [1997] by fitting a function (Eq 2.7) to a tilted atmosphere model for a range of different elevation angles. It is well established that the estimation of tropospheric horizontal gradients enables the use of low-elevation observations in the GPS processing, improving the position and tropospheric zenith delay estimates. For instance, Bar-Sever et al. [1998] showed that estimating the horizontal gradients and including observations at elevation angles down to 7° yields improved position repeatabilities compared to not estimating horizontal gradients and excluding measurements below 15°.

Similar to the derivation of a priori zenith delays (Böhm et al. [2006b]) through ray-tracing of a numerical weather model, Böhm and Schuh [2007] derived hydro-

static and wet horizontal gradients, known as linear horizontal gradients (LHG) by performing a two-dimensional ray-tracing of the ECMWF weather model. In their ray-tracing approach, they used the refractivity profiles from the ECMWF with a horizontal resolution of 0.25°. For each given station, they extracted the closest profile to the site, one refractivity profile in the immediate north and one profile in the immediate east. Then, they calculated the north-south and east-west horizontal refractivity gradients by differencing the profiles, weighting the differences with the height. They assumed that the horizontal refractivity gradients remain the same at any distance from the station, such that they only require three profiles per station. This is a limiting assumption for the accuracy of the ray-traced gradients, but needs much less computational time than a rigid ray-tracing like the one used for asymmetric Mapping Functions [Böhm et al., 2005]. They implemented the LHG gradients in a Very Long Baseline Interferometry (VLBI) analysis, and discovered that fixing the horizontal gradients to the LHG values improves the baseline repeatabilities, compared to when not estimating the gradients at all or when estimating the gradients only every 24 hours. However, they showed that estimating the gradients every 6 hours results in more repeatable estimates of baselines than fixing the gradients to the LHG.

In an attempt to enable the use of a priori tropospheric horizontal gradients in operational geodetic analyses, Böhm et al. [2013] introduced empirical static a priori gradients (APG), which are spherical harmonic expansion of the ray-traced gradients up to degree and order 9, and can be easily determined for any station. For their ray-tracing, they used the monthly averages over 40 years of ECMWF ERA40 reanalysis (1957-2001) with horizontal resolution of 1°. They calculated 5 tropospheric delays for each point on a 5° grid over the globe: one total zenith delay, and four slant delays at 5° elevation angle towards north, east, south and west. For each grid point, they averaged these five delays and considered the average as the symmetric part of the tropospheric delay for that point. Then for each of the four slant delays, they subtracted the symmetric delay from the slant delay, fitted these slant delays to the asymmetric delay model of Chen and Herring [1997] (Equation 2.6), and inverted the equations to estimate north-south and east-west gradients. They eventually averaged the gradients over all the 12 months, as they did not observe a significant time varying signal in the gradients. After deriving horizontal gradients in a 5° resolution grid, they used a least-squares approach to obtain a spherical harmonic expansion of these north-south and east-west gradients up to degree and order 9. They compared the APG gradients with the gradients estimated by GPS and VLBI, and discovered that the APG gradients are generally larger than the gradients estimated by geodetic analyses. This over-correction by the APG resulted in differences in the North and Up components of estimated GPS station positionswhen fixing the gradients to the APG compared to when estimating the gradients by Chen and Herring [1997] model. The differences reached up to about 5 mm for North and about 7 mm for height estimates.

Ray-traced LHG tropospheric gradients have been made available for selected IGS stations in http://ggosatm.hg.tuwien.ac.at/DELAY/ETC/LHG/GPS. For our experiment of

Figure 2.2, the LHG gradients are provided for 24 of the stations. For these 24 stations, we retrieved the LHG gradients, computed the APG gradients and compared them to the north-south and east-west gradients estimated every 6 hours from the GPS analysis for the whole period of 2011-2012. For these comparisons, we implemented the empirical site-specific model and used a 3° elevation cut-off angle. For each of the north-south and east-west gradients, we took the average of the gradients over the whole analysis period for each station. The mean gradients from the three different sources (LHG, APG and GPS) are compared in Figure 3.17. The stations in Figure 3.17 are sorted from the lowest latitude (HOB2) to the highest latitude (MCIL). As expected due to higher humidities at the equator, the mean north-south gradients estimated by GPS are mainly positive at the stations in the southern hemisphere, and negative in the northern hemisphere (Figure 3.17a). Exceptions to this are KARR with positive north-south gradients measured by GPS, and POHN and PIMO with positive gradients. The general trend in the comparisons of the north-south gradients between the APG and GPS estimates is similar to what Böhm et al. [2013] observed: the APG (black colour) generally overestimates the magnitude of the north-south gradients with a sign change in the equator. This overestimation is more clear for the stations in high latitudes of the southern hemisphere, and stations in the furthest north of the equator for our experiment. The LHG gradients (red colour), on the other hand, typically underestimate the magnitude of the north-south gradients with mean values which are much closer to zero than the GPS estimates. Both APG and LHG usually underestimate the east-west gradients compared to the gradients estimated by the GPS.

The mean north-south gradients measured by LHG are very close to the mean GPS estimates for ALIC (Figure 3.17a). Even for such station, however, there may be still inconsistencies in the time series of the gradients between the two sources. As an example of a station with a small mean bias of north-south gradients between LHG and GPS, Figure 3.18 shows the tropospheric horizontal gradients measured by GPS, LHG and APG for GPS station ALIC. While the mean north-south gradients are comparable between the GPS and LHG measurements, it is evident from Figure 3.18 that parts of both north-south and east-west gradient signals are not captured by the LHG gradients in early 2011. This shows that even for the stations where the mean LHG gradients are close to the mean GPS gradients, large errors could occur in the LHG gradients at times. These errors are most likely due to the simplifying assumptions made in the process of ray-tracing. For instance, only one neighbouring refractivity profile is used for differencing with the profile at a station to derive each of the horizontal gradients, which leads to the assumption that the horizontal gradients remain the same at any distance from the station. This assumption is slightly improved by the APG, in which the average of four low-elevation slant delays and one zenith delay at the station is first considered as symmetric delay, and the asymmetric delay model is fit to the four slant profiles to estimate horizontal gradients. The APG, however, is the empirical expansion of the temporal mean of such ray-traced gradients, and thus does not capture the time-varying signal of the gradients.

In order to assess if the ray-traced horizontal gradients are accurate enough to be

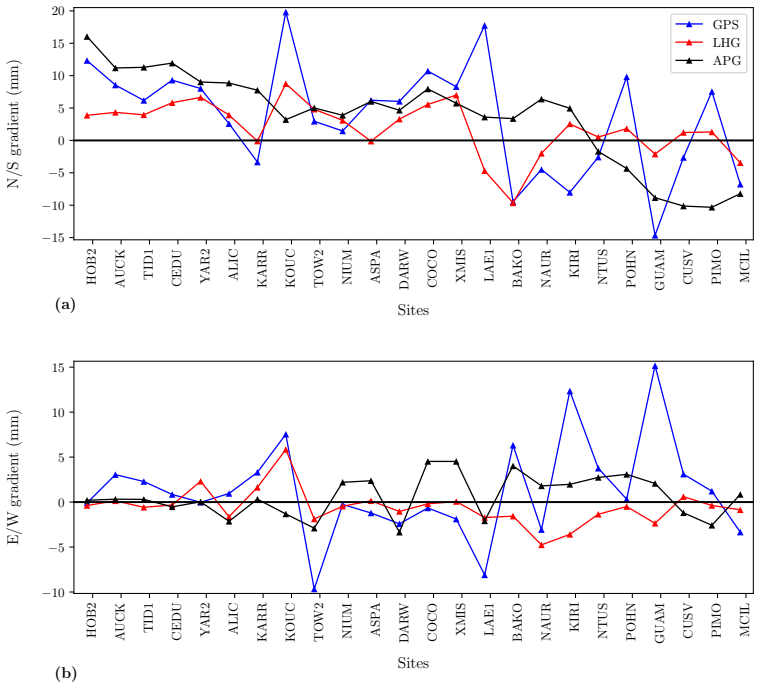

Figure 3.17: Comparison of (a) north-south and (b) east-west mean tropospheric gradients from three different techniques: GPS estimates (blue), LHG ray-traced gradients (red) and APG empirical static gradients (black). The stations are ordered according to their latitudes.

used as an alternative to estimating the horizontal gradients in the GPS analyses, we implemented both LHG and APG gradients in the analysis of Figure 2.2 for January 2012 and compared the repeatabilities of the estimates from six different approaches: 1) standard solution (no a priori gradients and estimating the horizontal gradients every six hours), 2) using the LHG gradients as initial values and still estimating the gradients, 3) using the APG gradients as initial values and still estimating the residuals, 4) estimating no gradients at all (assuming that the gradients are zero), 5) using the LHG gradients as a priori, and 6) using the APG gradient as a priori. We averaged the repeatabilities of the three position components and overlap ZTD estimates at midnight epochs over all the stations in the network for each of these six analyses, which are shown in Figure 3.19. For all of the analyses, the ESM is applied and the elevation cut-off angle is set at 3°.

Clearly, fixing the gradients to either zero, LHG or APG values degrades the repeatabilities of all the four estimated parameters, compared to estimating the gradients every six hours. The impact is larger for position components, particularly for the North component. When estimating the gradients, there is not any significant difference as to which a priori gradients is used as initial values in the least-squares inversion. This is because the horizontal gradients are generally small enough that

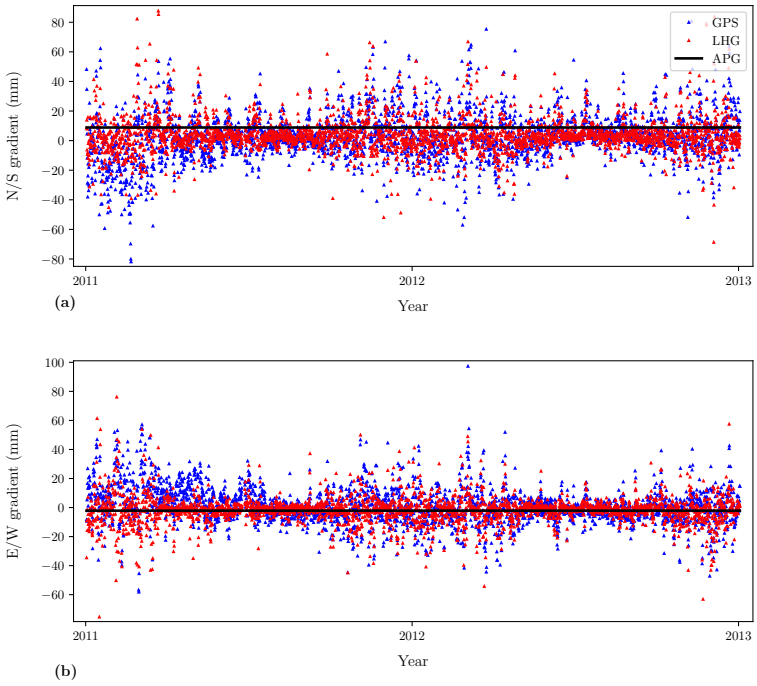

Figure 3.18: Comparison of (a) north-south and (b) east-west tropospheric gradients for the ALIC GPS station from three different techniques: GPS estimates (blue), LHG ray-traced gradients (red) and APG empirical static gradients (black).

initiating the inversion by zero gradients easily leads to convergence. If one decides not to estimate the gradients, there is a slight benefit in using the LHG gradients: the mean reduction in the WRMS when using the LHG as a priori compared to when assuming zero horizontal gradients are ∼3% for East, ∼17% for North, ∼8% for Up and -∼2% for ZTD estimates. The differences are very insignificant for the APG gradients. There are two main conclusions that one can make here: 1) Since the solutions with estimating the horizontal gradients are more repeatable than the solutions with the ray-traced gradients of LHG and APG as a priori, the estimated gradients, although potentially biased by systematic modelling errors, are likely more accurate than the ray-traced gradients; 2) If for any reason one prefers not to estimate the horizontal gradients in a GPS analysis (for reducing computational burden in real-time analyses e.g.), there is only a slight benefit in using the LHG gradients as a priori, mainly for North and Up components.

The approach we used to estimate the tropospheric horizontal gradients in all the above analyses, is to assume a two-axis tilted plane for the atmospheric refractivity, estimating two north-south and east-west gradients. The fact that the GPS estimates of these planar horizontal gradients yields more repeatable solutions than the ray-traced predictions, indicates that one may acquire even more precise estimates of the horizontal gradients by extending the two-axis assumption to a more complicated

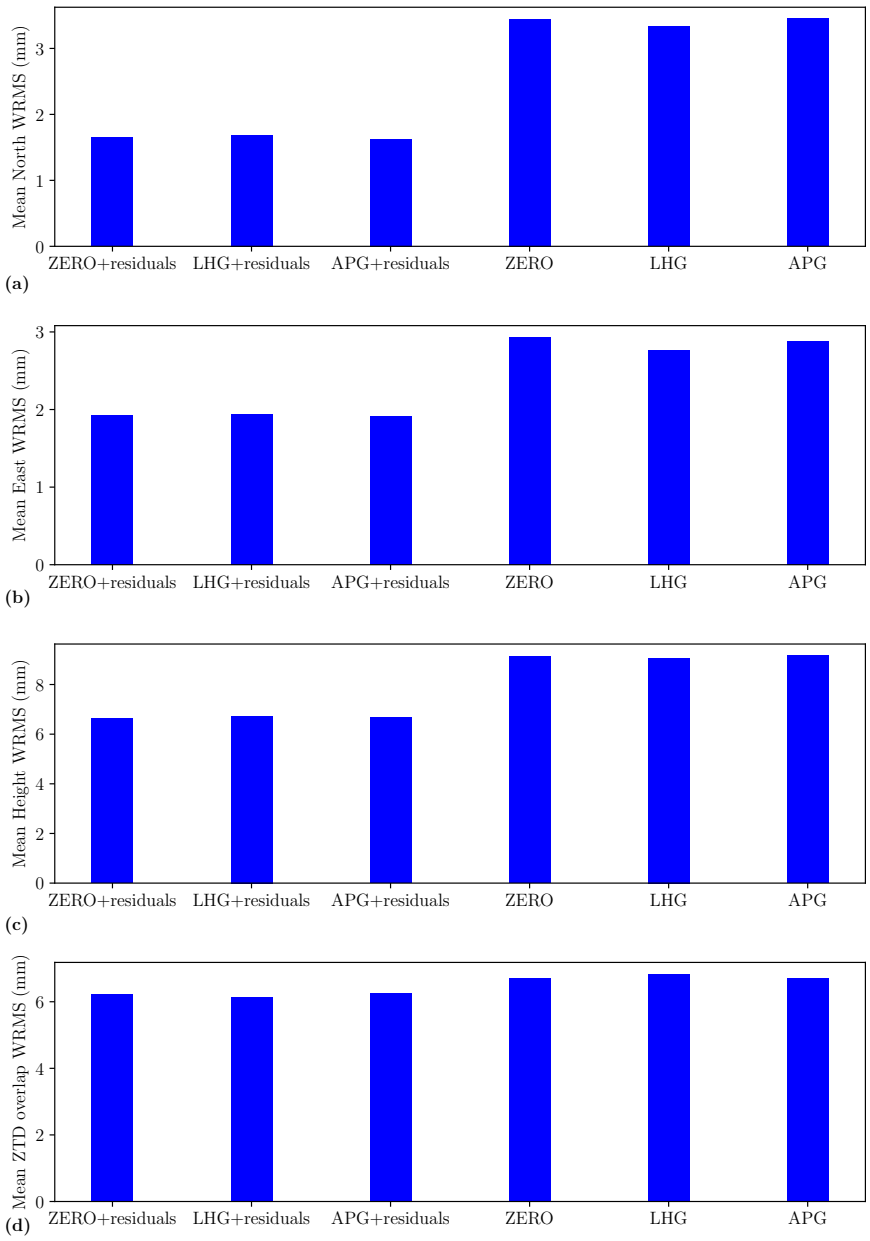

Figure 3.19: Mean WRMS values over all the stations for (a) North, (b) East, (c) height and (d) overlap ZTD estimates when taking different strategies in the estimation of horizontal north-south and east-west gradients in the GPS analysis: no a priori and estimating the gradients (ZERO+residuals), LHG as a priori and estimating the residuals (LHG+residuals), APG as a priori and estimating residuals (APG+residuals), fixing the gradients to zero (ZERO), fixing the gradients to LHG (LHG) and fixing the gradients to APG (APG).

model of tropospheric horizontal gradients in the GPS analysis. Such a more complicated model of horizontal gradients could be useful in particular abnormal weather

conditions where the planar assumption for the horizontal gradients may not be sufficient to capture the full asymmetry of the tropospheric refractivity field. A new directional model of horizontal gradients will be introduced and implemented in the next chapter.

3.4 Summary

Some of the modelling issues for the low-elevation observations in GPS analyses were discussed in this chapter. It was shown that while the use of low-elevation observations helps decorrelate zenith delay and height parameters, and despite the improvements in mapping functions over the last decade, the measurements at very low elevation angles (below 10°) still suffer from large modelling errors. While using a proper weighting scheme such as a piecewise linear weighting improves the solution repeatabilities by de-weighting observations based on the phase residuals, approaches that use improved observation equations for the measurements are additionally desirable, as they provide more accurate slant delays, which are useful e.g. in tomographic reconstructions of the troposphere or in the applications where horizontal changes of the refractivity are studied.

The use of low-elevation observations in our GPS analyses resulted in a general reduction in the estimates of tropospheric zenith total delay and increased scatter of position estimates. The sensitivity of the ZTD estimates to the elevation cut-off angle sometimes showed opposite patterns at nearby stations, which indicates that a large part of the errors in modelling the low-elevation measurements results from site-specific effects. Using the empirical site-specific model developed by Moore [2015] was shown to improve the scatters both in position and midnight overlap ZTD estimates by improving the antenna/radome PCV correction models and reducing the multipath impact. The use of ESM also reduced the sensitivity of the ZTD (and equivalent PW) to the choice of elevation cut-off angle by reducing the ZTD/PW estimates when a 10° cut-off is chosen and increasing the estimates at 3° cut-off.

A comparison of planar north-south and east-west gradients of the tropospheric delay between the GPS estimates and the ray-traced LHG and APG values showed that the GPS-estimated north-south gradients are generally smaller than the static APG gradients but larger than the time-varying LHG gradients, while the east-west gradients are typically underestimated by both APG and LHG. Moreover, although the LHG gradients are time-varying (unlike the APG gradients), they sometimes fail to capture the whole amplitude of the gradient signals. The simplifying assumptions in the derivation of LHG and APG gradients are most likely the cause for the inconsistencies between these ray-traced gradients and the gradients estimated by the GPS. Comparison of the GPS experiments using the LHG/APG gradients with the analyses using no a priori gradients verified that the GPS estimates of the horizontal gradients are likely more accurate than the ray-traced gradients (although still potentially biased by systematic modelling errors), since the solutions with the estimation of the tropospheric horizontal gradients yielded smaller scatters of the position and

ZTD parameters. However, the two-axis (planar) model which is conventionally assumed for the estimation of the tropospheric horizontal gradients in most current GPS analyses, may not be accurate enough at particular situations where the horizontal changes of the troposphere are not symmetric around a station. Therefore, part of the errors in modelling the low-elevation observations could be due to the simplified model of gradients which is currently used in the GPS analyses. In the next chapter, we will assess the impact of such mis-modelling at particular asymmetric gradient scenarios, and we will study how a more complex model could be useful in such situations.

Chapter 4

Directional model of tropospheric horizontal gradients

It was shown in the last chapter that the GPS estimates of north-south and east-west tropospheric gradients yield more repeatable solutions than the ray-traced horizontal gradients of LHG. However, the question then arises: is the two-axis north-south and east-west model of horizontal gradients always accurate enough for geodetic and/or meteorological purposes? In this chapter, we will show that under particular weather conditions with asymmetric horizontal changes of refractivity, the conventional tilted plane model of horizontal gradients fails to provide an accurate representation of tropospheric gradients. We introduce a new parametrization of tropospheric gradients (Masoumi et al. [2017]) whereby an arbitrary number of gradients are estimated as discrete directional wedges around a station vertical. We first assess the new directional model of gradients via simulations and show that the new model significantly improves the accuracy of recovered tropospheric zenith delays in asymmetric gradient scenarios. Then, we will show the impact of the model on the estimated gradients, zenith delays and position parameters in different case studies. In a case study of an extreme rain event that occurred in September 2002 in southern France, we show that the new directional parametrization is able to isolate the strong gradients in particular azimuths around the GPS stations consistent with the "V" shape spatial pattern of the observed precipitation. We also implement the directional gradient model in another study of a network of GPS stations in the Sierra Nevada region where highly asymmetric tropospheric gradients are known to exist, where the model significantly improves the repeatabilities of the stations in asymmetric gradient situations. Most of the contents of this chapter have been peer reviewed and published in Masoumi et al. [2017]. This chapter provides more detailed elaborations of the published paper.

4.1 Modelling of the tropospheric asymmetry

While the GPS meteorology studies in the past two decades have mostly focused on the estimation of tropospheric zenith delays, there have been more attention to the asymmetries in the tropospheric refractivity field in the recent years. Some research has been carried out to study the relationship between the accumulation of water

vapour and precipitation systems [e.g. Champollion et al., 2004; Van Baelen et al., 2011]. In a recent study by Labbouz et al. [2015], it was shown that the PW reached its maximum on average 20 minutes prior to precipitation maximum for 76% of the cases for a mid-latitude site in France, using five years of GPS and rain gauge measurements. Although such studies are still in early stages, and despite the unknown complications of weather systems, there still seems to be demand for further work on horizontal movements of the moisture in the atmosphere and the link with the formation of extreme precipitation events.

As mentioned in Chapter 2, mapping functions are used to map the delay from the observing angle of any GPS observation to the zenith angle above the site [e.g. Niell, 1996; Böhm et al., 2006a,b]. Such mapping functions generally assume that the troposphere is symmetric around the GPS site, and thus only depend on the elevation angle of observations and not on the azimuthal direction of the signal. However, horizontal heterogeneities in the tropospheric refractivity field are known to exist [e.g. Gardner, 1976; Davis et al., 1993; Gegout et al., 2011]; therefore, most geodetic analysts estimate additional linear horizontal gradient parameters in the form of north-south and east-west components [Chen and Herring, 1997]. Such a gradient model assumes that the troposphere is a plane with linear horizontal changes in zenith delay. While this is a reasonable approximation for most situations, there are cases when a plane does not well represent the atmospheric refractivity field. Such cases occur, for instance, when there is a strong moisture content in a specific direction at a site.

There have been attempts to better represent the asymmetry of the troposphere by using azimuth-dependent mapping functions rather than estimating linear gradients. Böhm et al. [2005] performed a line-of-sight ray-tracing every 30° in azimuth through interpolated slant refractivity profiles from the ECMWF numerical weather model to derive asymmetric mapping functions called Vienna Mapping Functions 2 (VMF2) as opposed to the symmetric version, VMF1. They then applied VMF2 mapping functions to a VLBI experiment, and found improvements in baseline length repeatabilities compared to a solution where the symmetric VMF1 mapping functions were used along with a planar gradient parameter estimation. In other words, the use of azimuth-dependent mapping functions not only removes the need for estimating additional gradient parameters in the geodetic analyses, also provides a more accurate representation of the azimuthal variability of tropospheric refractivity compared to the planar surface described by the classic Chen and Herring [1997] gradient model. However, VMF2 mapping functions require the derivation of 12 hydrostatic and wet coefficients per site per epoch (for 12 azimuthal nodes of 30°). This requires a much higher computational burden to perform the ray-tracing, compared to the derivation of only one hydrostatic and wet coefficient for VMF1 mapping functions. As of today, the author is not aware of the VMF2 coefficients being available in global grids for use in operational geodetic analyses. In another approach, Gegout et al. [2011] introduced Adaptive Mapping Functions (AMFs) to azimuthal anisotropy of the troposphere, which are based on Marini [1972] mapping functions of continued fraction form with the addition of a set of Fourier terms for azimuthal dependency

of the tropospheric delay. They evaluated the choice of the number of Fourier terms as well as the truncation number of Marini's continued fraction form by fitting adaptive mapping functions using several choices of the above parameters to ray traces of Integrated Forecasting System (IFS) of ECMWF, and studied the residuals of the delays. The best selection among the range of choices for their mapping functions was the AMF with three fractions and four Fourier terms (requiring a total of 27 coefficients), which resulted in accuracies of almost 1 mm for the delays. Gegout et al. [2011] also showed that, while the hydrostatic component is the largest part of the tropospheric delay, the non-hydrostatic part is the main contributor to the azimuthal heterogeneities of the delay, contributing about 90%. This means that the delays estimated due to horizontal gradients of the troposphere could be mainly related to changes in water vapour at tropospheric altitudes. It should be noted, however, that during particular weather conditions, such as deep convection during high precipitating events, there may be large hydrostatic gradients [Champollion et al., 2004]. Landskron et al. [2015] also derived higher order terms of gradient parameters from ray-traced tropospheric delays and used the extended gradients a priori in their VLBI experiment (however still using the standard planar gradient model in the VLBI solution). This yielded slightly improved mean baseline length repeatabilities for their experiment and reduced repeatabilities for 65% of the sites when compared to not using any a priori gradient. The scatter improvements were larger when they did not attempt to estimate gradient residuals in the VLBI solution. Eriksson et al. [2014] used ray-traced delays from Goddard Earth Observing System version 5 (GEOS-5) weather model to directly determine asymmetric mapping functions for each quasar observation in a VLBI analysis, and discovered improvements in position repeatabilities for about two-thirds of the stations in their experiment. In the Global Navigation Satellite System (GNSS) field, Hobiger et al. [2008] used ray-traced delays from a mesoscale model a priori in a GPS analysis, and realized that the use of these a priori slant delays, together with the estimation of linear gradient residuals, resulted in improved height repeatabilities for most of the sites (by 3% on average), but only slightly improved the horizontal scatters.

A common limitation of the above approaches is that they all rely on ray-tracing through a numerical weather model, which may lead to unrealistic delays when the model fails to produce accurate refractivity profiles. Moreover, complications are added in using such techniques in terms of the required amount of computational time and disk storage, which makes them difficult to apply operationally in GNSS analyses. Therefore, an NWM-independent, easy-to-implement technique for modelling the gradients (rather than using a priori information from external sources) might be a more practical alternative for operational GNSS analyses. A directional gradient model is developed in this thesis in which tropospheric horizontal gradients are estimated towards several azimuthal directions around the site, as opposed to the conventional technique where there are only north-south and east-west gradients estimated. This way, we are able to distinguish between different rates of horizontal changes of refractivity at different azimuths around the site.

As described in Chapter 2, the azimuthally asymmetric part of the tropospheric

delay (L_{az}) in GPS analysis is conventionally formulated in the form of linear north-south (L_{NS}) and east-west (L_{EW}) horizontal gradients [Davis et al., 1993]:

$$L_{az}(\varepsilon, \alpha) = L_{NS} m_{az}(\varepsilon) \cos\alpha + L_{EW} m_{az}(\varepsilon) \sin\alpha \tag{4.1}$$

where α is the azimuth angle of the observation, and m_{az} is the mapping function for gradients. The most commonly used mapping function was introduced by Chen and Herring [1997]:

$$m_{az}(\varepsilon) = \frac{1}{\sin(\varepsilon)\tan(\varepsilon) + C} \tag{4.2}$$

The gradient model of Equation 4.1 is based on the idea of estimating a linear gradient, and assumes that the refractivity values change linearly from one azimuthal direction of the site towards the opposite direction. In other words, tropospheric refractivity field is considered as a tilted plane. This is a good approximation in normal atmospheric conditions, but a more complicated model might be a better representative of spatial changes in refractivity in cases where there are isolated gradients at specific azimuth angles around the site. Our proposed directional model estimates gradients at discrete user-defined azimuth angles or nodes, using a piecewise function to relate neighbouring nodes to one another; therefore, the equation for the azimuth-dependent part of the tropospheric delay for our model becomes:

$$L_{az}(\varepsilon, \alpha) = \sum_{j=1}^{N} L_j m_{az}(\varepsilon) m_{PW}^{j}(\alpha) \tag{4.3}$$

where j is the number of nodes at which the gradients are estimated, and $m_{PW}^{j}(\alpha)$ is a piecewise function based on the azimuth angle of each observation. The piecewise function is defined such that each observation contributes to the estimate of the gradient at two neighbouring azimuthal nodes, where the level of contribution depends linearly on the angular distance between observation direction and the direction of

the estimated directional node azimuth:

$$
\begin{aligned}
&\textit{for j=1:}\\
&m^{j}_{PW}(\alpha) = \begin{cases} \frac{\alpha-(2\pi-\alpha^\star)}{\alpha^\star}, & \text{if } \alpha > 2\pi-\alpha^\star \\ \frac{\alpha^\star-\alpha}{\alpha^\star}, & \text{if } \alpha < \alpha^\star \\ 0, & \text{otherwise} \end{cases}\\
&\textit{for } 2 \le j \le N\textit{:}\\
&m^{j}_{PW}(\alpha) = \begin{cases} \frac{\alpha-(j-2).\alpha^\star}{\alpha^\star}, & \\ & \text{if } (j-2).\alpha^\star < \alpha \le (j-1).\alpha^\star \\ \frac{j.\alpha^\star-\alpha}{\alpha^\star}, & \\ & \text{if } (j-1).\alpha^\star < \alpha \le j.\alpha^\star \\ 0, & \text{otherwise} \end{cases}
\end{aligned}
\tag{4.4}
$$

where $\alpha^\star = 2\pi/N$ is the azimuthal grid spacing at which the gradients are estimated. The azimuth-dependent mapping functions for both conventional planar model and directional model are displayed in Figure 4.1.

The same mapping function described in Equation 4.2 is used in our directional model for mapping the elevation-dependent part of the gradients at each directional node to the zenith direction. We implemented the new model of directional gradients by modifying the GAMIT software, and then assessed the capability of the model to recover specific cases of gradients using a set of simulations, which are presented in the following section.

4.2 Simulations

To evaluate the capability of the proposed directional gradient model to recover tropospheric properties under a range of conditions, and to evaluate the directional model's impact on other estimated parameters in GPS least-squares solution, we analysed simulated GPS observations using GAMIT software for several different tropospheric gradient scenarios. The station geometry was defined by the set of eight existing permanent GPS stations shown in Figure 2.3, which span the Australian continent. We used the actual GPS constellation observation geometry for these sites on the 16 July 2010, simulating the GPS phase and pseudo-range observations using the set of models and parameters shown in Table 2.1.

We did not add any random noise to the simulated signals so that we could investigate the expected (i.e. noise-realization-independent) errors in the estimated parameters. In other words, we study how an error in the modelling of the tropospheric horizontal gradient propagates into different estimated parameters.

In our simulations, the troposphere is modelled as fully symmetric (i.e. no tropospheric gradients) for all sites except ALIC, where modelled gradients persist for

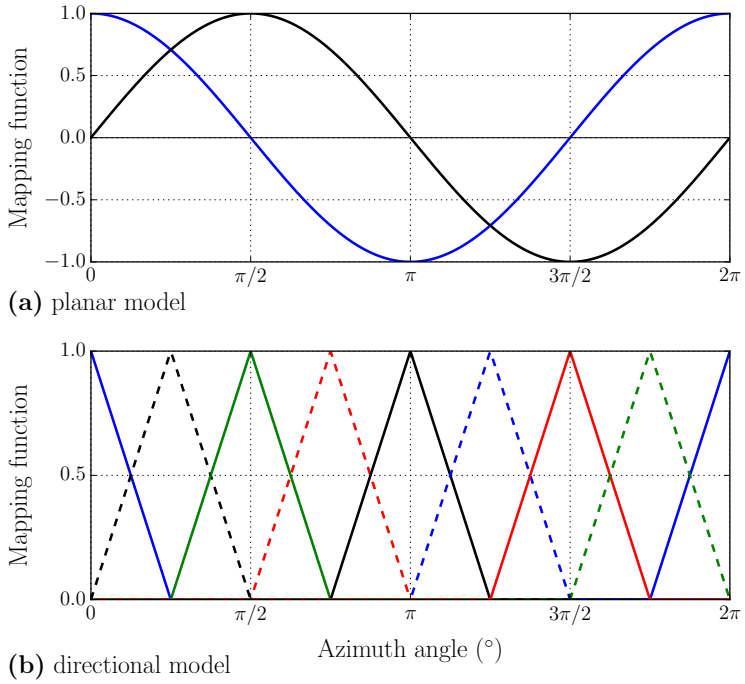

Figure 4.1: The azimuth-dependent mapping functions for (**a**) conventional planar model of gradients (Equation 2.6) and (**b**) directional gradient model with eight gradient parameters. Different colours/line styles show the mapping functions for different gradient parameters.

the entire day. Two different gradient scenarios are presented for ALIC: A) a simple planar and symmetric gradient scheme towards the north-east of the site (using Equation 4.1 for the full sky coverage around the station); i.e. positive gradients towards the north-east, and negative gradients towards the south-west (Figure 4.2a); and B) an asymmetric gradient scheme only towards the north-east, with no gradient when looking to the south-west of the station (Figure 4.2d). For the second scenario, we still use Equation 2.6 but apply it only for the half of the sky coverage in the azimuth range of $-\pi/4$ to $3\pi/4$ (we apply zero gradients for the rest of the sky coverage). We use the letters A and B, and the terms symmetric and asymmetric gradients, from this point on to refer to the two different gradient scenarios described above. We then try to recover the simulated gradients as well as station positions and zenith total delays by solving the least-squares problem using both the conventional planar and directional model of gradients. Except for the gradient model, we use the same models and parameters for both solutions (Table 2.1).

In the following sections, we show the effect of (1) the conventional planar gradient parametrization and (2) the directional gradient parametrization on GPS solutions for both A and B simulated gradient scenarios. We also assess how the inclusion of observations at different elevation angles impacts the misfit of the gradients using

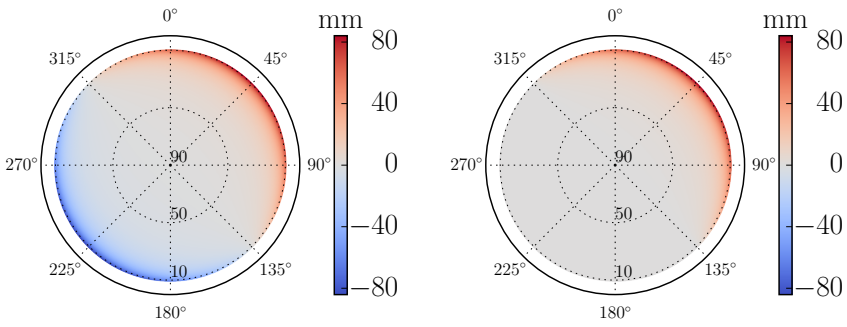

(a) Scenario A; simulated delays

(d) Scenario B; simulated delays

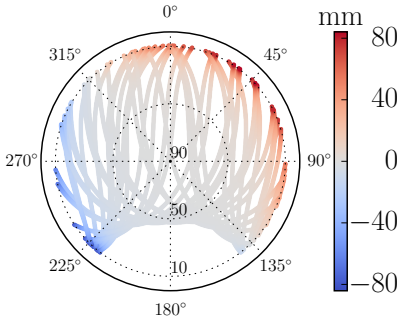

(b) Scenario A; estimated delays

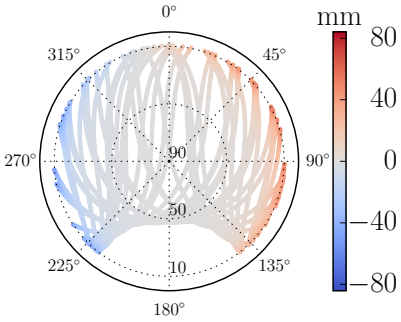

(e) Scenario B; estimated delays

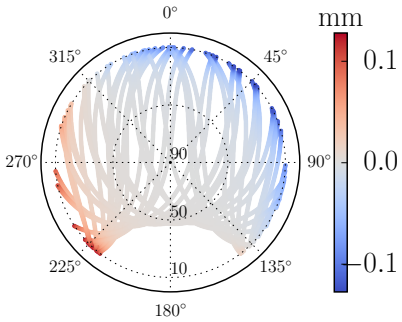

(c) Scenario A; errors in estimated delays

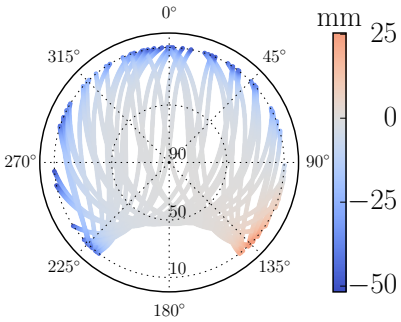

(f) Scenario B; errors in estimated delays

Figure 4.2: The slant delays due to the two different simulated scenarios of tropospheric gradients and the estimated delays using the planar model of gradients at site ALIC. (**a**) Simulated scenario A. (**b**) Estimated delays for scenario A. (**c**) Errors in the estimation of delays for scenario A. (**d**) Simulated scenario B. (**e**) Estimated delays for scenario B. (**f**) Errors in the estimation of delays for scenario B. Note the change in scale for 4.2c and 4.2f. The 1-sigma uncertainty on the maximum error in 4.2f is ∼5 mm.

an elevation cut-off sensitivity test. We then investigate the effect of mismodelling in the tropospheric gradients on different estimated parameters, and how the direc-

tional model could reduce these errors. A discussion of the correlations between estimated parameters in these different solutions then follows. Finally, we discuss the number of directional gradient estimation nodes, and its impact on the solutions.

4.2.1 Recovering simulated gradients using planar model parametrization

In this section, we present the results of the estimation of tropospheric gradients using the planar gradient model parametrization for the two simulated observation scenarios A and B.

4.2.1.1 Scenario A - symmetric gradients

The estimated planar tropospheric gradient delays for scenario A are displayed in Figure 4.2b. An elevation cut-off angle of 10° has been arbitrarily chosen for the solutions in Figure 4.2 as this is a commonly used cut-off for geodetic analyses. In these solutions, the position components are estimated along with tropospheric zenith total delays and gradient parameters. In this normal symmetric gradient scenario (scenario A; Figure 4.2a), the conventional planar model is able to fully recover the simulated gradients with errors of almost zero (Figure 4.2c).

4.2.1.2 Scenario B - asymmetric gradients

While the planar gradient model performed well in the simple symmetric gradient simulation scenario, it only partially recovers the gradients for the more complicated asymmetric gradient scheme of scenario B (Figure 4.2d). The planar model seriously underestimates the positive gradient delay in the north-east direction and estimates an erroneous negative gradient delay in the south-west direction, as well as a positive gradient delay in the south-east direction, where the gradients in fact should be zero (Figure 4.2e). As seen in Figure 4.2f, the errors reach values of larger than 50 mm at 10° elevation angle, which is well above the one-sigma uncertainty level of the relevant gradient estimate ($\sim$5 mm), and easily exceeds a three-sigma rule of thumb for statistical significance.

4.2.2 Recovering simulated gradients using directional model parametrization

4.2.2.1 Scenario A - symmetric gradients

Figure 4.3 shows the delays due to gradients when a directional model parametrization, with gradients estimated every 45° in azimuth, is implemented. For the symmetric simulated scenario A (Figure 4.3a), we are still able to recover the planar gradients well, although with slightly poorer accuracy than with the planar model (see Figure 4.3b and c). We observed errors of up to $\sim$7.5 mm for the gradient-induced delays at 10° elevation. This error occurs most likely because we are using a different

gradient model to estimate the horizontal gradients (the directional model of Equation 4.3) than the model we used to simulate the gradient delays in the observations (the planar model of Equation 4.1).

4.2.2.2 Scenario B - asymmetric gradients

The directional gradient parametrization shows its superiority over the planar model in the asymmetric simulated scenario B (Figure 4.3d). Unlike the planar model (Figure 4.2e and f), the directional approach (Figure 4.3e) retains the original simulated shape of the troposphere (positive gradients towards the north-east, and zero gradients towards the opposite direction). The errors in delays caused by gradients for this solution at 10° reach a maximum of only about 6 mm (Figure 4.3f) with a one-sigma uncertainty of ∼12 mm. This is significantly smaller than the ∼50±5 mm errors for this scenario using the planar model. The uncertainties, however, grow when using the directional model, which is a result of having more parameters in the least-squares inversion. It should be noted that the directional model with 45° azimuthal nodes for the estimation of gradients requires 8 gradient parameters per site per epoch, while the planar model only needs 2 parameters per site per epoch.

4.2.3 Elevation cut-off sensitivity of the gradient misfits

The results shown in Figures 4.2 and 4.3 are generated using a 10° elevation cut-off angle. However, the tropospheric horizontal gradients are largest at the lowest elevation angles. Although most geodetic analyses are currently performed using 10° elevation cut-off angles, studies aimed at tropospheric estimations suggest that using lower elevation observations increases the sensitivity of the solutions to the tropospheric zenith delays/precipitable water (e.g. Tregoning et al. [1998]). Therefore, it is recommended for GPS meteorology applications to include low-elevation observations in the analyses, as long as mapping function errors and local site-specific errors allow for accurate estimation of tropospheric parameters.

We performed the analysis for different choices of elevation cut-off angle (from 20° to 3°), and calculated the misfit in the tropospheric horizontal gradients. Figure 4.4 shows the gradient misfit as a function of the elevation cut-off angle set in the GPS processing for both the symmetric and asymmetric gradient simulation scenarios A and B using both planar and directional models. For each analysis, we calculated the misfit (δ) in the tropospheric horizontal gradients according to:

$$\delta = \sqrt{\frac{1}{N}\sum_{i=1}^{N}[(\frac{\hat{l}_i - l_i^t}{\sigma_i})^2]} \tag{4.5}$$

where $\hat{l}_i$ is the estimated gradient delay for the ith observation in the day, l_i^t is the corresponding true simulated gradient delay, σ_i is the 1-sigma uncertainty of the estimated gradient delay, and N is the number of observations for the whole day. Ideally, the misfit values should be zero, since there is no random noise added to

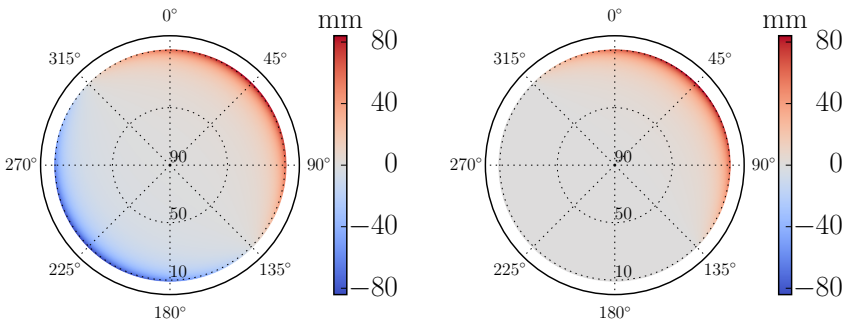

(a) Scenario A; simulated delays

(d) Scenario B; simulated delays

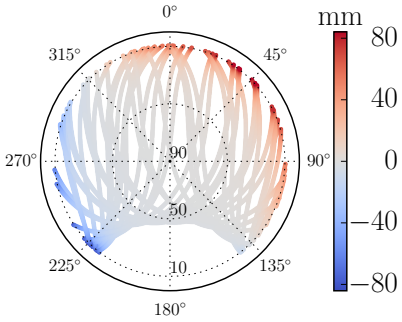

(b) Scenario A; estimated delays

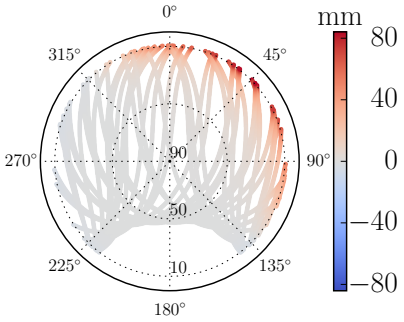

(e) Scenario B; estimated delays

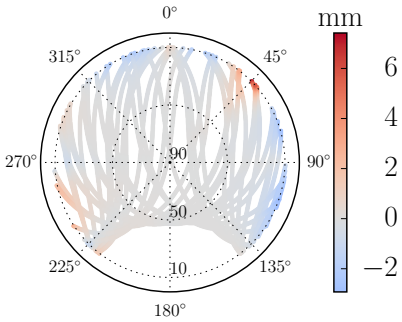

(c) Scenario A; errors in estimated delays

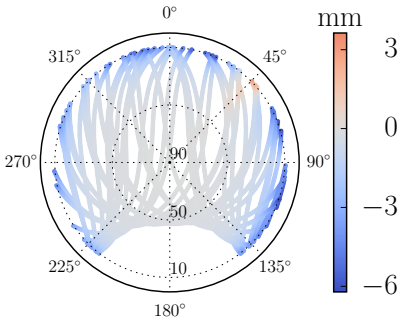

(f) Scenario B; errors in estimated delays

Figure 4.3: The slant delays due to the two different simulated scenarios of tropospheric gradients and the estimated delays using the directional model of gradients at site ALIC. (**a**) Simulated scenario A. (**b**) Estimated delays for scenario A. (**c**) Errors in the estimation of delays for scenario A. (**d**) Simulated scenario B. (**e**) Estimated delays for scenario B. (**f**) Errors in the estimation of delays for scenario B. Note the change in scale for 4.3c and 4.3f. The 1-sigma uncertainty on the maximum error in 4.3f is ∼12 mm.

the simulations, and the estimated gradient delays should be identical to the true gradient delays.

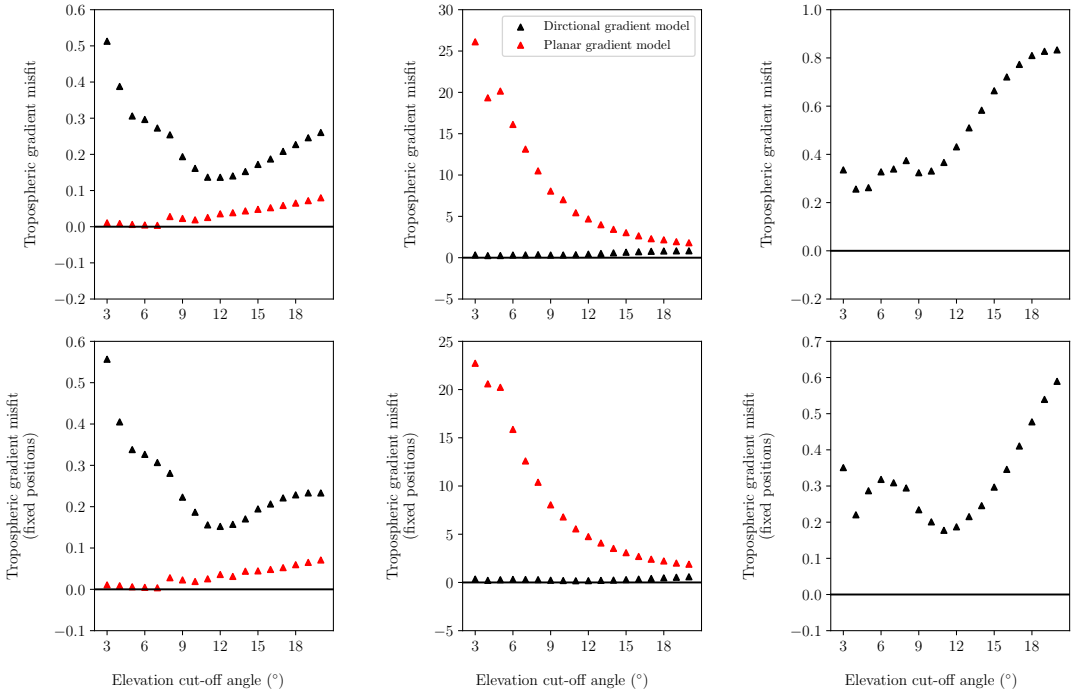

(a) Scenario A: symmetric gradients

(b) Scenario B: asymmetric gradients towards north-east only

(c) Scenario B: asymmetric gradients towards north-east only

Figure 4.4: Tropospheric gradient misfit as a function of elevation cut-off angle for (**a**) symmetric gradient simulation scenario A, and (**b** and **c**) asymmetric gradient simulation scenario B. Red triangles show the misfits when using the planar gradient model, and black triangles depict the misfits when using the directional model of gradients. Figure 4.4c is the same as Figure 4.4b but only displaying the misfits when using the directional model of gradients, to avoid the scale difference between the two models. The top plots are the misfits when the position components are estimated along with other parameters, and the bottom plots are the results from fixing the positions to their true values and only estimating tropospheric zenith delays and gradients.

Figure 4.4 shows the gradient misfit for different choices of the elevation cut-off angle. Looking at Figure 4.4a for the symmetric simulated scenario A, the misfits in the tropospheric gradients using the planar model are almost zero at elevation cut-off angles below 8°, and reaches about 0.1 at 20° cut-off. The directional model results in larger misfits at all elevation angles, but the misfits are still under 0.6. This higher misfit was also evident in Figure 4.3, and is a result of the differences between the models used for simulation and estimation of the tropospheric gradients.

For the asymmetric gradient scenario B (Figure 4.4b), the planar gradient model clearly results in large misfits up to about 25, whether we put loose constraints on the positions or fixing them to their true values. The misfit is largest when low-elevation observations are included. This is an important outcome of this study: while it

could be useful for tropospheric studies to include low-elevation observations, one has to consider the fact that in asymmetric gradient situations the planar model of the gradient is unable to properly model the horizontal changes of the tropospheric refractivity, and the addition of low-elevation observations actually degrades the solution.

The directional model, on the other hand, yields very small misfits of below $\sim$0.8 at all elevation cut-off angles, which is the result of a better parametrization of the gradients for this asymmetric condition, and shows that the directional gradient model is an improvement on the conventional planar model in the asymmetric gradient conditions.

Figure 4.4c displays only the gradient misfits from using the directional model to more clearly show the changes of the misfits with elevation cut-off. There is a general increase in gradient misfits when lower-elevation observations are excluded from the analyses, which indicates that the low-elevation observations can help the directional model to better resolve the gradients. Also, fixing the positions helps to reduce the level of gradient misfits (e.g. from $\sim$0.3 to $\sim$0.2 at 10° cut-off). There is, however, a small fluctuation in the gradient misfit at elevation angles below 10°, but to make a conclusion on whether this small increase in the gradient misfit is more harming than benefiting the solutions, it is important to also examine how the other derived parameters are impacted at these very low elevation cut-off angles. The impact on other parameters in discussed in the next section.

4.2.4 Impact on derived parameters

For the analyses performed in section 4.2.3, we also calculated the errors (estimated minus true values) in position and ZTD parameters. These biases are displayed in Figure 4.5 for different estimated parameters. It is evident from Figure 4.5a that under a normal symmetric gradient scenario with no data noise, both planar and directional gradient models estimate error-free parameters. The directional model, however, yields larger uncertainties (particularly as the elevation cut-off increases). These larger uncertainties could be reasonably attributed to the higher number of parameters, and are reduced for the ZTD estimates by removing the position components from the set of parameters to be estimated. Nevertheless, the small misfits in the tropospheric gradients when implementing the directional gradient model under symmetric scenario (seen in Figure 4.3c) do not yield any significant bias in the estimates of position and ZTD parameters.

Under the asymmetric gradient scenario (Figure 4.5b), the directional model clearly outperforms the planar model in the estimation of all parameters at elevation cut-off angles below 10°. The mismodelling of the tropospheric gradients by the planar model in this scenario results in errors in position and ZTD parameters, particularly when including low-elevation measurements. Latitude estimates by the planar model contain errors of up to about 1.5 mm at 3° cut-off, and longitudes are erroneous by about 1 mm at the same cut-off. The impact on the height and ZTD estimates are much larger: the errors reach about 10 mm for height and 6 mm for ZTD at 10°

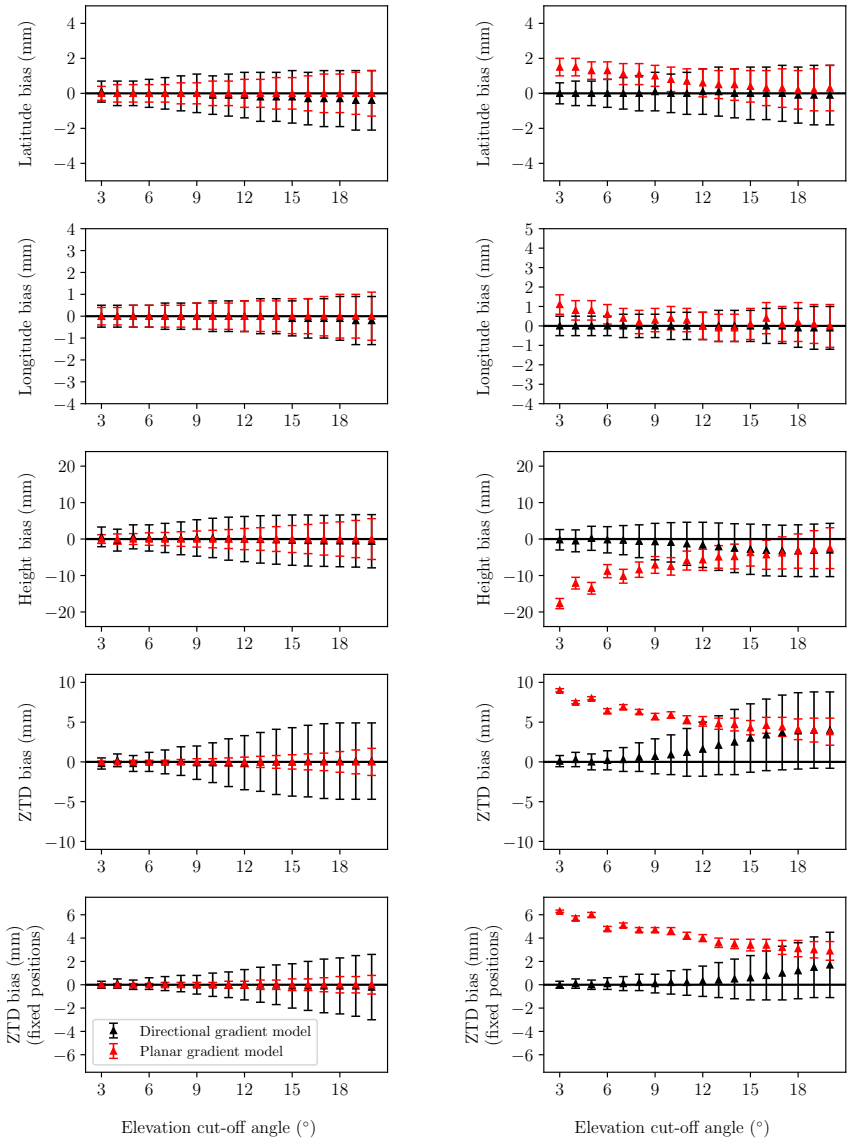

(a) Scenario A: symmetric gradients

(b) Scenario B: asymmetric gradients towards north-east only

Figure 4.5: Biases in the estimation of different parameters at site ALIC using conventional planar gradient model (red) and new directional gradient model (black) for (**a**) the simulated scenario A, and (**b**) the simulated scenario B. The errors shown for ZTD are the biases for daily mean values of zenith total delay. The error bars are the 1-sigma uncertainty of the estimates.

cut-off, and close to 20 mm for height and 10 mm for ZTD when including very low-elevation observations (down to 3°) in the solution. The significant growth of errors in parameters caused by the planar gradient model when decreasing the elevation cut-off angle stems from the fact that the contribution of horizontal gradients are

largest at low elevations; therefore, a more accurate representation of the gradients becomes more important when including low-elevation observations in the analysis of GPS data.

The more accurate representation of the tropospheric gradients of the asymmetric scenario B by the directional model resulted in improvements from the planar model for the estimation of all parameters (Figure 4.5b; black triangles). Unlike the planar model, the directional model enables the use of data down to very low elevation angles (3°) without introducing any error into any of the estimated parameters, which is a direct result of a much more accurate representation of the tropospheric gradients by the directional model as seen by better misfit of the gradients as observed in Figures 4.3 and 4.4. The uncertainties on the estimated parameters are larger than those generated by the planar model, as is expected by the higher number of parameters in the directional parametrization.

When setting higher elevation cut-off angles and using the directional gradient model, biases are introduced into height and ZTD parameters in the asymmetric gradient scenario. A higher misfit was also previously observed in the gradients (Figure 4.4c) for the same scenario when using higher cut-off angles. Both the gradient misfits and the errors in ZTD estimates, as well as their uncertainties, are reduced when fixing the positions to their true values. The fact that the use of low-elevation observations and/or fixing the position parameters to their true values yields more accurate estimates of the derived parameters indicates that these errors could be caused by possible high correlations between the parameters when using the directional model of gradients in the least-squares inversion. In the absence of noise, however, the estimates should contain zero errors, despite any correlations between the parameters. The existence of errors can therefore also be attributed to the different model we use to estimate the tropospheric horizontal gradients (Equation 4.3) compared to the model we used to simulate the gradients (Equation 4.1 with a constraint to generate only a half-sky gradient to the north-east). Possible correlations between the parameters when using the directional gradient model and the slightly different models for simulation and regression are probably the main drivers for the estimation errors; it is therefore worthwhile at this stage to inspect the correlation coefficients between the estimated parameters.

4.2.5 Correlations

Correlation coefficients between the estimated parameters are displayed for site ALIC in Figure 4.6 for the planar model and in Figure 4.7 for the directional model. Correlations are displayed for the 10° and 3° cut-off solutions to study the impact of low-elevation observations. We show correlations of the 10° cut-off solutions in the lower triangular matrices, and the correlations of the 3° cut-off solutions in the upper triangular matrices, and we put the two triangular matrices in the same figures to make the comparisons between high and low cut-off angles easier. The correlations are shown in absolute percentage terms. These absolute correlation percentages are also displayed as numbers on each matrix element, and the negative correlations are

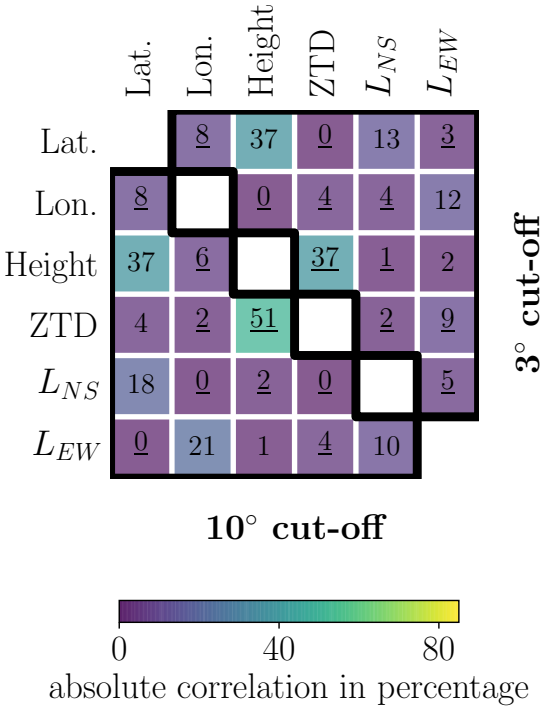

Figure 4.6: Correlations between different estimated parameters at site ALIC for simulation scenario B when using the conventional planar model of gradients at 10° cut-off (lower triangle) and 3° cut-off (upper triangle). The correlation coefficients are also displayed in percentage terms on each matrix element; the underscored numbers show negative correlations.

depicted as underscored numbers.

The well-known existence of high correlations between heights and zenith delays (e.g. Rothacher and Beutler [1998]) is evident from Figure 4.6 (lower triangle); this correlation is slightly reduced when including low-elevation observations in the solution (from -0.51 to -0.37). There are also correlations between height and latitude parameters (0.37). North-south and east-west gradient parameters are not correlated with height/ZTD nor with each other. Looking at Figure 4.7, on the other hand, suggests that the directional gradient parameters are highly correlated with heights, zenith delays and also with each other. The correlations between gradients and zenith delays are most significant. Including low-elevation observations (upper triangle of Figure 4.7) reduces the correlations between the gradient and height/ZTD parameters. These reduced correlations are probably one reason for the improved estimation errors of ZTD and height parameters when including low-elevation observations as observed in Figure 4.5. The between-gradient correlations, however, do not change significantly by including observations lower than 10°, which is consistent with the gradient misfits not changing significantly at elevation cut-off angles below 10° (Figure 4.4c). Low correlations between the southward gradients (L_5) and other parameters, seen in Figure 4.7, are simply because there are no low-elevation observations

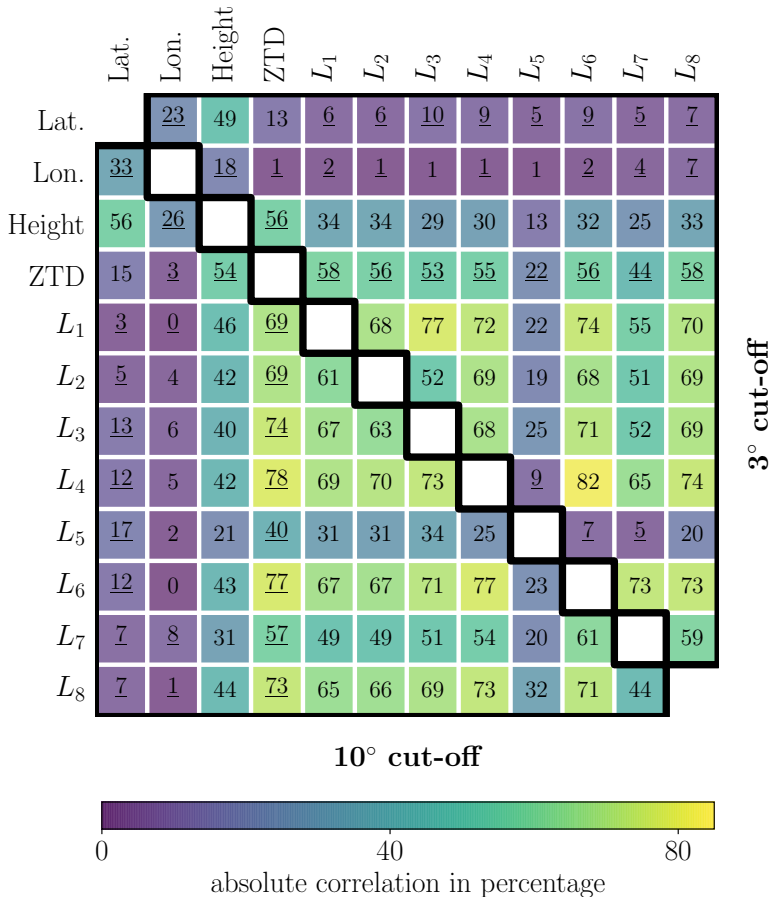

Figure 4.7: Correlations between different estimated parameters at site ALIC for simulation scenario B when using the directional model of gradients at 10° cut-off (lower triangle) and 3° cut-off (upper triangle). The correlation coefficients are also displayed in percentage terms on each matrix element; the underscored numbers show negative correlations.

in this direction.

Another way to mitigate the impact of the correlations is to fix the positions to their known values. The correlations from the fixed-position solutions are shown in Figure 4.8 in the same way as in Figures 4.6 and 4.7. High reductions in the correlations when fixing the positions are evident: ZTD/gradient correlations are reduced from the order of ∼0.7 to the order of ∼0.4 at 10° cut-off. These correlations are further reduced to the order of ∼0.25 when also including low-elevation measurements (and fixing the positions). Correlation levels between the gradient parameters themselves are also reduced when fixing the positions, either using a 10° or a 3° cut-off. The reduction in ZTD/gradient correlations appear as almost zero estimation errors of ZTD when tightly constraining positions to their known values (Figure 4.5b, and the relevant discussion in section 4.2.4).

Figure 4.9 shows the sensitivity of the correlation parameters to the choice of

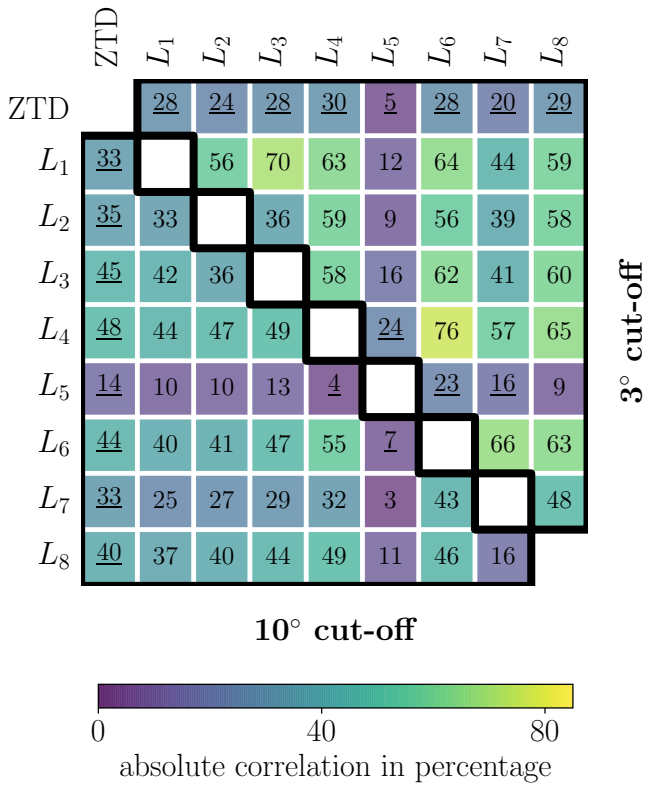

Figure 4.8: Correlations between different estimated parameters at site ALIC for simulation scenario B when using the directional model of gradients and fixing position components to their true values at 10° cut-off (lower triangle) and 3° cut-off (upper triangle). The correlation coefficients are also displayed in percentage terms on each matrix element; the underscored numbers show negative correlations.

elevation cut-off angle. The increased correlations between height and ZTD, and between gradients and height/ZTD/gradients, as a result of using the directional gradient model is evident. While including the low-elevation observations significantly reduces the height/ZTD correlations when using the planar gradient model (red triangles in Figure 4.9a top-left), the height/ZTD correlation does not significantly change by varying the cut-off angle when using the directional model (black triangles in Figure 4.9a top-left). However, the correlations between the gradients and height/ZTD parameters and the between-gradient correlations drop when using lower cut-off angles until around 5° with a slight increase from 5° to 3° cut-off. The increase in the between-gradient correlations when setting the cut-off angle below 5° is larger compared to the ZTD/gradient and height/gradient correlations, which is the reason for the 3° cut-off solution not observing significant reductions in correlations compared to the 10° cut-off solution as was seen in Figure 4.7. When fixing the position components, the level of correlations between directional gradients and ZTD/other directional gradient parameters is significantly reduced (black triangles in Figure 4.9b), which was also observed in Figures 4.7 and 4.8.

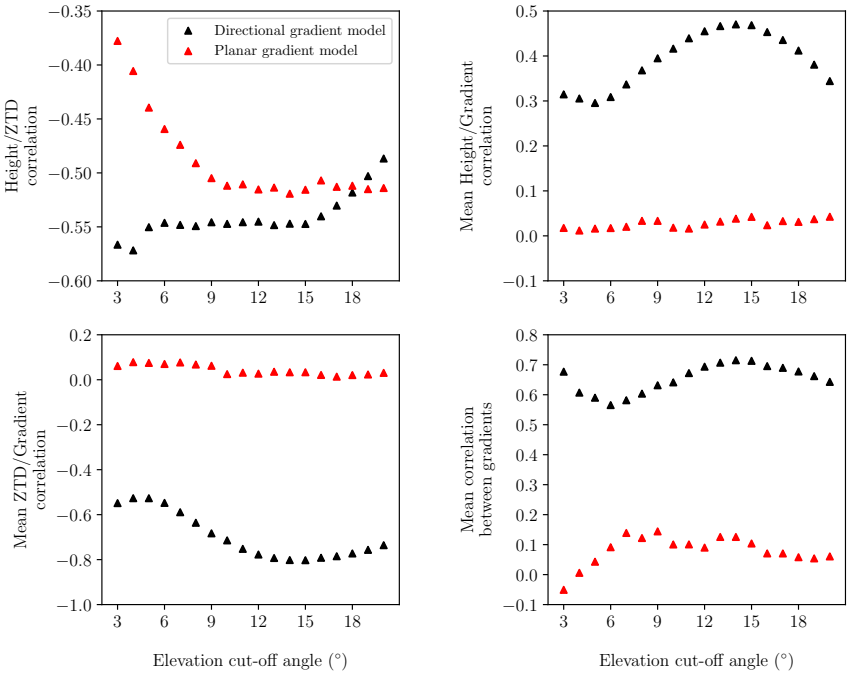

(a) Loose position constraints

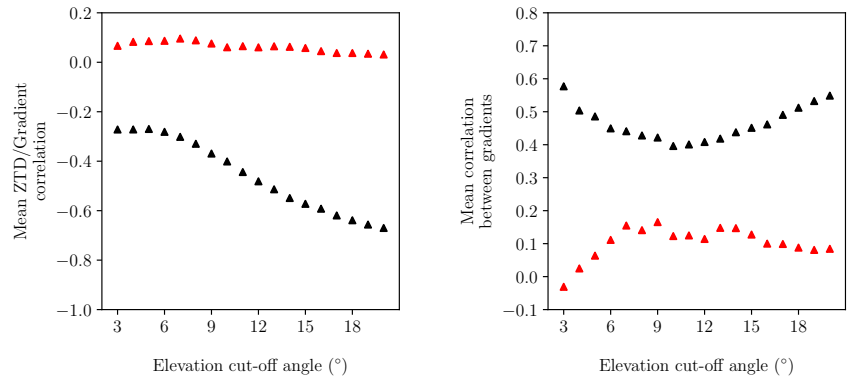

(b) Fixed positions

Figure 4.9: Correlation coefficients between different parameters as a function of the selected elevation cut-off, when using conventional planar (red triangles) and directional (black triangles) gradient model, for solution with **(a)** position components estimated along with tropospheric parameters, and **(b)** position components fixed to their true values. The statistics related to the directional gradient towards south are removed from the calculations as there are much less data contributing to this directional gradient, compared to all the other directions.

The investigation of the correlation coefficients between different estimated parameters showed that the high correlations between the new tropospheric directional

gradient parameters and height/ZTD parameters could be mitigated by including low-elevation observations and/or putting tight constraints on position parameters. This will lead to reduced errors in the estimation of height and ZTD parameters by either including low-elevation measurements or fixing the position parameters as seen in Figure 4.5b. The correlations between different directional gradient parameters is also reduced when fixing the position components, but does not significantly change by setting an elevation cut-off angle of 3° compared to a 10° cut-off. This leads to the gradient misfits being reduced when putting tight constraints on the position parameters, but not by including lower elevation observations than 10° (Figure 4.4c). The gradient misfits for the asymmetric gradient scenario are significantly smaller using the directional model than given by the planar model (Figure 4.4b).

4.2.6 Number of the directional gradient parameters

By default in this thesis, we estimate 8 directional gradient parameters for each station and each epoch, meaning that we set the size of pie-wedge sections of the model as 45°. However, one may choose to estimate a different number of directional gradients. A lower number of directional parameters may result in the gradients not being fully captured by the model, while choosing a very high number of directions may result in unnecessary high number of parameters, lower degree of freedom and higher computational time. We performed a series of tests to investigate the resolving power of the directional gradient model, estimating between 3 and 24 directional gradient parameters to recover the simulated asymmetric gradient from simulation scenario B, using a 3° elevation cut-off. For each tested number of directions, we derived the normalized root-mean-square error of the solution as well as the misfit in the tropospheric gradient estimates using Equation 4.5, which are displayed in Figure 4.10. It is evident from the NRMS and misfit results that estimating three or four directional gradient parameters does not accurately capture the gradient scheme of scenario B, leading to gradient misfits of larger than 5 and solution NRMS values of more than 0.10. Estimating five or six gradient parameters significantly reduces both gradient misfit and NRMS, but still results in gradient misfits of larger than 1 and NRMS of higher than 0.05. Once we estimate 8 gradient parameters, the misfit in the gradient and the solution NRMS reach values close to zero ($\sim$0.3 for gradient misfit and $\sim$0.01 for solution NRMS). By choosing more directional gradients than 8, the misfit does not change significantly. The higher misfit of the 4-direction model compared to the 3-direction model, as well as the higher misfits of 9-, 10- and 12-direction models compared to the 8-direction model, are probably related to the azimuthal location of the gradient estimation nodes with respect to the simulated (true) gradient shape. Nonetheless, it is clear from Figure 4.10 that, in order to resolve the gradient shape of the simulated scenario B with sufficient accuracy, estimating at least 5 gradient parameters is necessary, and estimating 8 gradient parameters is sufficient.

To more clearly show the effect of estimating different number of directional parameters, the gradient delay estimates, as well as the errors in the estimates of gradient delays, are displayed in Figures 4.11 and 4.12 for the asymmetric gradient

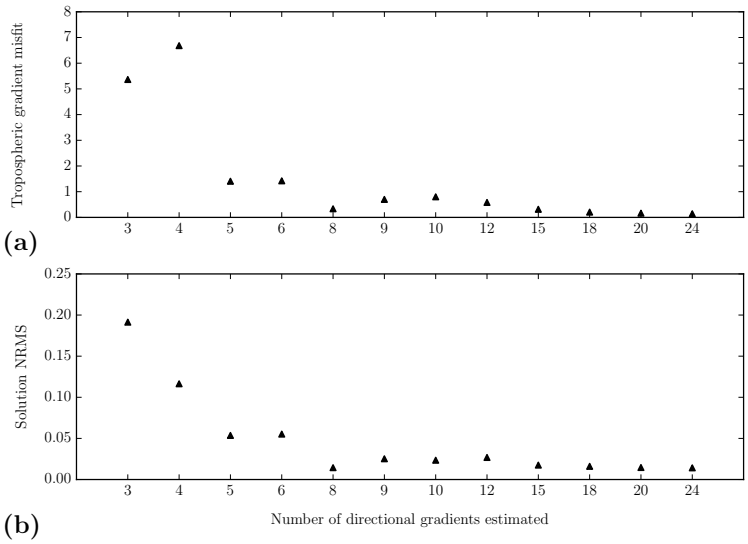

Figure 4.10: **(a)** The tropospheric horizontal gradient misfit, and **(b)** NRMS of the solution, as a function of the number of directional gradients estimated in the GPS analysis of the simulated asymmetric gradient scenario B.

scenario as sky plots for the solutions with 3, 4, 5, 6, and 8 directions. It is evident from Figure 4.11 that estimating at least 5 directional gradient parameters is required to avoid the erroneous negative gradients in the south-west of the station and the underestimation of positive gradients in the north-east. Figure 4.12 further shows that even estimating 5 gradient parameters results in errors in north-west, south-east and north-east of the station, and that a 8-direction model of tropospheric gradients yields almost zero errors in the estimation of gradient-induced delays at all azimuth and elevation angles.

The choice of the number of directional gradients also depends on the shape of the real gradient scheme (which is unknown in practice) and the number of observations available. We performed tests using post-fit residuals as an indicator to decide which gradient model (planar or directional/how many directional gradients) should be used for each station and day. However, due to the existing correlations between gradients and other parameters, some parts of the gradient signals are usually absorbed into other parameters, making it difficult to rely on post-fit residuals only to extract information about the gradient shape. Thus, a practical methodology for decision on an optimal model which can be relied on at all times remains a limitation of the current work. Nevertheless, using 8 directions seems to be an appropriate trade-off among the solutions with different number of directional gradient parameters.

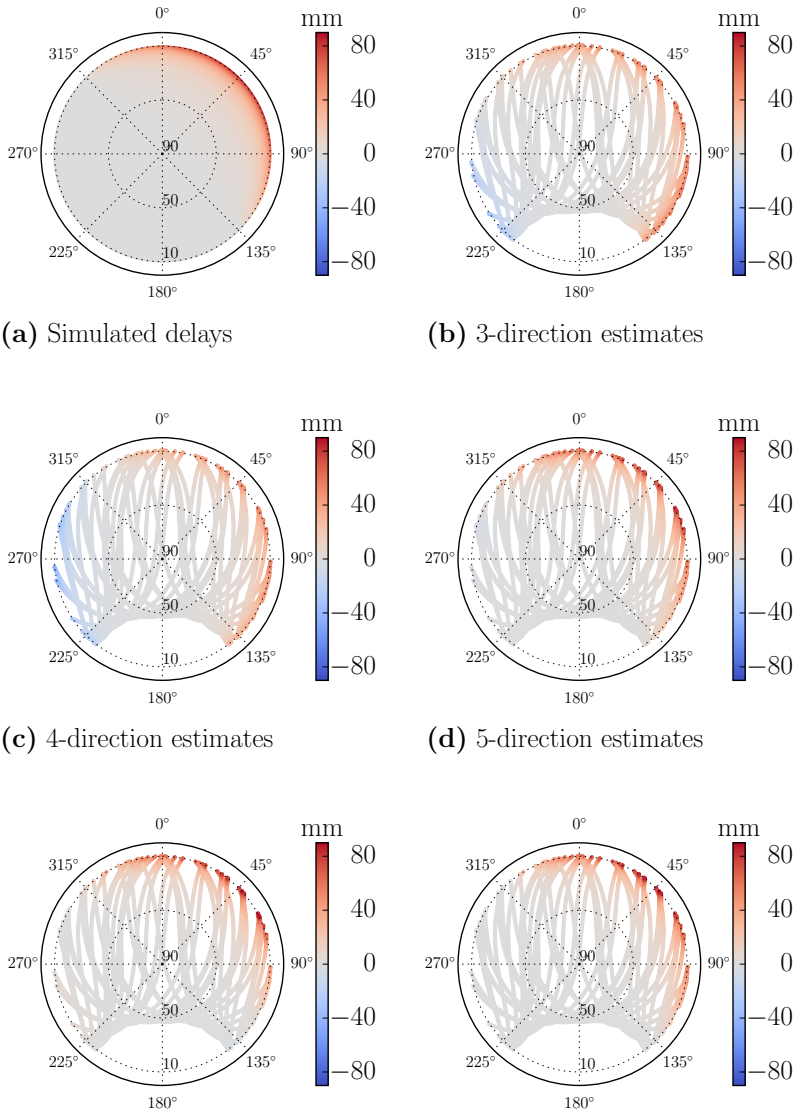

(a) Simulated delays

(b) 3-direction estimates

(c) 4-direction estimates

(d) 5-direction estimates

(e) 6-direction estimates

(f) 8-direction estimates

Figure 4.11: The gradient delay estimates by the directional gradient parametrization when varying the number of estimation nodes, as compared to the (true) simulated delays for the simulation scenario B: **(a)** simulated delays; **(b-f)** estimated gradient delays by the directional model with different numbers of estimation nodes.

4.2.7 Summary of the simulation study

The simulation study carried out in this section shows that the proposed directional model of gradients is able to improve parameter estimates for specific cases when the tropospheric delay horizontal changes do not follow a simple planar model. The largest impacts of mismodelling the gradients in these scenarios are seen on station height and ZTD parameter estimates. In general, while the directional gradient

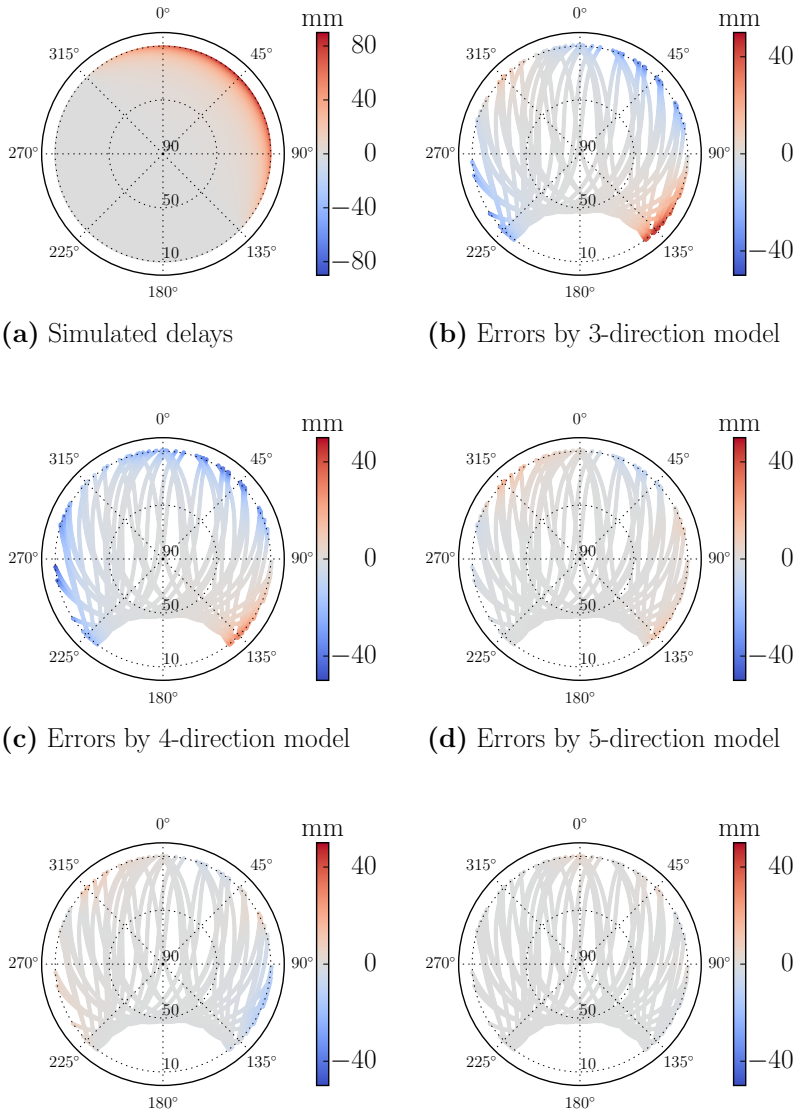

(a) Simulated delays

(b) Errors by 3-direction model

(c) Errors by 4-direction model

(d) Errors by 5-direction model

(e) Errors by 6-direction model

(f) Errors by 8-direction model

Figure 4.12: Errors in the gradient delay estimates by the directional gradient parametrization when varying the number of estimation nodes for the simulation scenario B: **(a)** simulated gradient delays; **(b-f)** errors in the estimated gradient delays by the directional model with different number of estimation nodes.

model results in slightly poorer misfits in the tropospheric gradients under normal symmetric gradient scenarios and higher uncertainties on all the estimated parameters (due to larger number of correlated parameters), it outperforms the conventional planar parametrization in abnormal asymmetric gradient situations. In such asymmetric conditions, the directional model allows the use of low-elevation observations, and results in improved estimates of height and ZTD compared to the planar model.

Both the uncertainties and errors in parameters estimated by the directional model can be reduced by including low-elevation observations and/or fixing or constraining station positions, thus reducing the correlations between gradient and height/ZTD parameters. Estimating 8 directional gradient parameters appears to provide the optimum trade-off between the increased resolving capability of the solution and the degree of correlations between parameters.

In the next two sections, we show the impact of using the directional model in two real case studies: the V-shape intense precipitation event that occurred in southern France causing flash flooding from heavy rainfall of September 2002, and the skewed position time series of Plate Boundary Observatory (PBO) sites in Mammoth Lakes area in California.

4.3 Case study of the 8-9 September 2002 torrential rain event in southern France

We have already shown in the simulations of section 4.2 that the directional model of gradients is able to improve our understanding of the tropospheric gradients (and consequently water vapour) in abnormal weather situations. It is also important to show the capability of the model by evaluating it on real case studies where there are isolated gradients at some directions around a GPS site. A very good example of such cases is the 8-9 September 2002 torrential rain event in southern France. The event was an extreme example of an intense, but common Cévenol episode that often impacts the Cévennes area between Massif Central mountains and the Mediterranean sea in autumn. A Cévenol episode is characterized by an intense upper-level cold trough between Ireland and the Iberian Peninsula that produces a low-level south wind flow in the southern France. The warm moist air from the Mediterranean sea is brought to the coast by this flow, and the topographic effect of the Alps, Pyrenees and Massif Central Mountains help to further destabilize the atmosphere above the region [Delrieu et al., 2005]. The particular extreme precipitation event of 8-9 September 2002 was reported to involve one of the highest precipitation amounts and river discharges ever recorded for a large area: the accumulated amount of rainfall during this event was more than 300 mm for a region of about 5000 km^2 over 48 hours [Champollion et al., 2004].

Thorough analyses of the 8-9 September flash-flood event are performed by e.g. Delrieu et al. [2005], Champollion et al. [2004] and Brenot et al. [2006]. Figure 4.13 shows the reanalysed rainfall maps for this event provided by the Cévennes-Vivarais Mediterranean Hydrometeorological Observatory (CVMHO). The reanalysis maps are derived by merging information from Météo France ARAMIS network of radars and hourly and daily rain gauge measurements operated by Météo France, the Service de Prévision des Crues du Grand Delta and Electricité de France using a kriging approach with external drift described by Delrieu et al. [2014]. A detailed description of the database the rainfall reanalysis data are retrieved from is given by Boudevillain et al. [2011].

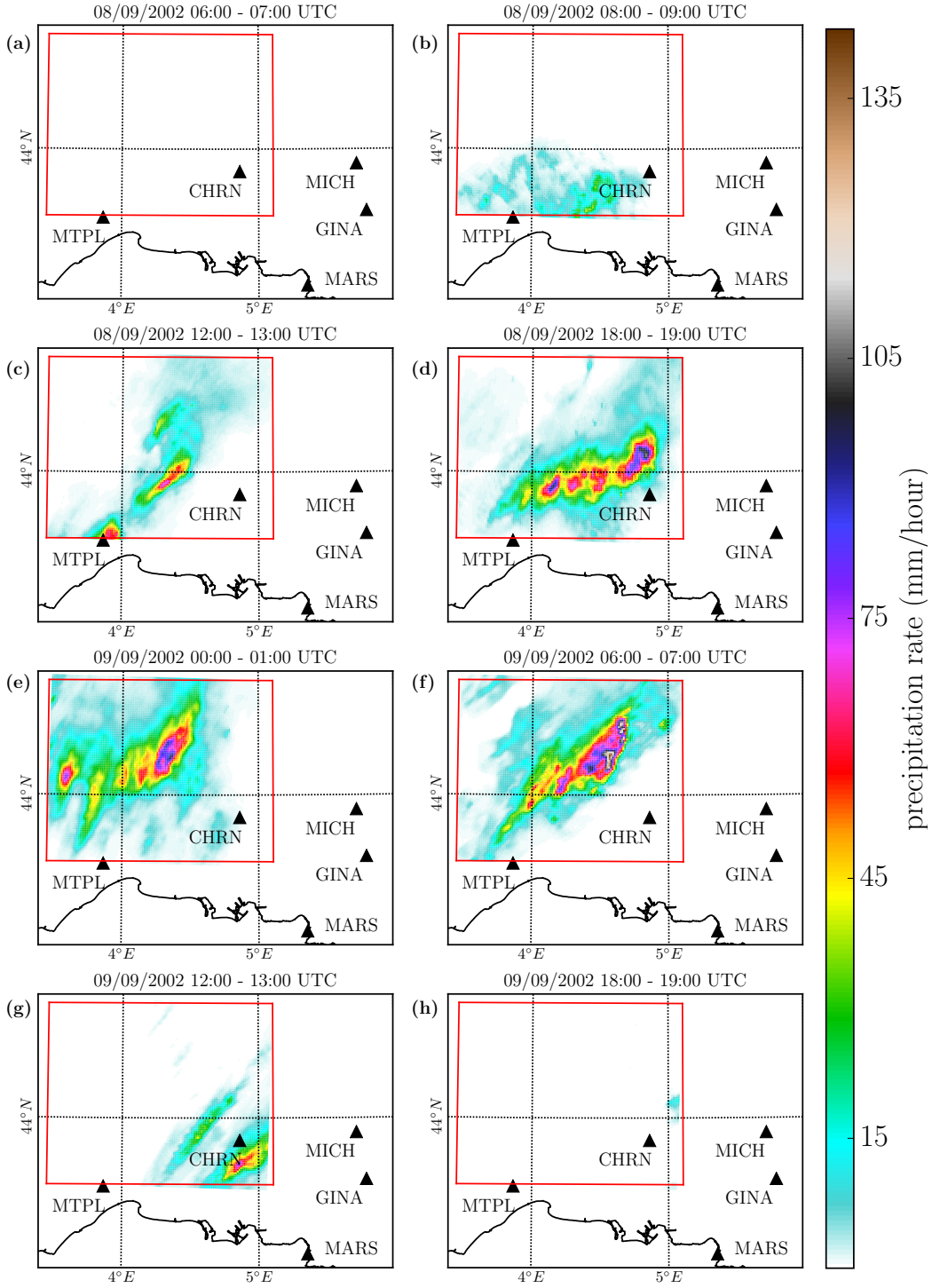

Figure 4.13: Hourly precipitation during the September 2002 event in the Gard region in southern France; the red box is the region where there is krigged data available from CVMHO SEVnOL. Data courtesy of (http://www.ohmcv.fr).

As for a typical case of Cévenol event, the elongated upper-level deep cold trough that formed between Ireland and Iberia on 8 September 2002 resulted in a southerly surface flow around the low-pressure system above the Mediterranean sea and south-eastern France at around 04:00 UTC, bringing the warm moist air from the sea to the Gard region starting from 08:00 UTC (Figure 4.13b). The tropopause-level south-westerly diffluent flow led to the convection being formed as a V shape (Figure 4.13d), with the maximum precipitation and cloud heights at the edge, and the clouds forming the branches of the V shape along Massif Central mountains. The region of precipitation persisted until the afternoon of 9 September, when the surface winds started weakening (as a result of the trough changing its direction from north-south to northwest-southeast), and the convective system shifted further east (Figure 4.13g), marking the end of heavy precipitation event [Delrieu et al., 2005; Champollion et al., 2004].

The GPS station at Montpelier (MTPL) is located very close to the edge of the V shape precipitation pattern, making the site an appropriate test case for the gradient model. We processed GPS data for a network of about 30 sites well distributed across the European continent, including the sites shown in Figure 4.13. Two separate solutions were carried out; one with the conventional planar model of gradients, and the other with estimating eight directional gradients around each site. We compared slant delays from both gradient models (Figure 4.14) at the epochs for which there are precipitation values (c.f. Figure 4.13). The empirical site-specific model introduced by Moore et al. [2014] and discussed in Chapter 3 was applied in both solutions in order to ensure that any site-specific errors, including multipath, were removed from the solutions. We first performed a solution for one month of data around the day of interest using the planar model of gradients and other parameters as stated in Table 2.1, then derived the ESM from the post-fit one-way residuals, and finally carried out both planar and directional model solutions while applying the derived ESM to both of them. In addition, for both cases we used the estimated monthly averaged positions a priori, and only estimated zenith delay and gradient parameters.

The gradient-induced delays recovered from a planar model (Figure 4.14a) provide some information about the spatial variability of the tropospheric delays: there is a strong gradient vector from the south of the MTPL site towards the north at the time of maximum precipitation (around 18:00 UTC). However, there is more information about this event that the planar gradient model has not been able to capture: the estimated delays derived by the directional model (Figure 4.14b) show a very clear isolated V shape, consistent with the V shape precipitation pattern seen in Figure 4.13, towards the north-east of the site, clearing out the positive gradients of the planar model towards the north-west. The V shape delay starts forming from the morning of the 8 September (even before the V shape precipitation forms), becomes stronger during the day, and reaches its maximum of about 75 mm (at 10° elevation angle) at around 18:00 UTC (which is about the same time when the precipitation also reaches its maximum). The isolated north-east gradient weakens throughout the rest of the day and the next day until it becomes similar to a planar eastward-only

Figure 4.14: Horizontal gradient delays estimated at site MTPL using (**a**) the conventional planar model, and (**b**) the directional model with 8 gradient estimation nodes. The horizontal gradients are isolated towards the north-east by the directional model.

gradient by the end of 9 September. Noticing the values of the delays at the maximum water vapour accumulation time (18:00 UTC) from the two models shows that the planar model underestimates the positive gradients towards the north-east (with

a delay estimate of about 50 mm at 10° elevation), and overestimates the values of negative gradients towards the south of the site (with a delay estimate of about -60 mm at 10° elevation), compared to the directional model with approximately 75 mm of positive delays towards the north-east and only -35 mm towards the south at 10° elevation angle.

The estimated delays using the two models for the site CHRN, which lies in a different location with regards to the precipitation system, are shown in Figure 4.15 for the maximum precipitation time. The precipitation system is positioned mostly towards the north-west of the site CHRN during the event (Figure 4.13c-f). Again, comparing the recovered gradients using the two models, it can be seen that the directional model has been able to isolate the gradients towards the north-west of the site, repairing the incorrect north-east gradients that are estimated by the planar model. While the differences in magnitudes of the gradients are small between the two models, the directional model reproduces a more accurate image of the tropospheric gradients (horizontal gradients towards the north-west, but no refractivity changes when moving towards the north-east of the station). This is consistent with the precipitation pattern observed in Figure 4.13d, in which there are high amounts of rainfall in the immediate north-west of CHRN, while the station falls in the south-eastern border of the precipitation pattern with constant amounts of rainfall when moving to the north-east of the site. Also, while the planar model estimates large negative gradients towards the south-east (due to its linear assumption for the gradients), the directional model is more accurately displaying that the refractivity changes are small when moving towards the south-east of the station, which is also consistent with Figure 4.13d where there is no precipitation occurring in the south-eastern side of CHRN at this epoch.

We have observed for the September 2002 heavy precipitation event that the use of our more sophisticated model of gradients helps to better understand the spatial variabilities of the tropospheric refractivity/water vapor for cases where there are complex patterns of moisture fields. However, the minimum elevation angle for the recorded observations at sites MTPL and CHRN for the case study of the southern France were 10°. Also, it is unfortunate that the GPS satellite constellation hole falls in the northern side of the stations, where the most significant amounts of refractivity exist, and therefore the impact of the directional gradient model is not sufficiently evident. The Gard region precipitation event shows the importance of using the directional model to estimate more realistic gradients, but does not show much impact on positions and ZTD's, most likely because of the lack of low-elevation observations (particularly in azimuthal directions of large gradients), and/or possibly because of insufficiently strong gradients to show the effect on other parameters. In the next section, we examine another case study in California which contains observations at very low elevations, which is an appropriate case for examining the impact on positions and ZTD's.

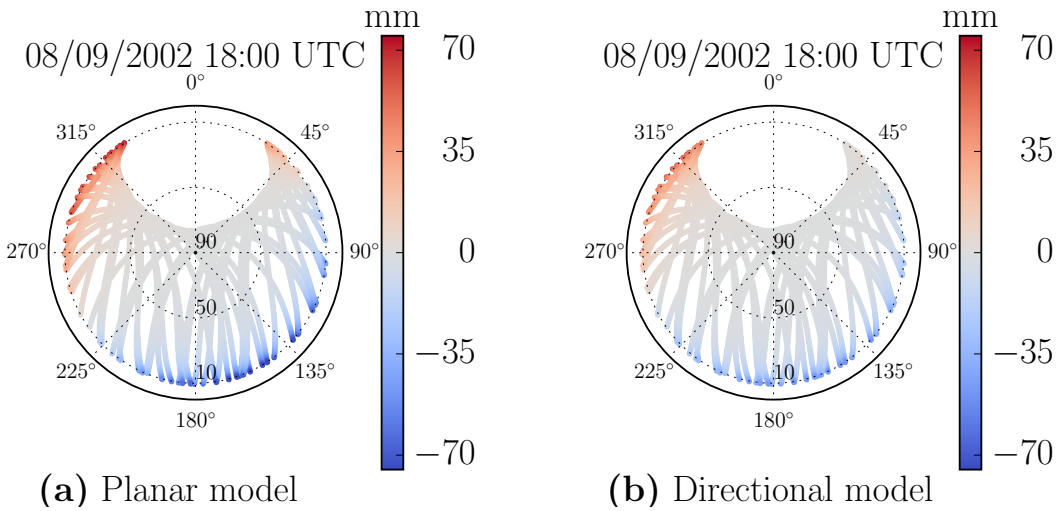

(a) Planar model **(b)** Directional model

Figure 4.15: Horizontal gradient delays estimated at site CHRN using (**a**) the conventional planar model, and (**b**) the directional model with 8 gradient estimation nodes. The horizontal gradients are isolated towards the north-west by the directional model.

4.4 Skewed time series of Plate Boundary Observatory network

The Plate Boundary Observatory is a network of about 1100 GPS stations and other measuring devices such as seismometers and strainmeters mostly across the western United States which are operated by UNAVCO for EarthScope (www.earthscope.org) and supported by the National Science Foundation. While the main objective of the PBO network is deformation studies of the active boundary zone between the Pacific and North American plates, the extended GPS network has introduced several geophysical applications including atmospheric studies [e.g. Jackson, 2003; Larson et al., 2008]. A well-known feature of some of the GPS stations of the PBO network, mostly concentrated around the Mammoth Lakes in the Sierra Nevada region in California, is the asymmetry of their position time series that occurs throughout the year, but is mostly observed during the winter time. The asymmetry appears as outliers in the position time series for several days with the most of outliers being in the same direction. Materna and Herring [2013] and Materna [2014] performed investigations on these skewed time series, and speculated that the presence of Lee waves at some particular directions around the sites may be the cause.

Lee waves are internal gravity waves caused by the flow of stably stratified air over steep uneven topography, which leads to oscillations in the atmosphere for restoring the hydrostatic equilibrium. The relative humidity of a raised parcel of air by the oscillation increases, that may create clouds [e.g. Glickman and Zenk, 2000]. The very steep topography in the eastern side of Sierra Nevada Mountains (dropping

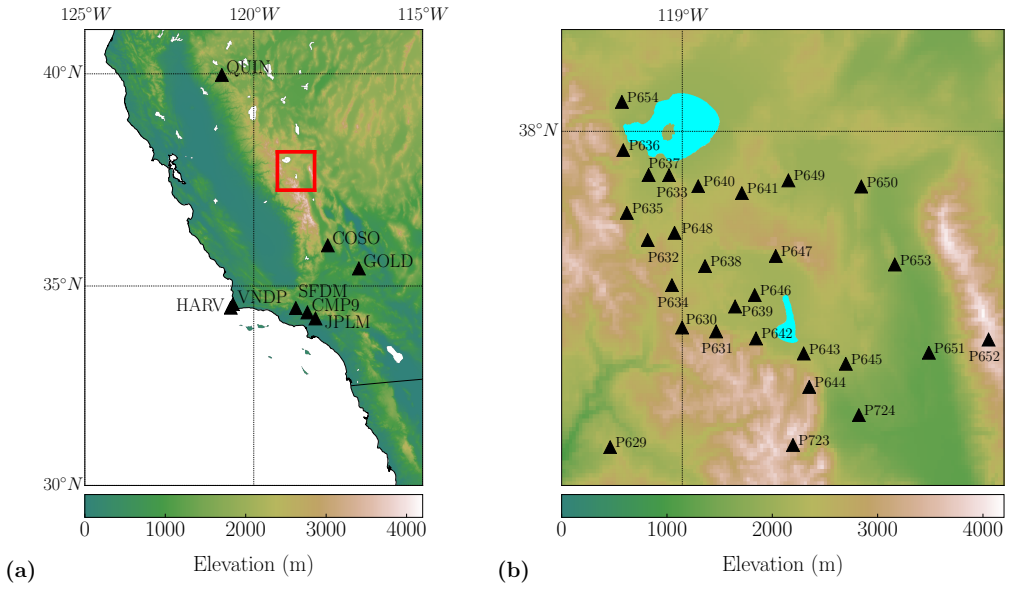

Figure 4.16: Sites from the plate boundary observatory network selected for the analyses and some of the far-field sites processed. **(left)** The red rectangle corresponds to the **(right)** frame location. The topography is retrieved from General Bathymetric Chart of the Oceans (GEBCO) 30″ grid.

from 4 km to 1 km in a horizontal range of around 10 kilometres as noted by Materna [2014]) causes strong Lee waves in this region, leading to large horizontal gradients of the humidity. Since the Lee waves only appear in a small horizontal distance, the stations in the eastern side of the Sierra Nevada mountain ranges are expected to observe large horizontal tropospheric gradients on their western directions with not as large gradients in their eastern sides (Figure 4.16). This one-sided gradient scheme could be the cause for the asymmetric patterns seen in the position time series of the stations around the Mammoth Lakes in the Sierra Nevada region. The directional gradient model is, therefore, a potential tool to isolate these asymmetric horizontal gradients around the stations in this region.

Here, we analyse the GPS time series of a set of PBO sites around the Mammoth Lakes (Figure 4.16) for the period 1 January 2012 to 30 March 2012, using both conventional planar and directional gradient models, in order to ascertain whether a more detailed gradient model is able to reduce the errors (and asymmetries) on position and ZTD estimates. The reference sites are chosen from the IGS core network such that we have stations in various directions around the PBO sites. Fortunately, most of the PBO RINEX files include very low-elevation observations: we chose an elevation cut-off angle of 3° to reduce the correlations between the estimation parameters and also to assess the impact of gradients at low elevations. In addition, we derived and implemented the ESM in the same way as in Section 4.3 (this time with four months of data) to remove any possible effect of site-specific errors such

as multipath. As we are using four months of observations for deriving the ESM, transient tropospheric effects originating from the local topography are not absorbed by the ESM.

Having investigated the position time series of our selected GPS network resulted from using both the conventional planar and the new directional model, the directional model was found to have only marginal impacts on horizontal components (consistent with the simulation results); therefore, we focus on the vertical component only for the rest of this case study. Figure 4.17a shows the scatter (WRMS) of the height time series for all the PBO stations in our analysis when using the directional model of gradients (black bars) compared to using the planar model (red bars). The stations in Figure 4.17 are sorted based on the WRMS of the planar solution. The height time series of the sites with higher scatters are generally improved in terms of WRMS, while the WRMS of the time series with low scatters are increased when using the directional model. For all the stations with WRMS of larger than 4 mm, except P654, the WRMS is reduced when taking advantage of the more complicated gradient model, with the largest improvements mainly for the worst sites. The increase in the WRMS of P654 is small and negligible compared to the reductions for other sites. For the majority of the stations with WRMS < 4.0 mm, on the other hand, the directional model increased the noise in the height time series. This is an important finding, as it shows that for particular weather scenarios when the tropospheric refractivity field does not follow a plane around the station, the directional model is able to help in better modelling the gradients, while it results in higher dispersion at normal (i.e. planar) atmospheric conditions. This increased scatter of time series in normal situations is most likely because of larger number of correlated parameters estimated in the solution, which is overcome by the improvement in gradient modelling at abnormal conditions but not at typical close-to-planar situations.

Materna [2014] investigated more than 1000 PBO stations and noticed that the outliers in the position time series of each site are mainly in the same direction relative to the mean of the time series. For this reason, they used the concept of skewness as a statistical measure for studying the shape characteristics of the distribution of position estimates. Skewness is defined as the expected value of the third moment of a distribution; a skewed distribution has a longer tail either right or left of the distribution peak, which corresponds to the presence of positive or negative outliers in the relevant data series. Skewness is therefore an appropriate statistic for investigating the deviation of a distribution from a normal distribution, and is useful for analysing the skewed outliers in the position time series of the PBO sites. We use the same definition of the normalized sample skewness (γ) as used by Materna [2014]:

$$\gamma = \frac{1}{N}\sum_{i=1}^{N}[(\frac{X_i - \mu}{\sigma})^3] \tag{4.6}$$

where N is the number of data points, X_i is the ith data point, and μ and σ are mean and standard deviation of the time series. The skewness values of the PBO GPS stations in our network are shown in Figure 4.17b in the same order that the

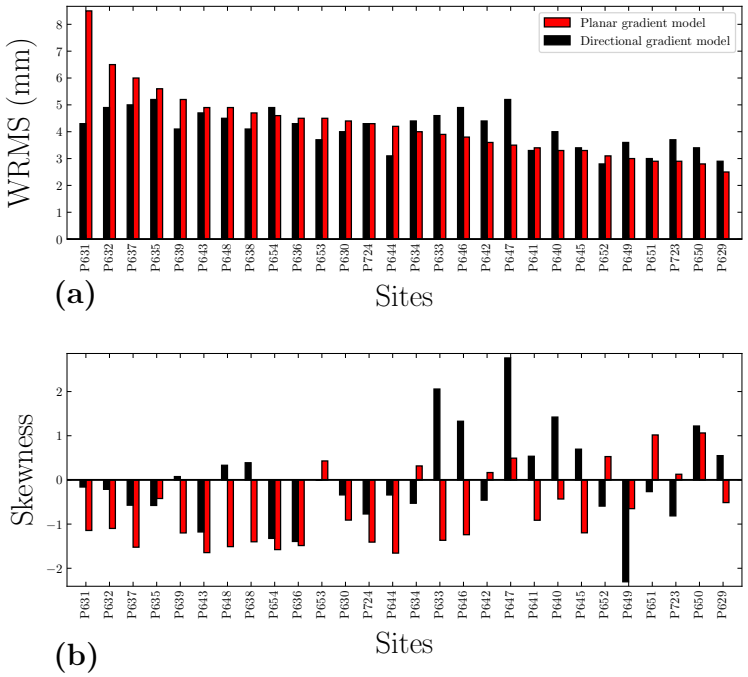

Figure 4.17: (**a**) WRMS and (**b**) skewness of the height position time series when using a directional gradient model (black bars) instead of a planar model (red bars), sorted based on WRMS of the planar gradient solution.

WRMS values are displayed. There are a few interesting points to notice: The height time series which are highly scattered are usually also highly skewed; using the planar gradient model, about 79% of the stations with WRMS larger than 4 mm have skewness values (red bars in Figure 4.17b) of larger than 1. It is also worthwhile noting that about 71% of the sites in the analysis using the planar gradient model have negatively skewed height time series and, except for one station (P653), all the highly scattered height time series (with WRMS larger than 4 mm) are negatively skewed. Looking at the skewness values resulted from using the directional gradient model (black bars in Figure 4.17b), it is evident that the directional model has led to improvements in almost all of the highly scattered sites. The only exception to this is P635 which sees a degradation of only 0.4 in skewness; compare this to 9 sites with reductions of larger than 1, and a reduction in the mean value of 1.10 for all the 13 highly scattered sites which are improved in terms of skewness. The degradation of the skewness for P635 despite the improvement in its WRMS is because the smaller standard deviation of the time series in the denominator of Equation 4.6 has a larger effect on the skewness than the smaller deviations of individual points from the mean in the numerator, which results in a higher skewness. It is therefore important to note both WRMS and skewness statistics as the second and third moments of the distributions.

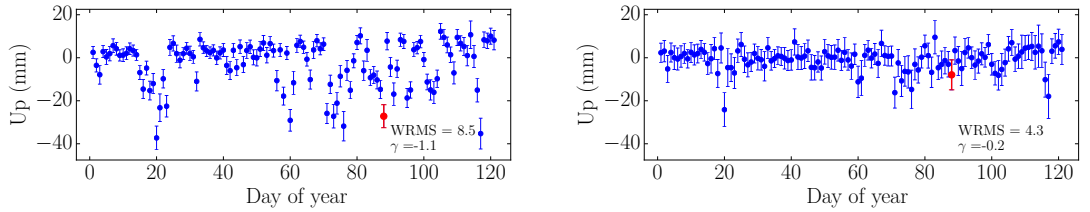

(a) Planar model **(b)** Directional model

Figure 4.18: Time series of the vertical positions for site P631 and for the period of 1 January 2012 to 30 April 2012 when using (**a**) the conventional planar model of gradients, compared to when using (**b**) the directional model for the gradients. WRMS and skewness (γ) are shown on the figures, and the date 28 March 2012 is signified by red colour.

As an example of the improvements for individual time series, the height time series of site P631, which sees the largest reduction in the WRMS, are shown in Figure 4.18. The large improvement (from 8.5 mm to 4.3 mm WRMS) in the repeatability of the time series is clearly observed when using the directional model (Figure 4.18b) instead of the planar gradient model (Figure 4.18a). The skewness is also improved from -1.1 for the planar model to only -0.2 for the directional model. This reduction in skewness occurs because several negative outliers were eliminated with the use of directional gradient parametrization.

We assumed previously that the skewness in height time series results from abnormal atmospheric conditions (i.e. a tropospheric refractivity/water vapour field that is not well represented by a plane around the GPS station). We will now evaluate this assumption by taking as an example one day of the height time series of the site P631 (28 March 2012; coloured in red in Figure 4.18) when there is a large error of about 20 mm introduced into the vertical component when using the conventional planar gradient model. The estimated delays due to gradients using the planar and the directional model for this single day are shown for 06:00 UTC in Figure 4.19a and b, respectively. The unusually large gradients (leading to delays larger than 120 mm at 10° elevation) towards the south-west of the site captured by the directional gradient model are not fully recovered by the planar model, which explains the reason for the ∼20 mm error in the height estimate of the station when using the planar model. The planar model underestimates the positive gradients towards the south-west (with maximum estimated delays of ∼50 mm at 10° compared to ∼120 mm delay by the directional model), and overestimates the negative gradients towards the opposite direction (with the estimation of about -50 mm of signal delay in the north-east compared to ∼-35 mm delay by the directional model); this leads to the large bias in the estimation of vertical position observed in Figure 4.18. Using the directional model has resulted in much more accurate estimates of both south-western positive gradients and north-eastern negative gradients, leading to the large improvement in estimation of the vertical position for the same day. Therefore, there

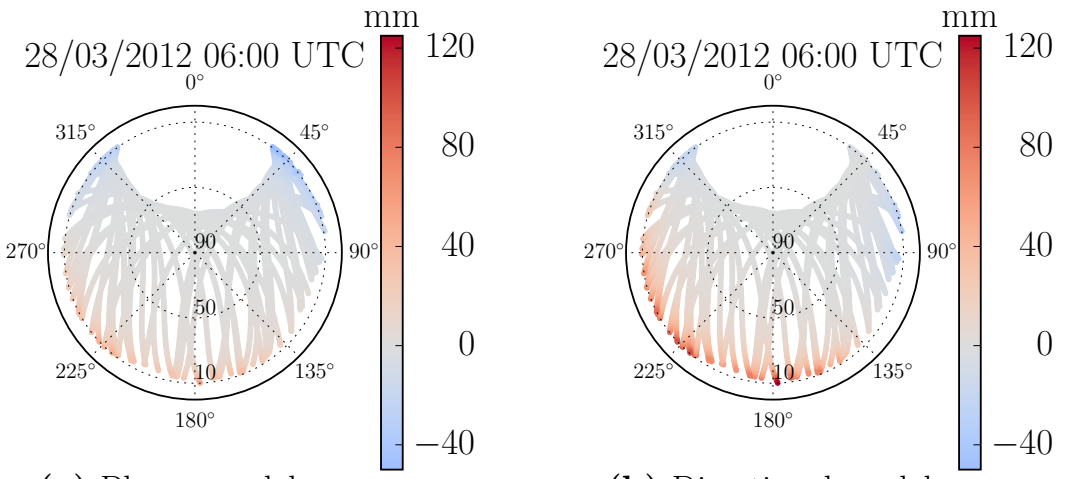

(a) Planar model **(b)** Directional model

Figure 4.19: Horizontal gradient delays for site P631 at 06:00 UTC of 28 March 2012 estimated by (**a**) the planar, and (**b**) the directional model for the gradients. Large horizontal gradients in the south of the station, captured by the directional model, are significantly underestimated by the planar model.

seems to be some tropospheric effect, not fully captured by the planar model but modeled by the directional approach, at the south-west of the site. This tropospheric moisture content could possibly be due to the presence of Lee waves as suggested by Materna [2014].

The phase residuals for the same day (28 March 2012) at station P631 are shown in Fig 4.20. The estimation of directional gradient parameters clearly resulted in reduced phase residuals, too: the phase RMS are reduced from 9.1 mm to 7.3 mm. When using the planar gradient model, large positive residuals up to about 90 mm are observed in the north-east and large negative residuals up to about -50 mm occur east of the station. These large residuals are the result of mismodelling the large gradients in the south-west of the station. By improved modelling of the directional gradients towards the south-west, most of the large residuals towards the east of the station are eliminated or significantly reduced.

The tropospheric zenith delay estimates are also affected by the mismodelling of the horizontal gradients. The estimates of tropospheric zenith wet delays using both planar and directional gradient models are shown in Figure 4.21 for the same day; there are differences of more than 15 mm in the estimation of ZWD from the two solutions, which are well above the uncertainty level of the estimates. On average, the planar model overestimates the zenith wet delays by ∼25% on this day, which is a result of not considering very large gradients towards the south-west of the station (Figure 4.19). The significance of this finding is that in the generation of zenith total delays for meteorological applications, such as for assimilation into numerical weather prediction models, it is recommended to include low-elevation observations

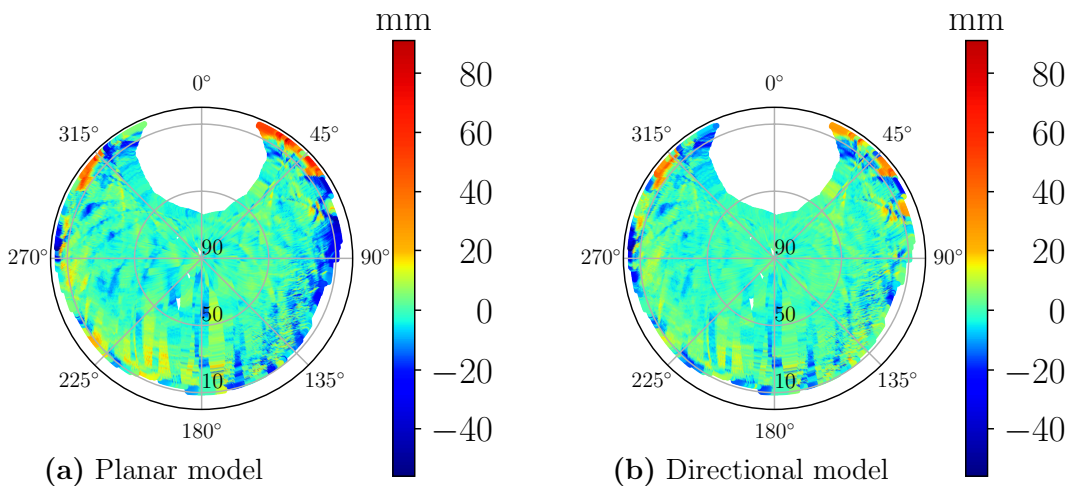

(a) Planar model
RMS = 9.1 mm

(b) Directional model
RMS = 7.3 mm

Figure 4.20: Phase residuals for site P631 on 28 March 2012 when using (**a**) the planar, and (**b**) the directional model for the gradients.

in order to decorrelate the height and ZTD parameters: however, not having the proper gradient model in specific asymmetric gradient conditions results in further biases in ZTD when including the low-elevation observations. Therefore, using our proposed directional gradient model is recommended in these asymmetric situations to avoid such errors at low elevation angles.

The results from the PBO stations in the Sierra Nevada region provide us with more evidence on the importance of using a more complicated model of gradients than a planar assumption for refractivity field in abnormal asymmetric gradient conditions. Using the directional gradient model, reduction in both scatter and skewness of the height time series are evident, and the estimates of height and tropospheric zenith delay are improved in the days with abnormal gradient schemes. In normal (symmetric) gradient conditions, on the other hand, the directional model leads to higher dispersion of the estimated parameters as a result of larger number of correlated parameters. Horizontal positions are not much impacted by the new directional gradient model, which signifies that there might be some effects other than only tropospheric conditions for the skewness in time series of horizontal components.

4.5 Summary

In both simulations and real case studies analysed in this chapter we have shown that, while the impact of mis-modelled gradients is minimal on horizontal positions, it becomes highly significant for the estimation of heights and tropospheric zenith delays in particular weather scenarios. The conventional model of gradients introduced by Chen and Herring [1997] performs well in normal tropospheric situations,

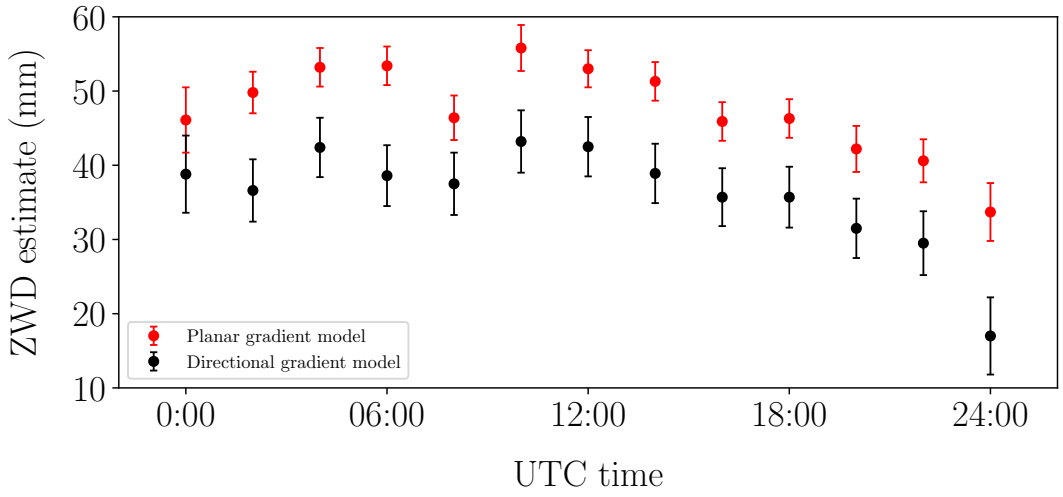

Figure 4.21: 2-hourly estimates of the zenith wet delays for site P631 on 28 March 2012 when using the planar model (red), compared to when using the directional model (black) for the gradients. On average, the planar model overestimates the zenith wet delays by ∼25% for this day.

but its planar assumption for horizontal changes of tropospheric delay fails to accurately model the gradients in abnormal weather conditions when there are isolated gradients in some directions of a station. Such weather situations can happen as a result of topography-induced gravity waves in the atmosphere. As a result, estimates of both vertical positions and tropospheric zenith delays are contaminated by the mismodelled gradients. This may appear as outliers in the height time series of a GPS station, and biases in the estimation of zenith total delays.

The proposed directional model developed and discussed in this chapter is able to provide a more accurate representation of the tropospheric horizontal gradients during complicated atmospheric situations where tropospheric gradients are highly non-linear. Application of the directional model results in significant improvements in the estimation of vertical position components (and correspondingly tropospheric zenith delays) for such highly heterogeneous weather conditions. For instance, the majority of outliers in skewed height time series of the Plate Boundary Observatory GPS stations in the Sierra Nevada region were removed by the directional gradient parametrization. Consequently, the directional gradient model is useful in the estimation of GPS vertical components and tropospheric delays in particular atmospheric conditions with highly non-linear gradients.

The impact of using an improper model for the gradients on the estimated parameters is more pronounced when including low-elevation observations. It is therefore particularly important in meteorological applications, such as assimilation in numerical weather models, where low-elevation observations may be used for decorrelating the zenith delay parameters and the vertical position components, to take advantage

of the more complicated model of directional gradients instead of the conventional planar model in atmospheric conditions when the refractivity field is highly heterogeneous. Since the impact of horizontal gradients is much larger on the slant GPS signals, in particular slant signals at low elevations, the use of the directional model for applications like GPS tomography that require the slant delay estimates will be useful.

The drawback of the directional model is the higher number of correlated parameters it introduces into the least-squares inversion, causing higher dispersion of the estimated parameters in normal homogeneous tropospheric conditions. Therefore, it is important to note that the directional model should be used only when the tropospheric refractivity gradients are highly asymmetric. The modified GAMIT version developed in this study is capable of selecting different gradient models (planar model and directional model with different number of directional gradient parameters from 3 to 24) for each station and day, but developing a technique to decide in advance how many number of gradient parameters to estimate for each station and day has yet to be developed.

Moreover, the analyses performed in this study were limited to the use of GPS observations, but the resolving power of the directional gradient model also depends on the amount of available data. Therefore, the impact of incorporating other GNSS measurements (e.g. GLONASS, Galileo and BeiDou) on the ability of a finer modelling of azimuthal heterogeneity of the water vapour field could be an interesting perspective for the future studies.

Chapter 5

Temporal constraints on tropospheric parameters

Unlike the position parameters, which can generally be assumed invariable over a day in static GPS data analysis, the tropospheric zenith wet delays and horizontal gradients may need to be estimated at several epochs during the day so as to capture the inherent variabilities in the troposphere, depending on the variability of tropospheric parameters in the station. Both zenith delays and horizontal gradients can be estimated using different approaches for temporal modelling from using either stepwise or piecewise linear functions with some form of temporal constraint controlling the level of parameter variability with time to using random walks at each observation epoch. In the GAMIT software used in this analysis, a piecewise linear function with temporal constraints is applied to both wet zenith delays and horizontal gradients using a stochastic process noise generated by a first-order Gauss-Markov (FOGM) processes. The Gauss-Markov process can be customized by changing the process noise levels and/or correlation times. In this chapter, we will study how using different noise levels for the FOGM process impacts the estimated parameters by tightening or loosening the amount of point-to-point variations that the tropospheric components are allowed to undergo. A brief introduction to the first-order Gauss-Markov process parameters used in GPS tropospheric modelling is given in Section 5.1. In Section 5.2, we perform a set of simulations in which we generate different scenarios of zenith wet delay and tropospheric horizontal gradients using Gauss-Markov processes with different noise levels. We then attempt to recover the ZWD and gradient parameters with different temporal constraints in the GPS daily analysis. We will show via the simulations how changing the temporal constraints on tropospheric components would affect the estimated parameters. In Sections 5.3 and 5.4, we will apply different temporal constraints on the tropospheric parameters in real experiments, and will investigate the impact on the solutions. We will also focus on particular days with very turbulent atmosphere, and will study how the standard constraints may be limiting the change allowed in tropospheric delays. Section 5.5 will provide a summary of the results of this chapter.

5.1 Parameters of the first-order Gauss-Markov process in GPS tropospheric modelling

It was pointed out in Chapter 2 that a first-order Gauss-Markov process is used as the stochastic constraints of the piece-wise linear function used for the estimation of tropospheric zenith wet delays and horizontal gradients. A first-order Gauss-Markov process, as described in Appendix B, can be defined by a variance (σ^2) and a correlation time (τ). These two parameters can be used to form the elements of the variance-covariance matrix (c_{ij}) of ZWD and horizontal gradients by Equation B.12 in Appendix B, which is repeated here:

$$c_{ij} = \sigma^2 exp(-\frac{|t_j - t_i|}{\tau}) \tag{5.1}$$

in which t_k is the time at kth estimation node of the parameter (either ZWD or a horizontal gradient).

The two parameters of the first-order Gauss-Markov process (σ and τ) can be adjusted to change the variance-covariance matrix elements. τ defines the correlation time of the process. A zero correlation time turns the Gauss-Markov process into white noise, and as the correlation time approaches infinity, the process becomes a random walk. By taking the correlation time as 100 hours for the span of 24 hours over a day, we assume that the variations of the tropospheric parameters are close to random walk.

The variance (σ^2), or equivalently the process noise variance ($\delta^2 = \sigma^2[1 - exp(-2\Delta t/\tau)]$ as described by Equation B.11), defines the level of variation allowed between the tabular points of the parameter in the estimation. By default, we use process noise variation (δ) of 20 $mm/\sqrt{hr}$ for ZWD and 10 $mm/\sqrt{hr}$ for horizontal gradients. The 10 $mm/\sqrt{hr}$ variation for the gradient parameter is for when the gradient is mapped to a 10° elevation angle. In practice, however, the process noise level of tropospheric parameters varies depending on the weather conditions. The process noise variance is small in stable weather conditions, while the noise level is high in turbulent atmospheric states. As an example to provide an insight into these variabilities, we calculated the point-to-point variations (δ_{apr}) of zenith wet delays across the globe using the VMF1 gridded values of ZWD (retrieved from http://ggosatm.hg.tuwien.ac.at/DELAY/GRID/VMFG/). The VMF1 gridded values have horizontal resolutions of 2° and 2.5° for latitude and longitude, respectively. To determine the point-to-point variation, we used Equation 5.2 below:

$$\delta^2_{apr} = \frac{1}{\Delta t_{apr}(N-1)} \sum_{i=2}^{N} [(y_i - y_{i-1})^2] \tag{5.2}$$

where $\Delta t_{apr} = 6\ hr$ is the time interval between the VMF1 ZWD values, N is the total number of ZWD values, and y_i is the ith ZWD value. We calculated the monthly point-to-point variations for January and July 2012, which are shown in Figure5.1. Both spatial and seasonal changes are evident in the hourly variations of ZWD. The

ZWD is generally more variable in summer time (January in the southern hemisphere and July in the northern hemisphere). The variations are the smallest in the polar regions (which are generally the driest areas), while they are significantly larger in regions in the Atlantic Ocean (both in the northern and southern hemisphere to the east of the American continent), the mid-latitudes of the Indian Ocean, and the North Pacific Ocean both in summer and winter (with typical increases in the summertime). In New Zealand and the southern parts of the Australian continent, the variations are significantly large in summer (up to about 16 $mm/\sqrt{hr}$), but very small in winter.

There have been some previous research that studied how tuning the process noise variances could impact the GPS estimates (e.g. Bar-Sever et al. [1998] and Miyazaki et al. [2003]). However, there have not been any study for investigating this calibration with the use of an empirical site-specific model, and most of the studies did not use low-elevation observations. In this chapter, we study how using higher or lower process noise variances in forming the variance-covariance matrix of the tropospheric parameters may change the estimates of these components. We perform this study first using a set of simulations in Section 5.2 and then on real case studies in Sections 5.3 and 5.4.

5.2 Simulations

Using the state transition equation of Equation B.3 and the noise variance of Equation B.11, one can generate a first-order Gauss-Markov process. To simulate different conditions of the troposphere, we generated a set of FOGM processes both for tropospheric zenith wet delays and horizontal gradients, and attempted to estimate the simulated values by setting different process noise variances in the GAMIT software. Similar to what was done in Chapter 4, we simulated the GPS phase observations of the stations shown in the network of Figure 2.3 using the set of models and parameters in Table 2.1 for the actual observing geometry of 16 July 2010. There are however a few discrepancies between the simulated signals generated here and those in Chapter 4. In order to generate more realistic simulated observations, we added random Gaussian noise to the observations using the standard GAMIT elevation-dependent weighting scheme given in Equation 5.3 using constant elevation-dependent values of: $a = 5$ mm and $b = 2.5$ mm:

$$s^2 = a^2 + \frac{b^2}{\sin^2(\varepsilon)} \tag{5.3}$$

This scheme introduces realistic data noise characteristics where observation standard deviations (s) at lower elevation angles are larger than observations at higher elevation angles.

For all the stations in the network except ALIC, instead of using the constant GPT values for the tropospheric zenith wet delays, we used the two-hourly zenith wet delays estimated by a GPS analysis which used the models and parameters in Table 2.1.

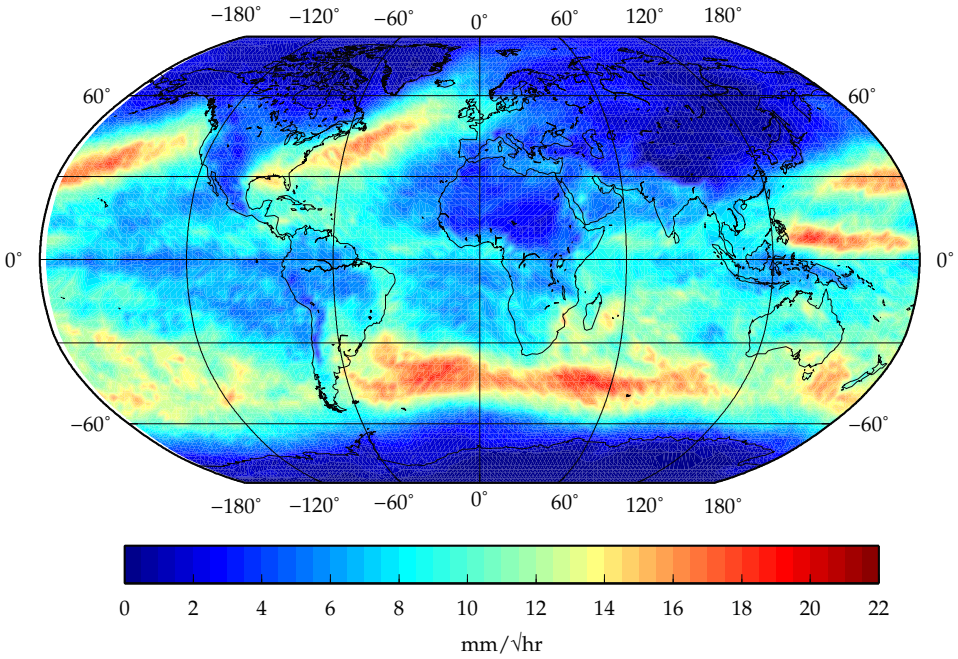

a) January 2012

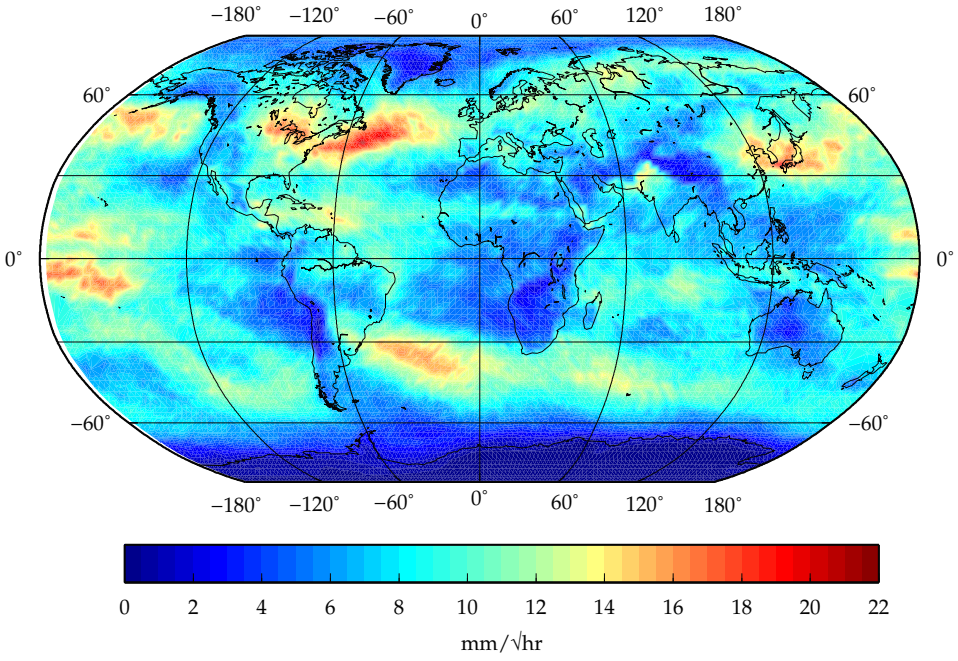

b) July 2012

Figure 5.1: Monthly point-to-point variation of zenith wet delays derived from VMF1 grids for (**a**) January and (**b**) July 2012.

We linearly interpolated the values of ZWD between these two-hourly estimates for any observation epoch in the simulations. Also, instead of considering zero gradients for all the stations except ALIC, we linearly interpolated the six-hourly estimates of North-South and East-West gradients in the simulations for these stations. For ALIC, we used different sets of FOGM processes with different process noise levels for both tropospheric zenith wet delays and horizontal gradients, which we discuss in the following sections.

A more realistic simulation of the zenith wet delays and the horizontal gradients would be to consider spatial correlations in the atmosphere in addition to the temporal correlations. However, the aim for the simulations in the following sections is to generate different levels of variabilities for the states of the atmosphere and assess how using different levels of constraints could impact the estimated parameters. Therefore, while including spatial correlations in the simulations would be a more realistic approach, only including the temporal correlations is still suitable for our analysis purpose here.

5.2.1 Simulations of the zenith wet delays

For the station ALIC, we simulated the two-hourly variations of ZWD as first-order Gauss-Markov processes with four different process noise levels (δ = 5, 20, 70, 150 $mm/\sqrt{hr}$) to produce four different scenarios. For each scenario, we first used Equations B.3 and B.11 to generate the states of the Gauss-Markov process every two hours, and then detrended the process and added a mean of 100 mm to the process to ensure that the ZWD varies around a reasonable mean value (the GPT value for ZWD for ALIC on the simulation day is 83.9 mm). We then linearly interpolated the two-hourly values of ZWD for all the observation epochs. while we could have generated Gauss-Markov instances at a higher temporal resolution, or even at every observation epoch, the aim here is to generate different sets of observations with different variability levels. Therefore, generating instances of a Gauss-Markov process at two-hour intervals and linearly interpolating the simulated values for the epochs between the two-hour intervals suffices our goal here.

For all of the scenarios, the six-hourly tropospheric North-South and East-West gradients for ALIC were modelled by a first-order Gauss-Markov process with δ = 10 $mm/\sqrt{hr}$ with added daily mean of 30 mm for the North-South gradients and -20 mm for the East-West gradients. A linear interpolation is also used for the horizontal gradients to determine the values between the six-hourly nodes.

The simulated ZWD values are shown in Figure 5.2 (left sub-plots) for the four different scenarios. We then attempted to estimate ZWD parameters along with position and tropospheric horizontal gradients using the standard models and parameters of Table 2.1. We also used different process noise levels (5, 20 and 50 $mm/\sqrt{hr}$) in forming the variance-covariance matrix of the ZWD parameters to solve the least-squares problem. The errors in the estimation of ZWD parameters using each of these three process noise levels in the variance-covariance matrix are depicted as error bars of different colours in the right sub-plots of Figure 5.2: the red colours

show a tight process noise level of 5 $mm/\sqrt{hr}$, the black colours represent a standard variation level of 20 $mm/\sqrt{hr}$, and the green colours depict a loose constraint of 50 $mm/\sqrt{hr}$.

The first simulated scenario (Figure 5.2a; $\delta = 5\ mm/\sqrt{hr}$) resembles a stable weather condition with small fluctuations of moisture over the day. Considering the high correlations between zenith delays and height parameters (e.g. as shown in Figure 4.6), one would expect that by using a tight constraint for the ZWD parameters, we may avoid these correlations to cause interferences between ZWD and height parameter estimates, and therefore reduce the errors in these parameters. However, it is clear from Figure 5.2a (right sub-plot) that using any process noise level, whether a tight or a loose variation level, the ZWD parameters are accurately estimated with the error bars containing the zero error. Using a looser constraint does not yield significantly higher errors in ZWD. The uncertainties on the estimates also do not change significantly. This indicates that unlike what one may expect as a result of high correlations between the ZWD and height parameters, allowing the ZWD to largely vary over the day does not add significant errors to the estimates of ZWD. This is however only valid when a piecewise linear function is used to model the delays. If one decides to use a random walk for modelling the temporal behaviour of the parameters, the constraints are likely to have more significant impacts.

The second simulated scenario (Figure 5.2b; $\delta = 20\ mm/\sqrt{hr}$) is a typical situation with the level of variations that occurs in many mid-latitude GPS stations at normal atmospheric conditions. Clearly, while both standard and loose noise levels perform accurately in estimating ZWD parameters (green and black error bars), the tight noise variation level of 5 $mm/\sqrt{hr}$ results in significant errors in the estimation of ZWD at some epochs, including an error of $\sim$15 mm at the first epoch of the day, which is above the one-sigma uncertainty level of the estimate. These errors occur because the tight constraint on the ZWD does not allow the wet delays to vary as much as needed. It is immediately inferred that the standard process noise level of 20 $mm/\sqrt{hr}$, which is typically used by GPS analysts, is sufficient for accurately estimating the ZWD parameters in normal weather conditions, and that setting a looser constraint does not harm the estimates, while having tighter constraints induces errors in such typical atmospheric conditions.

The two next simulated scenarios (Figure 5.2c and d; $\delta = 70$ and $150\ mm/\sqrt{hr}$) imitate more turbulent atmospheric states. Having investigated some real GPS solutions, the scenario with $\delta = 70\ mm/\sqrt{hr}$ occurs quite often in equatorial humid stations, while the scenario with $\delta = 150\ mm/\sqrt{hr}$ is very unlikely. In spite of this, there are days for some stations when while the atmosphere is not as turbulent as in Figure 5.2d for the whole day, the amount of change in ZWD in only 2 hours of the day is comparable to the changes seen in Figure 5.2d. We do not show the errors resulting from using the tight constraint of 5 $mm/\sqrt{hr}$ in Figure 5.2c and d, as there were extremely large errors due to the use of the tight constraints (up to $\sim$50 mm for scenario c and $\sim$120 mm for scenario d).

The standard solution with the allowed variation of 20 $mm/\sqrt{hr}$ still performs fairly accurately in the more turbulent atmosphere of Figure 5.2c with a maximum

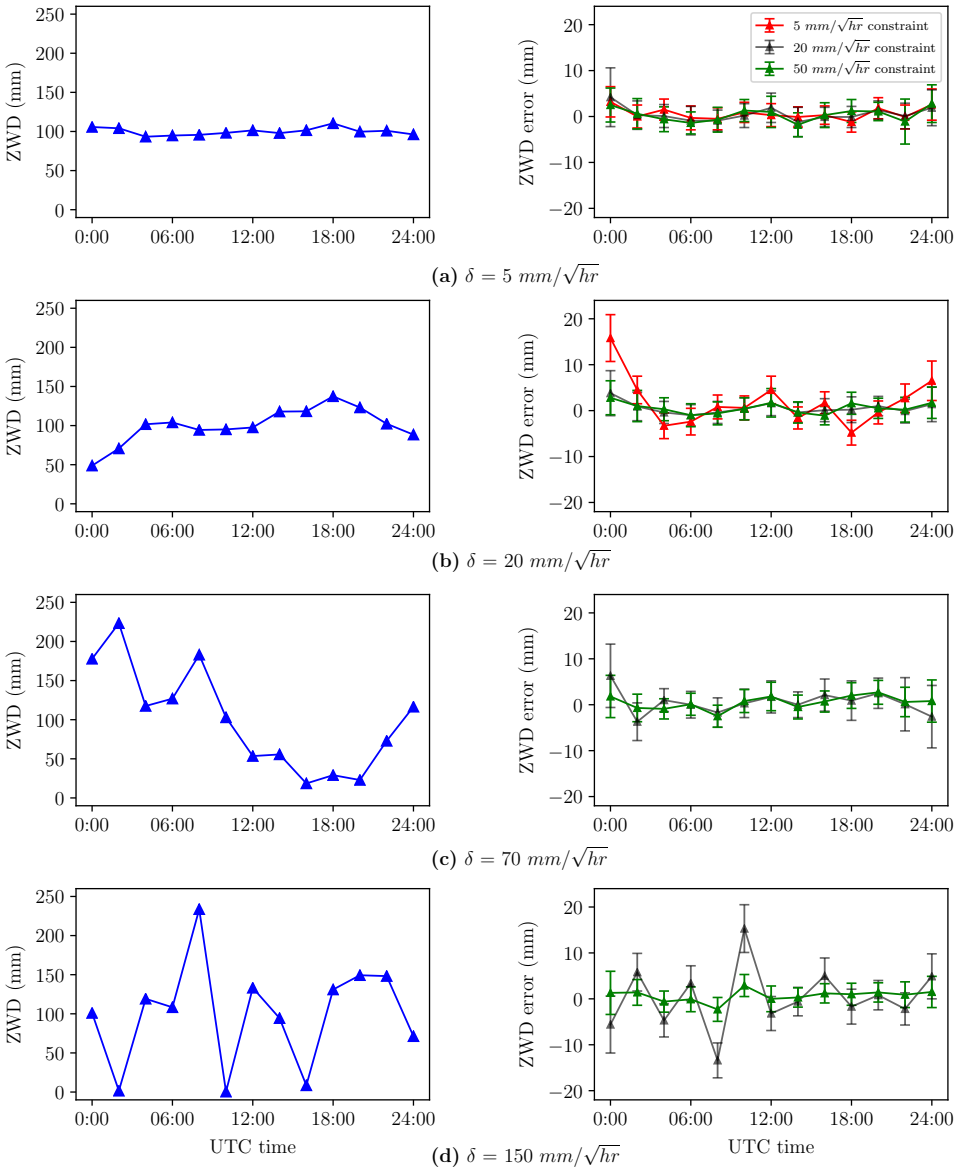

(a) $\delta = 5\ mm/\sqrt{hr}$

(b) $\delta = 20\ mm/\sqrt{hr}$

(c) $\delta = 70\ mm/\sqrt{hr}$

(d) $\delta = 150\ mm/\sqrt{hr}$

Figure 5.2: The simulated zenith wet delays for ALIC (left) and the estimation errors in recovering the simulated values (right) when choosing the process noise level of the first-order Gauss-Markov process used for the simulation as (**a**) 5, (**b**) 20, (**c**) 70, and (**d**) 150 $mm/\sqrt{hr}$. The colours of the error bars on the right sub-plots depict the process noise level used in forming the variance-covariance matrix of the ZWD parameters: red is a tight constraint of 5 $mm/\sqrt{hr}$, black is a standard constraint of 20 $mm/\sqrt{hr}$, and green is a loose constraint of 50 $mm/\sqrt{hr}$. The error bars display the 1-sigma uncertainty of the estimates. The errors resulted from the tight constraint for the simulation scenarios with process noise levels of 70 and 150 $mm/\sqrt{hr}$ (c and d) are very large and thus not shown on the plots.

error of 6.3±6.9 mm at the first epoch of the day. Using a looser constraint of 50 $mm/\sqrt{hr}$ reduces the errors of the ZWD estimates, although the differences between the two solutions are within the level of 1-sigma uncertainty. For instance, the error in the first epoch is reduced to 1.8±4.6 mm when using a noise level of 50 $mm/\sqrt{hr}$ in the estimation.

In the unlikely situation of tremendously variable atmospheric conditions (Figure 5.2d), the standard noise variation of 20 $mm/\sqrt{hr}$ (black error bars) causes significant errors of up to ∼15.3±2.9 mm in the estimation of zenith wet delays. In fact, the extremely large depletion in the amount of ZWD in only two hours from 08:00 UTC to 10:00 UTC is not completely captured when the standard constraints are applied: the ZWD is underestimated at 08:00 UTC but is overestimated at 10:00 UTC. Using a looser constraint of 50 $mm/\sqrt{hr}$ yields almost zero errors for all the epochs throughout the day.

We also examined using larger process noise levels in forming the variance-covariance matrix of the ZWD parameters in the least-squares solution, and observed that using even looser temporal constraints does not introduce significant errors to the estimates when using a piecewise linear function for temporal modelling of the delays. The fact that using loose constraints on ZWD variations does not significantly harm the solutions suggests that constraining the piecewise linear ZWD variations may in fact be unnecessary in GPS analyses, particularly given that constraining the ZWD parameters may induce errors at extreme weather situations with large changes in short amounts of time. It should be noted, however, that there may be other sources of error such as multipath that could correlate with zenith delays and may necessitate the use of constraints. Studying the effect of loosening the process noise levels in real GPS experiments can help to decide if choosing looser temporal constraints does not harm the estimates in actual experiments. Some real experiments will be performed in sections 5.3 and 5.4.

5.2.2 Simulations of the tropospheric horizontal gradients

Similar to what was done in the previous section for zenith wet delays, we used a set of first-order Gauss-Markov processes with different process noise levels (δ =2, 10, 50, 120 $mm/\sqrt{hr}$) to simulate six-hourly tropospheric North-South and East-West gradients for the station ALIC. For each simulated scenario, we detrended the generated Gauss-Markov process and added a mean value of 30 mm for the North-South and -20 mm for the East-West gradient. We then linearly interpolated the six-hourly gradients to all the observation epochs. Like the zenith wet delays, since the aim here is to assess how use of different levels of constraints could impact the estimated horizontal gradients with different levels of variability, producing Gauss-Markov instances at six-hour intervals suffices our goal.

In all the simulated scenarios, the ZWD was simulated using an identical first-order Gauss-Markov process with δ =20 $mm/\sqrt{hr}$. Then, we attempted to recover the tropospheric horizontal gradients along with other estimation parameters (ZWD and positions), using the standard settings of Table 2.1. In forming the variance-

covariance matrix of the tropospheric horizontal gradients, we used three different process noise levels: a tight constraint of 2 $mm/\sqrt{hr}$, a standard constraint of 10 $mm/\sqrt{hr}$, and a loose process noise variation of 50 mm. Figures 5.3 and 5.4 show the simulated scenarios (left sub-plots) and the estimation errors (right sub-plots) of North-South and East-West tropospheric gradients, respectively.

Similar observations as for the impact of using different process noise levels of ZWD in the estimation are also seen for the horizontal gradients of the troposphere. For the North-South gradients, all the three noise variation constraints perform almost equally well in estimating the gradients of the stable (δ =2 $mm/\sqrt{hr}$) and typical (δ =10 $mm/\sqrt{hr}$) scenarios (Figures 5.3a and b), and the differences between the estimates using different temporal constraints are all within the level of 1-sigma uncertainty of the estimates. In more variable gradient schemes of scenario c and d (Figure 5.3c and d; δ =50 and 120 $mm/\sqrt{hr}$), the tight constraint of 2 $mm/\sqrt{hr}$ results in significantly large errors of up to higher than -42$\pm$6.6 mm for scenarios c and larger than 100 mm for scenario d. For these two turbulent scenarios, the loose 50 $mm/\sqrt{hr}$ constraint yields more accurate estimates of North-South gradients compared to the standard 10 $mm/\sqrt{hr}$ constraints, although the induced errors by the standard solution are not significant considering the 1-sigma uncertainty levels.

Similarly for the East-West gradients, the solutions are not significantly different for stable and typical conditions of scenarios a and b, but the tight constraints result in a significant error of $\sim$-20$\pm$4.8 mm at 12:00 UTC for the more variable scenario c (Figure 5.4c). For the much more turbulent scenario d (Figure 5.4d), even the standard constraint of 10 $mm/\sqrt{hr}$ causes an error of $\sim$-86$\pm$19 mm at 00:00 UTC.

The simulation studies carried out in this section showed that the use of tight temporal constraints for the noise variations of tropospheric parameters induces errors into the estimates in unstable weather conditions by restricting the variations of the parameters throughout the day. On the other hand, using loose constraints does not significantly harm the estimates, as long as a piecewise linear function is used for modelling the time evolution of the delays. Therefore, it might be a good idea to always avoid constraints on tropospheric parameters if using a piecewise linear function to be able to capture substantial tropospheric variations in particular extreme weather conditions. Nevertheless, as mentioned before, one needs to study the impact of using different process noise levels on the parameter estimates in real case studies in order to draw a firm conclusion on this subject. In the following sections, we will investigate how the choice of process noise variation level affects the solutions in real experiments. We first study the stable atmospheric conditions of a set of Antarctic stations, and how changing the process noise levels of the tropospheric parameters impacts the solutions in these sites. Then we will examine the effect of process noise levels in more variable conditions of the stations across Australia and South Pacific.

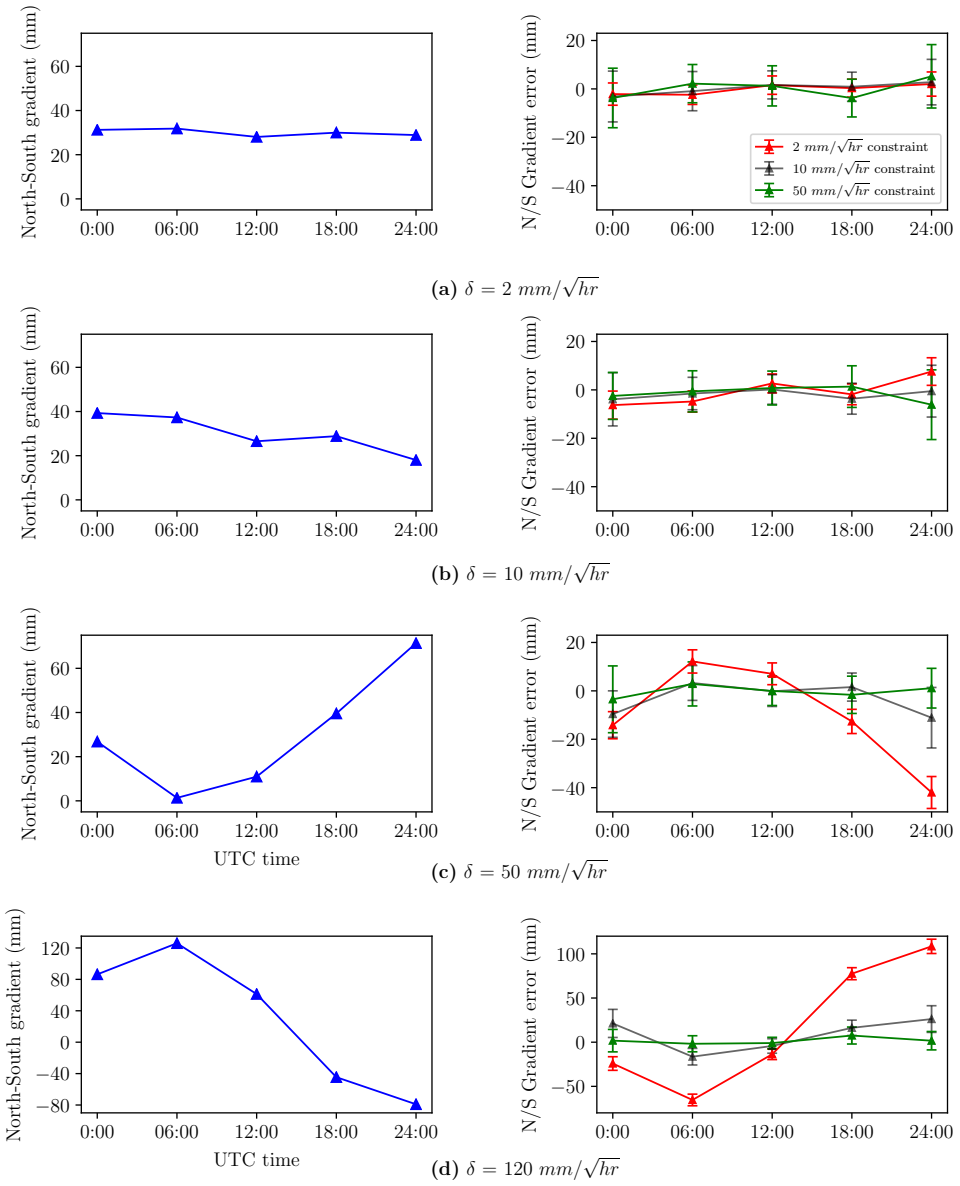

(a) $\delta = 2\ mm/\sqrt{hr}$

(b) $\delta = 10\ mm/\sqrt{hr}$

(c) $\delta = 50\ mm/\sqrt{hr}$

(d) $\delta = 120\ mm/\sqrt{hr}$

Figure 5.3: The simulated North-South tropospheric gradients for ALIC (left) and the estimation errors in recovering the simulated values (right) when choosing the process noise level of the first-order Gauss-Markov process used for the simulation as (**a**) 2, (**b**) 10, (**c**) 50, and (**d**) 120 $mm/\sqrt{hr}$. The colours of the error bars on the right sub-plots depict the process noise level used in forming the variance-covariance matrix of the ZWD parameters: red is a tight constraint of 2 $mm/\sqrt{hr}$, black is a standard constraint of 10 $mm/\sqrt{hr}$, and green is a loose constraint of 50 $mm/\sqrt{hr}$. The error bars display the 1-sigma uncertainty of the estimates. Note the change of scale for Figure 5.3d.

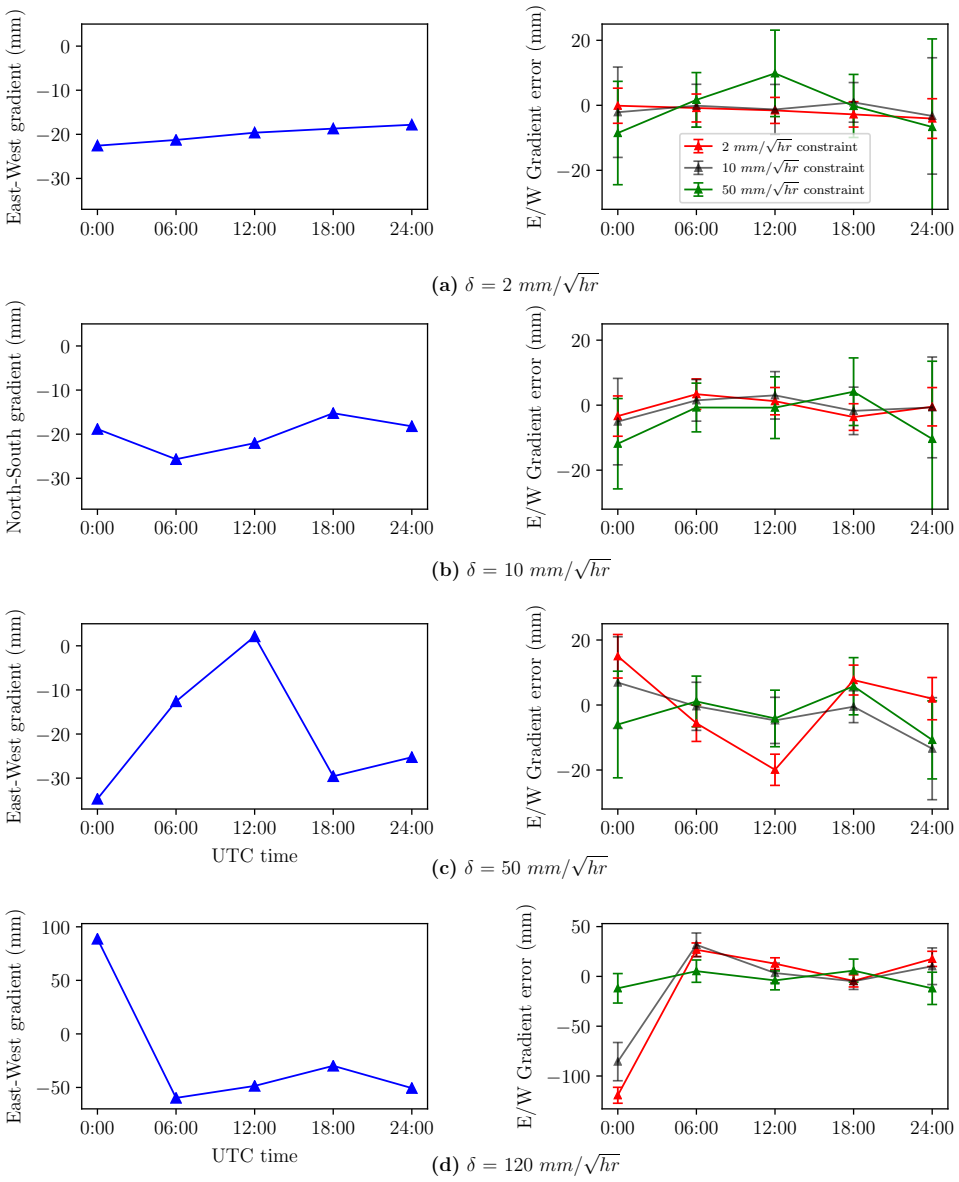

(a) $\delta = 2\ mm/\sqrt{hr}$

(b) $\delta = 10\ mm/\sqrt{hr}$

(c) $\delta = 50\ mm/\sqrt{hr}$

(d) $\delta = 120\ mm/\sqrt{hr}$

Figure 5.4: The simulated East-West tropospheric gradients for ALIC (left) and the estimation errors in recovering the simulated values (right) when choosing the process noise level of the first-order Gauss-Markov process used for the simulation as (**a**) 2, (**b**) 10, (**c**) 50, and (**d**) 120 $mm/\sqrt{hr}$. The colours of the error bars on the right subplots depict the process noise level used in forming the variance-covariance matrix of the ZWD parameters: red is a tight constraint of 2 $mm/\sqrt{hr}$, black is a standard constraint of 10 $mm/\sqrt{hr}$, and green is a loose constraint of 50 $mm/\sqrt{hr}$. The error bars display the 1-sigma uncertainty of the estimates. Note the change of scale for Figure 5.3d.

5.3 Stable tropospheric conditions in Antarctica

The dry and stable conditions in Antarctica (as observed e.g. in Figure 5.1) make this region an ideal area to study whether tightening the temporal constraints on tropo-

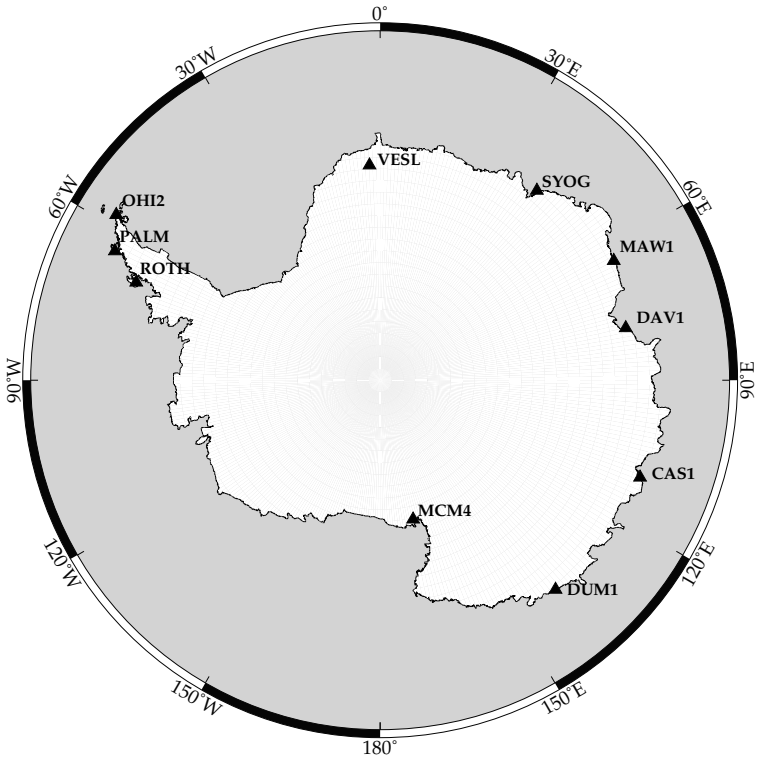

Figure 5.5: The Antarctic GPS stations included in the analyses for studying the impact of small process noise levels.

spheric parameters is able to improve the solutions in atmospheric conditions when the tropospheric delays do not drastically change in time. We processed GPS data over January 2012 for a network of 23 stations well distributed longitudinally in the southern hemisphere that includes a set of Antarctic sites shown in Figure 5.5. The locations of all the 23 stations used in this experiment along with the equipment used for the stations are listed in Appendix A, Table A.3. Like all other experiments in this study, we started the GPS processing by using the models listed in table 2.1. We also derived an empirical site-specific model (ESM) using the post-fit phase residuals of a standard solution, and carried out a second solution with the ESM applied. We then based our results on the ESM-applied solution, although the solutions without implementing the ESM led to the same conclusions about the use of process noise levels.

Using the tropospheric zenith wet delay and horizontal gradient estimates from a standard ESM-applied GPS analysis, we calculated the maximum hourly variation of ZWD and horizontal gradient parameters for all the stations in the network and for each day of observation. We used Equation 5.4 below to compute the maximum

hourly variation (δ_{max}) for each day:

$$\delta_{max}^2 = \frac{1}{\Delta t} \max_{2 \le i \le N} (y_i - y_{i-1})^2 \tag{5.4}$$

where Δt is the time interval between the parameter estimates (2 hr for ZWD and 6 hr for gradients), N is the number of estimates over a day (13 for ZWD and 5 for gradients), and y_i is the ith data point.

To show how different the levels of tropospheric variations are between the stations in the Antarctica and other stations in lower latitudes, Figure 5.6 shows the hourly variations of Equation 5.4 averaged over January 2012 for all the stations processed in the network. It is clear that the variations in both ZWD and horizontal gradients are much smaller in the Antarctic stations compared to the other sites. For zenith wet delays, for instance, the average variations in all the non-Antarctic stations is $\sim$20 $mm/\sqrt{hr}$ (same as the standard variation used in our GPS analyses), while the mean variation is below 5 $mm/\sqrt{hr}$ for the Antarctic sites. The smallest variations occur at MCM4, which is the station with the highest latitude, with a monthly mean variation of less than 3 $mm/\sqrt{hr}$ for all the three tropospheric components.

We used the daily maximum hourly variations of ZWD and gradient parameters calculated by Equation 5.4 for each site to generate calibrated process noise levels over different stations and days. We then carried out another experiment, whereby we used these variable process noise levels for zenith wet delays and horizontal gradients of the stations. All other models were held the same as the standard solution. Figure 5.7 shows a comparison of the repeatabilities of the position and tropospheric zenith delays between the solutions with the standard tropospheric process noise levels and calibrated noise levels. For the ZWD repeatabilities, we used the average WRMS of the overlap zenith delay estimates at day boundaries. It is evident that there is no significant change in the WRMS of any of the estimated components between the two solutions, with some parameters being slightly improved in terms of WRMS for some stations, but some parameters being degraded. The mean reductions over all the Antarctic stations when using the calibrated process noise levels are only from 0.78 mm to 0.75 mm for the North WRMS, from 0.69 mm to 0.68 mm for the East WRMS, and from 7.68 mm to 7.65 mm for the ZWD WRMS, and the mean height WRMS of 2.4 mm does not change when using the variable noise levels. All the reductions in all the components are clearly insignificant.

We also investigated the tropospheric zenith delay estimates from the two solutions with standard and calibrated process noise levels, and discovered that there was no single epoch in any of the Antarctic stations over the processing period at which the difference between the zenith delay estimates from the two solutions exceeds the 1-sigma uncertainty of the zenith delay. In addition, we repeated the experiments with only calibrating for ZWD and only calibrating for horizontal gradients, and observed similar results. Moreover, we performed the same study without using an ESM to assess whether the calibrated process noise levels have any significant impact in the presence of site-specific errors, but obtained similar results as implementing

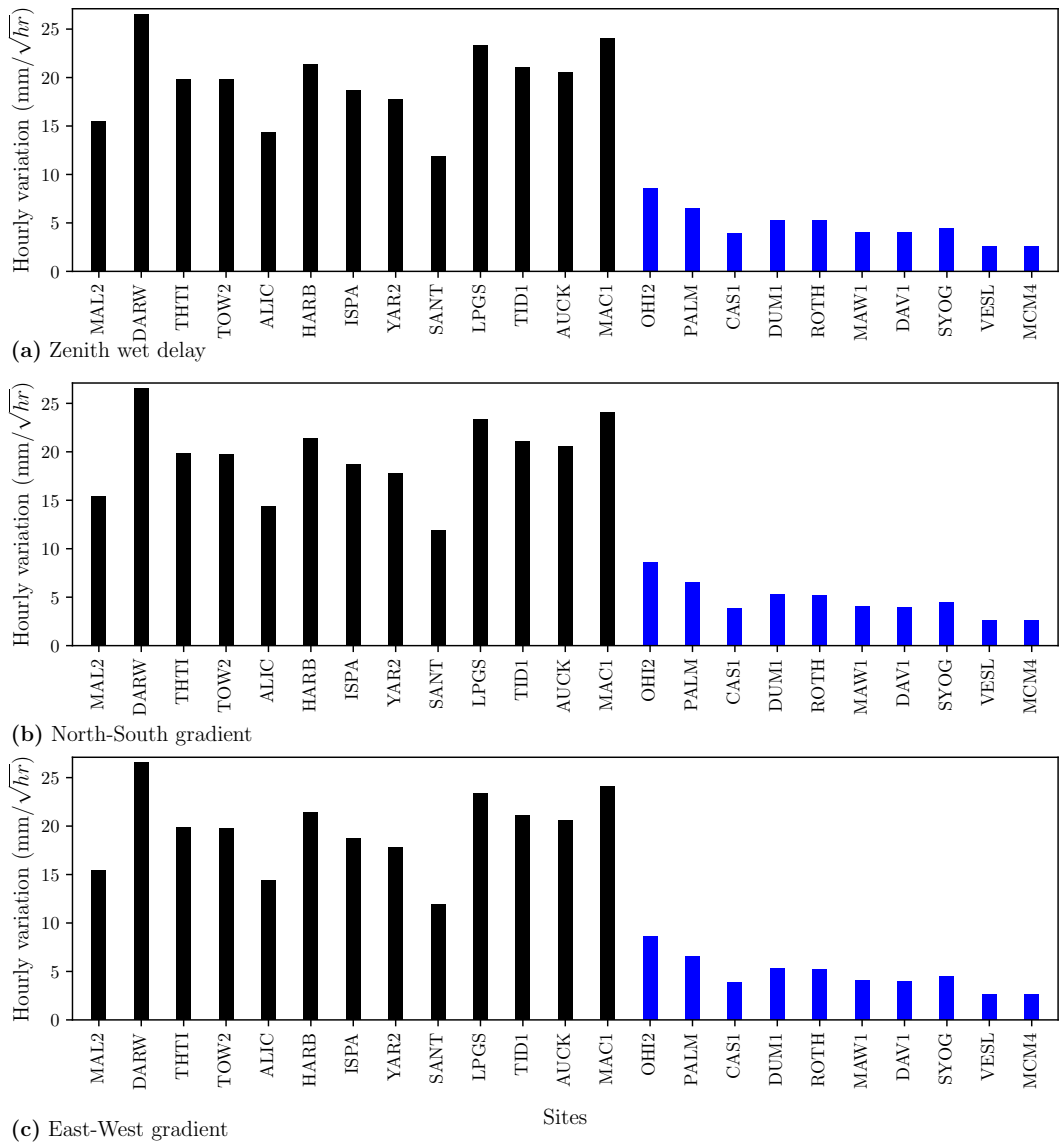

Figure 5.6: Monthly averaged maximum hourly variations of (**a**) zenith wet delay, (**b**) North-South gradient, and (**c**) East-West gradient for January 2012. The stations are sorted from the lowest to the highest latitudes. The sites in Antarctica are displayed in blue, and other stations are displayed in black.

an ESM.

The results from the Antarctic experiment are consistent with the outcome of the use of different process noise levels on simulated invariable tropospheric parameters, and show that allowing the ZWD and horizontal gradient parameters to largely vary by setting loose constraints does not introduce significant errors into the estimates. Therefore, there is no strong evidence that suggests the necessity of using temporal

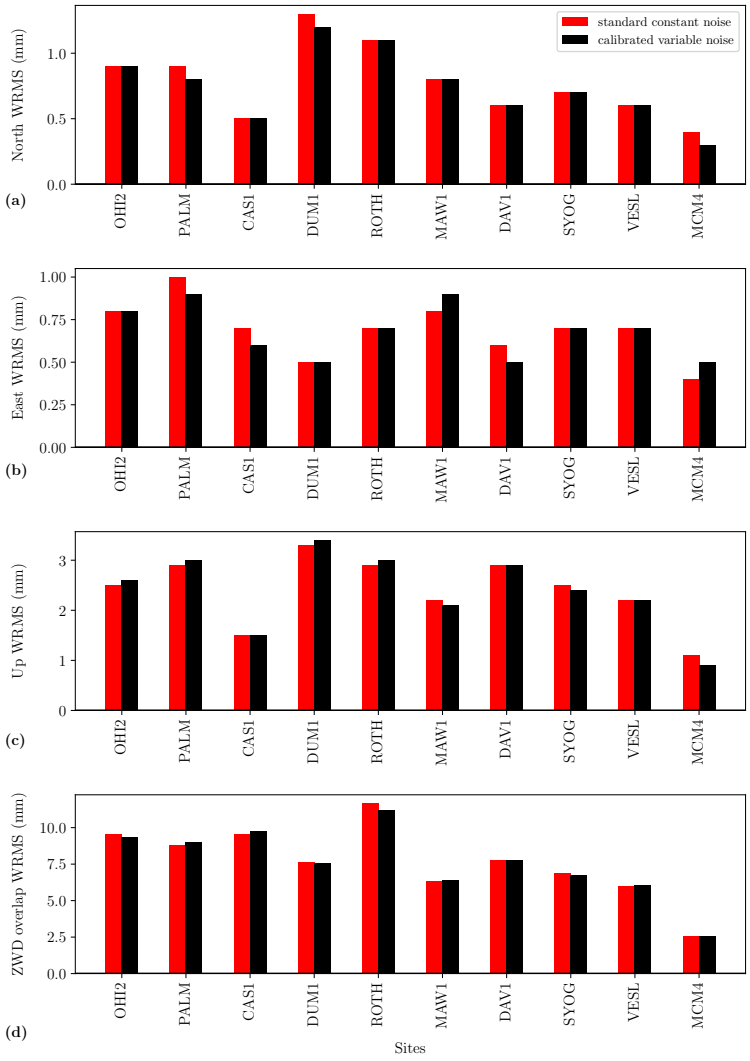

Figure 5.7: Comparison of the WRMS of different estimated parameters for the Antarctic stations in January 2012 between the solutions with standard constant (red) and calibrated variable (black) process noise levels for tropospheric zenith delays and horizontal gradients: (**a**) North WRMS, (**b**) East WRMS, (**c**) height WRMS, and (**d**) mean ZWD overlap WRMS at day boundary estimates.

constraints for estimating the tropospheric components, as long as a piecewise linear function is used for temporal modelling of the delays. The default standard constraints of 20 $mm/\sqrt{hr}$ for ZWD and 10 $mm/\sqrt{hr}$ for horizontal gradients appear to be loose enough for most atmospheric conditions (see e.g. Figures 5.1 and 5.6). There are, however, stations that may experience larger variations than these standard values, like the station in Darwin (DARW) that has a monthly mean value of over 25 $mm/\sqrt{hr}$ for the maximum hourly variation of the zenith wet delay (Figure 5.7a). The variations of the horizontal gradients of some of the stations in Figure 5.7 are also

larger than the standard 10 $mm/\sqrt{hr}$. Therefore, it is important to study whether the default constraints on the tropospheric parameters are too tight to allow large variations for the stations with more turbulent atmospheric conditions. In the next section, we perform an investigation on the use of calibrated temporal constraints in the Australian/Pacific stations of Figure 2.2 where there are larger tropospheric variations.

5.4 Turbulent tropospheric conditions

Tropospheric moisture content is not always as stable as in the Antarctic region. The water vapour content in the atmosphere varies temporally in mid-latitude and equatorial regions (as observed e.g. in Figure 5.1a and b). In Chapter 3, we performed two years of analyses (with and without an ESM) on the experiment of Figure 2.2 for 2011 and 2012. Here, using the ZWD estimates from the analysis with the implementation of an ESM, we calculated the maximum hourly variations of tropospheric zenith wet delays for each station and each day during the whole two-year period using Equation 5.4, which are displayed in Figure 5.8. We also calculated the percentage of the days when the maximum hourly variations were less than 10, 10-20, 20-30, 30-40 and more than 40 $mm/\sqrt{hr}$, shown in Table 5.1. The spatial and temporal changes in the variability of the tropospheric delays is evident. While higher-latitude stations in e.g. Alice Springs, Ceduna, Tidbinbilla, and Yarragadee generally experience consistently low variabilities, some equatorial stations like BAKO, DARW, GUAM and MAJU encounter larger variabilities than the typical 20 $mm/\sqrt{hr}$ at many of the days throughout 2011-2012. Also in stations with usually stable atmospheric conditions, the variabilities change over time. Such variations can be seen e.g. for YAR2 at Yarragadee or CEDU in Ceduna, South Australia.

To investigate whether the default temporal constraints of 20 $mm/\sqrt{hr}$ for ZWD and 10 $mm/\sqrt{hr}$ for horizontal gradients (Table 2.1) prevent changes in the tropospheric parameters by over-constraining these parameters, we performed an analysis with calibrated ZWD and horizontal gradient process noise levels. We concluded in the previous section that tightening the temporal changes of the tropospheric parameters when we know a priori that these parameters have small variabilities does not significantly alter the solutions compared to when using the default constraints; therefore, we set a minimum process noise level equal to the default constraints of Table 2.1 to avoid the risk of over-constraining the parameters. In other words, for a given station, a given day and a given parameter (ZWD or horizontal gradient), we set the maximum hourly variation of the parameter for that day (using Equation 5.4) as the process noise level only when this maximum variation is larger than the default constraints of Table 2.1. When the maximum hourly variation is smaller than the default constraint, we keep using the default value for the process noise level. Except for the tropospheric process noise levels, all other models and settings are the same as those mentioned in Table 2.1 and used for the ESM-applied analysis in Chapter 3. In this calibrated analysis, we used the same ESMs as in the ESM-applied

Station	Percentage of days with maximum hourly ZWD variation of					
	< 10	10-20	20-30	30-40	> 40	$mm/sqrt(hr)$
ALIC	55.0%	32.3%	9.1%	3.2%	0.4%	
ASPA	4.8%	53.2%	31.2%	8.1%	2.7%	
AUCK	26.5%	41.9%	18.2%	7.5%	5.9%	
BAKO	3.2%	50.0%	33.2%	10.2%	3.3%	
CEDU	36.8%	39.8%	15.0%	5.8%	2.6%	
COCO	8.7%	54.6%	27.3%	6.8%	2.6%	
CUSV	10.4%	54.6%	27.8%	5.1%	2.0%	
DARW	11.0%	45.9%	30.3%	10.2%	2.5%	
GUAM	3.7%	43.2%	31.6%	15.2%	6.4%	
HOB2	27.8%	41.6%	19.6%	7.0%	4.1%	
KARR	38.1%	37.3%	17.5%	5.0%	2.2%	
KIRI	9.1%	47.0%	29.6%	10.2%	4.2%	
KOUC	13.6%	59.0%	21.4%	4.7%	1.4%	
LAE1	8.4%	60.5%	27.8%	2.7%	0.5%	
LAUT	7.8%	54.6%	26.1%	9.4%	2.1%	
MAJU	3.4%	39.2%	37.0%	13.5%	6.9%	
MCIL	9.7%	55.5%	24.8%	6.8%	3.2%	
NAUR	11.9%	50.4%	27.3%	6.9%	3.4%	
NIUM	8.7%	55.7%	26.4%	6.3%	2.9%	
NTUS	7.2%	65.3%	22.5%	4.3%	0.8%	
PIMO	7.5%	52.3%	29.1%	8.4%	2.7%	
PNGM	7.7%	59.1%	26.4%	5.1%	1.7%	
POHN	4.3%	43.3%	37.3%	12.1%	3.0%	
SA39	10.2%	46.8%	29.6%	10.6%	2.8%	
SA40	8.9%	51.0%	27.8%	8.9%	3.3%	
SA42	9.7%	56.5%	28.2%	4.7%	0.9%	
TID1	28.8%	48.6%	15.7%	3.7%	3.2%	
TOW2	16.7%	57.8%	18.1%	5.8%	1.6%	
TUVA	3.9%	41.5%	33.8%	14.2%	6.6%	
XMIS	16.9%	60.2%	19.1%	3.1%	0.7%	
YAR2	32.7%	42.2%	16.9%	5.6%	2.5%	

Table 5.1: Statistics on the maximum hourly variation of ZWD

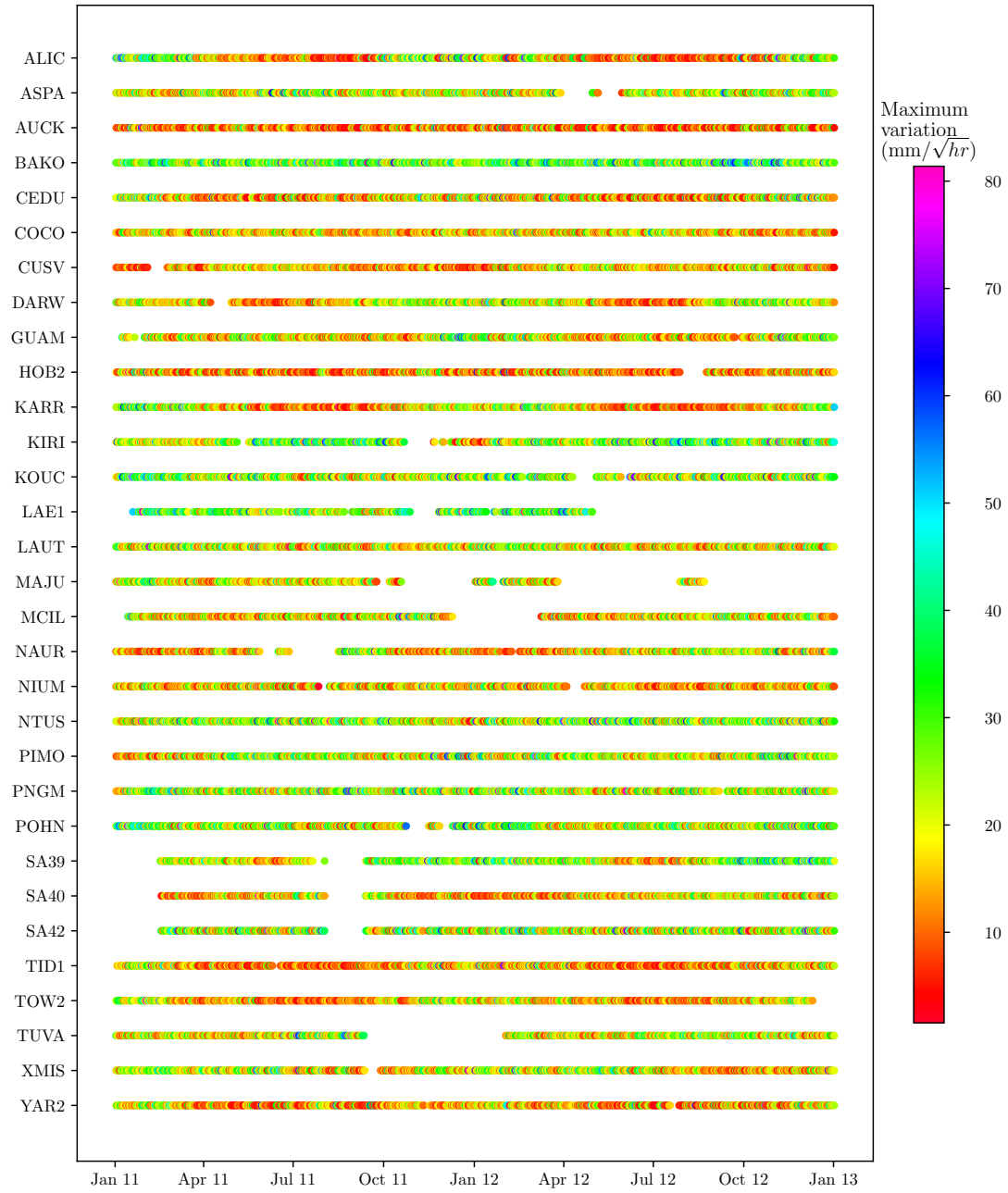

Figure 5.8: Maximum hourly variation of ZWD for different stations in the experiment of Figure 2.2.

solution of Chapter 3, used an elevation cut-off of 3°, and performed the analysis for the whole period of 2011-2012.

Figure 5.9 shows the monthly WRMS of the position components averaged over all the stations in the network using the solution with the default tropospheric pro-

cess noise levels and the calibrated temporal constraints for the tropospheric components. On average, there are small reductions in height WRMS for the first few months of 2011 and last few months of 2012, while the differences in height WRMS between the two solutions are very small in the other time periods. The reductions in height WRMS as a result of using calibrated process noise levels reach up to 2.3% (from 5.86 mm to 5.73 mm) in September 2012, while the maximum degradation in the height WRMS due to the use of calibrated noise levels is only 0.9% (from 4.92 mm to 4.97 mm) in June 2012. For the horizontal components of the positions, using the calibrated process noise level sometimes leads to degraded scatters, and sometimes leads to improved repeatabilities. For the North component, the largest improvement is 3.1% in February 2012, and the largest degradation is 1.5% in August 2012. For the East component, the largest improvement by the calibrated noise levels is 3.3% (March 2011) and the largest degradation is 4.0% (May 2012). However, the best indicator for the quality of the ZWD estimates is the height component, since the height is largely correlated with the zenith delay parameters.

To better understand how the height scatter is affected by the use of calibrated process noise levels for the tropospheric parameters, we calculated the mean of the monthly height WRMS values for each station over the whole two-year period. We then computed the reductions in the mean height WRMS when using calibrated process noise levels compared to when using the default temporal constraints for ZWD and horizontal gradient parameters (Figure 5.10). The reductions shown in Figure 5.10 are in terms of the square root of the mean variances of the monthly height time series. On average for the whole two years, 20 stations observe improved repeatabilities by using calibrated noise levels, while 11 stations have higher scatters when using the calibrated noise levels. However, the magnitude of the degraded repeatabilities are generally much smaller than the magnitude of the improvements. Except for SA39 (which has a degradation of 1.1 mm), none of the stations observe height WRMS degradation of more than 1 mm, while 8 stations have reductions of more than 1 mm in height scatter. The mean degradation in the stations with worsened height scatter is 0.5 mm, but the mean reduction in improved stations is 0.9 mm. The largest improvement occurs for the station MAJU (1.9 mm).

The results in Figures 5.9 and 5.10 show that on average, the height WRMS appears to be generally improved using the calibrated FOGM noise levels; however, for a few stations on select days, the use of calibrated noise levels appears to slightly degrade the results. Nevertheless, it is clear that level of improvement and number of sites showing improvement is greater than number of sites showing a degradation.

Figure 5.11a shows the maximum differences between the ZTD estimates from the solution with default process noise levels and the solution with calibrated noise levels over the whole period of 2011-2012. The difference in the ZTD made by using calibrated noise levels reaches a maximum value of up to about 48 mm, which is equivalent to a significant amount of $\sim$7 mm in precipitable water. While such amounts are significantly large, it is also important to note how often such cases occur. Figure 5.11b shows the number of ZTD differences between the two solutions with default and calibrated process noise levels which are larger than the 1-sigma

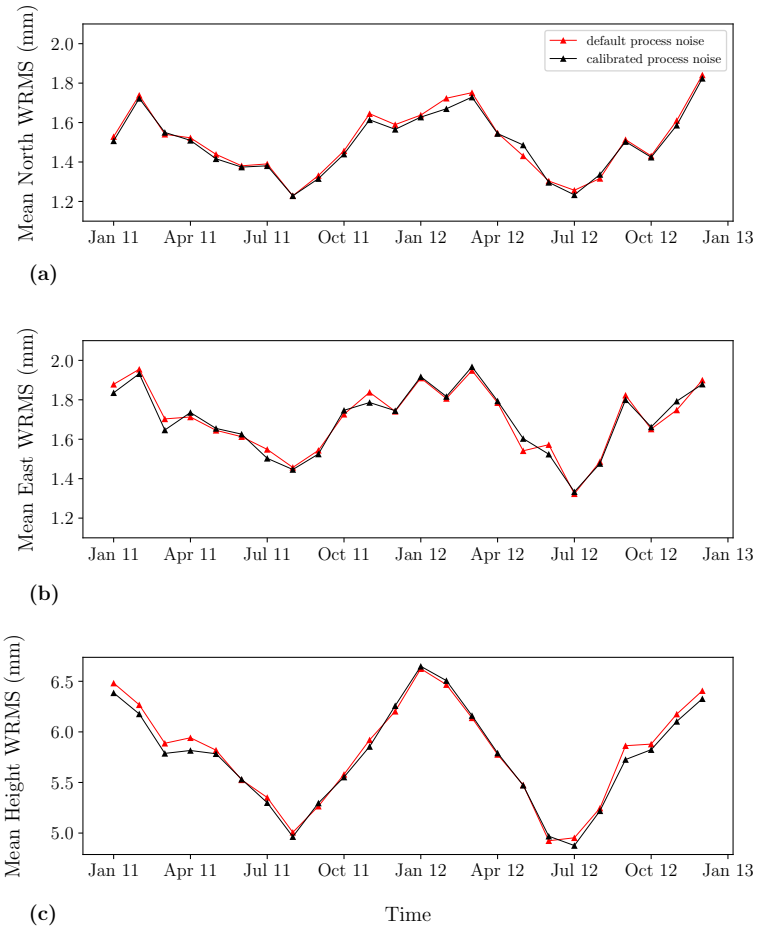

Figure 5.9: Monthly WRMS averaged over all the stations for (a) North, (b) East and (c) Up components of the positions when using the default (red) and calibrated (black) process noise levels for the temporal variations of the tropospheric zenith wet delay and horizontal gradients.

uncertainty level of the difference in ZTD. The station BAKO is the site with the highest number of occurrences of significant ZTD differences (differences larger than the 1-sigma uncertainty) with 86 occurrences over the two years. Recall that BAKO is one of the stations with improved height scatter (Figure 5.10) due to the use of calibrated process noise levels, which shows that the looser process noise levels are likely to have led to more accurate ZTD estimates for this station. After BAKO, SA39 and TUVA observe the highest number of significant ZTD differences with over 30 occurrences. SA39 is one of the few stations with degraded mean height WRMS, which indicates that the calibrated process noise levels may have led to less accurate ZTD estimates for this station. Other stations in the network also see some occurrences of significant ZTD differences up to just over 20 occurrences. Studying BAKO as the station with the largest significant ZTD differences made by relaxing the tropospheric process noise levels using the calibrated levels is interesting to have

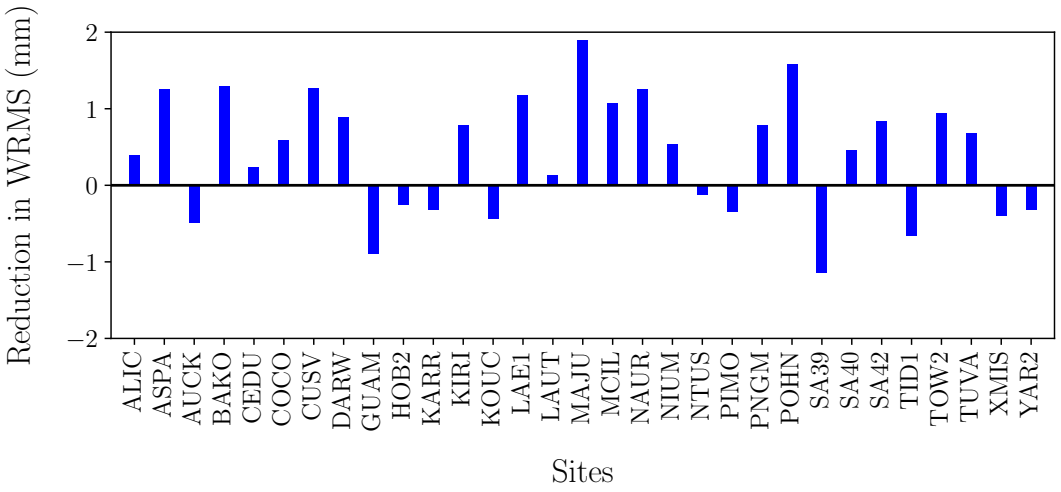

Figure 5.10: Reductions in the mean monthly WRMS of height components over 2011-2012 for different stations when using calibrated process noise levels for tropospheric zenith wet delays and horizontal gradients compared to when using default temporal constraints for the tropospheric parameters. Positive values represent improvements in the height repeatabilities when using calibrated noise levels, and negative values represent degradations.

a better insight into the cause of such differences. The following section will discuss the station BAKO, located in Jakarta, Indonesia.

5.4.1 Tropospheric variations of the station BAKO

After investigating the tropospheric estimates in BAKO, it was found that most of the ZTD differences made by using the calibrated process noise levels were due to the changes made in the tropospheric horizontal gradients, specifically the North-South gradients. Figure 5.12 shows the estimated horizontal gradients of the tropospheric delay in this station for 2011-2012 when using the calibrated process noise levels. While there are occasionally large East-West gradients estimated (Figure 5.12b), the magnitude of many of the estimated North-South gradients are unprecedented, reaching up to over 300 mm (when mapped to 10° elevation). The large North-South gradients prevail mostly during the relatively drier period of April to November. Over the most humid months of January and February, the estimated horizontal gradients are the smallest. Also, the large North-South gradients are typically negative, meaning that the tropospheric refractivity is generally larger in the south of the station than in the north of it. This asymmetry can also be seen in Figure 5.13, which shows the frequency histogram of the estimated North-South gradients separated into normal and abnormal days; normal days are the days when the tropospheric zenith delay discrepancies between the solutions with default and calibrated process

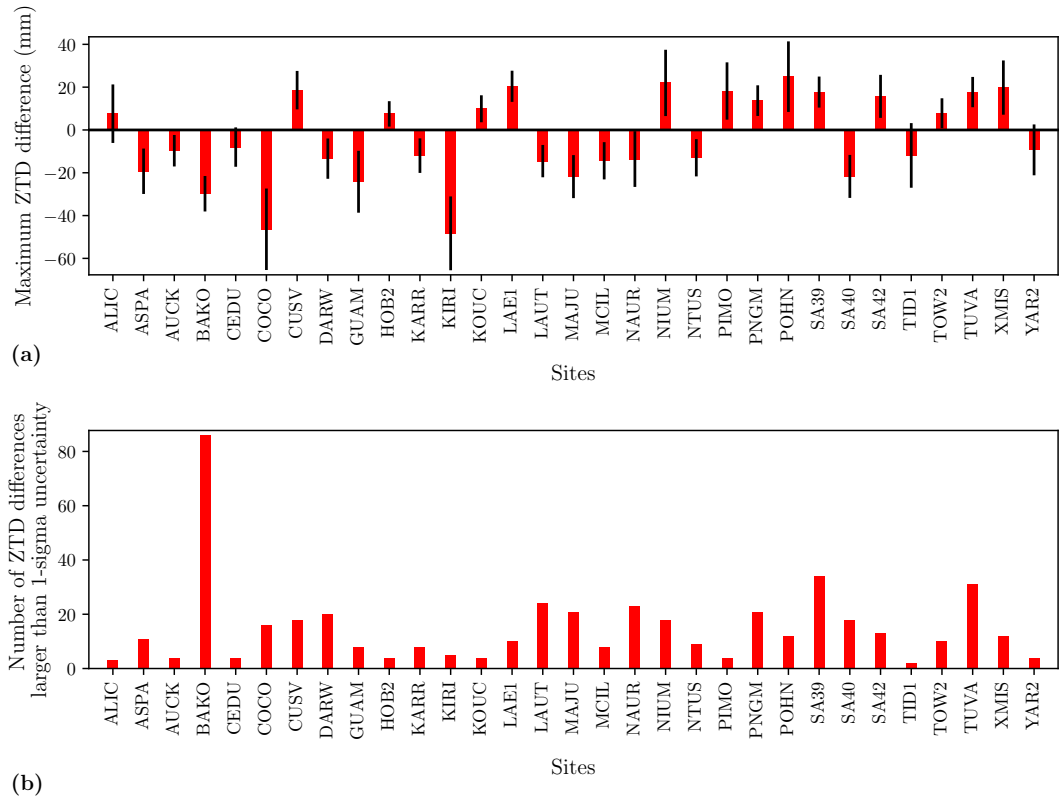

Figure 5.11: (**a**) Maximum differences between the tropospheric zenith delay estimates and (**b**) the number of ZTD differences larger than the 1-sigma uncertainty level, between the two solutions with default and calibrated process noise levels for tropospheric parameters over 2011 and 2012. Error bars in (**a**) are the 1-sigma uncertainties of the maximum ZTD differences.

noise levels are within the 1-sigma uncertainty levels, and the abnormal days are the days when these differences are larger than the 1-sigma uncertainty levels.

The skewed histogram of Figure 5.13b for the abnormal days (when the ZTD differences due to relaxing the tropospheric process noise levels are significant) and its comparison with the histogram for normal days (Figure 5.13a) show that the ZTD differences made by the calibrated noise levels for BAKO are occasionally due to the larger North-South gradients estimated when relaxing the noise levels on the gradient parameters.

We examined the tropospheric zenith delay estimates for BAKO, and discovered that the period of September to November 2012 observed a high number of occurrences of significant ZTD differences between the solutions with standard and calibrated process noise levels, which are occasionally due to the differences made in the estimated North-South gradients as seen in Figure 5.12a. We selected the period between 6 September and 15 November in 2012, and generated height time series for this time period. During this 71-day interval, there were 33 occasions distributed

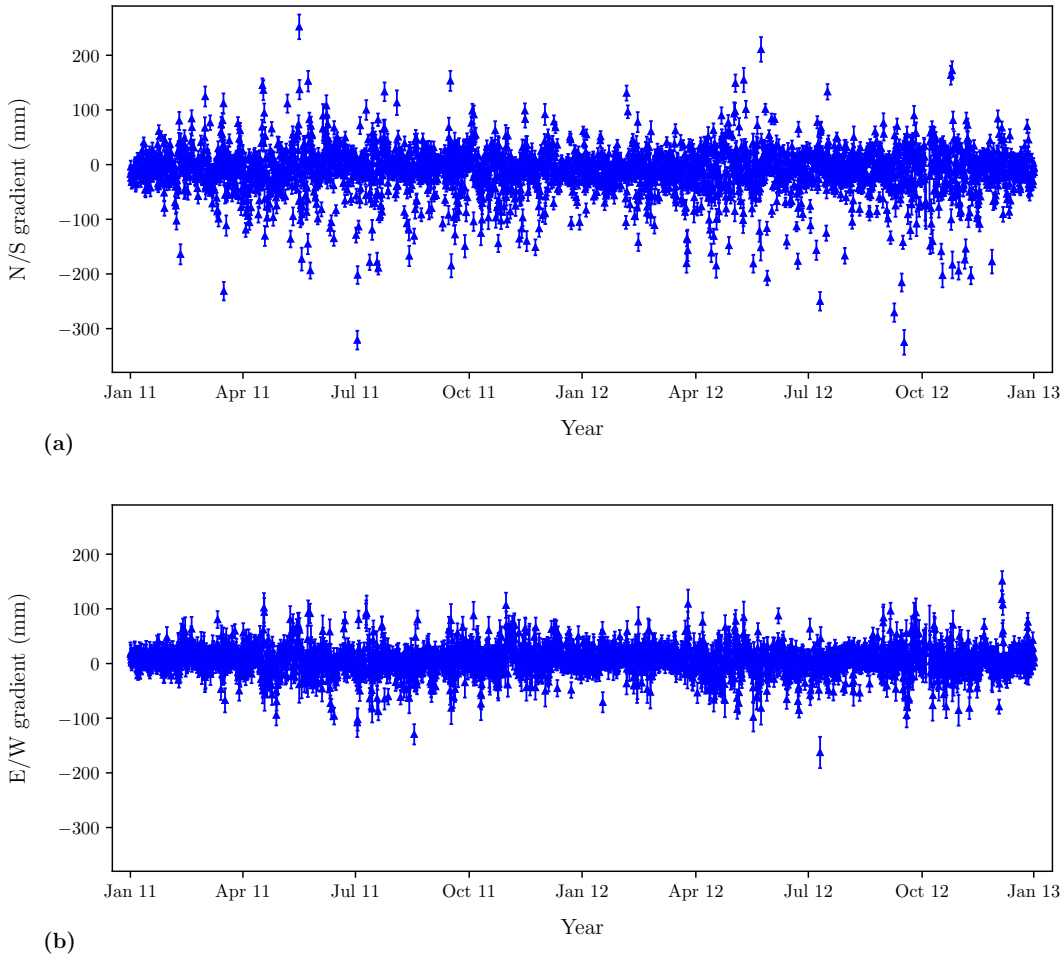

Figure 5.12: (**a**) North-South and (**b**) East-West gradient delays at 10° elevation for BAKO over 2011 and 2012 when using calibrated process noise levels for tropospheric parameters. Error bars are the 1-sigma uncertainties of the estimates.

over 16 individual days when the ZTD estimates were different between the two solutions with default and calibrated process noise levels by larger than the 1-sigma uncertainty level of the estimate differences. On average for these 16 days, the daily maximum estimate of the North-South gradients had a magnitude of 79.2 mm when using the default noise levels, while the magnitude of the mean daily maximum North-South gradient estimates was 125.4 mm when using the calibrated process noise levels. Figure 5.14 displays the height time series for BAKO during the above time period. Considering the days when the ZTD differences between the two solutions are larger than the 1-sigma uncertainty levels (red colours in Figure 5.14), some days (in particular day of year 259 and 310) show larger deviations from the mean

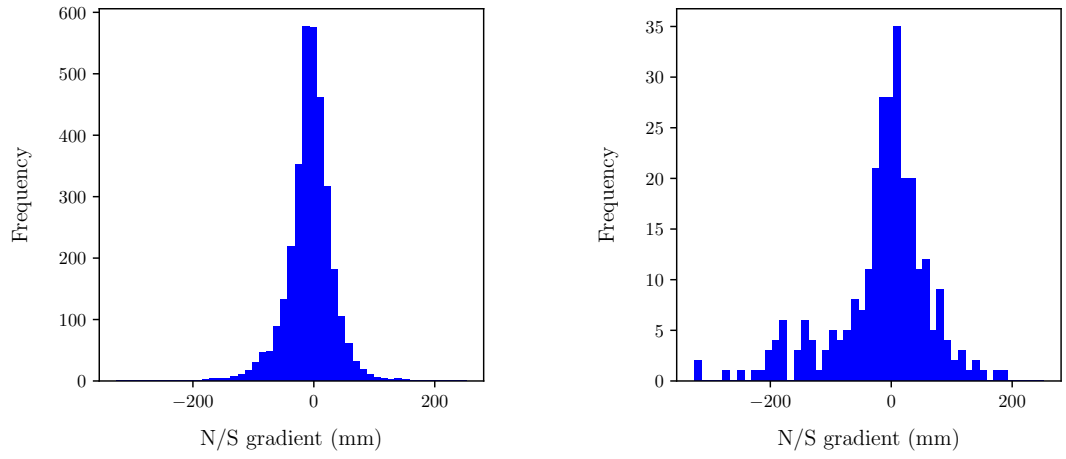

(a) Normal days **(b)** Abnormal days

Figure 5.13: Frequency histogram of the estimated North-South gradients in BAKO for (**a**) normal and (**b**) abnormal days over 2011-2012. Normal days are the days when the tropospheric zenith delay discrepancies between the solutions with default and calibrated process noise levels are within the 1-sigma uncertainty levels, and the abnormal days are the days when these differences are larger than the 1-sigma uncertainty levels.

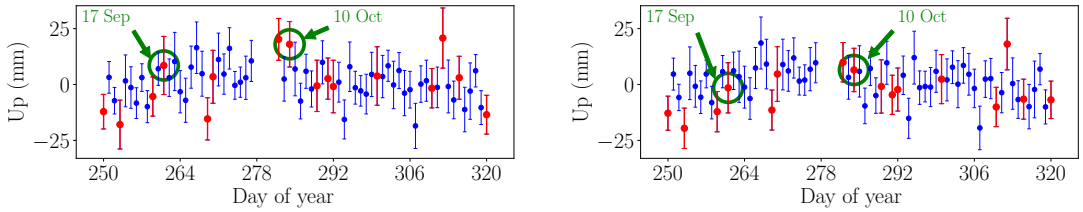

(a) Default noise (WRMS = 8.2 mm) **(b)** Calibrated noise (WRMS = 7.8 mm)

Figure 5.14: Time series of the vertical positions for site BAKO and for the period of 6 September 2012 to 15 November 2012 when using (**a**) the standard process noise levels, compared to when using (**b**) the calibrated noise levels for the tropospheric parameters. Days coloured in red are the days when the differences in tropospheric zenith delay estimates between the two solutions are larger than the 1-sigma uncertainty of the ZTD difference. 10 October and 17 September are circled in green; these dates will be investigated further in sections 5.4.1.1 and 5.4.1.2.

height when using the calibrated noise levels, but more days show smaller height deviations (e.g. day of year 261, 282, 284 and 320). On average, the WRMS of the vertical position time series is reduced from 8.2 mm to 7.8 mm by using the calibrated process noise levels for the tropospheric parameters instead of using the standard noise levels.

In the following sections, we look at the estimated tropospheric parameters on two different days: 10 October 2012 (day of year 284) when the estimated height of the station appears to have been improved by using the relaxed calibrated process noise levels, and 17 September 2012 (day of year 261) when there is no apparent improvement in the estimated height. For the following sections when we study individual days, we estimate the horizontal gradients every two hours to gain a better understanding of their variations throughout the day. Also for the calibrated solutions, we only use relaxed process noise levels for the horizontal gradients and still use the standard noise levels for the zenith wet delays in order to separate the effect of the relaxed constraints of the ZWD from the effect of the gradient constraints. However, some statistics of when the calibrated ZWD constraints are also used will be given when relevant.

5.4.1.1 10 October 2012

The estimated horizontal gradients and tropospheric zenith delays using both standard and calibrated process noise levels are displayed in Figure 5.15 for the station BAKO on 10 October 2012. For this day, the calibrated process noise level is 31 $mm/\sqrt{hr}$ for the horizontal gradient parameters. By loosening the process noise levels of the horizontal gradients using the calibrated noise levels, both North-South and East-West gradients are allowed to have much larger variations during the day. The estimated North-South gradient by the calibrated constraints (Figure 5.15a; black error bars) starts to grow in magnitude (with a direction towards the south) from 10:00 UTC, reaches a maximum of about -130 mm (when mapped to 10°) at 12:00 UTC and returns to normal conditions from 16:00 UTC. The standard process noise level of 10 $mm/\sqrt{hr}$ does not allow such variations. Similar variations are observed for the East-West gradients for this day (Figure 5.15b), which reach their maximum of about -130 mm at 14:00 UTC when using the relaxed constraints. These large discrepancies between the two solutions with different allowed variations for horizontal gradients result in significant differences in the estimated zenith wet delays (Figure 5.15c). At 12:00 UTC, the default gradient constraints (red error bars) result in an underestimation of 23.2 mm for zenith wet delay (equivalent to 3.82 mm of precipitable water), which is well above the 1-sigma uncertainty level ($\sim$5 mm for ZWD and $\sim$1 mm for PW). When relaxing the zenith wet delays too, the differences reach about 4.5 mm for precipitable water estimates (not shown here). This amount of difference for PW is very significant and needs to be considered when planning for assimilation of the GPS tropospheric delays into a numerical weather prediction model. On Figure 5.15c, we also show the estimated zenith wet delays when using a directional gradient parametrization using both standard (blue) and relaxed (green) process noise levels for the horizontal gradients. Similar behaviour as the planar model is observed when changing the process noise levels. The relaxed constraints on horizontal gradients result in much larger estimates of ZWD which are almost identical to the estimates by the planar model and relaxed gradient constraints at 12:00 UTC. However, when using the directional gradient parametrization and the

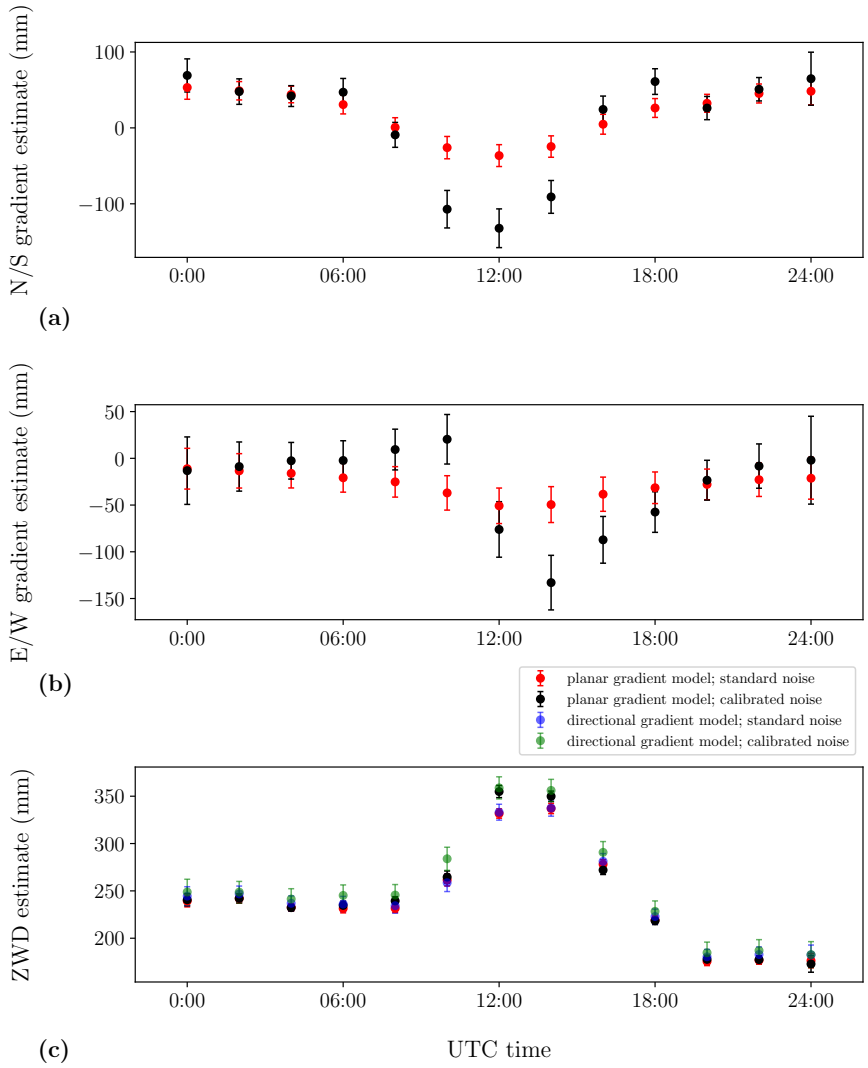

Figure 5.15: The estimates of the tropospheric parameters for BAKO on 10 October 2012 using the gradient model/process noise level of planar/standard (red), planar/-calibrated (black), directional/standard (blue) and directional/calibrated (green): (a) North-South gradients, (b) East-West gradients, and (c) zenith wet delays. Error bars are the 1-sigma uncertainties of the estimates. The calibrated process noise levels are only applied to the horizontal gradients (and not to the zenith delays).

relaxed gradient constraints, the estimated ZWD starts to differ from the estimated ZWD using standard gradient constraints earlier than when using the planar model (from 10:00 UTC).

To better understand the tropospheric conditions of BAKO on 10 October 2012, the estimated horizontal gradient delays are displayed as sky plots in Figure 5.16 using both planar and directional gradient models. The reason for underestimation of the zenith wet delays at 10:00 UTC by the planar gradient model compared to the

directional model is immediately revealed by comparing the estimated tropospheric horizontal gradient delays between the two models. While the planar model (Figure 5.16a) suggests a linear change of tropospheric refractivity towards the south of the station at 10:00 UTC, the directional model (Figure 5.16b) suggests that except for the south-west of the station, the refractivity in almost every other direction around the station is smaller than the refractivity above the station; this increases the estimated zenith wet delay compared to when using the planar gradient model.

The above overestimation of positive gradients by the planar gradient model persists for the whole day. However, the general trend of the negative horizontal gradients are similarly estimated by both models. Horizontal planar gradients of about 60 mm (at 10° elevation) exist towards the equator at the beginning of the day (Figure 5.16a); this is the normal condition at site BAKO and is expected due to higher water vapour content at equator than at higher latitudes. Based on the planar gradient model (Figure 5.16a), a strong southward gradient of refractivity starts from about 10:00 UTC, rotates towards the south-west and reaches its maximum at 12:00 UTC, and then continues to rotate to the north-west and north until the end of the day when the horizontal gradients return to normal condition of equator-ward gradients. The event is interpreted slightly differently by the directional gradient model (Figure 5.16b). The normal conditions of the beginning and the end of the day are similar to the planar gradient estimates, although there are different rates of refractivity changes from the south to the north of the station offered by the directional model. While the planar model offers a linear change of about 60 mm from the south to the north of the station, the directional model suggests that the rate of horizontal changes of refractivity retards as we move to the north; the negative gradients in the south are estimated by the directional model to be about -80 mm, while the positive gradients in the north of the station are $\sim$40 mm. Based on the directional gradient model, strong negative gradients start to form since around 08:00 UTC in the north-east of the station, but not as strong positive gradients appear in the south. In fact there are only small positive gradients (of maximum $\sim$30 mm) estimated in the south-west starting from 10:00 UTC and disappearing at 16:00 UTC; compare this to the strong southward positive gradients of up to $\sim$160 mm in the south-west at 12:00 UTC as estimated by the planar model. However, the rotation of the horizontal directional gradients follows a similar pattern as the planar gradients; the strong negative gradients are initially in the north-east at 10:00 UTC, but gradually rotate to south-east and south by the end of the day.

To better understand the weather conditions on this day, we can also look at weather model data on this day. Figure 5.17 shows the specific humidity at surface on 10 October 2012 from the Australian Community Climate and Earth-System Simulator (ACCESS) weather model developed by the Australian Bureau of Meteorology. The regional domain of the ACCESS weather model is used for these data. While the latest version of the ACCESS regional model has a horizontal resolution of about 12 km, its horizontal resolution used to be about 37.5 km back in 2012. This is a limiting factor because 37.5 km is relatively coarse for our purposes; Although we use a 3° elevation cut-off angle, the number of signals arriving at elevation angles below 5° is

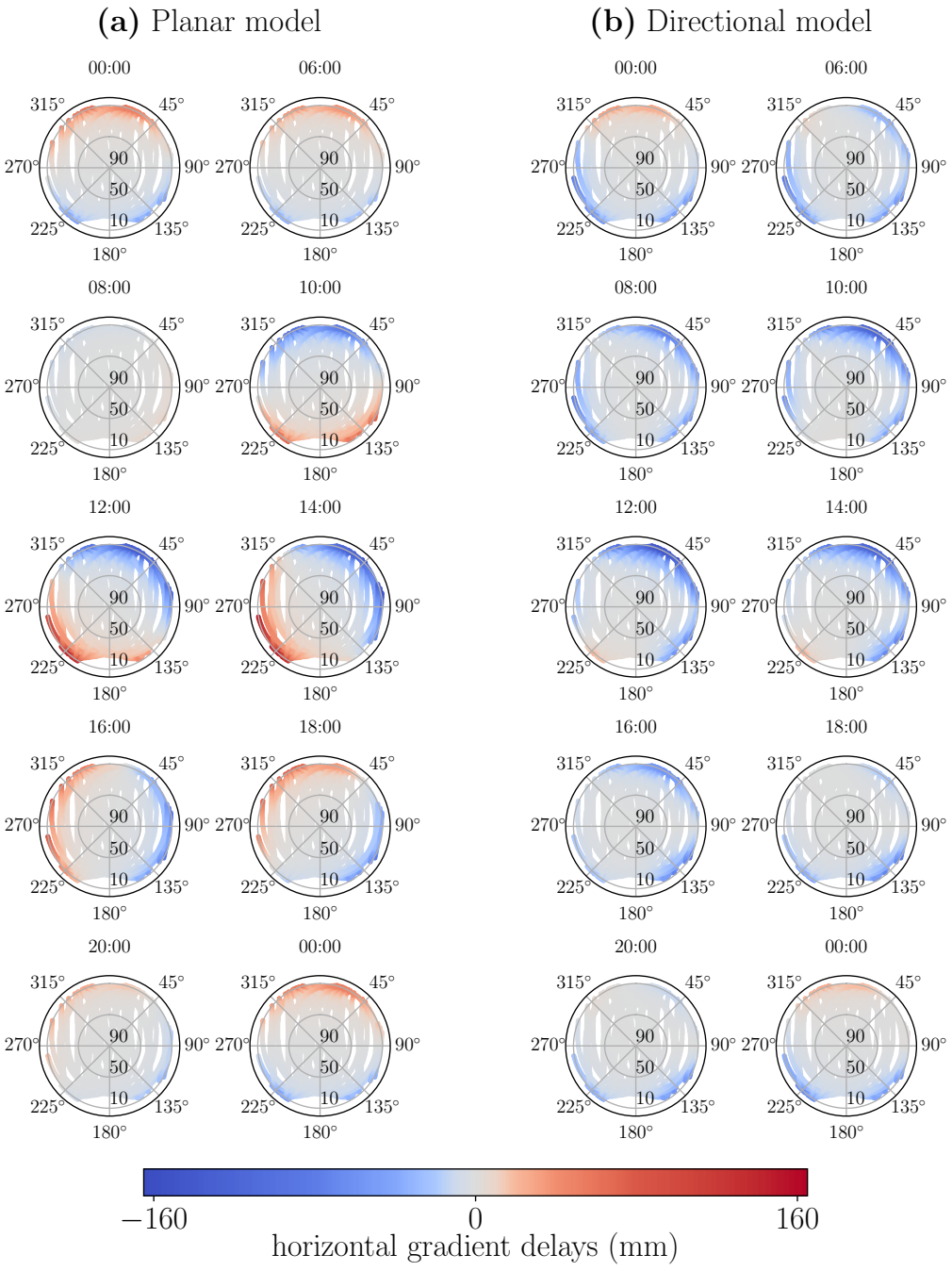

Figure 5.16: Horizontal gradient delays estimated at site BAKO on 10 October 2012 using (**a**) the conventional planar model, and (**b**) the directional model with 8 gradient estimation nodes. The relaxed calibrated process noise levels for horizontal gradients are used for both solutions. Some of the results at the beginning and end of the day (hours 2, 4, 6 and 22) are excluded to save page space. The horizontal gradients do not significantly vary at these epochs.

small, and the low-elevation observations are assigned much lower weights than the higher elevation observations.Considering a signal arriving at 3°, it scans horizontal distances of close to 200 km of the troposphere (assuming an approximate height of about 10 km for the tropopause layer below which most of the water vapour content exists); a signal arriving at 5° scans a horizontal distance of about 115 km, and a signal arriving at 10° horizontally scans only about 60 km of troposphere around the station. The 37.5 km resolution is therefore not a very high resolution for assessing the results, but still can provide us at least with a qualitative assessment of the event. For detailed information about the ACCESS model versions and domains, refer to https:http://www.bom.gov.au/australia/charts/about/about_access.shtml and the documents therein.

Comparing Figures 5.17 and 5.16, the specific humidity variations are consistent in a qualitative sense with the estimated horizontal gradients. While at the beginning of the day the specific humidity pattern is a typical pattern in which the moisture content is generally higher towards the equator, a patch of moisture gradually moves from the north of the station BAKO towards the station until 12:00 UTC when it starts to change direction towards west. At the end of the day, the specific humidity goes back to the normal situation. This change of attitude in the moisture content matches the change in the horizontal gradients observed in Figure 5.16: normal northward gradients at the beginning and end of the day, but increased tropospheric delay in BAKO at the middle of the day with respect to the north. This movement of a moisture patch towards BAKO, or in other words increase of the tropospheric delay above the station at the middle of the day, was also observed in Figure 5.15.

As discussed above for 10 October 2012 in BAKO, there are discrepancies between estimated horizontal gradients by the planar and directional models, with the most prominent differences being the overestimation of positive gradients in the south-west of the station by the planar model. This overestimation of positive gradients results in an underestimation of the ZWD at 10:00 UTC by $\sim$ 19 mm (equivalent to $\sim$3 mm in PW) as seen in Figure 5.15c. This shows that while it is important to allow enough variations for the horizontal gradients by relaxing the constraints, it is also important to use a more accurate gradient parametrization; while we used loose constraints for the horizontal gradients, the estimated ZWD at 10:00 UTC (Figure 5.15c) do not enlarge as long as we are using the planar gradient model, because the higher wet delay to be estimated in BAKO due to large negative gradients in the north-east is to some extent compensated by the large positive gradients estimated in the south-west (Figure 5.16a). Once we use the directional gradient model, the ZWD estimate at 10:00 UTC is amplified due to the strong negative gradients in almost all the directions around the station and close to zero gradients in the south-west (Figure 5.16b). Nevertheless, the use of relaxed process noise levels increases the ZWD estimates at 12:00 UTC whether using planar or directional model, and the estimates are almost identical to each other at this time epoch using either of the two models.

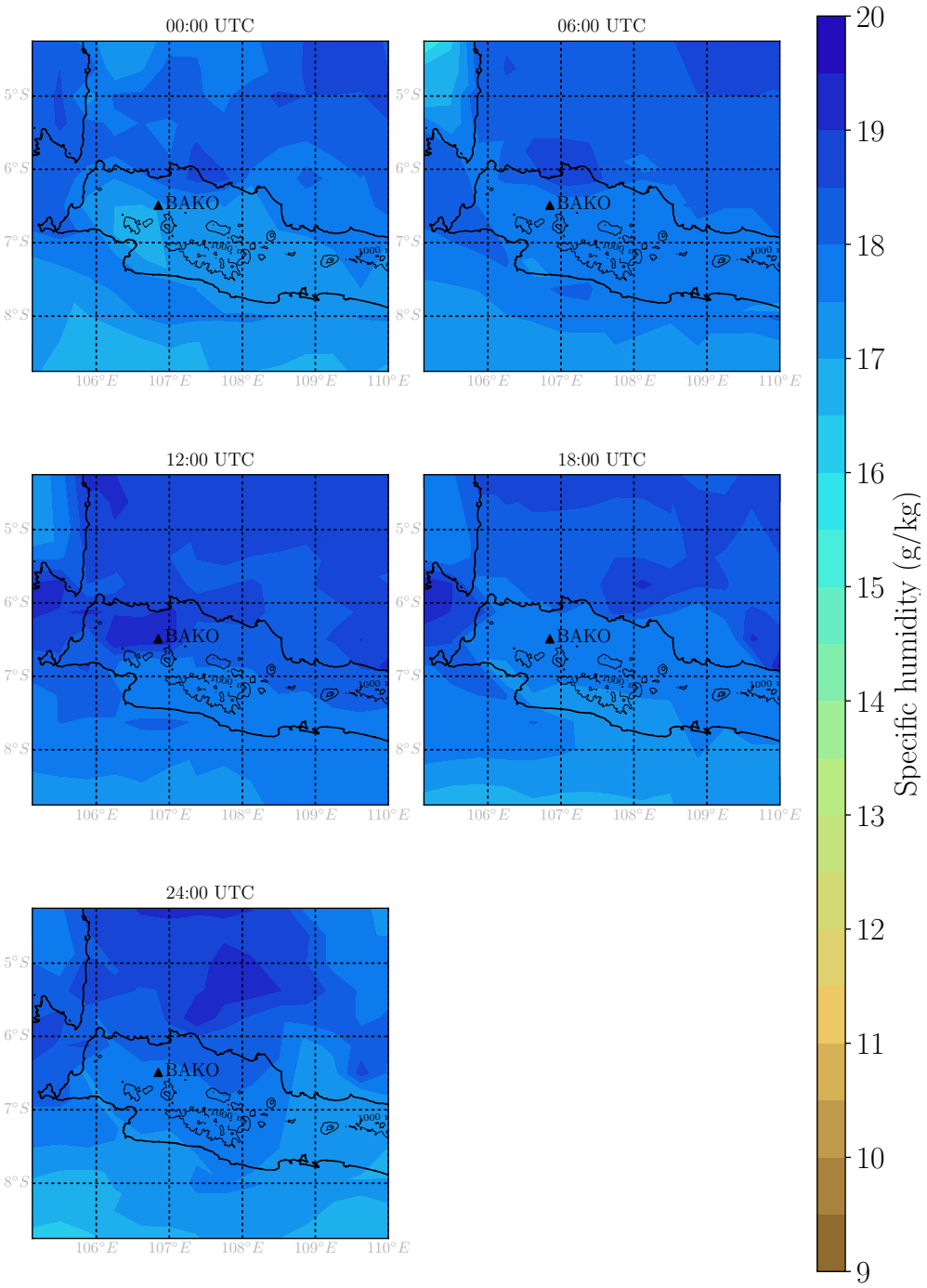

Figure 5.17: Surface Specific humidity from ACCESS weather model for 10 October 2012. GPS station BAKO is displayed as a triangle. The topography from GEBCO is depicted by contour lines every 1000 meters. Mount Pangrango, the dormant volcano in the south-east of the station, is about 3019 meters in height.

5.4.1.2 17 September 2012

17 September 2012 is another extreme case for BAKO. When relaxing the constraints on horizontal gradients by using the calibrated process noise levels of 32 $mm/\sqrt{hr}$, the estimated North-South gradients reach extremely large values of about -330 mm at 10° elevation (Figure 5.18a; black error bars). The sudden increase of negative North-South gradients from 08:00 UTC to 10:00 UTC (becoming almost four times larger, from ∼-90 mm to ∼-340 mm) is dubious. The resultant ZWD estimates at 10:00 UTC (Figure 5.18c; black error bars) differ from when using the standard process noise levels (red error bars in Figure 5.18c) by ∼43 mm (equivalent to ∼7 mm of precipitable water). When using a directional gradient model, however, the difference made in the ZWD estimates between the solutions with the relaxed and the standard constraints is only ∼13 mm (equivalent to ∼2 mm of PW). The looser constraints still trigger the directional gradient model to estimate larger zenith delays but not as large as the estimates by the planar gradient model.

A comparison of the estimated horizontal gradient delays between the solutions with planar and directional gradient model (both using relaxed process noise levels for horizontal gradients) is given in Figure 5.19. Unlike the case study of 10 October 2012 (Figure 5.16) where the planar gradient model largely overestimated positive gradients in the south of BAKO, the positive gradients estimated in the south of BAKO on 17 September 2017 are in fact also suggested to a large extent by the directional gradient model (Figure 5.19). Focusing particularly at 10:00 UTC for instance, the estimated positive gradients in the south of BAKO by the planar model reach values of around 300 mm (at 10° elevation), and the estimated positive gradients in the same direction by the directional model reach about 250 mm; this is a reduction of only ∼17%, compared to a ∼80% differences between the positive gradients of the two gradient models observed at 10:00 UTC of 10 October (cf. Figure 5.16 and the discussion therein). On the other hand, the negative horizontal gradients in the north of BAKO are largely overestimated by the planar gradient model. The northward horizontal gradients are estimated to be approximately -330 mm by the planar model, while their estimates by the directional model is -180 mm (a reduction of ∼45%). While the planar gradient model assumes a linear increase of tropospheric delays from north to the south of the station, the directional model offers a smaller rate of refractivity in the north of the station than in the south. The consequence is that the planar model suggests a wetter station since the zenith wet delay is assumed to significantly decrease when moving to the north of the station, while the directional model does not allow the station to be as wet because the reduction in the ZWD when moving to the north is assumed to occur with a smaller rate than the rate suggested by the planar model. This overestimation of ZWD by the planar gradient model is clear in Figure 5.18c.

The specific humidity from the ACCESS weather model for the above example is displayed in Figure 5.20. In this case, we cannot see the southward horizontal gradients observed in Figure 5.19; the humidity is higher towards the north for the whole day. However, one may notice the movement of the moisture content from the

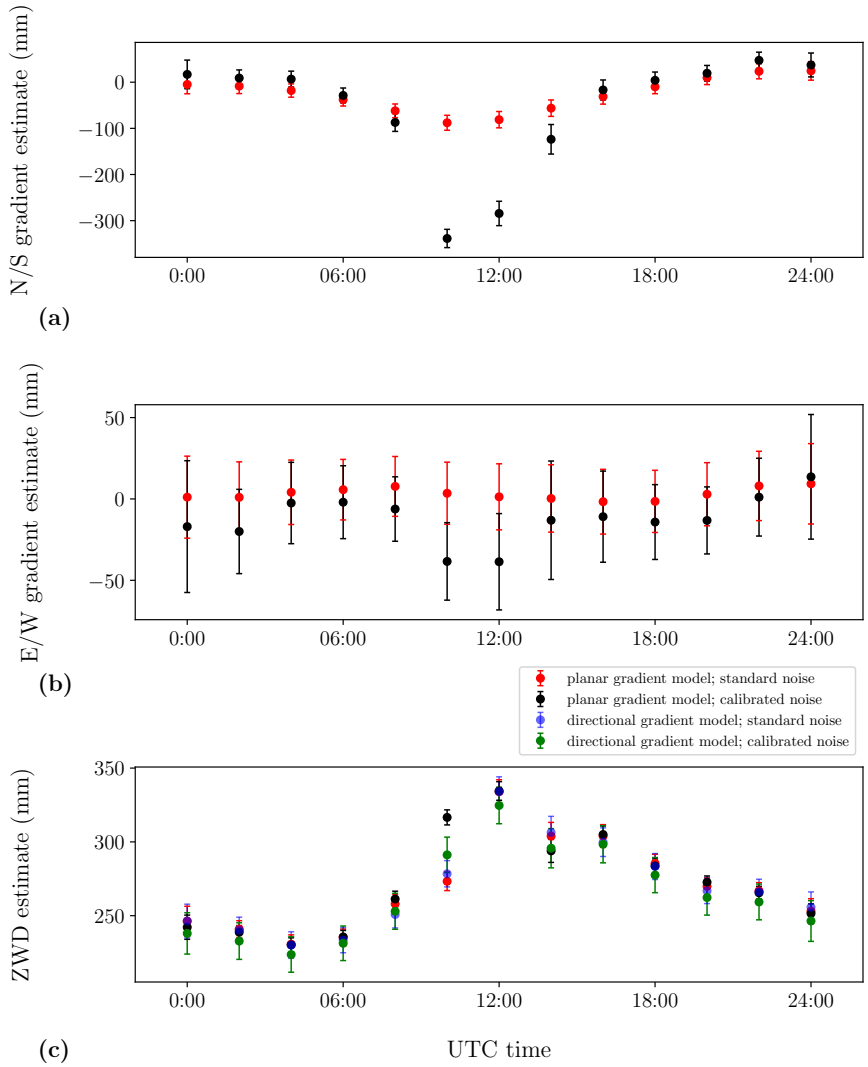

Figure 5.18: The estimates of the tropospheric parameters for BAKO on 17 September 2012 using the gradient model/process noise level of planar/standard (red), planar/-calibrated (black), directional/standard (blue) and directional/calibrated (green): (a) North-South gradients, (b) East-West gradients, and (c) zenith wet delays. Error bars are the 1-sigma uncertainties of the estimates. The calibrated process noise levels are only applied to the horizontal gradients (and not to the zenith delays).

north towards the station BAKO from the beginning to the middle of the day, which leads to an increase in the humidity above the station BAKO at 12:00 UTC (as also observed in Figure 5.18). As mentioned before, the fact that we cannot see similar horizontal gradients in the moisture content as observed by GPS could be related to the low horizontal resolution of the ACCESS weather model in 2012.

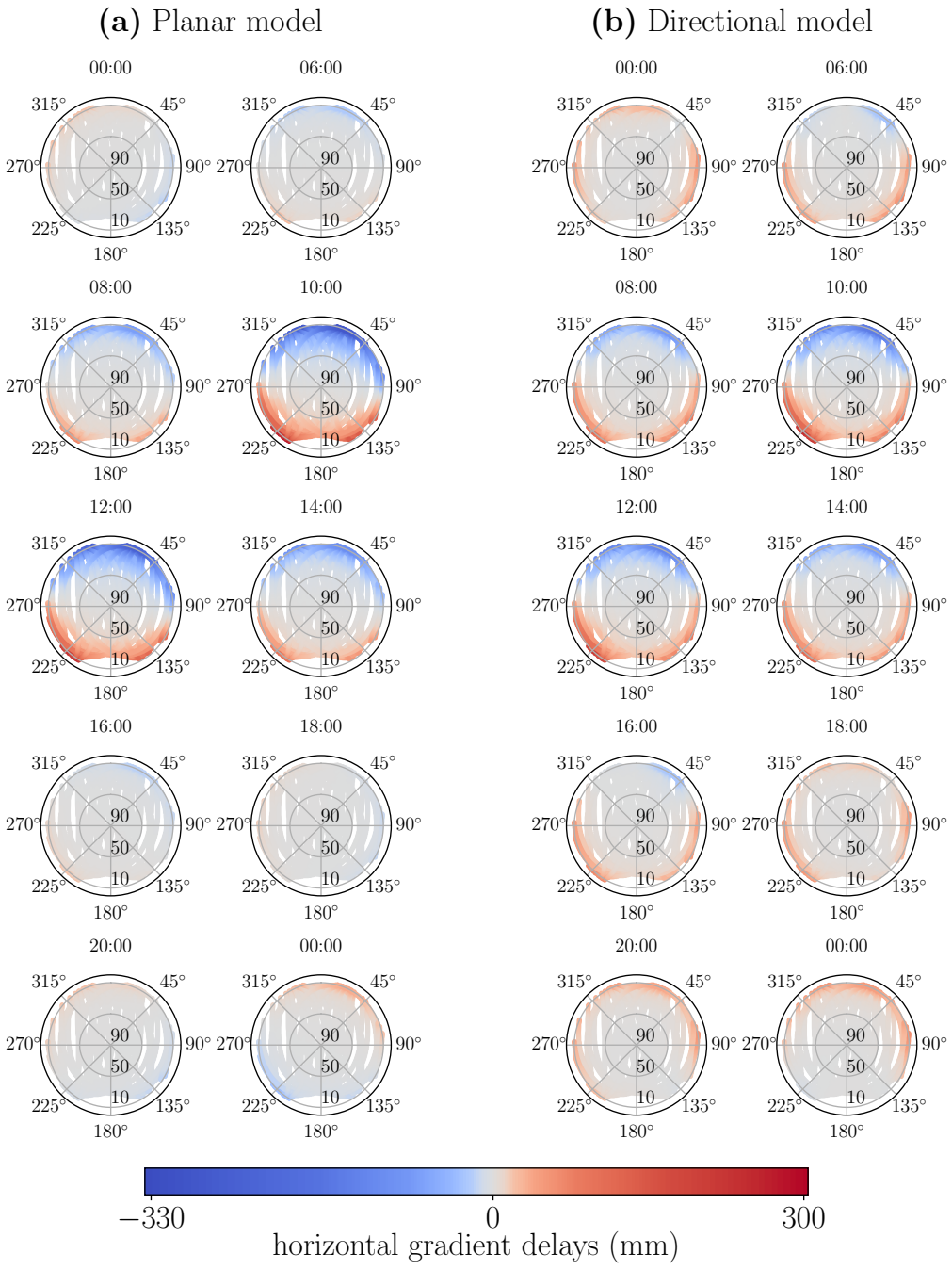

Figure 5.19: Horizontal gradient delays estimated at site BAKO on 17 September 2012 using (**a**) the conventional planar model, and (**b**) the directional model with 8 gradient estimation nodes. The relaxed calibrated process noise levels for horizontal gradients are used for both solutions. Some of the results at the beginning and end of the day (hours 2, 4, 6 and 22) are excluded to save page space. The horizontal gradients do not significantly vary at these epochs.

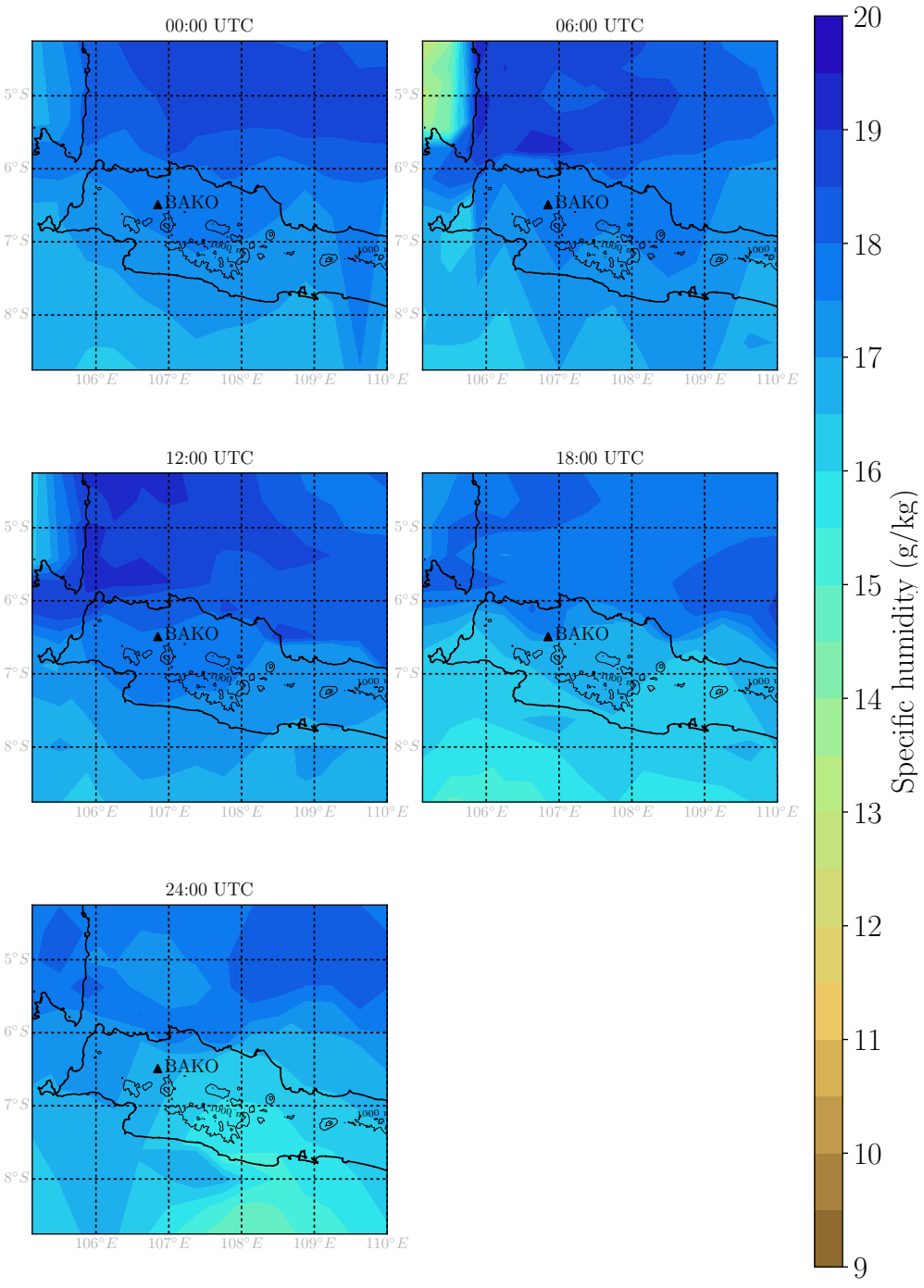

Figure 5.20: Surface Specific humidity from ACCESS weather model for 17 September 2012. GPS station BAKO is displayed as a triangle. The topography from GEBCO is depicted by contour lines every 1000 meters. Mount Pangrango, the dormant volcano in the south-east of the station, is about 3019 meters in height.

5.4.1.3 Phase residuals

The tropospheric horizontal gradients estimated when relaxing the constraints in the above examples are unusually large, and may be the effect of some unmodelled errors other than the tropospheric delays that are absorbed into the horizontal gradients in the least-squares solution. We believe that we have removed a large part of the systematic site-specific errors using an empirical model; however, there might be temporal variations in the site-specific errors that are not removed by simple stacking of the residuals. It is also worthwhile to investigate the phase residuals on the days when the large tropospheric horizontal gradients are estimated and compare them with the residuals of the normal days to ensure that the phase residuals on abnormal days resemble actual tropospheric impacts. The ionosphere-free phase residuals of the solution with standard tropospheric process noise levels are shown in Figure 5.21 between 04:00 UTC and 16:00 UTC on three consecutive days from 16 to 18 September 2012. As discussed in the previous section, large horizontal gradients are estimated between 10:00 UTC and 14:00 UTC on 17 September 2012. On the same day, large phase residuals are observed particularly from 08:00 UTC to 12:00 UTC (Figure 5.21b). It is important to note that the same satellites do not exhibit such large residuals on the days before and after 17 September (Figures 5.21a and c), which shows that the effect is not likely to be related to the specific satellite-receiver geometry. This type of increase in the phase residuals over a few hours of a day is usually attributed to the tropospheric effects that are not properly modelled. Therefore, the estimated tropospheric horizontal gradients when relaxing the constraints are probably the result of the actual tropospheric delays.

5.4.2 An example of highly variable zenith delays

While the highly variable horizontal gradients are the main driving factor for most of the differences made in zenith delays estimates by relaxing the tropospheric process noise levels, there are also cases where the constraints on the zenith tropospheric delays appear to be too tight to allow enough variations. As an example, Figure 5.22 shows the tropospheric parameter estimates for ASPA on 23 March 2012 using the standard 20 $mm/\sqrt{hr}$ process noise levels (red error bars) and the relaxed calibrated process noise levels of 51 $mm/\sqrt{hr}$ (black error bars) for the zenith wet delays. The standard process noise levels for the horizontal gradients were used for both solutions, and were shown to have little impact on the solutions. The horizontal gradients are not significantly different between the two solutions (Figure 5.22a and b). The zenith wet delay estimate at 08:00 UTC, however, is underestimated by the standard ZWD process noise level by about 20 mm (equivalent to $\sim$3 mm of precipitable water vapour) when compared to the solution with relaxed constraints for ZWD. Considering the uncertainty of about 8 mm for ZWD (and $\sim$1 mm for PWV), this amount of difference is statistically significant. This example shows that in addition to the horizontal gradient process noise levels, the standard constraints of 20 $mm/\sqrt{hr}$ on the ZWD are also sometimes too tight to allow enough variations for the ZWD.

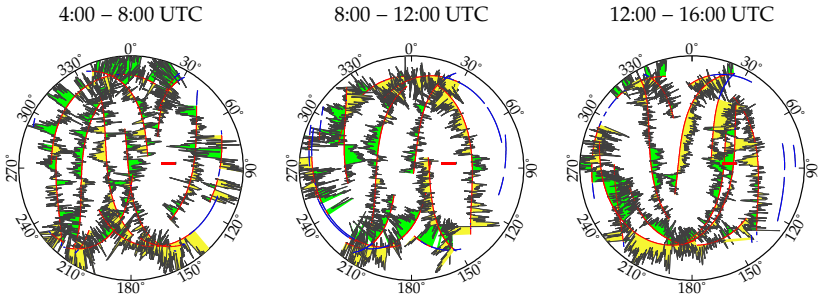

(a) 16 September 2012

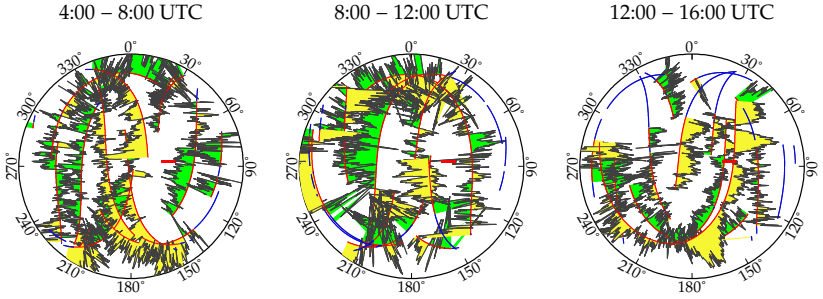

(b) 17 September 2012

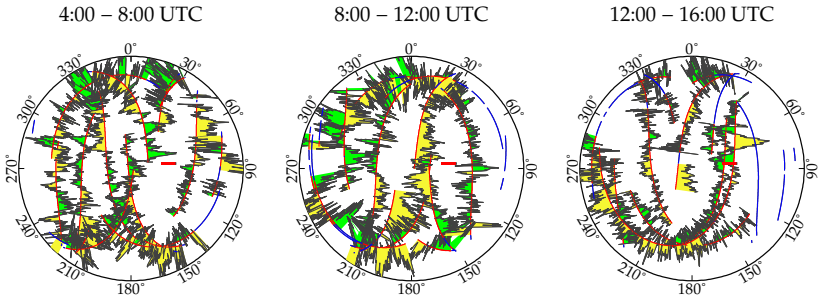

(c) 18 September 2012

Figure 5.21: Ionosphere-free phase residuals (in cycles) for BAKO on (**a**) 16, (**b**) 17 and (**c**) 18 September 2012. The length of the red scale on the figures is equal to one cycle. The green colours depict positive residuals and yellow colours show negative residuals.

5.5 Summary

The simulations and real experiments carried out in this chapter showed that tightening the process noise levels of the tropospheric parameters when one knows a priori that the variabilities of these parameters are of small amplitudes, does not significantly change the parameter estimates. On the other hand, tightening the noise

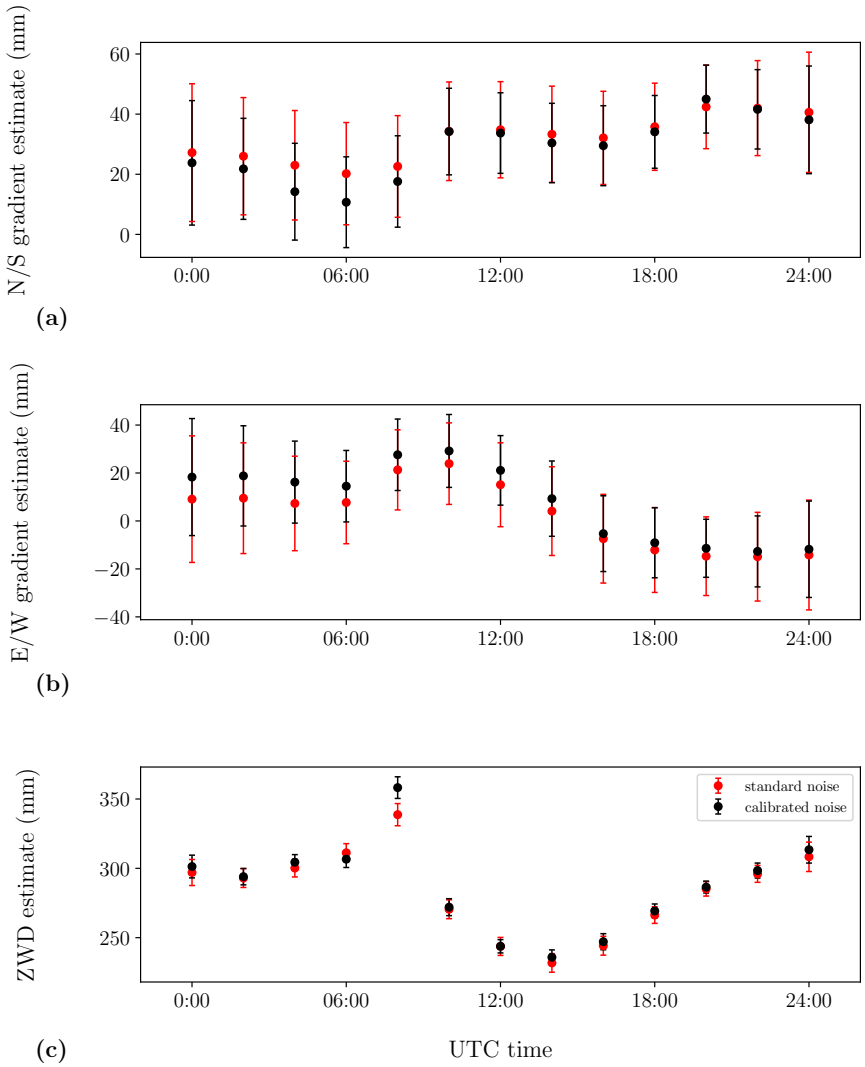

Figure 5.22: The estimates of the tropospheric parameters for ASPA on 23 March 2012 using the standard (red) and calibrated (black) process noise levels: (a) North-South gradient, (b) East-West gradient and (c) zenith wet delay. Error bars are the 1-sigma uncertainties of the estimates.

levels bears the risk of over-constraining the parameters, which leads to inaccurate estimates.

There are occasions when the standard conventional process noise levels of the tropospheric parameters are too tight to allow enough variations between tabular points in a day for zenith delays and horizontal gradients of the troposphere. In general, relaxing the tropospheric process noise levels improves the repeatabilities of the vertical positions in turbulent tropospheric conditions (cf. Figure 5.10). Much improvement in height repeatability is observed for a station in Jakarta, Indonesia (BAKO) when there are very large southward gradients estimated by relaxing the gradient noise levels. However, when there are complex horizontal asymmetries of

the tropospheric refractivity that cannot be accurately modelled by a two-axis planar model, biases may result from allowing large linear horizontal gradients to be estimated. Therefore, it is important for meteorological purposes, when one seeks to accurately estimate tropospheric delays, to use a more complicated model of the horizontal gradients such as the directional model introduced in Chapter 4 in conjunction with relaxed constraints. Otherwise, allowing the horizontal gradients to be freely estimated and using an oversimplified model of horizontal gradients may induce further errors to the zenith delay estimates.

We assumed that the horizontal gradients estimated in Jakarta are actual tropospheric gradients. The long-term site-specific errors were removed beforehand by an empirical model, and the phase residuals were not consistent for the same satellite PRN across all days, which minimizes the possibility of the errors related to the specific satellite-receiver geometry to have interfered with the tropospheric gradients. However, more investigation is required to understand the sources of the errors that may have interfered with the tropospheric gradients. There is a possibility that some unknown source of error is absorbed into the estimated horizontal gradients (and thus not absorbed into the heights, improving the height scatters). If there is such effect, it should have a similar pattern to the tropospheric effects, occurring in random days but mostly in the dry season.

Chapter 6

Conclusion

This thesis was an investigation on state-of-the-art GPS tropospheric modelling. Much focus was on improving the modelling of the low-elevation observations, which are able to provide useful information about the spatial variabilities of the troposphere in the local environment around a GPS station. Abnormal weather conditions when there are unusual variations of the refractivity either spatially or temporally were specifically considered. The findings of this thesis contribute to different operational and research fields. GPS analysts who are interested in the tropospheric products are able to use the discoveries in this work to achieve the most accurate results by using the recommended strategies and modelling techniques. Atmospheric researchers may also use the outcome of this work (particularly the more complex model of horizontal gradients introduced in Chapter 4) to monitor and study particular atmospheric phenomena.

The findings of Chapter 3 showed the impact of the site-specific effects on the tropospheric estimates in GPS analysis and the importance of mitigating them for meteorological applications. In particular, it was shown that an empirical model can be used to correct the site-specific errors for low-elevation observations to a large extent, and that such an empirical site-specific model can significantly reduce the sensitivity of the tropospheric zenith delay estimates to the choice of elevation cut-off angle. This is an important outcome of this work, which shows that using such techniques to mitigate the site-specific errors is not only important for the geodetic purposes, but is also essential for meteorological purposes when including low-elevation observations is desired. However, one should keep in mind that the benefit of the ESM can only be certainly confirmed for the repeatability (precision) of the estimates, and not necessarily for the accuracy of the estimates. This is because the initial solutions that the ESM is built on itself may suffer from biases resulting from the site-specific errors being absorbed by the estimated parameters. While the ESM captures the site-specific errors reflected in phase residuals, it is unable to capture the errors absorbed by estimated parameters.

GPS estimates of linear horizontal gradients were shown to result in more repeatable solutions than the model values currently available. However, the conventional two-axis tilted atmosphere model is not always an accurate representation for horizontal changes of the atmospheric refractivity. Mis-modelling the horizontal gradients of the troposphere in the situations when these gradients are not symmetric

leads to errors in all the estimated parameters, but the largest impacts are on height and tropospheric zenith delay estimates. A new approach for modelling the horizontal gradients of the tropospheric delay was introduced in Chapter 4 in which the horizontal gradients are estimated as pie wedges in several directions around the GPS station. This new parametrization was proved to significantly improve the parameter estimates (particularly heights and tropospheric delays) in abnormal weather conditions with asymmetric horizontal gradients of the refractivity. This new parametrization can be used to resolve the issues regarding the skewed position time series that occur in regions with particular topography-atmosphere interaction where e.g. topography-induced gravity waves cause atmospheric phenomena like Lee waves. The findings of Chapter 4 are also significant contributions to monitoring such particular weather conditions, and thus can be used in atmospheric research to study the characteristics of these events.

An analysis and discussion of the process noise levels for both tropospheric zenith delays and horizontal gradients was performed in Chapter 5. The first outcome of this chapter was that as long as we use a piecewise linear function for temporal modelling of the tropospheric delays, there was generally no need to constrain the temporal changes of the tropospheric parameters tighter than the standard constraints that are representative of typical atmospheric conditions in a mid-latitude site, even if we know a priori that the troposphere is much less variable than in such a station. On the other hand, it was found that the standard constraints are sometimes too tight to allow enough variations for the tropospheric delays. In particular, the standard constraints on the horizontal gradients of the troposphere were found too tight in several occasions in our analysis. However, it was also found out that in unusual weather conditions with asymmetric gradient schemes, the simplified planar model of horizontal gradients may lead to inaccurate estimates (of horizontal gradients and zenith delays) when relaxing the temporal constraints on the horizontal gradients. Therefore for meteorological purposes and when the asymmetry in the tropospheric refractivity cannot be accurately represented by a simple planar model, it is important to use a more complex parametrization of horizontal gradients such as the directional model introduced in Chapter 4 in conjunction with loose temporal constraints to achieve the best estimates for both tropospheric zenith delays and horizontal gradients.

The findings of this research can be used as a basis for analysis centres for implementation of some of the new approaches in routine GNSS data processing. Inclusion of low-elevation observations is important for meteorological purposes; however, there are errors associated with very low elevation observations that limit the use of them. Use of an empirical model of the site-specific error in conjunction with a proper stochastic model such as a piecewise linear weighting which gives weights to the observations according to the residuals associated with them is recommended as an appropriate approach for the routine processing. An empirical model could be derived and updated regularly (e.g. once month or when the equipment change) for every station. Also, in places where the troposphere is known to behave highly asymmetrically, the use of a directional horizontal gradient model is recommended.

The analysis of the temporal constraints in Chapter 6 of this thesis were based on the use of a piecewise linear approach for the tropospheric delay estimation, in which case the use of constraints are not recommended. However, in many of the routine data processing centres, the tropospheric parameters are now estimated in high temporal resolutions, sometimes at every observation epoch using e.g. a random walk process. The use of constraints becomes much more important when a higher temporal resolution is required for the estimation of tropospheric zenith delays and horizontal gradients.

6.1 Future work

There are areas for future directions of this research. The findings of this thesis were much focused on improvements in the modelling of low-elevation observations. Much improvement was found to occur as a result of using both empirical mitigation of site-specific errors and use of an asymmetric gradient parametrization. The use of these two techniques along with allowing enough variations for horizontal gradients of the tropospheric refractivity via relaxing the temporal constraints leads to more accurate estimates of tropospheric slant delays. This is an improvement that can be used in meteorological applications where the use of low-elevation observations and/or tropospheric slant delays is desirable. Such applications include assimilation of the GPS-derived tropospheric delays into numerical weather prediction models and the tomographic reconstructions of the troposphere.

We noticed in Chapter 4 that the directional parametrization of the horizontal gradients suffers from higher number of correlated parameters, which leads to higher uncertainties and parameter dispersions in normal atmospheric conditions. Therefore, a technique to decide in advance how many number of horizontal gradients should be estimated for each station and day is desired.

While the use of the directional gradient model significantly improved the repeatabilities of the vertical position components in asymmetric gradient scenarios, the time series of horizontal positions in our studies were not much impacted by the use of the directional gradient model. This could be due to even more complicated atmospheric conditions with areas of consecutively high and low refractivity, as one may expect due to the existence of parallel rows of clouds with windows in between in a Lee wave occurrence. Therefore, an even more complicated model of horizontal gradients which also includes a discrete elevation dependency may help further improve the estimates of tropospheric delays, which could lead to improved horizontal position estimates. Such a parametrization will estimate horizontal gradients not only in several azimuthal directions around the station but also in different elevation bins. There will be limitations to this more complex model which should be considered: there may not be enough number of observations in some elevation-azimuth bins to resolve for the tropospheric horizontal gradients; also, the estimates will be further uncertain as a result of the lower degrees of freedom. The first step to discover whether adding discrete elevation dependencies to the horizontal gradient

parametrizations is to simulate checkerboard gradient scenarios with discrete bins of positive and negative horizontal gradients, and investigate the impact on horizontal positions. If one can find a large impact on horizontal positions due to mis-modelling of this checkerboard gradient scenario, then it is worthwhile to develop a gradient model with discrete elevation dependency in GPS analysis and assess the model for the case studies like the Lee waves in the Sierra Nevada region.

In Chapter 5, we observed extremely large tropospheric horizontal gradients. We also compared these GPS estimates with the specific humidities from the ACCESS weather model, and saw some consistencies between the two dataset. However, there have been also inconsistencies between the GPS estimates of horizontal gradients and the information from the ACCESS weather model, which may be due to the low horizontal resolution of the ACCESS model back in 2012. Therefore, repeating a similar assessment using data from a more recent date, when the ACCESS weather model has improved horizontal resolution, is desirable to confirm whether the GPS-estimated horizontal gradients are in fact due to a weather phenomena.

A piecewise linear function with stochastic constraints was used to model the temporal variations of tropospheric zenith delays and horizontal gradients. However, modelling these parameters as random walks may better represent the time evolution of them at sub-hourly time scales, and has the advantage of providing these parameters with a higher temporal resolution. Investigating the benefits of modelling the tropospheric zenith delays and horizontal gradients as random walks instead of piecewise linear functions and how the conclusions of Chapter 5 may be affected by a different modelling approach is an interesting area of future work.

Over the whole analyses performed in this thesis, only GPS observations were used. However, more GNSS satellites are being launched and the analysis software are now becoming capable of processing newer GNSS observations (such as GLONASS, Galileo, and BeiDou). Therefore, it is worthwhile to use the techniques introduced in this thesis on multi-GNSS observations. In particular, the performance of directional gradient model heavily depends on the amount of data available; the larger number of observations will lead to higher degrees of freedom for finer resolving power of the gradients. The higher number of observations may also allow the estimation of discrete horizontal gradients across different azimuth and elevation bins with acceptable uncertainties.

We used a relative positioning technique (a double-difference approach) for the analyses performed in this thesis, which has advantages like the removal of clock errors by differencing the observations. However, one could also carry out the analyses using a Precise Point Positioning (PPP) approach. The PPP method has the advantage that one can perform the analyses using the observations from the individual stations separately; therefore, there is no need to select a proper reference station which could be far away from the area affected by severe weather. Also, the usefulness of the proposed models can be discussed and interpreted on station-by-station basis without the observations from one station affecting the estimates at another station. As a result, assessing the effectiveness of the proposed models, in particular the directional gradient model of Chapter 4, using a PPP approach is recommended.

Appendix A

Metadata for GPS stations

The information regarding the GPS stations used in this thesis is summarized in Tables A.1 and A.2.

Station	Latitude	Longitude	Ellipsoidal height (m)	Approximate Monument height (m)
ALIC	23.67°S	133.89°E	603.2	0.5
ASPA	14.33°S	170.72°E	53.5	6
AUCK	36.60°S	174.83°E	132.7	1.3
BAKO	6.49°S	106.85°E	158.1	0.5
CEDU	31.87°S	133.81°E	144.7	0
COCO	12.19°S	96.83°E	-35.3	0.5
CUSV	13.74°N	100.53°E	74.3	2
DARW	12.84°S	131.13°E	125.1	0.5
GUAM	13.59°N	144.87°E	201.9	unknown
HOB2	42.80°S	147.44°E	41.0	0.5
KARR	20.98°S	117.10°E	109.1	0.5
KIRI	1.35°N	172.92°E	36.2	1.5
KOUC	20.56°S	164.29°E	84.1	2
LAE1	6.67°S	146.99°E	140.3	0.011
LAUT	17.61°S	177.45°E	89.6	1.5
MAJU	7.12°N	171.36°E	33.7	2
MCIL	24.29°N	153.98°E	35.7	3
NAUR	0.55°S	166.93°E	46.2	1.5
NIUM	19.08°S	169.93°W	46.2	1.5
NTUS	1.35°N	103.68°E	75.4	1.5
PIMO	14.64°N	121.08°E	95.5	1.6
PNGM	2.04°S	147.37°E	116.3	1.5
POHN	6.96°N	158.21°E	90.7	1.5
SA39	12.42°S	130.89°E	84.9	unknown
SA40	0.52°S	166.92°E	50.0	unknown
SA42	2.06°S	147.43°E	85.9	unknown
TID1	35.40°S	148.98°E	665.3	5
TOW2	19.27°S	147.06°E	88.1	unknown
TUVA	8.53°S	179.20°E	38.4	1.5
XMIS	10.45°S	105.69°E	261.5	2
YAR2	29.05°S	115.35°E	241.3	unknown

Table A.1: Approximate locations of the GPS stations used in the experiment of Figure 2.2 along with the monument heights above the ground. The locations are estimated, and the monument heights are from station log files (ftp://ftp.ga.gov.au/geodesy-outgoing/gnss/logs).

Station	Date range	Receiver type	Antenna type	Radome type	Elevation mask
ALIC	2011-01-01 to 2011-07-20 2011-07-21 to 2012-12-31	Leica GRX1200GGPRO	AOAD/M_T LEIAR25.R3	None	0° 0°
ASPA	2011-01-01 to 2011-01-10 2011-01-11 to 2012-12-31	Trimble NETR5	TRM55971.00	None	5° 0°
AUCK	2011-01-01 to 2011-02-28 2011-03-01 to 2012-12-31	Trimble NETRS Trimble NETR9	TRM41249.00 TRM55971.00	None	4° 3°
BAKO	2011-01-01 to 2011-04-30 2011-05-01 to 2012-12-31	Leica GRX1200+GNSS Leica GRX1200GGPRO	LEIAT504GG	LEIS	0°
CEDU	2011-01-01 to 2011-05-17 2011-05-18 to 2012-12-31	ASHTECH UZ-12 Trimble NETR8	AOAD/M_T	AUST	0°
COCO	2011-01-01 to 2011-10-23 2011-10-24 to 2012-12-31	Trimble NETR5 Trimble NETR8	AOAD/M_T	None	0°
CUSV	2011-01-01 to 2012-12-31	Trimble NETRS	TRM41249.00	None	0°
DARW	2011-01-01 to 2012-12-31	Leica GRX1200GGPRO	ASH700936D_M	None	0°
GUAM	2011-01-01 to 2012-12-31	ASHTECH UZ-12	ASH701945B_M	JPLA	4°
HOB2	2011-01-01 to 2012-12-31	Leica GRX1200GGPRO	AOAD/M_T	None	0°
KARR	2011-01-01 to 2012-12-31	Trimble NETR8	TRM59800.00	None	0°
KIRI	2011-01-01 to 2012-12-31	Trimble NETR9	TRM59800.00	None	0°
KOUC	2011-01-01 to 2012-12-31	Trimble NETR5	TRM57971.00	TZGD	5°
LAE1	2011-01-01 to 2012-12-31	ASHTECH Z-XII3	ASH700936A_M	None	5°

LAUT	2011-01-01 to 2012-04-24 2012-04-25 to 2012-12-31	ASHTECH UZ-12 Trimble NETR9	ASH701945C_M TRM59800.00	SCIS None	0°
MAJU	2011-01-01 to 2012-04-24 2012-04-25 to 2012-12-31	ASHTECH UZ-12 Trimble NETR9	ASH701945C_M TRM59800.00	SCIS None	0°
MCIL	2011-01-01 to 2012-12-31	Trimble 5700	TRM29659.00	DOME	5°
NAUR	2011-01-01 to 2011-01-10 2011-01-10 to 2012-12-31	Leica GRS1200+GNSS	LEIAR25.R3	None LEIT	0°
NIUM	2011-01-01 to 2012-12-31	Trimble NETRS	TRM41249.00	None	4°
NTUS	2011-01-01 to 2012-12-31	Leica GRX1200GGPRO	LEIAT504GG	None	0°
PIMO	2011-01-01 to 2012-12-31	ASHTECH UZ-12	ASH701945C_M	None	4°
PNGM	2011-01-01 to 2012-09-07 2012-09-08 to 2012-12-31	ASHTECH UZ-12 Trimble NETR9	ASH701945C_M TRM59800.00	SCIS None	0°
POHN	2011-01-01 to 2011-12-06 2011-12-07 to 2012-12-31	ASHTECH UZ-12 Trimble NETR9	ASH701945C_M TRM59800.00	SCIS None	0°
SA39	2011-01-01 to 2012-12-31	Trimble NETRS	TRM41249.00	None	0°
SA40	2011-01-01 to 2012-12-31	Trimble NETRS	TRM41249.00	None	0°
SA42	2011-01-01 to 2012-12-31	Trimble NETRS	TRM41249.00	None	0°
TID1	2011-01-01 to 2012-12-31	Trimble NETR8	AOAD/M_T	JPLA	0°
TOW2	2011-01-01 to 2011-09-22 2011-09-23 to 2012-12-31	LEICA GRX1200GGPRO	AOAD/M_T LEIAR25.R3	AUST None	0°
TUVA	2011-01-01 to 2012-01-30 2012-01-31 to 2012-12-31	ASHTECH UZ-12 TRIMBLE NETR9	ASH701945C_M TRM59800.00	SCIS None	0°

XMIS	2011-01-01 to 2012-12-31	Leica GRX1200GGPRO	ASH701945C_M	None	0°
YAR2	2011-01-01 to 2012-05-22	ASHTECH UZ-12	AOAD/M_T	JPLA	0°
	2012-05-23 to 2012-09-27			None	
	2012-05-28 to 2012-12-31			JPLA	

Table A.2: Equipment used for the GPS stations of Figure 2.2 for the period 2011-2012. Only receiver and antenna types are summarized in this table. Changes in the equipment when using the same or a different version of the same type is not highlighted. Such changes can be found in the stations log files in ftp://ftp.ga.gov.au/geodesy-outgoing/gnss/logs.

Station	Lat./Lon./H	Monument height (m)	Receiver type	Antenna type	Radome type	Elevation mask
ALIC	23.67°S/133.89°E/603.2 m	0.5	Leica GRX1200GGPRO	AOAD/M_T	None	0°
AUCK	36.60°S/174.83°E/132.7 m	1.3	Trimble NETR9	TRM55971.00	None	3°
CAS1	66.28°S/110.52°E/22.6 m	unknown	Leica GRX1200GGPRO	AOAD/M_T	AUST	0°
DARW	12.84°S/131.13°E/125.1 m	0.5	Leica GRX1200GGPRO	ASH700936D_M	None	0°
DAV1	68.58°S/77.97°E/44.5 m	unknown	Leica GRX1200GGPRO	LEIAR25.R3	LEIT	0°
DUM1	66.67°S/140.00°E/-1.4 m	1	ASHTECH Z-XII3	ASH700936E	SNOW	15°
HARB	25.89°S/27.71°E/1558.1 m	3	Trimble NETR9	TRM59800.00	None	3°
ISPA	27.12°S/109.34°W/112.5 m	1.7	ASHTECH UZ-12	ASH701945E_M	SCIT	0°
LPGS	34.91°S/57.93°W/29.8 m	1.7	AOA Benchmark ACT	AOAD/M_T	None	0°
MAC1	54.50°S/158.94°E/-7.0 m	unknown	Leica GRX1200+GNSS	AOAD/M_T	AUST	0°
MAL2	3.00°S/40.19°E/-21.5 m	1	JPS Legacy	ASH701945C_M	None	0°
MAW1	67.6°S/62.87°E/59.2 m	1.5	Leica GRX1200GGPRO	AOAD/M_T	AUST	0°
MCM4	77.84°S/166.67°E/98.0 m	0.1	ASHTECH UZ-12	AOAD/M_T	JPLA	4°
OHI2	63.32°S/57.90°W/33.1 m	1.4	JPS E_GGD	TPSCR.G3	TPSH	0°
PALM	64.78°S/64.05°W/31.2 m	2.03	ASHTECH UZ-12	ASH700936D_M	SCIS	4°
ROTH	67.57°S/68.13°W/39.8 m	unknown	Leica GRX1200+GNSS	LEIAR25	LEIT	0°
SANT	33.15°S/70.67°W/723.0 m	0.6	ASHTECH UZ-12	AOAD/M_T	JPLA	4°
SYOG	69.01°S/39.58°E/50.1 m	1.5	Trimble NETRS	AOAD/M_T	DOME	10°
THTI	17.58°S/149.61°W/98.5 m	unknown	Trimble NETR8	ASH701945E_M	None	3°

TID1	35.40°S/148.98°E/665.3 m	5	Trimble NETR8	AOAD/M_T	JPLA	0°
TOW2	19.27°S/147.06°E/88.1 m	unknown	LEICA GRX1200GGPRO	LEIAR25.R3	None	0°
VESL	71.67°S/2.84°W/862.4 m	unknown	TPS GB-1000	TRM29659.00	TCWD	0°
YAR2	29.05°S/115.35°E/241.3 m	unknown	ASHTECH UZ-12	AOAD/M_T	JPLA	0°

Table A.3: Approximate locations and the equipment used for the GPS stations of the experiment analysed in Section 5.3 as of January 2012. The locations are estimated, and the information are extracted from the station log files in ftp://ftp.ga.gov.au/geodesy-outgoing/gnss/logs.

Appendix B

First-order Gauss-Markov processes

As described in Chapter 2 (Equations 2.8 to 2.11), both tropospheric zenith wet delays and horizontal gradients are modelled in our GPS analyses as piecewise linear functions between the estimation nodes throughout a day with variations constrained by a first-order Gauss-Markov process.

A first-order Gauss-Markov process is a stochastic process which satisfies both Gaussian and Markov properties:

(a) Gaussian property: every finite linear combination of samples has a Gaussian joint probability distribution.

(b) Markov property: given the past and present states of the process, the conditional probability distribution of future states depends only on the present state and not on the past states of the process. For a discrete-time process of random variables $X_1, ..., X_n$, the sequence is a Markov process if

$$P(X_{k+1} = x | X_1 = x_1, X_2 = x_2, ..., X_k = x_k) = P(X_{k+1} = x | X_k = x_k) \tag{B.1}$$

where $P(X_j = x_j | X_i = x_i)$ is the conditional probability of X_j given X_i. In other words, a discrete-time Markov process has the property that each state of the process depends only on the previous state, and not on the states before the previous state.

A stationary first-order Gauss-Markov process has the autocorrelation function of the form below [e.g. Brown and Hwang, 1997]:

$$\rho(\Delta t) = \sigma^2 \exp(-\Delta t / \tau) \tag{B.2}$$

where Δt is the time interval between the states, σ^2 is the variance and τ is the correlation time of the process. As Δt approaches infinity, the autocorrelation $\rho(\Delta t)$ approaches zero; therefore, the process needs to be zero-mean.

Considering the two properties of a first-order Gauss-Markov process as above, a state transition equation for such a process can be written as Equation B.3 below:

$$x_{k+1} = \Phi_k x_k + w_k \tag{B.3}$$

where x_k is the state of the process at time t_k following a Gaussian distribution, Φ_k is the first-order Gauss-Markov state transition function, and w_k is an uncorrelated zero-mean Gaussian noise. As explained by Ji [2011], one can determine the transition function by multiplying both sides of Equation B.3 by x_k and taking the expectation from both sides:

$$E[x_k x_{k+1}] = E[\Phi_k x_k^2] + E[x_k w_k] \tag{B.4}$$

Since w_k is uncorrelated with x_k, and the expectation of x_k is zero, the above equation can be rewritten as below:

$$COV(x_k, x_{k+1}) = \Phi_k VAR(x_k) \tag{B.5}$$

with *VAR* and *COV* denoting variance and covariance functions. The above equation is equivalent to:

$$\rho(\Delta t) = \Phi_k \rho(0) \tag{B.6}$$

where Δt is the time difference between the two states. By replacing Equation B.2 in the above equation, the transition matrix is determined to be as Equation B.7 below:

$$\Phi_k = exp(-\Delta t/\tau) \tag{B.7}$$

The variance of the process noise can be derived by multiplying both sides of Equation B.3 by x_{k+1} and replacing the x_{k+1} in the second term of the right hand side by $\Phi_k.x_k + w_k$:

$$x_{k+1}^2 = \Phi_k x_k x_{k+1} + w_k[\Phi_k x_k + w_k] \tag{B.8}$$

Taking the expectation from both sides of the above equation, we get:

$$VAR(x_{k+1}) = \Phi_k COV(x_k, x_{k+1}) + VAR(w_k) \tag{B.9}$$

which yields:

$$VAR(w_k) = \rho(0) - \Phi_k \rho(\Delta t) \tag{B.10}$$

Replacing the variance and covariance by Equation B.2 and the transition function by Equation B.7 gives the process noise variance ($\delta^2 = VAR(w_k)$):

$$\delta^2 = \sigma^2[1 - exp(-2\Delta t/\tau)] \tag{B.11}$$

In forming the variance-covariance matrix for both ZWD and gradient parameters, it is assumed that the variations of these parameters follow a first-order Gauss-Markov process, which makes the ijth component of the variance-covariance matrix (c_{ij}) as below (using the autocorrelation function of Equation B.2):

$$c_{ij} = \sigma^2 exp(-\frac{|t_j - t_i|}{\tau}) \tag{B.12}$$

where t_k is the time at kth estimation node of the parameter. Considering that the

time interval between the ZWD/gradient parameter estimates is constant throughout the day, the above equation takes the matrix form of Equation 2.10 in Chapter 2.

Appendix C

ESM impact on the stations with elevation-dependent-only PCV models

It is mentioned in Section 3.2.3 that five of the stations in the experiment of Figure 2.2 (LAUT, MAJU, PNGM, POHN and TUVA) used antenna model ASH701945C_M with SCIS radome for a significant time during 2011-2012 when the analyses of Chapter 3 are carried out (also see Appendix A). The standard IGS08 antenna PCV model for this antenna type/radome combination has an elevation dependency only, and is independent of the azimuth angle of the observations. We excluded the results for these five stations from the comparisons made in Section 3.2.3 to avoid the incorrect IGS antenna PCV models affecting the conclusions made in the capability of the ESM on reducing site-specific errors including the multipath. The results for these five stations are presented in this Appendix for completeness.

Figures C.1 and C.2 show the reductions in the WRMS of height and ZTD estimates after applying the empirical site-specific model (similar to Figures 3.10 and 3.11) for the five stations with no azimuth dependency in their IGS standard PCV models. One would expect that the ESM could significantly improve the repeatabilities of the estimated parameters for these stations, as the original standard PCV model is highly inaccurate. However, as seen in both of the Figures C.1 and C.2, the improvement is not as expected; the ESM even degraded some of the solutions particularly when including observations at very low elevation angles.

For the height scatters at 10° elevation angle cut-off (Figure C.1a), the WRMS of MAJU increases after the use of the ESM, but the WRMS is decreased for the other four stations. However, when setting the elevation cut-off angle at 3° (Figure C.1b), the WRMS of LAUT and PNGM also increase as a result of using the ESM. More or less similar results are observed for the overlap ZTD repeatabilities (Figure C.2); at 3° elevation cut-off angle in particular, the WRMS increased for LAUT, MAJU and PNGM.

Figures C.3 and C.4 show the photos from different angles of the stations MAJU and PNGM. There are a couple of large radars at each of the three different directions North, East and West around the station MAJU; however, these radars are in

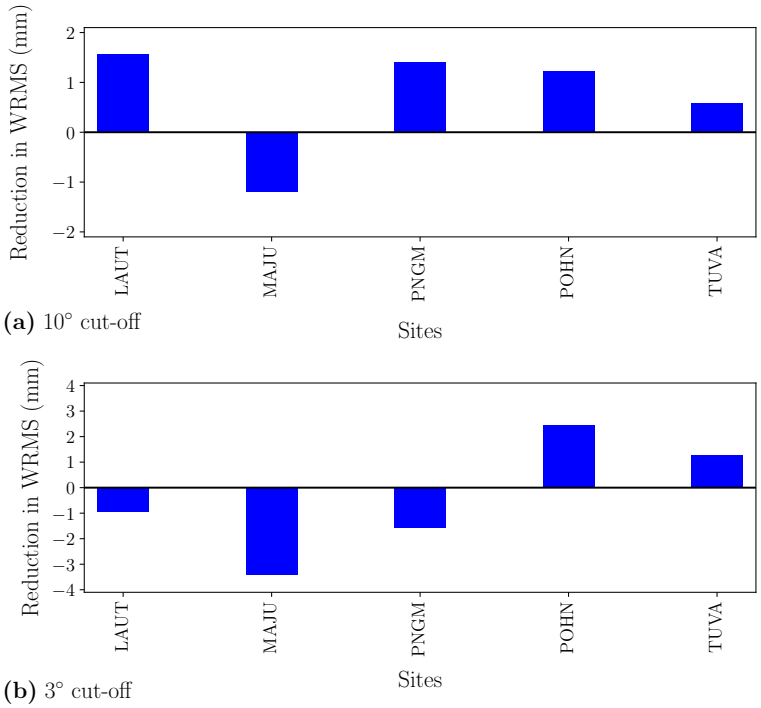

(a) 10° cut-off

(b) 3° cut-off

Figure C.1: The reduction in the average monthly WRMS of the height estimates due to ESM when the elevation cut-off angle is set at (a) 10° and (b) 3°.

a fairly long distance from the GPS station and should not significantly affect the observations. For the station PNGM, there is no major structure around the station, and the trees are fairly far from the station. Therefore, the results do not seem to be affected by the local structures around the stations. The ESM maps are displayed as sky plots for both MAJU (Figure C.5) and PNGM (Figure C.6).

The degradation in the height and ZTD repeatabilities for these stations as a result of using the ESM, particularly when low-elevation observations are included, could be caused by the change in the number of low-elevation measurements used in the solutions as decided by the outlier detection procedure before inverting the least-squares equations in GAMIT. The outlier removal process takes a sliding window for phase observations, calculates the pre-fit residuals for each observation at the window, and removes any observation for which the deviation of the residual from the mean residual of the window is higher than a specified criteria. When using the standard IGS antenna PCVs, a large number of low-elevation observations could have been detected as outliers because of their extremely high residuals compared to the computed model. When using the ESM, however, the improved PCVs for low elevations yields much better modelling of the observations and consequently much smaller residuals. This leads to a higher number of low-elevation observations kept in the processing when using the ESM. Clearly, these additional observations are still contaminated by other large modelling errors (e.g. in tropospheric mapping

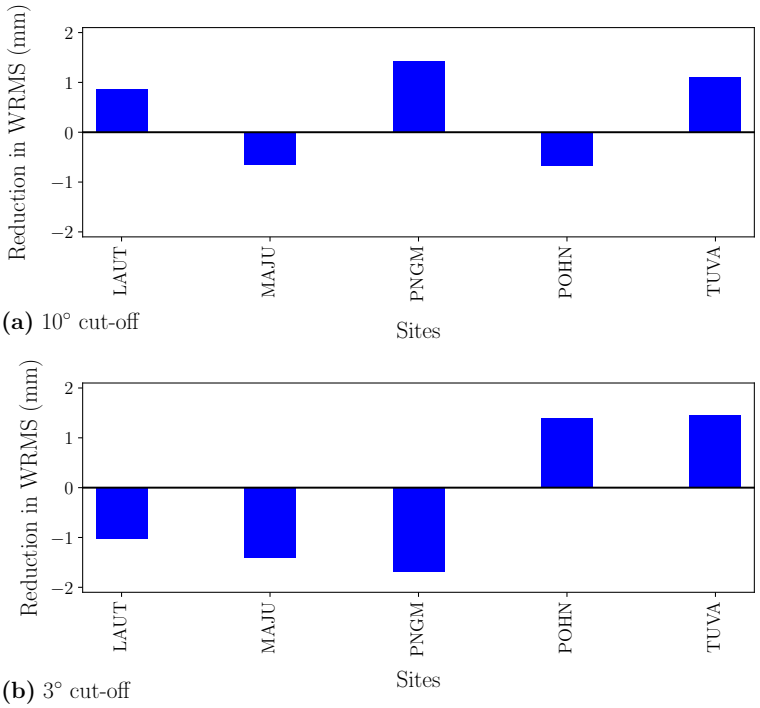

(a) 10° cut-off

(b) 3° cut-off

Figure C.2: The reduction in the mean overlap WRMS of the zenith total delay estimates at midnight epochs due to ESM when the elevation cut-off angle is set at (a) 10° and (b) 3°.

functions), as expected for typical low-elevation observations; therefore, they induce estimation errors and higher scatters in the position time series.

The increased number of the observations kept in the processing when using the ESM is demonstrated by Figure C.7, which shows the increase in the number of the observations below 10° included daily for each station when the ESM is applied compared to when the standard IGS antenna models are used for all the stations in the experiment of Figure 2.2. The ESM has generally resulted in more number of observations passed through the outlier removal procedure for the majority of the stations and days. The largest discrepancies in the number of observations between the solutions with and without the ESM are observed for the three stations LAUT, MAJU and PNGM, interestingly three of the stations which have used Ashtech ASH701945C_M antenna with SCIS radome for some time and see degraded repeatabilities for heights and ZTDs at 3° (Table A.2 and Figures C.1 and C.2).

It is interesting to note the data availabilities and equipment changes for these three stations (Table A.2) and their relation to the reduced differences in the number of observations between the two solutions with and without the ESM observed in Figure C.7. For the station MAJU, the ESM caused much higher number of measurements to be included in the solution until 25 March 2012 when the station stopped collecting data (Figure C.7 and Table A.2). The stations LAUT and PNGM continued

(a) North view (b) East view

(c) South view (d) West view

Figure C.3: Photos of the GPS station MAJU in Marshall Islands (https://www.igs.org/igsnetwork).

collecting data for the whole two-year period; however, they lost huge amounts of low-elevation observations as outliers before 25 April 2012 for LAUT and 8 September 2012 for PNGM when not applying the ESM, while the increase in the number of used data due to the application of the ESM was much smaller after the above dates. There were also large increases in the number of low-elevation data for the station POHN until 7 December 2011 after which the number of low-elevation observations passing the outlier removal process remains almost the same for the two solutions with and without the ESM. Indeed, the above dates were the times when the equipment had been changed for these four stations (Table A.2); The Ashtech antenna and receivers for these stations are replaced by Trimble equipment on these dates. As mentioned before, since the standard IGS PCV model for the specific antenna/radome type used before the above dates (Ashtech ASH701945C_M with SCIS radome) for all the four stations (MAJU, LAUT, PNGM and POHN) has no azimuthal dependency, the low-elevation observations were poorly modelled by the IGS antenna PCV, resulting in removal of many of these observations as outliers. TUVA, on the other hand, saw higher discrepancies between the two solutions after putting in place the Trimble equipment instead of Ashtech equipment; the differences are however small and both positive and negative. Deriving the ESM and using it

(a) North view (b) East view

(c) South view (d) West view

Figure C.4: Photos of the GPS station PNGM in Papua New Guinea (https://www.igs.org/igsnetwork).

as the new PCV model for the four stations LAUT, MAJU, PNGM and POHN resulted in much smaller residuals for these stations, which led to a large number of low-elevation data not being thrown out as outliers. This yielded increased scatter of heights and ZTDs for MAJU, LAUT and PNGM when implementing the ESM compared to when using the standard PCV model, particularly when including very low elevation observations (Figures C.1 and C.2). Therefore, it is important to take into consideration this change in the observations included in the least squares solution when comparing the solutions.

In section 3.2.3 we also performed analyses by using the same observation geometry for the solutions with the standard IGS PCV models and the ESM. Figures C.8 and C.9 show the reductions in the repeatabilities of heights and ZTDs due to the use of ESM when keeping the observation geometry fixed for LAUT, MAJU, PNGM, POHN and TUVA (similar to Figures 3.13 and 3.14). Except for the ZTD WRMS at 10° elevation cut-off angle, the scatters of both height and ZTD are reduced after implementing the ESM for all the five stations when fixing the observation geometry. The reductions here are due to both the improved modelling of the PCV and modelling of other effects such as multipath by the ESM.

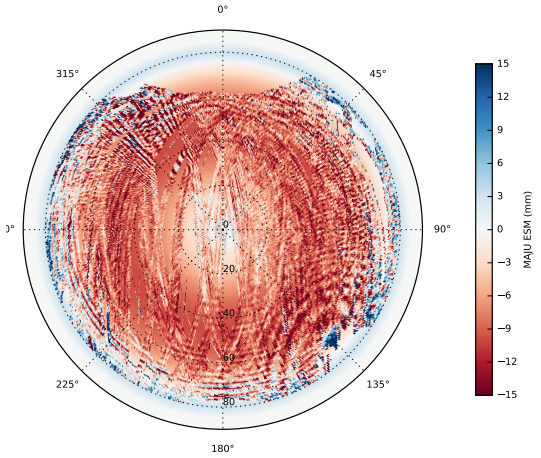

Figure C.5: ESM map of the station MAJU valid from the beginning of 2011 to 24 March 2012. AN ASHTECH antenna (ASH701945C_M) with SCIS radome was used in this period (Table A.2).

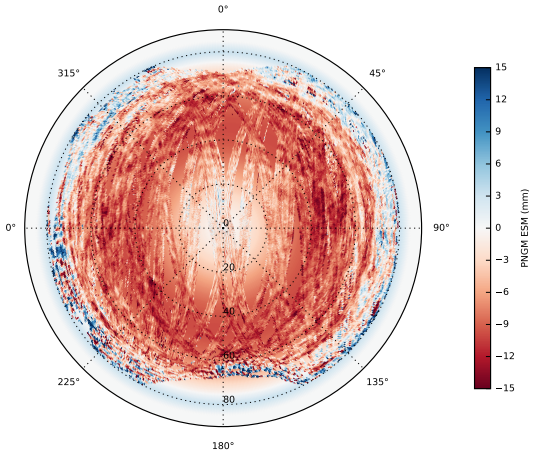

Figure C.6: ESM map of the station PNGM valid from the beginning of 2011 to 7 September 2012. AN ASHTECH antenna (ASH701945C_M) with SCIS radome was used in this period (Table A.2).

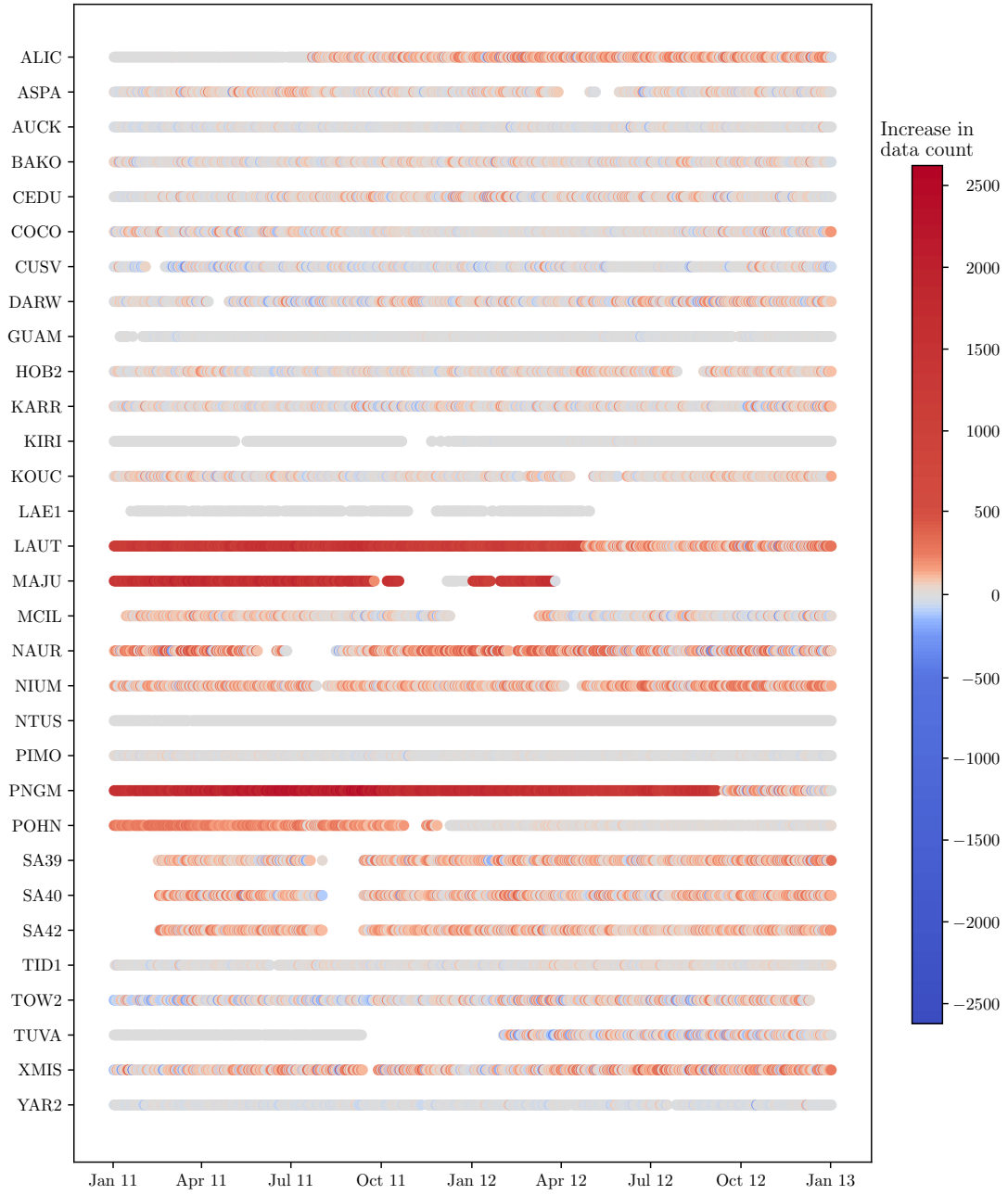

Figure C.7: Increase in the daily number of observations below 10° passed through the outlier removal procedure when using the ESM as opposed to when using the IGS08 antenna PCVs over 2011-2012.

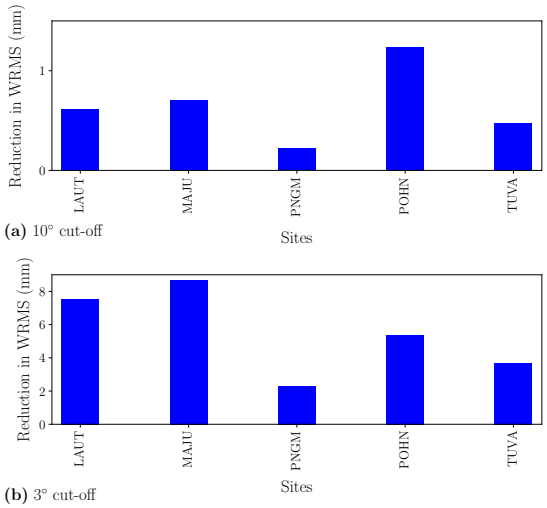

Figure C.8: The reduction in the average monthly WRMS of the height estimates due to the ESM for different stations when the elevation cut-off angle is set at (a) 10° and (b) 3°. The observation geometry is held the same for both solutions with and without the ESM.

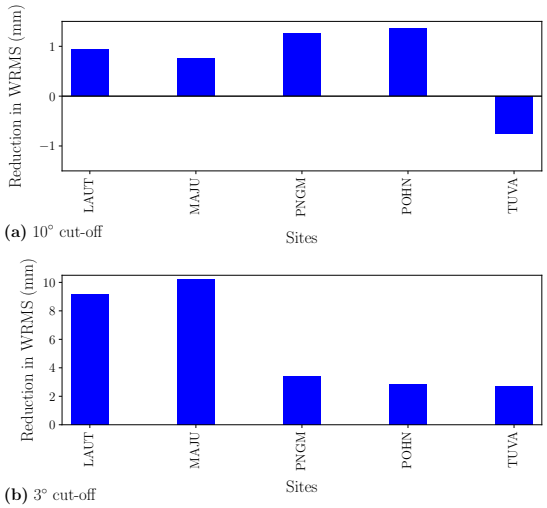

Figure C.9: The reduction in the mean overlap WRMS of the zenith total delay estimates at midnight epochs due to the ESM for different stations when the elevation cut-off angle is set at (a) 10° and (b) 3°. The observation geometry is held the same for both solutions with and without the ESM.

Bibliography

2014. ARM tropical western pacific description. http://www.arm.gov/sites/twp. Accessed: 2014-11-28. (cited on page 14)

Agnew, D. C. and Larson, K. M., 2007. Finding the repeat times of the GPS constellation. *GPS solutions*, 11, 1 (2007), 71–76. (cited on page 35)

Altamimi, Z.; Collilieux, X.; and Métivier, L., 2011. ITRF2008: an improved solution of the international terrestrial reference frame. *Journal of Geodesy*, 85, 8 (2011), 457–473. (cited on page 8)

Askne, J. and Nordius, H., 1987. Estimation of tropospheric delay for microwaves from surface weather data. *Radio Science*, 22, 3 (1987), 379–386. (cited on page 12)

Askne, J. I. and Westwater, E. R., 1986. A review of ground-based remote sensing of temperature and moisture by passive microwave radiometers. *Geoscience and Remote Sensing, IEEE Transactions on*, , 3 (1986), 340–352. (cited on pages 14 and 30)

Baire, Q.; Bruyninx, C.; Legrand, J.; Pottiaux, E.; Aerts, W.; Defraigne, P.; Bergeot, N.; and Chevalier, J., 2014. Influence of different GPS receiver antenna calibration models on geodetic positioning. *GPS Solutions*, 18, 4 (2014), 529–539. (cited on page 33)

Bar-Sever, Y. E.; Kroger, P. M.; and Borjesson, J. A., 1998. Estimating horizontal gradients of tropospheric path delay with a single GPS receiver. *Journal of Geophysical Research: Solid Earth*, 103, B3 (1998), 5019–5035. (cited on pages 1, 11, 46, and 93)

Bennitt, G. V. and Jupp, A., 2012. Operational assimilation of GPS zenith total delay observations into the met office numerical weather prediction models. *Monthly Weather Review*, 140, 8 (2012), 2706–2719. (cited on pages 1 and 13)

Bevis, M.; Businger, S.; Chiswell, S.; Herring, T. A.; Anthes, R. A.; Rocken, C.; and Ware, R. H., 1994. GPS meteorology: Mapping zenith wet delays onto precipitable water. *Journal of Applied Meteorology*, 33, 3 (1994), 379–386. (cited on page 12)

Bevis, M.; Businger, S.; Herring, T. A.; Rocken, C.; Anthes, R. A.; and Ware, R. H., 1992. GPS meteorology: Remote sensing of atmospheric water vapor using the Global Positioning System. *Journal of Geophysical Research: Atmospheres*, 97, D14 (1992), 15787–15801. (cited on page 5)

Bilich, A. and Larson, K. M., 2007. Mapping the GPS multipath environment using the signal-to-noise ratio (snr). *Radio Science*, 42, 6 (2007). (cited on page 35)

Bilich, A. and Mader, G. L., 2010. GNSS absolute antenna calibration at the national geodetic survey. In *Proceedings of the 2010 ION GNSS Conference*. (cited on page 33)

Blewitt, G., 1989. Carrier phase ambiguity resolution for the global positioning system applied to geodetic baselines up to 2000 km. *Journal of Geophysical Research: Solid Earth*, 94, B8 (1989), 10187–10203. (cited on page 7)

Bock, Y., 1991. Continuous monitoring of crustal deformation. *GPS World*, 2, 6 (1991), 40–47. (cited on page 35)

Bock, Y. and Melgar, D., 2016. Physical applications of GPS geodesy: a review. *Reports on Progress in Physics*, 79, 10 (2016), 106801. (cited on page 8)

Böhm, J., 2007. *Tropospheric delay modelling at radio wavelengths for space geodetic techniques*. Institutes of the Course on "Geodesy and Geoinformation" of the Vienna University of Technology. (cited on page 10)

Böhm, J.; Ess, M.; and Schuh, H., 2005. Asymmetric mapping functions for CONT02 from ECMWF. *Proceedings of the 17th working meeting on European VLBI for geodesy and astrometry, eds. M. Vennebusch and A. Nothnagel*, (2005), 64–68. (cited on pages 47 and 56)

Böhm, J.; Heinkelmann, R.; and Schuh, H., 2007. Short note: a global model of pressure and temperature for geodetic applications. *Journal of Geodesy*, 81, 10 (2007), 679–683. (cited on page 10)

Böhm, J.; Niell, A.; Tregoning, P.; and Schuh, H., 2006a. Global Mapping Function (GMF): A new empirical mapping function based on numerical weather model data. *Geophysical Research Letters*, 33, 7 (2006). (cited on pages 10 and 56)

Böhm, J. and Schuh, H., 2007. Troposphere gradients from the ECMWF in VLBI analysis. *Journal of Geodesy*, 81, 6-8 (2007), 403–408. (cited on pages 19 and 46)

Böhm, J.; Urquhart, L.; Steigenberger, P.; Heinkelmann, R.; Nafisi, V.; and Schuh, H., 2013. A priori gradients in the analysis of space geodetic observations. In *Reference Frames for Applications in Geosciences*, 105–109. Springer. (cited on pages 19, 47, and 48)

Böhm, J.; Werl, B.; and Schuh, H., 2006b. Troposphere mapping functions for GPS and very long baseline interferometry from European Centre for Medium-Range Weather Forecasts operational analysis data. *Journal of Geophysical Research: Solid Earth*, 111, B2 (2006). (cited on pages 1, 8, 9, 13, 46, and 56)

Boudevillain, B.; Delrieu, G.; Galabertier, B.; Bonnifait, L.; Bouilloud, L.; Kirstetter, P.-E.; and Mosini, M.-L., 2011. The cévennes-Vivarais Mediterranean Hydrometeorological Observatory database. *Water Resources Research*, 47, 7 (2011). (cited on page 77)

Braun, J.; Rocken, C.; and Liljegren, J., 2003. Comparisons of line-of-sight water vapor observations using the global positioning system and a pointing microwave radiometer. *Journal of Atmospheric and Oceanic Technology*, 20, 5 (2003), 606–612. (cited on page 2)

Brenot, H.; Ducrocq, V.; Walpersdorf, A.; Champollion, C.; and Caumont, O., 2006. GPS zenith delay sensitivity evaluated from high-resolution numerical weather prediction simulations of the 8–9 september 2002 flash flood over south-eastern france. *Journal of Geophysical Research: Atmospheres*, 111, D15 (2006). (cited on page 77)

Brown, R. G. and Hwang, P. Y., 1997. *Introduction to random signals and applied Kalman filtering: with MATLAB exercises and solutions*. Wiley. (cited on page 141)

Bureau of Meteorology, 2010. *Operational implementation of the ACCESS numerical weather prediction systems: NMOC Operational Bulletin No. 83*. Australian Government, Bureau of Meteorology. (cited on page 2)

Byun, S. H.; Hajj, G. A.; and Young, L. E., 2002. Development and application of GPS signal multipath simulator. *Radio Science*, 37, 6 (2002). (cited on page 35)

Cadeddu, M. P.; Liljegren, J. C.; and Turner, D. D., 2013. The atmospheric radiation measurement (ARM) program network of microwave radiometers: instrumentation, data, and retrievals. *Atmospheric Measurement Techniques*, 6, 9 (2013), 2359–2372. doi:10.5194/amt-6-2359-2013. http://www.atmos-meas-tech.net/6/2359/2013/. (cited on pages 14 and 30)

Champollion, C.; Masson, F.; Van Baelen, J.; Walpersdorf, A.; Chéry, J.; and Doerflinger, E., 2004. GPS monitoring of the tropospheric water vapor distribution and variation during the 9 september 2002 torrential precipitation episode in the Cévennes (southern france). *Journal of Geophysical Research: Atmospheres*, 109, D24 (2004). (cited on pages 1, 56, 57, 77, and 79)

Chen, G. and Herring, T., 1997. Effects of atmospheric azimuthal asymmetry on the analysis of space geodetic data. *Journal of Geophysical Research: Solid Earth*, 102, B9 (1997), 20489–20502. (cited on pages 1, 8, 10, 46, 47, 56, 58, and 88)

Choi, K., 2007. *Improvements in GPS precision: 10 Hz to one day*. Ph.D. thesis, University of Colorado at Boulder. (cited on page 36)

Choi, K.; Bilich, A.; Larson, K. M.; and Axelrad, P., 2004. Modified sidereal filtering: Implications for high-rate GPS positioning. *Geophysical Research Letters*, 31, 22 (2004). (cited on page 35)

Davis, J. L.; Elgered, G.; Niell, A. E.; and Kuehn, C. E., 1993. Ground-based measurement of gradients in the "wet" radio refractivity of air. *Radio Science*, 28, 6 (1993), 1003–1018. (cited on pages 10, 56, and 58)

Davis, J. L.; Herring, T. A.; Shapiro, I. I.; Rogers, A. E. E.; and Elgered, G., 1985. Geodesy by radio interferometry: Effects of atmospheric modeling errors on estimates of baseline length. *Radio Science*, 20, 6 (1985), 1593–1607. (cited on page 9)

Delrieu, G.; Nicol, J.; Yates, E.; Kirstetter, P.-E.; Creutin, J.-D.; Anquetin, S.; Obled, C.; Saulnier, G.-M.; Ducrocq, V.; Gaume, E.; et al., 2005. The catastrophic flash-flood event of 8-9 september 2002 in the gard region, france: A first case study for the cévennes-vivarais mediterranean hydrometeorological observatory. *Journal of Hydrometeorology*, 6, 1 (2005), 34–52. (cited on pages 77 and 79)

Delrieu, G.; Wijbrans, A.; Boudevillain, B.; Faure, D.; Bonnifait, L.; and Kirstetter, P.-E., 2014. Geostatistical radar–raingauge merging: a novel method for the quantification of rain estimation accuracy. *Advances in Water Resources*, 71 (2014), 110–124. (cited on page 77)

Dilssner, F.; Seeber, G.; Wübbena, G.; and Schmitz, M., 2001. Impact of near-field effects on the GNSS position solution. In *Proceedings of the 21st International Technical Meeting of the Satellite Division of the Institute of Navigation (ION GNSS 2008), Miami, Florida*, 612–624. (cited on page 35)

Dong, D.; Herring, T.; and King, R. W., 1998. Estimating regional deformation from a combination of space and terrestrial geodetic data. *Journal of Geodesy*, 72, 4 (1998), 200–214. (cited on page 22)

Dow, J. M.; Neilan, R. E.; and Rizos, C., 2009. The international IGS service in a changing landscape of global navigation satellite systems. *Journal of Geodesy*, 83, 3 (2009), 191–198. (cited on pages 7 and 8)

Duan, J.; Bevis, M.; Fang, P.; Bock, Y.; Chiswell, S.; Businger, S.; Rocken, C.; Solheim, F.; van Hove, T.; Ware, R.; et al., 1996. GPS meteorology: Direct estimation of the absolute value of precipitable water. *Journal of Applied Meteorology*, 35, 6 (1996), 830–838. (cited on pages 9 and 14)

Elósegui, P.; Davis, J.; Jaldehag, R.; Johansson, J.; Niell, A.; and Shapiro, I., 1995. Geodesy using the Global Positioning System: the effects of signal scattering on estimates of site position. *Journal of Geophysical Research: Solid Earth*, 100, B6 (1995), 9921–9934. (cited on page 33)

Eriksson, D.; MacMillan, D. S.; and Gipson, J. M., 2014. Tropospheric delay ray tracing applied in VLBI analysis. *Journal of Geophysical Research*, 119, 12 (2014), 9156–9170. (cited on page 57)

Fang, P.; Bevis, M.; Bock, Y.; Gutman, S.; and Wolfe, D., 1998. GPS meteorology: reducing systematic errors in geodetic estimates for zenith delay. *Geophysical Research Letters*, 25, 19 (1998), 3583–3586. (cited on page 20)

Gardner, C., 1976. Effects of horizontal refractivity gradients on the accuracy of laser ranging to satellites. *Radio Science*, 11, 12 (1976), 1037–1044. (cited on pages 10 and 56)

Gegout, P.; Biancale, R.; and Soudarin, L., 2011. Adaptive mapping functions to the azimuthal anisotropy of the neutral atmosphere. *Journal of Geodesy*, 85, 10 (2011), 661–677. (cited on pages 10, 56, and 57)

Glickman, T. S. and Zenk, W., 2000. *Glossary of meteorology*. American Meteorological Society. (cited on page 82)

Hatanaka, Y.; Sawada, M.; Horita, A.; and Kusaka, M., 2001. Calibration of antenna-radome and monument-multipath effect of GEONET-Part 1: measurement of phase characteristics. *Earth, planets and space*, 53, 1 (2001), 13–21. (cited on page 19)

Herring, T.; Floyd, M.; King, R.; and McClusky, S., 2015a. GLOBK reference manual: global Kalman filter VLBI and GPS analysis program. release 10.6. (2015). (cited on page 8)

Herring, T.; King, R.; Floyd, M.; and McClusky, S., 2015b. GAMIT reference manual, release 10.6, department of earth, atmospheric, and planetary sciences. *Massachusetts Institute of Technology*, (2015). (cited on pages 7 and 8)

Herring, T.; King, R.; Floyd, M.; and McClusky, S., 2016. Introduction to GAMIT/-GLOBK, release 10.6, department of earth, atmospheric, and planetary sciences. *Massachusetts Institute of Technology, Cambridge, Massachusetts*, (2016). (cited on page 7)

Herring, T. A., 1992. Modeling atmospheric delays in the analysis of space geodetic data. *Proceedings of Refraction of Transatmospheric Signals in Geodesy, eds. J. C. De Munck and T. A. Spoelstra, Netherlands Geodetic Commission Publications on Geodesy*, 36 (1992). (cited on page 10)

Herring, T. A.; Davis, J. L.; and Shapiro, I. I., 1990. Geodesy by radio interferometry: The application of Kalman filtering to the analysis of very long baseline interferometry data. *Journal of Geophysical Research: Solid Earth*, 95, B8 (1990), 12561–12581. (cited on pages 1, 9, and 22)

Hobiger, T.; Ichikawa, R.; Takasu, T.; Koyama, Y.; and Kondo, T., 2008. Ray-traced troposphere slant delays for precise point positioning. *Earth, planets and space*, 60, 5 (2008), e1–e4. (cited on page 57)

Hofmann, B.; Lichtenegger, H.; and Collins, J., 2001. *Global Positioning System: Theory and Practice*. Springer. (cited on pages 7 and 35)

Holmes, C. E., 2012. *Queensland Floods Commission of Inquiry: Final Report*. Queensland Floods Commission of Inquiry. (cited on page 1)

Hurst, K. J. and Bar-Sever, Y., 1998. In-situ GPS antenna phase center calibration. *OPS/MET, Tokyo (available under https://trs.jpl.nasa.gov/bitstream/handle/2014/20513/98-1504.pdf?sequence=1)*, (1998). (cited on page 35)

Jackson, M. E., 2003. Geophysics at the speed of light: Earthscope and the plate boundary observatory. *The Leading Edge*, 22, 3 (2003), 262–267. (cited on page 82)

Ji, K. H., 2011. *Transient signal detection using GPS position time series*. Ph.D. thesis, Massachusetts Institute of Technology. (cited on page 142)

Johansson, J. M., 1998. GPS antenna and site effects. In *Advances in Positioning and Reference Frames*, 229–236. Springer. (cited on page 33)

Kalnay, E., 2003. *Atmospheric modeling, data assimilation and predictability*. Cambridge University Press. (cited on page 1)

Kaniuth, K. and Huber, S., 2003. An assessment of radome effects on height estimates in the EUREF network. *EUREF Publication*, , 12 (2003), 97–102. (cited on page 34)

King, M. A. and Watson, C. S., 2010. Long GPS coordinate time series: multipath and geometry effects. *Journal of Geophysical Research: Solid Earth*, 115, B4 (2010). (cited on page 33)

Kouba, J., 2009. A simplified yaw-attitude model for eclipsing GPS satellites. *GPS Solutions*, 13, 1 (2009), 1–12. (cited on pages 7 and 8)

Labbouz, L.; Van Baelen, J.; and Duroure, C., 2015. Investigation of the links between water vapor field evolution and rain rate based on 5 years of measurements at a midlatitude site. *Geophysical Research Letters*, 42, 21 (2015), 9538–9545. (cited on pages 1 and 56)

Lagler, K.; Schindelegger, M.; Böhm, J.; Krásná, H.; and Nilsson, T., 2013. GPT2: Empirical slant delay model for radio space geodetic techniques. *Geophysical Research Letters*, 40, 6 (2013), 1069–1073. (cited on pages 10 and 13)

Landskron, D.; Hofmeister, A.; and Böhm, J., 2015. *Refined Tropospheric Delay Models for CONT11*, 1–5. Springer Berlin Heidelberg, Berlin, Heidelberg. doi:10.1007/1345_2015_56. http://dx.doi.org/10.1007/1345_2015_56. (cited on page 57)

Larson, K. M.; Small, E. E.; Gutmann, E. D.; Bilich, A. L.; Braun, J. J.; and Zavorotny, V. U., 2008. Use of GPS receivers as a soil moisture network for water cycle studies. *Geophysical Research Letters*, 35, 24 (2008). (cited on page 82)

Lau, L. and Cross, P., 2007. Development and testing of a new ray-tracing approach to GNSS carrier-phase multipath modelling. *Journal of Geodesy*, 81, 11 (2007), 713–732. (cited on page 35)

Liou, Y.-A.; Teng, Y.-T.; Van Hove, T.; and Liljegren, J. C., 2001. Comparison of precipitable water observations in the near tropics by GPS, microwave radiometer, and radiosondes. *Journal of Applied Meteorology*, 40, 1 (2001), 5–15. (cited on pages 2, 30, 31, and 32)

Lyard, F.; Lefevre, F.; Letellier, T.; and Francis, O., 2006. Modelling the global ocean tides: modern insights from FES2004. *Ocean Dynamics*, 56, 5-6 (2006), 394–415. (cited on pages 7 and 8)

MacMillan, D. S., 1995. Atmospheric gradients from very long baseline interferometry observations. *Geophysical Research Letters*, 22, 9 (1995), 1041–1044. (cited on page 10)

Marini, J. W., 1972. Correction of satellite tracking data for an arbitrary tropospheric profile. *Radio Science*, 7, 2 (1972), 223–231. (cited on page 56)

Masoumi, S.; McClusky, S.; Koulali, A.; and Tregoning, P., 2017. A directional model of tropospheric horizontal gradients in Global Positioning System and its application for particular weather scenarios. *Journal of Geophysical Research: Atmospheres*, (2017). (cited on page 55)

Materna, K., 2014. *Analysis of atmospheric delays and asymmetric positioning errors in the global positioning system*. Undergraduate thesis, Massachusetts Institute of Technology. (cited on pages 82, 83, 84, and 87)

Materna, K. and Herring, T., 2013. Analysis of skewed GPS position estimates: Effects of coupling local topography and atmospheric conditions. In *AGU Fall Meeting Abstracts*, vol. 1, 0907. (cited on page 82)

McCarthy, D. D. and Petit, G., 2004. IERS conventions (2003). Technical report, International Earth Rotation and Reference Systems Service (IERS), Germany. (cited on pages 7 and 8)

Miyazaki, S.; Iwabuchi, T.; Heki, K.; and Naito, I., 2003. An impact of estimating tropospheric delay gradients on precise positioning in the summer using the japanese nationwide GPS array. *Journal of Geophysical Research: Solid Earth*, 108, B7 (2003). (cited on page 93)

Moore, M., 2015. *Empirical modelling of site-specific errors in GPS observations*. Ph.D. thesis, The Australian National University. (cited on pages ix, 33, 34, 35, 36, and 52)

Moore, M.; Watson, C.; King, M.; McClusky, S.; and Tregoning, P., 2014. Empirical modelling of site-specific errors in continuous GPS data. *Journal of Geodesy*, 88, 9 (2014), 887–900. (cited on pages 2, 19, 35, 36, 37, and 79)

Niell, A. E., 1996. Global mapping functions for the atmosphere delay at radio wavelengths. *J. Geophys. Res.*, 101, B2 (1996), 3227–3246. (cited on page 56)

Pavlis, N. K.; Holmes, S. A.; Kenyon, S. C.; and Factor, J. K., 2012. The development and evaluation of the Earth Gravitational Model 2008 (EGM2008). *Journal of Geophysical Research: Solid Earth*, 117, B4 (2012). (cited on pages 7 and 8)

Pérez-Ramírez, D.; Whiteman, D. N.; Smirnov, A.; Lyamani, H.; Holben, B. N.; Pinker, R.; Andrade, M.; and Alados-Arboledas, L., 2014. Evaluation of AERONET precipitable water vapor versus microwave radiometry, GPS, and radiosondes at ARM sites. *Journal of Geophysical Research: Atmospheres*, 119, 15 (2014), 9596–9613. (cited on page 2)

Queensland Reconstruction Authority, 2011. *Operation Queenslander: The State Community, Economic and Environmental Recovery and Reconstruction Plan 2011-2013*. Brisbane: Queensland Government. (cited on page 1)

Ray, J.; Altamimi, Z.; Collilieux, X.; and van Dam, T., 2008. Anomalous harmonics in the spectra of GPS position estimates. *GPS Solutions*, 12, 1 (2008), 55–64. (cited on page 35)

Riihimaki, L., 2014. personal communication. (cited on page 14)

Rocken, C.; Ware, R.; Van Hove, T.; Solheim, F.; Alber, C.; Johnson, J.; Bevis, M.; and Businger, S., 1993. Sensing atmospheric water vapor with the Global Positioning System. *Geophysical Research Letters*, 20, 23 (1993), 2631–2634. (cited on page 14)

Rothacher, M. and Beutler, G., 1998. The role of GPS in the study of global change. *Physics and Chemistry of the Earth*, 23, 9 (1998), 1029–1040. (cited on pages 20 and 69)

Saastamoinen, J., 1972. Atmospheric correction for the troposphere and stratosphere in radio ranging satellites. *The Use of Artificial Satellites for Geodesy*, (1972), 247–251. (cited on pages 8, 9, 13, and 14)

Schmid, R.; Dach, R.; Collilieux, X.; Jäggi, A.; Schmitz, M.; and Dilssner, F., 2016. Absolute IGS antenna phase center model igs08. atx: status and potential improvements. *Journal of Geodesy*, 90, 4 (2016), 343–364. (cited on page 33)

Schmid, R.; Steigenberger, P.; Gendt, G.; Ge, M.; and Rothacher, M., 2007. Generation of a consistent absolute phase-center correction model for GPS receiver and satellite antennas. *Journal of Geodesy*, 81, 12 (2007), 781–798. (cited on pages 7 and 8)

Seeber, G., 2003. *Satellite geodesy: foundations, methods, and applications*. Walter de Gruyter. (cited on pages xiv, 7, 34, and 35)

Springer, T.; Beutler, G.; and Rothacher, M., 1999. A new solar radiation pressure model for GPS satellites. *GPS Solutions*, 2, 3 (1999), 50–62. (cited on pages 7 and 8)

Tregoning, P.; Boers, R.; O'Brien, D.; and Hendy, M., 1998. Accuracy of absolute precipitable water vapor estimates from GPS observations. *Journal of Geophysical Research: Atmospheres*, 103, D22 (1998), 28701–28710. (cited on pages 2, 14, 16, 20, 31, and 63)

Tregoning, P. and Herring, T., 2006. Impact of a priori zenith hydrostatic delay errors on GPS estimates of station heights and zenith total delays. *Geophysical Research Letters*, 33, 23 (2006). (cited on pages 1, 9, and 16)

Tregoning, P. and Watson, C., 2009. Atmospheric effects and spurious signals in GPS analyses. *Journal of Geophysical Research: Solid Earth*, 114, B9 (2009). (cited on pages 2, 8, 10, and 16)

Van Baelen, J.; Reverdy, M.; Tridon, F.; Labbouz, L.; Dick, G.; Bender, M.; and Hagen, M., 2011. On the relationship between water vapour field evolution and the life cycle of precipitation systems. *Quarterly Journal of the Royal Meteorological Society*, 137, S1 (2011), 204–223. (cited on pages 1 and 56)

Wells, D.; Beck, N.; Kleusberg, A.; Krakiwsky, E. J.; Lachapelle, G.; Langley, R. B.; Schwarz, K.-p.; Tranquilla, J. M.; Vanicek, P.; and Delikaraoglou, D., 1987. Guide to GPS positioning. In *Canadian GPS Assoc*. (cited on page 7)

Wu, J. and Hsieh, C.-H., 2010. Statistical modeling for the mitigation of GPS multipath delays from day-to-day range measurements. *Journal of Geodesy*, 84, 4 (2010), 223–232. (cited on page 35)

Wübbena, G.; Schmitz, M.; and Boettcher, G., 2006. Near-field effects on GNSS sites: analysis using absolute robot calibrations and procedures to determine corrections. In *Proceedings IGS Workshop 2006, Darmstadt, Germany*, 8–12. (cited on page 35)

Wübbena, G.; Schmitz, M.; Menge, F.; Seeber, G.; and Völksen, C., 1997. A new approach for field calibration of absolute GPS antenna phase center variations. *Navigation*, 44, 2 (1997), 247–255. (cited on page 33)

Wübbena, G.; Schmitz, S.; and Prüllage, A., 2011. On GNSS station calibration of near-field multipath in RTK-networks. In *International Symposium on GNSS, Space-based and Ground-based Augmentation Systems and Applications, Berlin*. (cited on page 35)

Xu, G. and Xu, Y., 2016. *GPS: theory, algorithms and applications*. Springer. (cited on page 7)